



The
University
Of
Sheffield.

INSIGNEO
Institute for *in silico* Medicine

Modelling the femur strength in a virtual postmenopausal osteoporotic population for application to *in silico* clinical trials

Qiao Li

A thesis submitted in partial fulfilment of the requirements for the degree of
Doctor of Philosophy

INSIGNEO Institute for in silico Medicine
Department of Mechanical Engineering
The University of Sheffield

Submission Date: 19th November 2021

Abstract

Osteoporosis is a common disease that primarily affects elderly women and can potentially lead to hip fractures. Due to the high morbidity and mortality of hip fracture, the assessment of hip fracture risk is crucial in the management of osteoporosis. Femur strength is a key determinant of hip fracture risk, but it cannot be measured *in vivo*. Dual-energy X-ray absorptiometry (DXA) and Quantitative Computed Tomography (QCT) are commonly used densitometry techniques to measure bone mineral density (BMD). DXA is less expensive than QCT and is associated with lower radiation dose. Hence, DXA based areal BMD (DXA-aBMD) is often used to define endpoints in the clinical trials of medical interventions treating osteoporosis, being considered as a surrogate measure of femur strength, and by extension, of fracture risk. However, QCT can characterize true volumetric BMD (vBMD) and femur geometry. When this information is combined with subject-specific finite element modelling (QCT-SSFE), a much higher accuracy in predicting both femur strength and hip fracture risk can be achieved compared to DXA-aBMD. Therefore, the use of QCT-SSFE to define clinical trial endpoints could lead to more accurate determination of the efficacy of candidate interventions.

The use of QCT-SSFE in clinical trials is more feasible through virtual cohorts, due to the cost and radiation considerations mentioned above. A virtual population can be created based on a small group of physical subjects (in this study the Sheffield cohort was used). Distributions of biomechanical parameters (*e.g.*, femur geometry and material properties) in the virtual cohort reflects those in a target physical population. The virtual population is then used to augment the number of physical patients in the clinical trials. Thus, the overall aim of this PhD thesis is to develop a suitable approach to generate a virtual population with identical distributions of femur biomechanical parameters to those observed in a target population.

Several past studies have demonstrated that femur strength is influenced primarily by vBMD distribution and to a lesser extent by geometry (*i.e.*, size and shape). However, generating virtual cohorts from physical patients even considering only the variability of vBMD remains a challenge. This is because distributions of vBMD in target populations are unknown, and its relationship with aBMD (a biomechanical parameter for which distribution are better known) is poorly defined. Also, the characterisation of bone strength distribution in virtual cohorts has not been thoroughly investigated before.

In addition, the independent influence of femur geometry on femur strength has also been analysed in physical cohorts with limited size. A more detailed analysis of this influence (such as conducted on a virtual population) can inform what proportion of femurs need to be drawn from the tails of femur geometry distribution, in order that a representative distribution of femur strength – and of functions derived from it (such as fracture risk) – are achieved in that cohort.

The above challenges are met in this study as follows. First, local vBMD changes corresponding to the change of aBMD at femoral neck are predicted. This is achieved by developing two models (homogenous and density-specific algorithms). A key advantage of these models over existing approaches reported in the literature is that the models can be applied to a physical cohort without regard to the discretization used to create FE models of femur from CT images. The results showed that density-specific algorithm explained the variability of local vBMD in the physical cohort much better (17.2% root-mean-squared error in fitting) compared to the homogeneous algorithm (34.5%). These algorithms can be applied to a physical femur FE model in order to generate virtual CT-based FE models, corresponding to any number of different aBMD values, while femur geometry is held fixed. The virtual CT-based FE models can be identified with new virtual patients, or the same physical patient but at different timepoints over a period of ageing, or both (*i.e.*, a new virtual patient ageing over a period of time). This aspect of the present study concludes by analysing in detail the influence of change in aBMD on femur strength in sideways loading condition.

Second, the independent effect of femur length on femur strength (*i.e.*, keeping femur vBMD and shape fixed) is investigated. Virtual patients based on physical patients in the Sheffield cohort are generated by a simple scaling method. The sensitivity studies show that femur strength distribution is highly insensitive to femur length variation; to the point that variation in femur strength due to variation in femur length is smaller than the uncertainty in predicting femur using the QCT-SSFEE approach.

Future development is envisaged along two directions: a bone loss algorithm including the effect of mechanoregulation and generating virtual population of past clinical trials using Bayes' theorem to determine the size of virtual cohort.

Acknowledgement

I would like to express my sincere thanks to many people for their kindness and support throughout my PhD journey.

First, I would like to express my deepest appreciation to Dr. Pinaki Bhattacharya for constructive guidance, constant support, and endless patience since my first day in Sheffield. He is not just a supervisor but also a mentor to me. It is really my honor and luck to be your first PhD student.

Many thanks should also go to Prof. Claudia Mazza and Prof. Marco Viceconti for giving me the opportunity to explore the charm of biomechanics and virtual physiological human. I would never forget how excited I was when I first heard about VPH four years ago. Thank you for leading me to this new world.

Also, I am grateful to Dr. Xinshan Li, Dr. Enrico Dall'Ara and Prof. Damien Lacroix for the precious advice at the group meeting. I would also like to thank Prof. Miguel Juarez for his support in statistics and math.

My thanks are extended to Dr. Muhammad Qasim, Dr. Zainab Altai and Dr. Sachin Prabhu for sharing their knowledge in biomechanics and help in understanding CT2S. I would also like to thank Dr. Will Furnass for the professional support of HPC.

I also wish to thank all people in IMSB group and INSIGNEO. It has been a real pleasure to be a member of such a wonderful group.

Thanks PGR support team at the department of Mechanical Engineering on managing any administrative process. Especially thanks Chez for keeping me up to speed on each PhD milestones.

Additionally, I would like to thank my sponsor, the Shun Hing group and Mong Family Foundation to financially support my PhD.

Family is always my safety blanket. Without the unconditional love and unwavering support from my mum and dad, I would have never made it to this point.

Finally, I would like to give my special thanks to Hao Ding (Perhaps at this time I should refer you as Dr. Ding, lol). I would have never finished my thesis without your encouragement and company. By the way, the answer is yes.

Publication

The author has contributed to the following publications during the production of this thesis:

1. Bhattacharya P, Li Q, Lacroix D, Kadiramanathan V, Viceconti M. A systematic approach to the scale separation problem in the development of multiscale models. PLoS One, 2021, 16:1–26.
2. Li Q, Paggiosi MA, Eastell R, Bhattacharya P. A mathematical description of ageing-related decrease in localised volumetric bone mineral density in the proximal femur of elderly British women (in preparation).
3. Li Q, Paggiosi MA, Eastell R, Bhattacharya P. Predictions of age-specific hip fracture incidence in elderly British women based on a virtual population model (in preparation).

The work included in this thesis has also been disseminated at a number of conferences, workshops and supervisions which are listed below:

Conference proceedings

“Towards a virtual population of femur strength”. Proceeding published with ISBN 978-1-9996465-2-3. Li, Q., Prabhu, S., et al, BioMedEng2019, 2019.9

Oral presentations

1. “Predictions of Age-specific Hip Fracture Incidence in Elderly British Women based on a Virtual Population Model”. Li, Q., Prabhu, S., et al, CompBioMed2019, 2019.10, London, UK.
2. “Towards a virtual population of femur strength”. Proceeding published with ISBN 978-1-9996465-2-3. Li, Q., Prabhu, S., et al, BioMedEng2019, 2019.9, London, UK.
3. “Loss of bone strength depends on where bone is lost”, Prabhu, S., Li, Q., et al, ESB2019, 2019.7, Vienna, Austria.
4. “Proximal femur CT scans of British postmenopausal women show that bone loss is tissue dependent”. Prabhu, S., Li, Q., et al, ISB/ASB2019, 2019.7, Calgary, Canada.

5. “How weak is your future bone?” Li, Q., Engineering Researcher Symposium 2019 (Best talk in Mechanical Engineering), Sheffield, UK.

Poster presentations

1. “Towards a virtual population for evaluating hip fracture risk”. Q.Li, S. Prabhu, Z. Altai, M. Qasim, M. Viceconti, P. Bhattacharya., 2019.5, INSIGNEO showcase 2019, Sheffield, UK.

2. “Femur length distribution in osteoporotic British women”. Q. Li, P. Bhattacharya, M. Viceconti, 2018.5, INSIGNEO showcase 2019, Sheffield, UK.

Workshops and supervisions

1. Challenge 3 leader, Modelathon2020, 2020.1, Sheffield, UK.

2. Attendee and honoured best hand-on session award, the 4th Virtual Physiological Human Summer School, 2019.6, Spain, Barcelona.

3. Supervisor, INSIGNEO student summer placement, 2019.6-2019.9, Sheffield, UK.

Contents

Abstract.....	i
Acknowledgement	iii
Publication	v
Contents.....	vii
Abbreviation	xi
1. Overview	1
1.1 Introduction	1
1.2 Aims	2
1.3 Organisation of the thesis	3
2. Background	5
2.1 Epidemiology of osteoporosis	5
2.2 Epidemiology and burden of osteoporotic fractures.....	6
2.3 Most common anatomical sites for osteoporotic fractures	6
2.3.1 Wrist fracture	7
2.3.2 Vertebral fracture	7
2.3.3 Hip fracture	8
2.4 Postmenopausal Osteoporosis.....	9
2.5 Bone biology	9
2.5.1 Spatial organisation of bone tissue	11
2.5.2 Changes in bone tissue over time	13
2.6 Diagnosis of osteoporosis	14
2.7 Bone densitometry techniques	15
2.7.1 Roentgen method	15
2.7.2 Single-energy absorptiometry.....	16
2.7.3 Dual-energy absorptiometry	16
2.7.4 Quantitative computed tomography.....	18
2.8 Fracture risk assessment using regression models.....	22
2.9 Fracture classification and risk assessment using QCT-based finite-element analysis	24
2.10 Pharmacological management of osteoporosis	30

2.11 Clinical trials	32
2.12 <i>In silico</i> clinical trials	34
3. Bone loss without mechano-regulation	37
3.1 Introduction	37
3.2 Materials and Methods	43
3.2.1 Clinical cohort	43
3.2.2 Bone loss algorithm.....	44
3.2.3 Coefficient identification.....	47
3.2.4 A spatio-temporal atlas of local vBMD change.....	50
3.3 Results.....	51
3.3.1 Homogenous algorithm.....	51
3.3.2 Density-specific algorithm.....	52
3.3.3 A spatio-temporal atlas of local vBMD change	59
3.4. Discussion and conclusions	61
3.4.1 Homogenous algorithm.....	61
3.4.2 Density-specific algorithm.....	62
3.3.3 A spatio-temporal atlas of local vBMD change over a 6-year period	66
3.4.3 Limitations	71
4. Sensitivity of femur strength to variation in aBMD	73
4.1 Introduction	73
4.2 Method	75
4.2.1 FE analysis of physical patients (Sheffield cohort).....	75
4.2.1.1 Geometry and mesh.....	76
4.2.1.2 Material properties of physical patient	76
4.2.1.3 Reference system.....	77
4.2.1.4 Multiple loading conditions.....	78
4.2.1.5 Boundary constraints	79
4.2.1.6 Failure criterion.....	80
4.2.2 Generation and FE analysis of virtual patients	81
4.2.2.1 Material properties list extraction.....	83
4.2.2.2 Determining and mapping new properties	83
4.2.3 Virtual population analysis.....	86

4.3 Results.....	88
4.3.1 The rate of bone strength changing with respect to aBMD.....	89
4.3.2 Linearity assumption testing	90
4.3.3 Estimation of MinPatS for 5-year age-specific groups	91
4.4 Discussion and conclusions	92
4.4.1 The rate of change of bone strength with respect to aBMD	93
4.4.2 Estimation of MinPatS for 5-year age-specific groups	95
4.4.3 Pipeline of generating virtual population with varied aBMD	96
5. Sensitivity of femur strength to variation in femur length	98
5.1 Introduction	98
5.2 Methodology.....	101
5.2.1 Physical patients (Sheffield cohort).....	101
5.2.2 Generation and FE analysis of virtual patients	101
5.2.2.1 Full-femur anatomy estimation.....	103
5.2.2.2 Determination of femoral dimensions	103
5.2.2.3 Anatomy similarity	104
5.2.2.4 Affine Scaling.....	105
5.2.2.5 QCT-SSFE modelling	106
Mesh scaling and convergence analysis	106
Side-fall loading conditions	107
Boundary constrains	108
5.3 Results.....	109
5.3.1 Correlation between body height and femur length.....	109
5.3.2 Anatomical similarity check.....	111
5.3.3 Scaling factors	112
5.3.4 FE analysis results.....	112
5.4 Discussion	116
5.4.1 Body height vs. Femur length.....	116
5.4.2 Femur strength vs. femur length.....	119
5.4.3 Limitations	121
5.5 Conclusion.....	122
6. Conclusion and future work	124

6.1 The change of local vBMD with respect to aBMD	124
6.2 Virtual osteoporotic population with aBMD derived from epidemiological data.....	126
6.3 Virtual osteoporotic population with varied femur length.....	127
6.4 Future directions	128
6.4.1 Bone loss accounting for mechanoregulation	129
6.4.2 Generating virtual populations to re-investigate clinical trials.....	132
Reference.....	134
Appendices	157
List of Figures	157
List of Tables	163

Abbreviation

aBMD	Areal bone mineral density
ARF0	Absolute risk of current hip fracture
ARF10	Absolute risk of hip fracture over a 10-year period
AUROC	Area under the receiver operating characteristic curve
BH	Body height
BMC	Bone mineral content
BMI	Body mass index
Ct-vBMD	Cortical volumetric bone mineral density
DXA	Dual-energy X-ray absorptiometry
FE	Finite element
FL	Femur length
FN	Femoral neck
FRAX	Fracture Risk Assessment Tool
HSA	Hip structural analysis
In-vBMD	Integral volumetric bone mineral density
ISCT	<i>in silico</i> clinical trials
IT	Intertrochanter
MBB	Minimum bounding box
MinPatS	Minimum pathological strength
MPC	Multi-point constrains
NURBS	Non-Uniform Rational B-Splines
PBM	Peak bone mass
QCT	Quantitative computed tomography
r.m.s.	Root mean squared
RMSE	Root mean squared error
ROI	Region of interest
SAM	Statistical appearance model
SD	Standard deviations
SED	Strain energy density
SEE	Strain energy error

SSFE	Subject-specific finite element modelling strength
SSM	Statistical shape model
T	Trochanter
Tb-vBMD	Trabecular volumetric bone mineral density
TH	Total hip
vBMD	Volumetric bone mineral density
VOI	Volume of interest
VPH	Virtual Physiological Human

1. Overview

1.1 Introduction

Osteoporosis is a common disease among the elderly, especially for postmenopausal women. It is estimated that around 200 million people suffer from osteoporosis worldwide [1]. Even though osteoporosis is not fatal, it can lead to fragility fractures resulting in massive health-care costs and catastrophic reduction of life quality, and even death. It was reported that one in two women and one in five men over the age of 50 will experience one or more fragility fractures in their remaining lifetime [2]. Among all fragility fractures, hip fracture draws the most attention due to high morbidity and mortality rate. According to the National Hip Fracture Database, only 10% of people after experiencing hip fractures can fully recover to their states before fracture and more than half of them need to be taken care of by others [3].

It is necessary to identify who is at a high risk of hip fracture and provide proper treatment to prevent fractures. In current clinical practice, osteoporosis is diagnosed by the T-score of dual energy X-ray absorptiometry-based measurement of areal bone mineral density (DXA-aBMD). However, aBMD is only an indirect estimator of bone strength which is the key determinant of hip fracture risk. It is reported that the standard error of the linear regression between aBMD and bone strength is 22% [4]. In the last two decades, another approach, quantitative computed tomography-based subject-specific finite element model (QCT-SSFE) has been developed. This technology has now matured to a status where bone strength can be predicted with 6-7% higher accuracy by using QCT-SSFE than by using DXA-aBMD [4]. Based on QCT-SSFE predicted femur strength, a multiscale model to predict absolute risk of current hip fracture (ARF0) was able to classify hip fracture status with better head-to-head accuracy (area under the received operating characteristic curve, or AUROC of 85%) than femur strength (AUROC of 82%) [5].

Besides accurately diagnosing the risk of fracture in advance, pharmacological interventions are also important for the management of osteoporosis and prevention of fractures. Vast investigations have been conducted regarding the efficacy and safety of these

pharmacological interventions over the last five decades. Some rare but severe side effects and uncertain long-term efficacy of these drugs increase concerns of patients and thereby lead to low compliance to treatment [6,7]. One possible way to overcome these concerns is to develop a new drug with minor side effect and high efficacy for long term treatment. Any drug must undergo rigorous clinical trials before commercial distribution in order to evaluate the risk of potential toxicity and assess its efficacy. Although clinical trials are carefully designed, catastrophes may still occur leaving lifelong harm to the participants. Additionally, in many countries the traditional placebo-controlled trial of anti-osteoporosis drugs is considered as unethical to patients with high fracture risk when fracture is selected as the primary endpoint [8]. Given the high association with fracture risk, bone strength is considered as a common surrogate endpoint in such trials [4]. To estimate bone strength, the state-of-the-art method QCT-SSFE, as its name suggests, requires patients' QCT images as necessary inputs. However, the high radiation dose and expensive cost increases the difficulty in recruiting enough volunteers.

Such concerns could be reduced by *in silico* clinical trials (ISCT), which use computational models and simulations to assess devices and drugs [9]. Recently, the US congress and the European Parliament agreed to recommend ISCT as an additional tool for advancing the development of drugs and medical devices [9]. Several successful early adoptions have also been reported in the literature [10]. These adoptions offer an inspiration to use virtual patients in the clinical trials of new osteoporotic drugs. Hence, there is a need to investigate a proper approach of generating virtual population to improve the statistical significance of clinical trials.

1.2 Aims

The overall aim of this thesis is to develop a pipeline that can generate virtual populations for enriching physical cohorts recruited in studies of osteoporosis and its interventions. This thesis aims to achieve the following objectives:

- 1) To determine rates of change in local QCT-vBMD with respect to change in DXA-aBMD which explain the variability of QCT-vBMD in a physical cohort of postmenopausal British women.

Influence of mechano-regulation on the rates of change is neglected, and two separate constraints on the rates are considered:

- a) Homogenous algorithm: the rate of bone loss is uniform within the femur volume.
 - b) Density-specific algorithm: the rate of bone loss depends on the local vBMD.
- 2) To use the bone loss algorithms developed in objective 1 to explore the sensitivity of QCT-SSFE predicted bone strength to aBMD while bone geometry is fixed.
 - 3) To use virtual population approach to investigate the sensitivity of QCT-SSFE predicted bone strength to femur length while the aBMD and bone shape is fixed.

1.3 Organisation of the thesis

To achieve the objectives listed above, this thesis is organised into six chapters.

Chapter 1 overviews the main topic, motivation and methodological framework of the thesis.

Chapter 2 details the fundamental concepts on which this thesis is based. This includes epidemiology, diagnosis and management of osteoporosis. The state-of-the-art fracture risk assessment techniques are described. The concept of *in silico* clinical trials is also reviewed in this chapter.

Chapter 3 presents the study on predicting local bone loss in the absence of mechano-regulation. A description of clinical cohort and two bone loss algorithms are provided. The methods to determine the best-fit algorithm parameters are verified, the best-fit parameter values are compared with past results of similar nature reported in the literature and the implications of these comparisons are discussed in detail.

Chapter 4 presents a study on the influence of variation in aBMD on femur strength. The process of generating a virtual population possessing different aBMD distribution but with identical femur length is provided. The sensitivity of femur strength on aBMD is reported, compared with similar results in literature. Advantages and limitations of the current approach are discussed.

Chapter 5 presents the study on the influence of variation in femur length upon femur strength. The process of generating a virtual population possessing different femur length but with fixed vBMD distribution and femur shape is provided. The sensitivity of femur strength upon femur length is reported, and the implications on generating virtual cohorts are discussed.

Chapter 6 summarizes the main findings and highlights the contributions to the-state-of-the-art achieved in this thesis. Plans for future works are also provided at the end of this chapter.

2. Background

This chapter provides an overview of the prevalence of osteoporosis and osteoporotic hip fractures, highlighting its socioeconomic burden on individuals and the wider society. The mechanism of the most common form of osteoporosis – postmenopausal osteoporosis – is reviewed in detail. Methods for the diagnosis of osteoporosis are then critically analyzed. Non-invasive methods of bone quality assessment are analyzed in particular, as these lay down the context for the objectives of the present work. Basic information of clinical trials and concepts of *in silico* clinical trials are introduced at the end of this chapter, which outlines the promising application of virtual population.

2.1 Epidemiology of osteoporosis

Osteoporosis is a common chronic metabolic disorder in humans, which leads to the loss of bone. Osteoporosis affects an enormous number of people and osteoporotic fractures result in massive health-care costs to individuals and the society.

Studies published from 2000–2010 reported that at least 200 million people across the world were affected by osteoporosis [1]. The US Surgeon General’s Report (2004) stated that around 10 million Americans aged over 50 were osteoporotic and there were a further 34 million population at risk of this disease [11]. In Europe, it was estimated by a suite of studies that approximately 22 million women and 5.5 million men suffered from osteoporosis in 2010 [12,13].

The prevalence of osteoporosis is continuously increasing as the population ages. In the UK, the number of people aged over 50 is expected to rise from 22 million to 32 million in 40 years between 2010 and 2050. As a result, the UK osteoporotic population is projected to increase by about 59% to over 5 million individuals in 2050 [12,14]. The future prevalence of osteoporosis is potentially even worse in Asia reported by a range of studies [14–16]. By 2050, China and India, the two most populous nations of the world, will each have well over 600 million individuals aged over 50 years [14,15]. These estimations near doubling over current numbers makes for a bleak future, especially given to the existing high rates of prevalence of

osteoporosis in the over-50 populations in these countries (China: 35% in 2013 [16] and India: over 40% in 2016 [15]).

2.2 Epidemiology and burden of osteoporotic fractures

The loss of bone due to osteoporosis leads to compromised bone strength. Thus, osteoporotic bone can break from mechanical forces that would not normally break a healthy bone. When such fragility, or 'low energy' fractures occur, these can reduce the quality of life and even cause death.

Worldwide, more than 9 million fragility fractures occur each year, which means there is one new osteoporotic fracture patient every 3 seconds [17]. It is estimated that one in two women and one in five men over the age of 50 will experience one or more fragility fractures in their remaining lifetime [2]. In 2010, globally around 158 million individuals aged 50 years or more were at high risk of fragility fractures [18]. Asia had the largest at-risk population (84 million), accounting for 53% of all targeted individuals found above fracture threshold. Although Europe accounted for 20% or less of the global burden, it must be noted that the number of at-risk individuals is increasing everywhere [18]. In particular, it is predicted that by 2030 there would be more than 3 million osteoporotic fractures in total across the six largest European nations: Germany, Italy, France, the United Kingdom (UK), Sweden and Spain [17].

Osteoporotic fractures reduce the quality of life, and substantially increase both bone-associated morbidities and short-term mortality. This leads to a huge financial burden to society. Direct costs in the European Union (EU) were estimated at €32 billion (£21 billion) in 2000. This figure is expected to reach €77 billion (£51 billion) in 2050 [19]. In the United States (US), direct health care expenditures for fragility fractures exceeded \$17 billion (£12 billion) in 2005 and were projected to increase to \$25 billion (£18 billion) by 2025 [20]. In the UK, it is reported that more than half million fragility fractures occur each year, with an estimated associated annual expense to the National Health Service (NHS) exceeding £4.4 billion in 2010 [21].

2.3 Most common anatomical sites for osteoporotic fractures

The most common sites of fragility fractures are the wrist (distal radius), the spine (vertebrae) and the hip (proximal femur). Below the aetiology and epidemiology of osteoporotic fractures at these sites is briefly reviewed.

2.3.1 Wrist fracture

Wrist fracture generally occurs during the hard landing of a fall from a standing height on an outstretched arm. The lifetime risk of sustaining a wrist fracture is 5.72 times higher in women than in men aged over 50 years [2]. The incidence of wrist fractures shows a different pattern than that of vertebral and hip fractures (see below). The epidemiology has significant sexual dimorphism. For men, the incidence remains throughout life within a small range: below 1.9 per 1000 person-years (py). For women, it increases steeply from the perimenopausal period and reaches a plateau around 6.9 per 1000 py at 85 years of age [22]. Relative to vertebral and hip fractures, wrist fractures normally occur earlier in the course of life, as elderly women appear to have worse neuromuscular control and are more likely to fall onto their hips than wrists [23]. Hence, occurrence of wrist fractures is sometimes considered an early sign of osteoporosis.

2.3.2 Vertebral fracture

Vertebral fracture is poorly defined. Most vertebral fractures are asymptomatic, being caused by accumulated daily activities such as lifting, as opposed to one-off events such as falls. Patients suffering vertebral fractures will often go on with life without presenting to a physician. Even when patients present to the physician, the symptoms can vary from mild discomfort to severe back pain requiring hospitalization. Clinical diagnosis is based on the occurrence of vertebral body shape change (also referred as 'vertebral deformity') [24]. The situation is further complicated by the fact that vertebrae can deform due to unrelated reasons such as Scheuermann's disease [24]. As such, the age-standardised prevalence reported by different agencies varies from 9.8 to 29.3 per 1000 py in women and from 0.2 to 13.6 per 1000 py in men [24–26]. Although the diagnosis criteria of vertebral fractures are less consistent and majorities do not come to clinical attention, it still plays an important role in the evaluation of skeletal fragility, as it helps in the prediction of future fractures and may alter treatment therapies of osteoporosis [27].

2.3.3 Hip fracture

Most hip fractures occur after a fall from standing height or less and the direction of the fall is known to be important: a sideways fall directly on to the hip is more likely to cause a fracture than is falling forward [28]. Hip fracture attracts more attention among all fragility fractures because it causes significant morbidity including deterioration of the quality of life, increased mortality and healthcare cost.

Globally, around 3.94 million hip fractures are estimated to occur in 2025, rising to 6.26 million in 2050 [26]. Approximately 90% of hip fractures are observed in people above 50 years of age. The incidence of these fractures rises dramatically with age. The 10-year risk for women at 50 years old is 0.3%, which increases to 8.7% at 80 years old [2,24]. For men at the same ages, the numbers are 0.2% and 2.9% respectively [2,24]. Therefore, the burden of hip fracture for an aging population is expected to aggravate. These numbers also highlight that the age-standardised incidence in women is approximately twice of that in men [29]. The epidemiology of hip fractures has a remarkable geographical variation. The highest incidence, observed in north western Europe, is more than 10-fold above the lowest incidence, observed in Africa and northern Latin America [29].

Due to the severity of the injury, hip fracture nearly always requires admission to hospital and surgical treatment. The National Hip Fracture Database (NHFD) report provides the numbers (reviewed below) indicating the success of treatment in the UK [3]. Over 65,000 people aged over 60 were admitted to hospital because of hip fractures in 2017, with a mean length of hospital stay around 21 days. Although hip replacement surgery is performed routinely, 6.9% patients died within 30 days of surgery, and another 23% died within one year. This excess mortality is typically due to complications from hip surgery arising from old age. The NHFD report also showed that, even after 120 days of being discharged from the hospital, 90% of patients needed specialist care for both medicine and surgery, 9% became permanently immobile, 53% could no longer live independently, and only 10% recovered to a state where they could move without a walking aid.

In addition to the negative impact to life quality, hip fractures also cause tremendous pressure on public healthcare expenditure [30]. It is reported that in the UK costs from hip fractures to

NHS were estimated at £2.3 billion in 2016, accounting for nearly half of annual cost of fragility fractures (£4.4 billion) [31]. Furthermore, from 2016 to 2066, additional 8.6 million people are expected to be over 65 years old (26% of the total population), which will double the number of fragility fractures if no changes are made to the current practice [32,33].

Due to the high socioeconomic burden of hip fractures, the remainder of the thesis will focus on fragility fractures at this anatomical site only.

2.4 Postmenopausal Osteoporosis

Facts and figures presented in the previous sections indicated that the prevalence of osteoporosis and osteoporotic fractures are higher in women than in men. In fact, the aetiology of postmenopausal osteoporosis is distinct from other forms of osteoporosis. It cannot be simply defined as osteoporosis when women reach menopause (*i.e.*, a woman might have a secondary form of osteoporosis since childhood and might be (untreated) osteoporosis when she reaches menopause). It has to be confirmed by analysis of bone turnover, since postmenopausal osteoporosis occurs due to the deficiency in oestrogen and androgen. This causes bone resorption to dominate over bone formation and leads to trabecular bone loss. This form of osteoporosis is also known as type I primary osteoporosis. As its name suggests, this is the most common form of osteoporosis, and the remainder of this thesis is concerned with this form of osteoporosis. Other categories of osteoporosis arise from consideration of the factors that affect bone metabolism. Type II primary osteoporosis, or senile osteoporosis, refers to systemic bone loss induced by ageing. It is found in both sexes and predominantly leads to cortical bone loss [34]. Secondary osteoporosis refers to situations where one can identify a clear aetiologic mechanism, for example due to drugs such as glucocorticoids or due to conditions such as chronic kidney disease [35].

2.5 Bone biology

Even though millions of hip fractures occur worldwide each year, researchers estimate that over half of these are preventable [36]. However, this requires, first and foremost, an accurate diagnosis of hip fracture risk. The present section will review the basic biology of bone with

attention to aspects that are relevant to fracture risk. Most of the description given here can be found in standard texts on bone biology such as Burr et al (Chapter 1, 4& 5), Pawelec et al (Chapter 2) and Marcus et al (Chapter 1, 19, 22) [37–43]. Later sections will trace the historical development of methods of osteoporosis diagnosis up to the state-of-the-art. This critical review will lay the foundation for the objectives of this thesis.

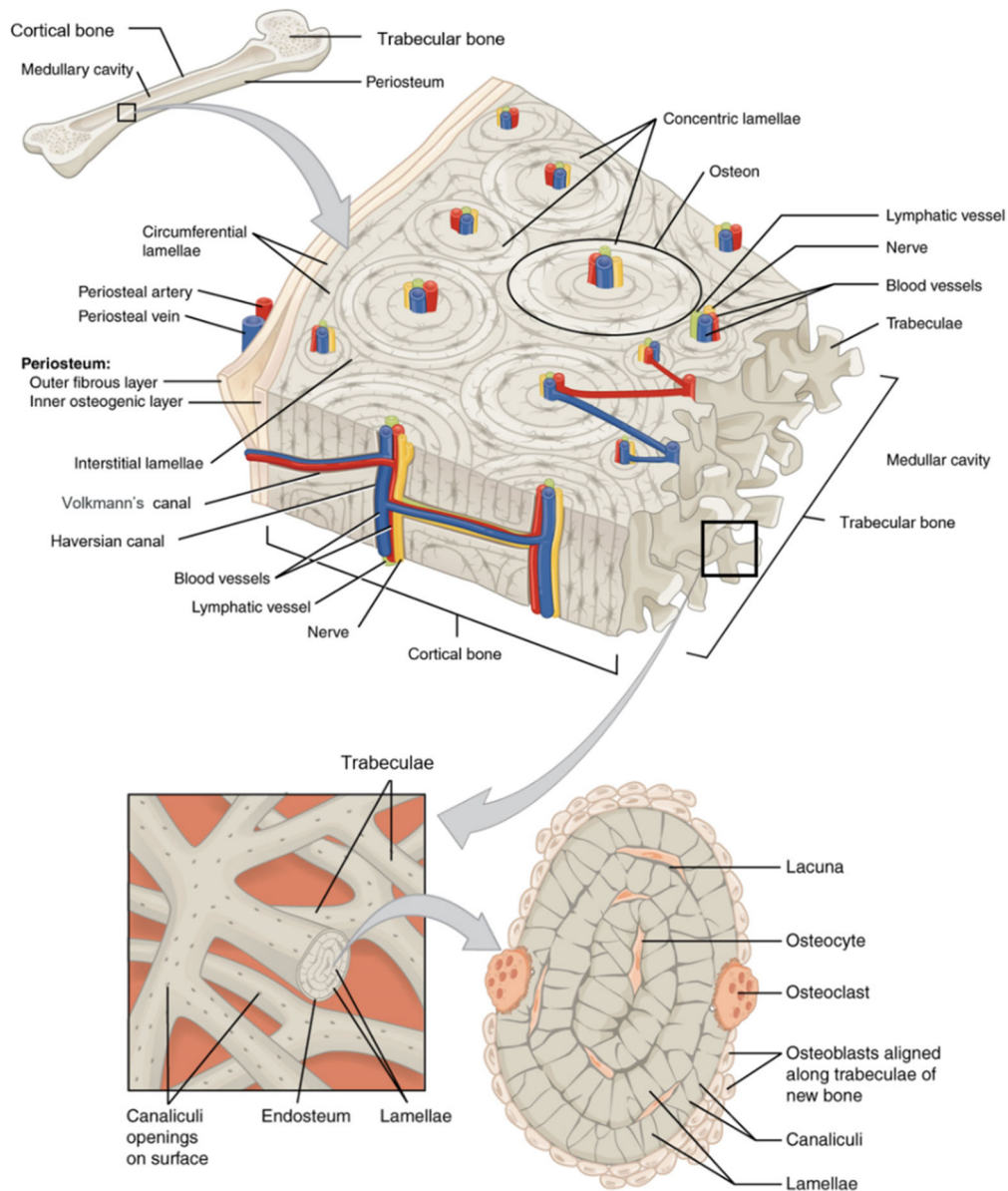


Figure 2.1 Schematic diagram of cortical and trabecular bone. Lamellae are arranged into osteons and trabeculae, which constitute cortical and trabecular bone respectively. The periosteum consists of two layers (outer fibrous layer and inner osteogenic layer) that wraps the surface of bone. Reproduced from Biga et al [44] with permission.

2.5.1 Spatial organisation of bone tissue

The term bone has two distinct meanings. The first refers to bone as an organ, such as the upper arm (humerus), the upper thigh (femur), the lower jaw (mandible), etc. The second refers to the material constituting the bone organ. When intending the second meaning, often the term “bone tissue” is used. Two types of bone tissue can be identified throughout the adult human skeleton: cortical (compact) bone and trabecular (cancellous or spongy) bone (Figure 2.1).

Cortical bone is mainly present under the periosteum (Figure 2.1) and in the diaphysis of long bones. It comprises approximately 80% of the total bone mass in the body [45]. It is denser, stiffer and stronger than trabecular bone *i.e.*, elastic modulus and yield stress of cortical bone are generally higher, as shown in Figure 2.2, and as such, it provides support and protection functions.

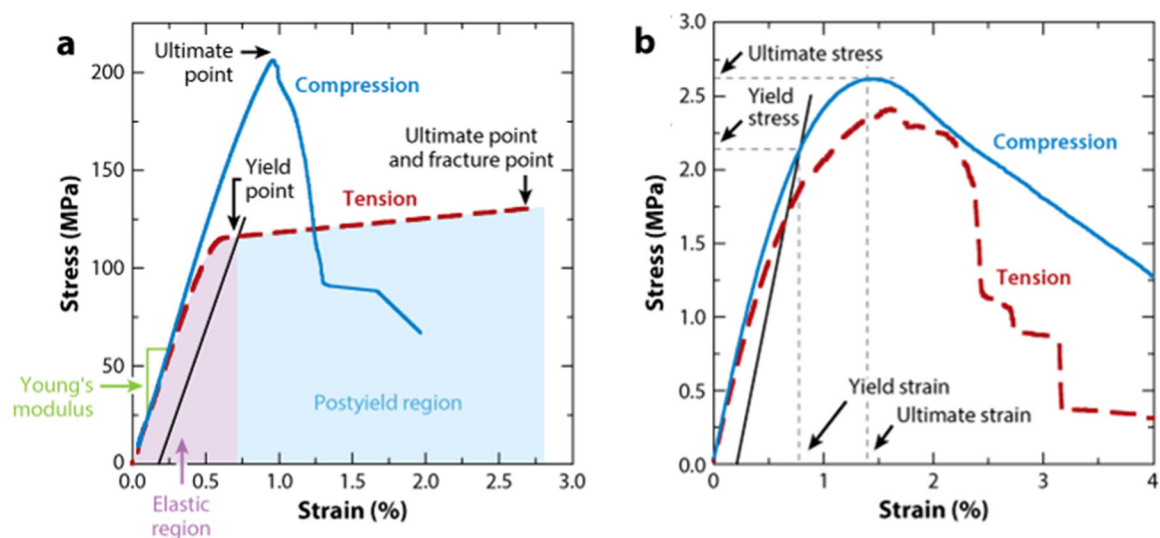


Figure 2.2 Stress-strain curves of monotonic tensile and compressive tests for human femoral (a) cortical bone along the longitudinal direction and (b) trabecular bone along the principal direction. Reproduced from Morgan et al [46] with permission.

The basic structural unit of cortical bone is the osteon (Figure 2.1). Osteons comprise lamellae arranged concentrically around the Haversian canal which contains blood vessels. Within an individual lamella, the inorganic bone mineral (hydroxyapatite crystal) is bound to organic

collagen fibres that are aligned to a preferred direction. Bone mineral is the primary load-bearing constituent of bone, and the measurement of bone mineral density plays a leading role in diagnosis and management of osteoporosis. The preferred direction of collagen fibres changes from one lamella to another (i.e., through the thickness of the osteon) giving rise to a cross-ply structure (Figure 2.3). Throughout the osteon volume, bone cells called osteocytes are embedded in pores known as lacunae which are themselves connected via fluid channels known as the lacuna-canalicular network. Blood vessels in the Haversian canal supply the osteocytes in the osteon.

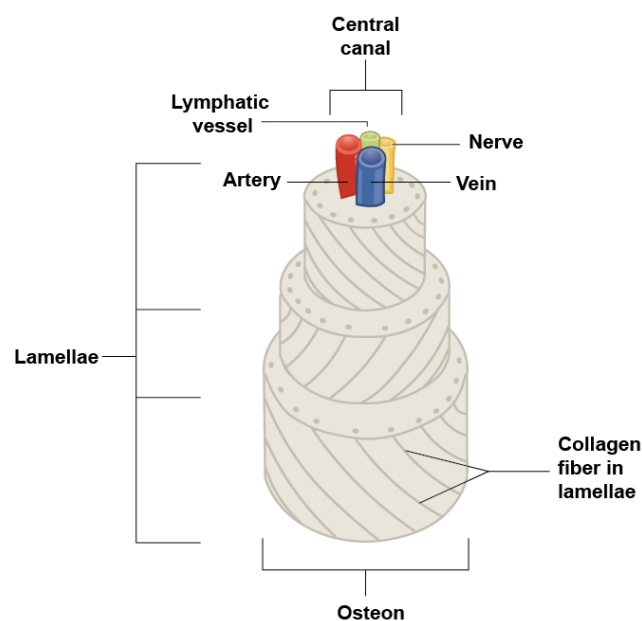


Figure 2.3 Schematic diagram of osteon. Osteons comprise lamellae arranged concentrically around the Haversian canal. Reproduced from Biga et al [44] with permission.

Trabecular bone is found generally in the metaphysis of long bones and has larger surface to volume ratio compared to cortical bone. It is composed of a network of intersecting plate- and rod-like structures called trabeculae. These constitute around a quarter of total tissue volume, with remaining space filled with marrow and blood vessels [37]. Despite being less stiff, the special foam-like microstructure of trabecular bone allows it to sustain more strain before failure (Figure 2.2b). Trabeculae are aligned along the lines of major compressive or tensile stress which enables effective distribution of load using the minimal amount of material. The material of trabecular bone is the same mineralised collagenous matrix that

comprises the lamella of the osteons. However, collagen fibres within an individual trabecula do not possess a preferred orientation.

2.5.2 Changes in bone tissue over time

Bone is a living, active tissue that houses blood vessels and consists of various cells, proteins, and minerals, which enable it to grow and renew throughout life. Before birth, bone develops by intramembranous and endochondral ossification, which refer to the transformation into hard bone of basic connective tissue and cartilage tissue respectively. From birth to adulthood, the process of endochondral ossification is mainly responsible for the increase in length of limbs and the resulting increase in skeletal mass. At the same time, the process of bone modelling is also present, which leads to change in skeletal form. Changes in skeletal form include the appearance of natural features such as tuberosities, crests, etc. but also the appearance of subject-specific variations in these features. It is important to note that unlike intramembranous and endochondral ossification, bone modelling involves only bone-specific cells, namely, osteoclasts, osteoblasts and osteocytes. Bone modelling is characterised by two separate processes, bone resorption by osteoclasts, bone formation by osteoblasts, with osteocytes playing a role in the control of these processes. Furthermore, in bone modelling, these processes typically occur at distinct locations. For example, bone formation at the outer surface and bone resorption at the inner surface allows a long bone to increase in circumference.

Once peak bone mass (PBM) is attained – typically by the mid-twenties for both sexes – the normal adult skeleton goes into a state of homeostasis. This is characterised by nearly equal rates of bone formation and bone resorption. The main process active in this period is called bone remodelling, whereby old bone is replaced by new bone by coupling bone resorption and formation at the same spatial location [47,48]. Remodelling allows the body to repair microfractures and maintain a healthy skeleton, and the adult skeleton is completely renewed by remodelling every 10 years. Intramembranous and endochondral ossification processes are active in adults only during fracture healing.

The rates of bone formation and resorption are controlled by hormonal signalling (both local and systemic) and to some extent also by mechano-regulation (mechanical stresses and

strains). Oestrogen and androgen levels play an important role in hormonal signalling. As menopause changes these levels (in favour of resorption), homeostasis is disrupted and can lead to a pathological loss of bone. Note that bone formation and resorption processes occur on the surfaces of bone tissue exposed to blood vessels. As trabecular bone has a larger exposed surface than cortical bone, it is more vulnerable to postmenopausal osteoporosis.

2.6 Diagnosis of osteoporosis

Osteoporosis is referred as a “silent” disease because typically poor bone quality has no outward symptoms. Hence it is challenging to detect it until fracture occurs. In the past, it was difficult to define osteoporosis in clinical terms as bone mineral density (BMD)-focused measurement does not fully reflect all risk factors for fractures, whereas a fracture-based identification fails to include individuals at risk. Historically, “osteoporosis” was first referred as a term to describe porous bones observed in post-mortem by a French pathologist Jean Lobstein in 1820s [49]. Prior to the 1940s, except for senility induced osteoporosis, all other cases were ascribed as “idiopathic” (or unexplained) osteoporosis. Fuller Albright’s work in the 1940s clearly established postmenopausal osteoporosis as a separate mechanism [49]. Later researchers attempted to define osteoporosis in more specific ways. However, various emphasis on different aspects did not reach international consensus until the publication of the World Health Organization (WHO) diagnostic criteria in 1994 [50].

Table 2.1 WHO definition of osteoporosis based on T-score of BMD [51].

Classification	T-score
Normal	> -1
Osteopenia	$-2.5 < \text{T-score} \leq -1$
Osteoporosis	≤ -2.5
Established osteoporosis	≤ -2.5 with presence of fragility fracture

The current diagnostic criteria (see Table 2.1) are based on the subject’s T-score, which is the difference between their BMD and the mean BMD in a reference population (young healthy sex-matched adults), expressed in standard deviations (SD) of the latter. Mathematically, it is

written as Equation 2.1.

$$\text{T-score} = \frac{\text{Subject BMD} - \text{Mean BMD of Young Healthy Adults}}{\text{SD BMD of Young Healthy Adults}} \quad (\text{Equation 2.1})$$

Here, BMD is measured by dual energy X-ray absorptiometry (DXA). It is important to specify the region of interest for BMD measurement, *e.g.* the femoral neck, as well as the reference population *e.g.* women aged 20-29 years in the NHANES III database [51].

2.7 Bone densitometry techniques

Although it is acknowledged that bone mineral density (BMD)-focused measurement does not fully reflect all risk factors for fractures, it is essentially synonymous with the diagnosis of osteoporosis. This section briefly reviews and compares the advantages / disadvantages between the historically important BMD measurement methods and the various measures adopted. Table 2.2 provides a summary of this comparison at the end of this section.

2.7.1 Roentgen method

Since Wilhelm Conrad Roentgen discovered X-rays in 1895 and made the first photograph of his wife's hand, researchers quickly realized the clinical importance of X-rays, as it unlocked the visual access of the inner structure, especially bone, of living subjects. Later many researchers were devoted to the application of X-rays in revealing the secrets of the skeleton and examining fractures and dislocations of bone. In 1901 Weston Price firstly attempted to quantify bone using bisecting technique based on dental radiograph, and successors further developed several bone measurements methods based on roentgen sources [52]. However, the relatively insensitiveness of conventional X-ray to bone minerals and variability of X-ray sources and films discouraged later attempts. Therefore, simple radiography methods were almost abandoned, and the usage was limited to semiquantitative evaluations of cortex and trabecular morphology. These semiquantitative evaluation methods still exist for some clinical uses because of their simple requirements (plain radiographs). The most widely known application is the Singh method which evaluates the change of trabecular pattern at the hip and has been confirmed as an effective tool in epidemiological studies of hip fracture [53,54].

2.7.2 Single-energy absorptiometry

Alongside the development of roentgen methods, researchers also attempted to measure bone mass by using radionuclides instead of a roentgen radiation source. The major advantage of radionuclide over a roentgen source is that its emissions have distinct energies rather than a continuous spectrum, which is necessary to calculate the relationship between transmission of photon beam (film blackening) and bone mineral content.

In 1963 Cameron et al proposed the first commercially available bone mass measurement technique – single-photon absorptiometry (SPA) – which uses ^{125}I or ^{241}Am as radioactive source and a scintillation detector system as counting technique to quantify photon beam transmission [55]. This method eliminates errors caused by the variability of X-ray films and reduces errors introduced by the presence of soft tissue around the bone by subtracting the amount of soft tissue absorption from the total absorption. Due to its low cost, ease of application, high precision, and low radiation exposure, use of SPA was widespread at the end of last century [56]. However, SPA requires the scanned site to have a flat parallel surface and be soaked in water or other soft tissue equivalent materials, which limits the site to be limbs, typically the forearm. With the development of X-ray sources and detectors, single-energy X-ray absorptiometry (SXA) has gradually replaced SPA. The basic physical principles of SXA are identical to SPA but using the X-ray beam rather than the γ -ray source. Compared to SPA, SXA avoids the need for radionuclide isotopes (low radiation dose) and increases the scanning efficiency and precision by higher photon flux.

2.7.3 Dual-energy absorptiometry

The application of SPA and SXA was limited by the fact that it can only be used for measuring the peripheral skeleton, but bone densitometry of hip and spine are crucial for predicting fragility fracture risk. Thus, dual-photon absorptiometry (DPA) and dual-energy X-ray absorptiometry (DXA) were developed and applied to meet the need in more clinically relevant sites.

DPA was introduced in the 1970s and ^{153}Gd was most commonly used radionuclide which could emit both low-energy (44 keV) and high-energy (100 keV) photons [57]. The different

attenuation of two energy photons in bone and soft tissue allowed bone minerals of more clinically relevant sites (such as spine, hip, and whole body) to be calculated without the need for a water bath. Due to the radionuclide decay, the light source in DPA had to be replaced annually. A low photon flux causes scanning times to be considerably long (whole body of 40-60 mins) and images to be poor spatial resolution (3mm) [58,59]. These limitations led to the transition from DPA to DXA.

The first commercially available DXA scanner was published by Hologic Inc in 1987. The basic concept and operation of DXA in bone densitometry is as same as DPA, except using X-rays as radiation source. Bone minerals and soft tissues are separated by optimised two energies of X-ray beams. There are two main types of energies systems among different DXA manufactures: one is that X-ray tube potential is alternated from low energy (70-100kVp) to high energy (140kVp), while the other is using rare earth filter to separates the X-ray distribution into two energy photons, 40keV and 70keV for low and high energies respectively [60].

DXA measures the areal BMD (DXA-aBMD, units: $\text{g}\cdot\text{cm}^{-2}$) which is the bone mineral content (BMC) in grams divided by the two-dimensional projected area in cm^2 of bone site being scanned. Because aBMD reported by different manufacturers for the same individual could be different, T-score (Equation 2.1) and Z-score (Equation 2.2) were developed as derived measures.

$$\text{Z-score} = \frac{\text{Subject BMD} - \text{Mean BMD of Same Age Adults}}{\text{SD BMD of Same Age Adults}} \quad (\text{Equation 2.2})$$

In contrast with the T-score, the Z-score is computed relative to a reference population of the same age as the subject. The typical regions of interest for measuring DXA-aBMD at the hip are the femoral neck, trochanter and total hip.

Several technical limitations in the general application of DXA for diagnosis should be recognised. First, the BMD derived by DXA is a two-dimensional value, namely areal BMD (aBMD), rather than a true volumetric density. Second, the presence of other bone diseases in the elderly such as osteomalacia and osteoarthritis may also affect the accuracy of aBMD

measurements [61]. Third, DXA is limited in measuring the mass distribution in cortical and trabecular bone compartments and in the evaluation of bone geometry and microstructure, which are the domain of QCT [62].

It is important to note that proper positioning of the patient during DXA scans must be ensured to avoid BMD measurement errors. For example, patients must internally rotate the femur for 15-25° after lying down on the scanning table to ensure that the long axis of the femoral neck is parallel perpendicular to the X-ray beams [63]. Other positions in the hip scanning could cause 0.9-4.5% error for femoral neck BMD, because a misalignment of the femoral neck relative to the scan table would foreshorten the bone area and increase aBMD correspondingly [64]. The rectangular box defining the femoral neck measurement varies according to the manufacturer: for GE Lunar (Figure 2.4a), the femoral neck box is at the narrowest and lowest density section of the neck, usually in the middle between the femoral head and the trochanter; for Hologic (Figure 2.4b), the box is located on the distal part of the femoral neck [63].

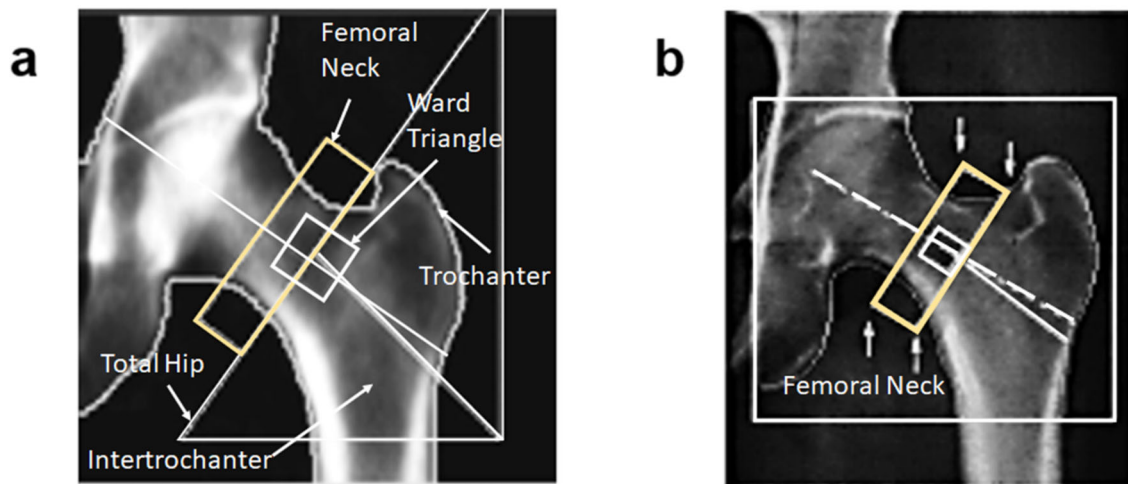


Figure 2.4 Examples of DXA scans at proximal femur (**a** Lunar and **b** Hologic). The region of interest for femoral neck is marked in yellow rectangular box. Reproduced from El Maghraoui et al [63] with permission from Oxford University Press.

2.7.4 Quantitative computed tomography

Quantitative computed tomography (QCT) is performed using X-rays and generates a series

of two-dimensional slices which are reconstructed into a three-dimensional model. An in-depth introduction to QCT imaging for bone can be found elsewhere. The brief overview provided here draws on the recent review by Adams [65]. CT images are derived by two steps: data acquisition of initial scan and mathematical calculation to achieve tomographic reconstruction. The typical scan region for proximal femur normally includes 1-2 cm above the femoral head and a few cm below the lesser trochanter and the main volumes of interest consist of femoral neck, the trochanter and intertrochanteric region. Greyscale numbers in CT images are normalized to dimensionless Hounsfield Units (HU). HU is calculated from a linear transformation of the X-rays' attenuation coefficients, with air and water arbitrarily defined as -1000HU and 0HU respectively. As tissue density is proportional to the attenuation rate of X-rays, HU is also proportion to density. Hence, the denser the bone is at a particular location, the more X-rays get absorbed, the whiter CT images appear, and the higher is the HU number. Volumetric bone mineral density (vBMD, in $\text{g}\cdot\text{cm}^{-3}$) of each voxel in the scanned volume of interest is obtained from HU using calibration phantoms. Typical phantoms are simultaneously scanned with the patient (in-scan phantoms, Figure 2.5a) and are made from a series of solid or liquid materials (such as certain known concentrations of calcium hydroxyapatite or potassium diphosphate) that have similar X-ray attenuation coefficient to bone. If no in-scan phantoms are applied in QCT, either internal BMD calibration or asynchronous BMD calibration must be performed [66]. It is noticeable that the results from different types of calibration phantoms are not interchangeable. Hence, anthropomorphic standardization phantoms (ASPs) are designed to reduce QCT inter-scanner differences and control the measurement quality between DXA and QCT. One commonly adopted ASP is the European Spine Phantom (ESP) proposed by Kalender et al [67]. However, a recent study indicates that even calibrated with ASP, inter-scanner differences of QCT-based BMD measurement still remain significant [68].

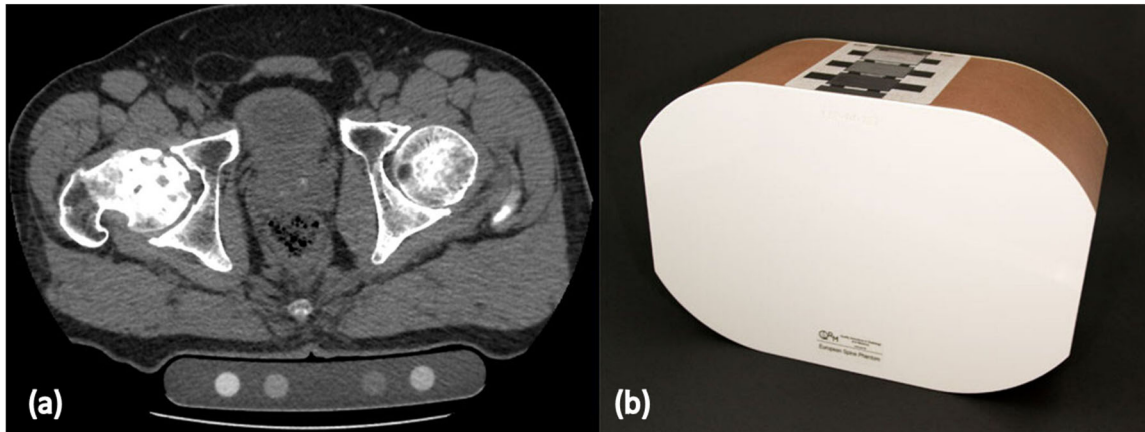


Figure 2.5 (a) An example of a four-element in-scan phantom (B-MAS200, Kyoto Kagaku, Kyoto, Japan), placed under the hip: the phantom is made of urethane foam ($0 \text{ mg}\cdot\text{cm}^{-3}$) containing known density hydroxyapatite rods ($50 \text{ mg}\cdot\text{cm}^{-3}$, $100 \text{ mg}\cdot\text{cm}^{-3}$, $150 \text{ mg}\cdot\text{cm}^{-3}$, and $200 \text{ mg}\cdot\text{cm}^{-3}$). Reproduced from Uemura et al [69] with license from Springer Nature and Copyright Clearance Centre; and (b) European Spine Phantom used for cross-calibration between scanners and quality control. Reproduced from European Spine Phantom [70].

Application of QCT for osteoporosis diagnosis is limited by certain factors. The main limitation is that there is no direct correspondence between QCT based vBMD and the more well-established DXA-based T-score [71]. To address this, some researchers have proposed an adaptation to transform QCT derived vBMD into DXA-equivalent aBMD, referred as computed tomography X-ray absorptiometry (CTXA), which might extend the clinical utility of QCT [72]. However, QCT also presents distinct advantages over DXA. One important advantage is that a threshold ($\sim 0.45 \text{ mg}\cdot\text{cm}^{-3}$) can separate cortical and trabecular bone regions of interest (ROIs) within QCT images [73]. The outputs of QCT typically include vBMD, volume, bone mass for each bone compartment. As trabecular bone is predominantly lost in postmenopausal osteoporosis, separate measurement of trabecular vBMD can potentially improve diagnosis [65]. The heterogeneity of marrow and fat distribution in bone, partial volume effects and sensitivity to threshold levels used to separate cortical and trabecular bone influence the actual improvement that can be realised. Nevertheless, as opposed to DXA-aBMD, QCT provides a size-independent volumetric bone mineral density. This is a major advantage of this technique. Hence, although the radiation dose and cost of QCT is higher than DXA, it can be used to estimate bone strength of proximal femur, and further to predict hip fracture risk [65], which will be discussed in detail in Section 2.9.

Table 2.2 Characteristics of common bone densitometry techniques. Adapted from Cummings et al [74] and Sheu et al [75]. *Precision error for SPA and DPA are from Kanis et al [76]

Technique	Sites	Source	Precision error	Advantages	Disadvantages
Roentgen	Hip	X-rays	NA	Simple requirement	Insensitive to bone minerals
SPA	Limbs	Radioisotope I^{125}	2-5% *	Ease of application	Limited to peripheral site; need for replacing light source
SXA	Limbs	X-rays	1-3%	Low radiation dose; high efficiency	Limited to peripheral site
DPA	Hip, spine	Radioisotope Gd^{153}	8-10% *	Wide applicability for different sites	High radiation dose; need for replacing light source; poor spatial resolution
DXA	Any clinical site	X-rays	1-2%	High precision for fracture risk prediction	Sensitive to patient's positions; affected by other bone diseases
QCT	Any clinical site	X-rays (CT)	2-4%	vBMD; cortical and trabecular bone measurements	High cost; high radiation dose; fewer analysis guidelines

2.8 Fracture risk assessment using regression models

In the US, of the 2 million people sustaining fragility fractures annually, around 15% experience a second fracture in the successive 2-3 years after fracture. This causes an additional financial burden to the society of over \$6.3 billion (approximately £4.5 billion) [36]. The fact that these individuals at high risk of osteoporotic fracture remained untreated even after sustaining the first fracture, underscores the commonly acknowledged large “osteoporosis treatment gap”. Large treatment gaps have also been reported in Europe where around 55%-75% women were above the threshold risk for fragility fracture but did not receive any osteoporosis treatment [77–79].

The treatment gap in management of osteoporosis is partly caused by therapy discontinuation, but also by insufficient case finding (*i.e.* diagnosis) in the first place [80]. Poor diagnosis is partly due to over-reliance on medical practitioners’ experience [81]. The development of T-score based classification is a great step forward to address this issue. Yet, several studies have revealed that this test has high specificity but low sensitivity [50]. More than half of fragility fractures occur in postmenopausal women who are not distinguished as osteoporotic according to WHO criteria and many of these women are neglected from receiving proper treatments [82–85]. One possible explanation for low sensitivity of T-score test is that sole use of aBMD only accounts for one aspect for fracture risk (*i.e.* the quantity of bone), and there may exist other significant and independent determinants of fracture risk [84]. Some studies illustrated that apart from low aBMD, age, previous history of fracture, low body weight, physical inactivity, drug usage, alcohol intake are some clinical factors that contribute independently to fracture risk [19,61,83]. Therefore, multifactorial regression models (such as the Garvan Fracture Risk Calculator, CAROC assessment tool, QFracture) have been developed to accurately investigate individuals at high-risk of fragility fractures. Arguably, one of the most successful of these is Fracture Risk Assessment Tool (FRAX) [86,87] and is reviewed below.

FRAX is a computer-driven fracture risk assessment tool for people aged between 40 and 90 years based on well-validated clinical risk factors (such as age, body mass index, tobacco and alcohol usage, fracture history and rheumatoid arthritis etc.) with or without DXA-derived

bone mineral density at femoral neck, that outputs the 10-year probability of major fragility fractures or hip fractures (see Figure 2.6 as an example) [87]. As fracture risks varies markedly in different countries (greater than 10-fold), the FRAX algorithm is calibrated by local population data and presently there are 72 country-specific models available for application [88]. For some multi-ethnic countries where the epidemiology of fracture for specific ethnic groups is known, for example US and Singapore, ethnicity-based models are provided for more accurate estimations [88].

Country: **UK** Name/ID: [About the risk factors](#)

Questionnaire:

1. Age (between 40 and 90 years) or Date of Birth
 Age: Date of Birth: Y: M: D:

2. Sex Male Female

3. Weight (kg)

4. Height (cm)

5. Previous Fracture No Yes

6. Parent Fractured Hip No Yes

7. Current Smoking No Yes

8. Glucocorticoids No Yes

9. Rheumatoid arthritis No Yes

10. Secondary osteoporosis No Yes

11. Alcohol 3 or more units/day No Yes

12. Femoral neck BMD (g/cm²)
 T-score: -2.2

BMI: 22.7

The ten year probability of fracture (%)

with BMD

Major osteoporotic	12
Hip Fracture	3.1

[View NOGG Guidance](#)

If you have a TBS value, click here:

Figure 2.6 An example of interface of FRAX estimation for a 72-year-old UK female with no high-risk clinical features and a femoral neck aBMD of 0.726 g·cm⁻² [88].

By incorporating clinical risk factors, FRAX improves not only the chances of early detection, but FRAX-derived fracture risk is also applied as intervention thresholds in some countries. For example, according to the US National Osteoporosis Foundation, the decision to initiate pharmacologic treatment should be based partially on whether 10-year probabilities of a major osteoporotic fracture or hip fracture are above specific thresholds [89]. A study expressed a concern that this single threshold derived from cost-effectiveness analysis would underestimate fracture risk for younger people while overestimate it for older ones [90]. In

the UK, age-dependent treatment thresholds, currently adopted by the National Osteoporosis Guideline Group (NOGG) guideline (easily accessed via FRAX UK calculator website), are based on setting fracture probability for women without prior fractures equivalent to women with a prior fracture [91]. Yet, it is notable that these thresholds should not substitute the clinical judgement. Instead, it is a guidance to assist clinicians for making treatment decisions [92].

Several important limitations of FRAX need to be considered. First, falls and height loss (>4cm) are crucial factors of high fracture risk, but these are either accounted for using surrogate measures, or excluded altogether from the FRAX algorithm [93]. Second, risk factors such as tobacco and alcohol intake and glucocorticoids usage have dose-dependent effects. However, only average exposure is assumed in the risk calculation process. This requires the general practitioner to adjust – somewhat arbitrarily – the computed risk based on the actual dose [92]. Thirdly, despite previous fracture history being taken into account in the algorithm (only a binary option), not all fractures are equal in risk for recurrent fractures [94]. For example, a prior clinical vertebral fracture or multiple prior fractures carry much higher risks than others. Fourthly, the focus of the major fragility fractures (hip, clinical spine, forearm and proximal humerus) may lead to underdiagnosis of other fractures associated with osteoporosis, for example pelvic and rib fractures [87].

2.9 Fracture classification and risk assessment using QCT-based finite-element analysis

Perhaps the most important limitation of regression models such as FRAX is that these models evaluate risk without including the mechanism leading to fractures. This section will introduce the state-of-the-art of biomechanical modelling of hip fracture risk with the aim of identifying areas needing further development.

As stated above, falls contribute considerably to hip fracture risk. Around 30% of people over 65 years old and 50% of people over 80 years old will experience at least one fall per year [95,96]. Yet, risk of fall is highly variable across subjects and predicting personalised fall risk is an open challenge. Although almost all hip fragility fractures are caused by a fall to the side,

only 1-3% of falls result in hip fractures [96,97]. Hence, besides the frequency of falling, the severity and direction of falls also independently contribute to fragility fracture [98,99]. Perhaps the most important contributor to high hip fracture risk is low bone strength under sideways fall loading. Bone strength depends on the mechanical competence of the bone tissue and to some extent on the shape of the bone (organ) [100]. The mechanical competence of bone tissue is dependent on the density of bone mineral present (as measured by BMD), but also on its multiscale organisation [101]. Furthermore, the influence of bone tissue mechanics on whole femur strength is modulated by bone tissue mechanical heterogeneity within the femur. Such heterogeneity obviously cannot be captured by a single DXA-aBMD value. Hence, current densitometric measures exclude several contributing factors to femur strength, let alone hip fracture risk. Lastly, when considering 10-year hip fracture risk, it is important to consider how bone is lost over the 10-year period. This information is missed by DXA or QCT based densitometry at only one time point (the start of the risk assessment period).

Considering the above lacunae, this thesis aims to develop a model to predict loss in bone strength over time. In the remainder of this section, the development of mechanistic models of femur strength prediction based on QCT images will be discussed. Following this, the state-of-the-art in predicting bone loss over time will be reviewed.

The finite element method (FEM) is a widely used numerical approach for solving complex engineering problems involved with partial differential and integral equations. Hence, QCT-based finite element (FE) modelling of bone biomechanics can incorporate complex three-dimensional geometry, sophisticated constitutive behaviour and loading conditions [102]. Consequently, it possesses a natural advantage compared to DXA-aBMD in the assessment of femur strength. This is supported by the excellent reproducibility of QCT (1.0–1.5% coefficient of variation), although this relies on well-trained technicians executing the scan [65]. The general procedures of QCT-based FE modelling are shown in Figure 2.7. To obtain a 3D geometry of bone from QCT images, segmentation process is required. A range of software (such as AMIRA, ITK-Snap, ScanIP etc.) with various levels of automatization are available for this purpose. Once the femur is segmented, the QCT image data is used to also estimate the distribution of mechanical properties of porous bone tissue throughout the femur volume,

discretised at the level of individual finite elements. Element-wise elastic moduli are determined based on the average vBMD in each element using empirical relations, which are themselves determined from mechanical tests on ex vivo samples. This approach is founded on several assumptions, which can be broadly grouped into two sets as discussed below.

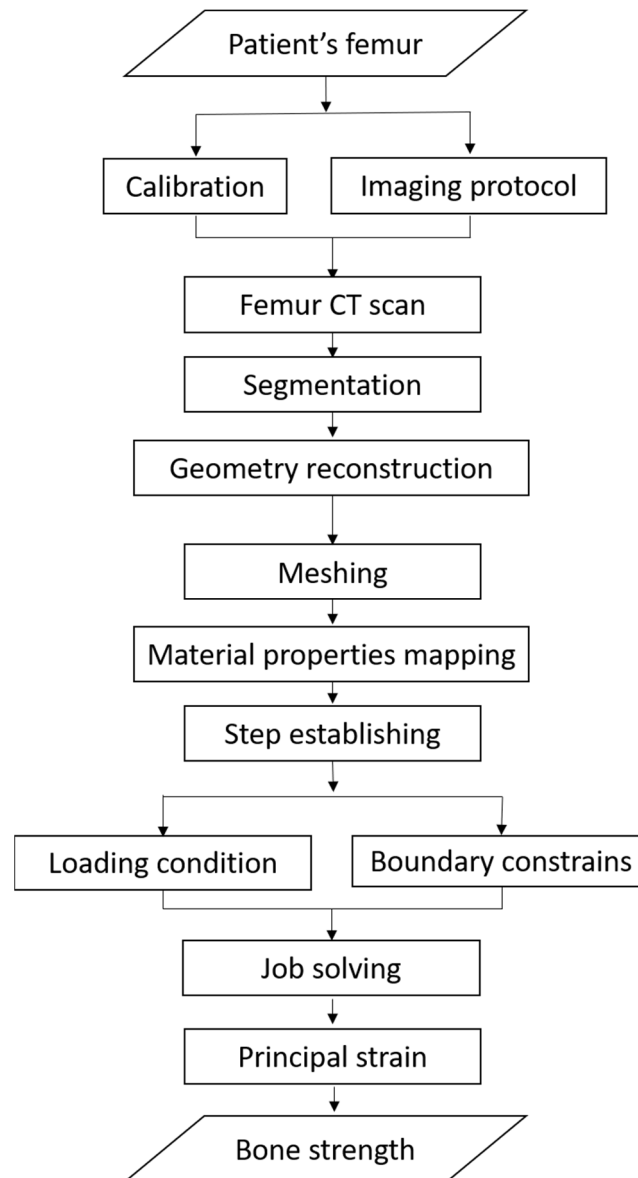


Figure 2.7 The flowchart of QCT-SSFE modelling general procedures.

The first set of assumptions relates to the estimation of true bone mineral density (as measured experimentally) from the radiological density (ρ_{QCT}), *i.e.*, the density calculated from CT images. As bone is a porous material, there are three types of density determined experimentally of this crucial mechanical property, which are tissue density (ρ_{tissue} , the fresh

and wet mineralised bone mass divided by the actual volume of bone tissue), apparent density (ρ_{app} , the same amount of bone mass over the actual bone volume plus vacuous spaces), ash density (ρ_{ash} , the ash weight over the actual volume), respectively [103]. Note that phantoms used in CT imaging are not a perfect substitute of bone, as the proximal femur is a complex structure consisting of trabecular and cortical bone. Especially, whereas phantoms are homogeneous, trabecular bone is heterogeneous at typical CT spatial resolution. Differences in the mineral composition process between phantom and bone also gives rise to differences in CT attenuation coefficients [104]. Besides, accurate characterization of local bone density is essential to improve the accuracy of existing FE models. Therefore, in order to better predict bone mechanics using subject-specific CT-based modelling, several corrections have been proposed for the equivalence of ρ_{QCT} to ρ_{ash} and ρ_{app} . A linear correction to determine ρ_{ash} from ρ_{QCT} (ρ_{QCT}/ρ_{ash}) has been proposed for cortical bone [105] or trabecular [106,107] separately. Yet, some researchers prefer a single ρ_{QCT}/ρ_{ash} relationship based on its straightforward employment in FE modelling. This is justified also by its excellent accuracy: the determination coefficient for the single relationship is $R^2=0.997$, which exceeds $R^2=0.937$ and $R^2=0.954$ for trabecular and cortical tissue respectively [104].

The second set of assumptions is related to the prediction of bone tissue mechanical properties from bone mineral density. A number of single- or two-parameter power functions [108–111] or linear relationships [112,113] were reported in the literature to predict elastic modulus (E) from ρ_{app} or ρ_{ash} . One of the most referenced forms of this relationship is $E=\alpha(\rho_{app})^\beta$, where β has been found to be close to 2 with high certainty [114]. Among various reported relationships, Morgan's relationship ($E=6.950(\rho_{app})^{1.49}$) has been shown to produce accurate strain prediction and is applicable to a wide range of bone density [115]. Similar to the ρ_{QCT}/ρ_{ash} relationship, the density–elasticity relationship might be considered piecewise by distinguishing trabecular and cortical bone [116,117]. Most mechanical tests have been conducted on bone tissues excised from donors who were healthy or suffered from primary osteoporosis. Hence, most empirical density–mechanics relationships of bone tissue available in the literature are strictly correct for such populations only [118,119]. Such density–mechanics relationships (an example seen in Figure 2.2) yield parameters for bone tissue mechanical constitutive equations. A related question is when higher order formulations of bone tissue mechanical constitutive equations (*e.g.* material heterogeneity, anisotropy,

viscoelasticity, plasticity, failure) are employed [120–124], whether these influence femur strength to a degree that significantly influences hip fracture risk as well. Yet another question is whether the corresponding constitutive parameters can be identified in a subject-specific manner with sufficient precision from ρ_{QCT} alone.

These questions have been addressed to an extent by the large number of studies conducted on the application of QCT-based subject-specific Finite Element (QCT-SSFE) models. In 1985, Basu et al. first applied QCT-SSFE to investigate the stress distribution in human femur [125]. Since then, QCT-SSFE method was rapidly developed to achieve higher automatic generation and better accuracy. Most state-of-the-art QCT-SSFE models agree on the requirements that are key to accurate prediction, such as imaging requirements. Imaging protocol (*e.g.* tube voltage and current variations) and reconstruction protocol (*e.g.* convolutional kernel) considerably affect CT numbers (HU) and image resolution, which further affects the measurement of BMD [126]. Hence, CT voltage generally is selected to be 120-140 kV, because the effect of current variations upon HU at this voltage range can be neglected [127]. The typical spatial resolution used is 0.625 mm slice thickness and 0.3-0.7mm in-plane pixel sizes [62]. Optimised reconstruction protocols are applied to minimise the reconstruction error at a given number of CT slices to avoid over-dose of X-ray radiation [128,129].

There are some areas in which the algorithms do not have consensus. Meshing is one of fundamental steps of QCT-SSFE. In the standard procedure, the first is to mask the bone segment by Non-Uniform Rational B-Splines (NURBS), then fill the porous spaces among bone microstructures to become a solid model and finally discretize the bone into FE meshes. As bone exterior surfaces are complicated, sometimes it is difficult to convert bone surface model into solid model, which hinders mesh generation. In such circumstances, directly using bone exterior surfaces to generate the mesh can be treated as an alternative approach. However, both approaches are user-intensive and time-consuming. To improve automation and speed, a morphing algorithm has been proposed. Here a template mesh is deformed onto a subject-specific geometry extracted from CT images [130]. The accuracy of morphing algorithm in predicting strains was excellent (RMSE% <10%) and was comparable with standard meshes ($p=0.11$) as reported by Grassi et al [130]. However, Qasim et al. [131] found this technique reduced QCT-SSFE ability in predicting hip fracture risk.

The sideways fall loading conditions has been simulated using a wide variety of boundary constraints in different studies. These choices strongly affect the prediction accuracy of the femur strength. The trochanteric region is either constrained directly against the loading direction [132–135], or by imposing a contact interaction with a planar surface at the impact location [136,137]. For the distal end, some studies chose to fully constrain it [133,138,139], while others allowed the rotation at a hinge node [135–137,140]. A range of studies indicated that directly constraining the great trochanter can cause the overestimation of femur strength [126,140,141]. Altai et al. investigated and reported the effect of different boundary conditions, in particular non-linear contact models, multi-point constraints (MPC) and linear models [141]. With regard to classifying fracture status, they found that the area under the receiver operating characteristic curve (AUROC) for the contact model was 0.82, which exceeded the AUROC=0.80 for the remaining models. However, the latter two models were considerably less computationally expensive to execute, with the average running time of one typical simulation for contact, MPC, linear models being 1 hour, 8 minutes and 3 minutes respectively [141].

There is also a rather weak consensus on the failure criteria to be applied to estimate the fracture load. The criteria that have been applied are based on the principal strain, the principal stress, the von Mises strain and the von Mises stress criteria. Strain-based criteria are motivated by the experimental observation that bone failure is driven by deformation and several studies have found it to be effective in terms of goodness of fit achieved with respect to experimental data [142–144]. Stress-based criteria have been adopted by other studies [145–147] and attempts to compare it with the strain-based criteria have produced inconclusive outcomes [145,148,149].

Thus, in selecting the most appropriate approach for each step of the modelling pipeline the study objective and resources available must be carefully considered. Schileo et al [104] validated a QCT-SSFE modelling procedure that involved: calibration of CT dataset by the ESP [150], an automatic inhomogeneous material-mapping procedure (BoneMat V3 software, Rizzoli Institute, available at www.biomedtown.org) [104,129,149,151,152], a normalization of ash density to apparent density [106,153], a density-elasticity ($E(\rho_{app})$) relationship derived from a robust experiment protocol based on femoral neck specimens [110], an assumed

homogeneous Poisson ratio [154], a femoral reference system defined by anatomical landmarks in the femur [155], and an implementation of maximum principal strain based failure criterion [143]. The validation of this pipeline demonstrated a normalized root mean squared error (RMSE) of only 7% in predicting local strain [104]. The results have good agreement with other similar approaches reported in literature [132,156,157]. Building on the pipeline of Schileo et al, Falcinelli et al. showed that applying multiple loading conditions to include both posterolateral and anterolateral falls is crucial in simulating side-fall situations [157,158]. Qasim et al found that for scans containing on the proximal femur, the femur anatomical orientation can be adequately estimated from the geometry of the full femur taken from an anatomical atlas and achieve excellent discrimination of fracture status [131]. Altai et al. reported non-linear large-sliding contact boundary constrains could improve the discrimination accuracy still further [141]. Viceconti et al. reviewed the available literature of QCT-SSFE techniques in 2018 and noted that the field of QCT-SSFE modelling has matured to the point that accuracies of only 15-16% standard error of the estimate (%SEE) in predicting femur strength can be expected from state-of-the-art models [4]. Indeed, one such state-of-the-art QCT-SSFE pipeline, namely VirtuOst® (O.N. Diagnostics, Berkeley, CA) has been cleared for clinical use by the United States Food and Drug Administration [159].

2.10 Pharmacological management of osteoporosis

Interventions are a key component in the management of osteoporosis and prevention of fractures. Non-pharmacological interventions generally try to reduce the frequency and impact of falls. Pharmacological interventions – discussed in more detail below – mainly aim at the correction of deficiencies of vitamin D and calcium, and the imbalance between bone resorption and bone formation [160].

Pharmacological interventions experienced a rapid and significant development during the last 50 years. Several investigations conducted on the pharmacological interventions exhibit a good efficacy of preventing fractures. Recent studies of pharmacological interventions for correcting the deficiencies of vitamin D and calcium have mainly focused on optimising the intake dose. For instance, it is recommended for the elders to have 800 IU/d vitamin D supplements, daily intake of 1200 mg calcium intake and 1g/kg body weight protein in the

management of fragility fractures [161]. However, the studies of pharmacological interventions for improving imbalances of bone remodelling are more directly linked to the fracture prevention efficacy. A brief description of these pharmacological interventions and their efficacy are provided below:

1) Anabolic treatment (PTH)

PTH remodels bone tissue by stimulating osteoblasts formation and restraining osteoclast formation to restore the bone biomechanical competence [162]. The truncated PTH, teriparatide, has been reported to reduce the risk of vertebral fractures and clinical fractures in a multicentre, double-blinded, double-dummy, randomised controlled trial. After two years treatment, the new occurrence of vertebral fractures and clinical fractures are reduced by 28% and 30% respectively [163].

2) Antiresorptive treatment (Denosumab, potent bisphosphonates)

Denosumab is an antiresorptive agent targeting the RANK-ligand (RANKL) to inhibit osteoclast activity, reduce bone resorption and increase the bone density. A study of 36-month FREEDOM trial found a reduction of vertebral fractures, hip fractures and nonvertebral fracture by 68%, 40% and 20% respectively [164]. Similarly, the mechanism of bisphosphonates is to restrain osteoclast activity and to further inhibit bone formation. The reduction efficacy of bisphosphonates has been evaluated to be 35% for all fractures, 50% for vertebral fractures and 25% for non-vertebral fractures, which is slightly lower than that of denosumab [165].

3) Bone formation-sparing antiresorptive treatment (Odanacatib)

Odanacatib is an inhibitor candidate of cathepsin K (a cystine protease extensively expressed in osteoclasts) that inhibits bone resorption and increases the bone density. Cathepsin K is one of the most attractive targets in osteoporosis pharmacological treatment. A 5-year trial of 50-mg weekly dose Odanacatib treatment shows good preservation of trabecular and cortical bone and continued reduction of fracture risk [166]. However, due to its cardiovascular adverse effects in postmenopausal women, the development of Odanacatib was terminated at Phase III stage [167].

Even though the pharmacological interventions demonstrate good efficacy in preventing fractures per se, the adherence and compliance of these interventions remain low due to the fear of side effects, cost effectiveness and unproven efficacy in specific scenarios [6]. The main side effect of bisphosphonates is the excess risk of atypical femur fractures and osteonecrosis of the jaw. The cost per quality adjusted life year (QALY) is generally used to judge the cost effectiveness. Depending on the choice of pharmacological interventions and its price, the cost per QALY is different [168]. And it is apparent that individuals at higher risk of fracture are more cost-effective [169]. However, the long-term efficacy of these medications is not obvious or unproven due to the lack of trials. For example, an extension study of bisphosphonates treatment showed that the bone mineral density remained unchanged after 5 years [7].

2.11 Clinical trials

Therefore, there is still an unmet need to develop a new drug with fewer side effects, higher efficacy for long term disease outcomes and higher cost-effectiveness. Any drug must undergo a rigorous assessment before commercially distribution due to the risk of potential toxicity. Today, the widely (and only) accepted and indispensable procedure to evaluate the safety and efficacy of drugs or any medical products is to test them *in vivo* (*i.e.* in the living organism), first in laboratory and in animal testing (preclinical trials) and then on humans (clinical trials) [170]. Clinical trials are the most important step in the development pipeline of a new drug prior to its manufacturing and marketing. Clinical trials are generally separated into four phases based on the different aims and scales: clinical pharmacology (Phase I), clinical investigations (Phases II and III), and post-marketing studies (Phase IV) [171]. The brief descriptions of these four phases are provided below [171]:

Phase I: The aims of Phase I are to evaluate the safety, tolerated dosage, and acute side effects of the drugs. A small group of healthy volunteers (20-100) are normally recruited, unless, in some cases of cancer, parts of diseased volunteers are needed. Commonly this phase will undergo several months and approximately 70% of drugs move to Phase II.

Phase II: The aim of Phase II is to assess the drug's biological activity, efficacy and feasibility on the targeted patients, *i.e.*, 'proof of concept' and 'dose-finding'. The number of volunteers

(100-300) involved in the Phase II trial is required to be larger than that of Phase I trial. The volunteers should be the corresponding patients that suffer from the drug's targeted disease, such that the side effect and efficacy can be tested properly. Length of studies in Phase II vary from several months to two years and only around one third of drugs move to Phase III.

Phase III: The aim of Phase III is to assess the clinical value of the drugs and monitor the long-term or rare adverse reactions, since Phase III is the trial prior to the marketing of the drugs, known as 'pre-marketing phase'. It can be considered as an updated expansion and verification of Phase II with an even larger group of patients (300-3000). The typical duration of a Phase III trial is between one to four years and approximately 30% of drugs pass to the market.

Phase IV: The aim of Phase IV is to assess the performance of the drugs after marketing.

Based on the three pre-market phases discussed above, it is obvious that the development of new drugs is extremely challenging due to the high expense and time-consumption, especially for Phase III. US Food and Drug Administration (FDA) estimate the cost of pivotal trials for new drugs to be \$19 million based on the median value of all tested drugs in 2015-2016 [172]. In addition, there are some concerns associated with the clinical trials including high failure rate and ethnicity. A ten-year study (2006-2015) on the clinical development success rates found that the possibility of new drugs passing all safety and efficacy requirements starting from Phase I through to market approval was lower than 10% [173]. Ethical problem is the other main concern strongly associated with participants' safety and rights. Clinical trial catastrophes may occur where some originally healthy volunteers end up with serious problems and even lose their lives during the trials. For example, in what was widely broadcast as the "Elephant Man" trial incident, all six healthy volunteers suffered life-threatening reactions caused by TGN1412, a drug confirmed as safe and efficacious in preclinical studies, at Northwick Park Hospital in 2006 [174]. These concerns are driving researchers to find alternative techniques, including *in vitro* clinical trials and *in silico* clinical trials, to refine, reduce and partially replace clinical trials.

2.12 *In silico* clinical trials

Unlike the *in vitro* clinical trials that collect specimens from patients to test the reaction to specific drugs or medical treatment, *in silico* clinical trials are developed by computational models and simulations to assess devices and drugs [9]. The term '*in silico* clinical trials (ISCT)' was not introduced until 2011 when VPH institute raised it up to the European Commission [170]. The previous description, Virtual Physiological Human (VPH), originated from a publication "seeding the EuroPhysiome: a roadmap to the virtual physiological human" in 2007 [170]. Recently, the US Congress and the European Parliaments agreed to recommend ISCT as an additional tool for advancing the development of drugs and medical devices [9]. The application of *in silico* clinical trials is to form virtual cohorts by computational modelling, which are then used to predict the performance of the drugs or medical devices, such as safety and efficacy for specific patients [175]. Given the fact that the patient-specific models are simulated by computer, *in silico* clinical trials are capable of protecting the volunteer patients from the unexpected side effects and drug interactions. The potential usage of *in silico* clinical trials in different phases of clinical trials are briefly described below [175].

Phase I: ISCT could be used to assist the estimation of effective dose, toxic dose and optimal dose using the mathematical optimization model. However, due to the complexity of the biological scenario, a set of differential equations with a 'cost' is required to represent biological variability and reproduce particular circumstances.

Phase II: ISCT is capable of seeking and covering all possible side effects, especially those rare and adverse effects that are challenging to be observed in conventional clinical trials. This is achieved by producing virtual patients with characteristics that are intermediate between real patients. Since a larger group of virtual patients generated by ISCT offers a more comprehensive risk analysis of the drugs or medical devices, the number and the health risk of patients involved in clinical trials could be reduced. That is to say the clinical trials could be refined and partially replaced.

Phase III: Similar to Phase II, the usage of ISCT in Phase III is mainly to reduce the number of patients required for testing. With the increase of enrolled patients, the efficacy of the drugs or medical devices also could be better estimated. Meanwhile, the expense and time for

testing are reduced significantly, as execution of the simulation is much quicker than the testing in clinical trials.

Besides the health protection and clinical trial reduction, ISCT could also provide a more precise and personalized treatment strategy for different patients. Based on the stated advantages, researchers are exploring this novel domain and there are several successful early adoptions. One well-known example is Type I Diabetes Mellitus Padova/UVA simulator where a group of 300 virtual patients, consisting of children, adolescents and adults, were developed to approximate the inter-subject variability of the physical population. The virtual population was employed to test the safety of a closed-loop control algorithm for people with Type I Diabetes [176]. The simulator was authorised by the FDA as an alternative to preclinical trials in 2008 and since then it has been adopted as primary test bed for new control algorithms [175,177].

These adoptions offer an inspiration to use virtual patients in the clinical trials of new osteoporotic drugs. In conventional clinical trials of drugs to treat osteoporosis, large sample sizes are required (normally 2000-8000 patients for 3 years in Phase III trials) and imply massive costs for pharmaceutical companies [178]. Additionally, in many countries placebo-controlled trials are considered as unethical for high-risk patients; a case in point is a trial with hip fracture as the primary endpoint [8]. Given the high association with skeletal fragility and disease severity, bone strength is instead considered as a surrogate endpoint in such trials [4]. However, true bone strength measurement is a destructive exercise, and therefore aBMD based on DXA is commonly used as a surrogate of bone strength. This situation could be much improved if one could run the placebo arm on a large number of virtual patients on whom bone strength could be estimated more accurately than with DXA-aBMD. As reviewed in detail in Section 2.9.1, QCT-based finite element models predict bone strength with much higher accuracy than DXA-aBMD. Indeed, some mechanistic models have leveraged the high accuracy of the QCT-SSFE method, and combined it with other factors such as fall frequency and fall severity to predict absolute hip fracture risk [5,179–181]. As mentioned in Section 2.8, the 10-year absolute risk of hip fracture (ARF10) has long been used to drive clinical management of osteoporosis [8], although currently it is estimated using non-mechanistic (*i.e.*, regression) models such as FRAX. Bhattacharya et al defined the current absolute risk of

hip fracture ARF0 in a similar manner, predicted it using a novel multiscale algorithm and showed that it could classify hip fracture status (AUROC=0.85) even more accurately than QCT-SSFE based strength (AUROC=0.82) [5].

To extend this pipeline to predict ARF10, a model to predict the age-related changes in physiology needs to be included. As bone strength is one of the most important predictors of fracture risk, a minimal version of such a model should account for bone loss over a 10-year period. Therefore, the main focus of this thesis is to develop a model for bone loss and investigate the sensitivity of bone strength to bone loss relative to bone shape and size. The most important challenge in developing this model is that obtaining repeat CT measurements is not possible due to the high radiation dose (1.3-3.2 mSv for QCT) and expense (£78 for one area CT scan) involved [4]. However, once such a model can simulate bone loss over a 10-year period in a cohort of virtual patients, remaining physiological changes (in body weight and height and in fall frequency) with age can be modelled with relative ease based on epidemiological data, thus clearing the way for the use of ARF10 modelling pipeline in ISCTs.

3. Bone loss without mechano-regulation

Chapter 2 reviewed the state-of-the-art in clinical management of osteoporosis. It was found that clinical decision making is strongly linked to the absolute risk of hip fracture over a 10-year period (ARF10). ARF10 is also a key endpoint in clinical trials of osteoporosis drugs. Hence, this thesis is motivated to improve the computational models that will enable a better prediction of ARF10. Chapter 2 also showed that the state-of-the-art computational models can accurately classify hip fracture status between fracture and control subjects based on proximal femur CT images. This is attributed to the accurate prediction of QCT-based FEM on femur strains (93%) and strength (85%) under fall loading. However, the current computational models are limited to predicting hip fracture risk at the time of clinical presentation and the prediction of long-term risk is missing. As strength is the most important determinant of fracture risk, it is necessary to predict how femur strength changes over time in a subject. As bone mineral density is a key determinant of femur strength, there is a need to model the change of bone mineral density over time in osteoporotic patients.

3.1 Introduction

Bone, unlike the first impression, is a living tissue that undergoes permanent remodelling throughout our lives. Bone remodelling (Figure 3.1) is a process of removing the old bone followed by generating new bone. Osteoclast and osteoblast are the main cells involved in this process: osteoclasts take part in the bone resorption, while osteoblasts are responsible for bone formation. Throughout the growth period, from birth to early adulthood, bone changes in size, with bone deposition predominating bone resorption. The peak bone mass (PBM) is achieved normally in the mid-twenties. Even after reaching skeletal maturity, bone turnover is still active in adulthood, which helps to repair micro-damages, adapt to the changing patterns of stress and maintain calcium homeostasis [182]. After reaching the peak, resorption starts to exceed formation, resulting in a physiological decline of bone mass with age. The decrease becomes much more rapid with the onset of menopause in women in their later 40s or early 50s. It has been reported that women can lose around 15% of bone mineral content on average over the first ten years after menopause [183].

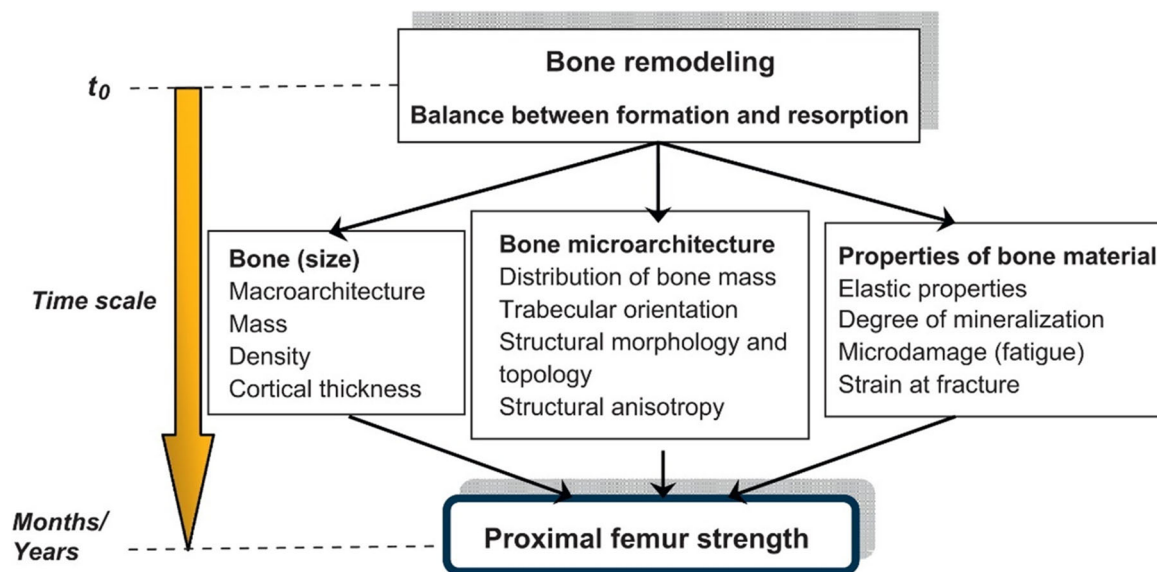


Figure 3.1 Bone remodelling affects the bone size, microarchitecture, and material properties, which cumulatively influences proximal femur strength. Reproduced with permission from Hambli et al [134].

After that the rate of bone loss gradually slows down to a steady rate for the rest of life (see Figure 3.2). The long-term imbalance of bone remodelling can result in the progression to osteoporosis and fractures. Even though some attempts have been made to monitor osteoporosis based on biochemical markers of bone remodelling, these techniques currently have limited clinical utility due to the enormous temporal and interpatient variations [184,185]. Hence, current methods for assessing involutional bone loss still rely mostly on the non-invasive assessment of bone mineral density, such as dual-energy X-ray absorptiometry (DXA) or quantitative computed tomography (QCT).

Several studies based on DXA-aBMD have been conducted to investigate bone loss in the femur due to aging. Among others, Cvijetic et al (see Figure 3.2) and more recently Paggiosi et al found a negative linear relationship between age and aBMD [186,187]. Paggiosi et al reported that the rate of aBMD decline in the femoral neck (~27%) over a 55-year period was the fastest across all regions over the same period: intertrochanteric, 20%; total hip, 21% and trochanteric, 24%. Although the loss rates reported by different studies vary somewhat, all of them indicate that bone loss rate exhibits heterogeneity within femur. However, while DXA

can be used to assess the BMD of a particular region of interest (ROI) within the femur, it still provides a relatively crude estimation of the heterogeneity of BMD. Fractures are often propagated from microcracks at small local weakness points. That DXA-aBMD only explains 60-70% of bone strength [188–190] is partly because it is an inadequate measure of the underlying local BMD distribution. Moreover, due to the intrinsically two-dimensional nature of DXA, the discrimination of regions by BMD, such as into trabecular and cortical bone tissue regions is somewhat limited.

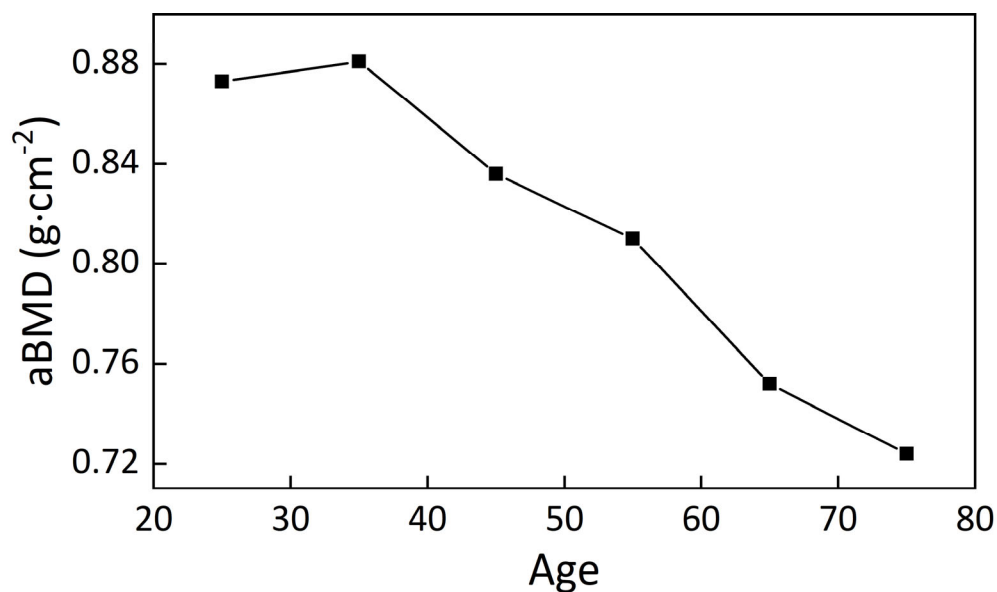


Figure 3.2 Bone mineral density in dependence of age in the proximal femur of women. Reproduced with permission from Cvijetic et al [187], copyright of Massachusetts Medical Society.

In contrast, QCT can overcome this lacuna through advanced 3D acquisition and analysis techniques that enable the measurement of distances, surfaces, volumes and volumetric BMD (vBMD) in various ROIs. Thereby, more recent studies utilize QCT to assess bone loss in greater detail. Here too, the heterogeneity of bone loss rate is evident. In general, the remodelling rate of cortical bone is between 2 to 5% per year, while trabecular bone responds faster to metabolic changes and thereby remodels faster [191]. More specifically, in females in the femoral neck region, cortical and trabecular bone densities decline on average by 3.5% and 8.6% per decade [192]. It was observed that in 100 women over 70 years of age, women preserved more cortical bone at inferoanterior quadrants of femoral neck and superior

quadrants were most affected by aging [192]. However, because 80% of the skeleton consists of cortical bone, the absolute amount of bone loss is similar for both compartments in the first decade. Both cortical and trabecular bone contribute to femoral strength, whereas the relationships are complex and still a matter of debate [73]. Some suggest that the contribution of two tissues was proportionate to their mass, while the others demonstrated that age-related cortical thinning and growing asymmetry of femoral internal structure increases hip fracture risk [193–195].

The previous QCT studies analysed relatively large ROIs, such as total hip, femoral neck, femoral head, intertrochanter and trochanter [196–199] or in certain longitudinal and cross-sections [192,194,200–203]. This limits their direct application to QCT-SSFE where vBMD information is needed at the level of a finite-element (Chapter 2: typical edge length ~3mm) and throughout the proximal femur volume. Such information is currently unavailable. Furthermore, notwithstanding the advantages of QCT over DXA, the expensive cost, additional radiation exposure and limited availability of QCT scanners make it challenging to regularly monitor bone loss status in the general population. In contrast, there exists a huge amount of data regarding aBMD and some studies have shown that vBMD measured by QCT is correlated with DXA-aBMD [204–206]. Thus, one might opportunistically use existing aBMD-based bone loss data in combination with current QCT scans to predict local vBMD change and further enable the prediction of future bone strength.

There are few in vivo studies establishing correlations between DXA-aBMD and QCT-vBMD. A study by Amstrup et al [207] tested correlations between DXA-aBMD and cortical vBMD measured by QCT in 98 postmenopausal women (age: 56-76 years). All women were scanned by DXA (Hologic Discovery scanner) and QCT (Philips Brilliance multidetector CT scanner) at their left hip region. Areal BMD was measured at total hip (TH-aBMD) and femoral neck (FN-aBMD), while trabecular (Tb), cortical (Ct) and integral (In) vBMD were measured at the same regions. The threshold for separating cortical from trabecular bone was set at $0.350 \text{ g}\cdot\text{cm}^{-3}$. The strongest correlation was observed between TH-aBMD and TH-In-vBMD with positive regression coefficient (β) of 0.355 (aBMD unit: $\text{g}\cdot\text{cm}^{-2}$). Positive and significant correlations were also found between In- and Tb-vBMD and aBMD at TH and FN, whereas Ct-vBMD correlated negatively and significantly with aBMD at both sections. All set with significant

correlations indicated that QCT-vBMD is a good indicator of aBMD. The large variation in regression coefficients showed different response of vBMD in different regions according to the change of aBMD. The authors also cautioned against using a fixed cortical threshold due to the potential influence of transitional bone.

In another *in vivo* study [208], both healthy men and women (aged 40 to 90 years,) were analysed for FN-aBMD – measured using DXA (GE Lunar Prodigy) – and Tb-vBMD, Ct-vBMD and total vBMD at the femoral neck – measured using QCT (GE Light Speed) of the proximal femur. Trabecular and cortical bone were automatically segmented by a software program. Srinivasan et al reported that for women, Tb-vBMD and Ct-vBMD increased by 0.243 and 0.315 $\text{g}\cdot\text{cm}^{-3}$, respectively, per 1 $\text{g}\cdot\text{cm}^{-2}$ increase in aBMD. However, the correlation between Ct-vBMD and FN-aBMD was found to be relatively low ($r^2=0.38$) and Ct-vBMD was found to be relatively independent with age ($p=0.204$, non-zero linear regression coefficient), both results suggesting that cortical bone was not subject to aging. Unfortunately, the confidence in these conclusions is somewhat limited by resolution of QCT scans in that study (slice thickness 2.5 mm, in-plane voxel size 0.74 mm) at which thin laminar structures, *e.g.*, femoral neck cortex cannot be accurately captured [209]. Srinivasan et al also mentioned that bone loss for elderly women was faster than elderly men [208]. In summary, despite the fact that some studies investigated the relationship between DXA-aBMD and vBMD, the dependence of the spatial distribution of vBMD loss rates in the proximal femur with respect to loss of aBMD remains poorly understood. This lacuna needs to be met in order to develop a spatio-temporal atlas of vBMD change in the proximal femur; such an atlas is necessary to predict future bone strength and long-term hip fracture risk.

A recent study by Farzi et al constructed a two-dimensional version of such an atlas [210]; with pixel-level median aBMD values in dependence of age and BMI. The atlas was obtained using an automatic pipeline to model spatio-temporal pixel-wise DXA-aBMD change in the proximal femur. Farzi et al segmented proximal femurs from the DXA scans of 13,338 Caucasian women (aged 20–97 years) and resampled all scans to an isotropic spatial resolution of $0.5\times 0.5\text{ mm}^2$. The scans were registered with anatomic landmarks to map them to a template femur. Pixel-level temporal BMD evolution was modelled using quantile regression. The results showed that bone loss was heterogeneous, but in general bone mass

was most preserved at superior trochanteric region, inferior femoral neck and trochanteric region until 70s. The atlas showed an overall decline in aBMD with aging and low BMI, respectively. It also presented site-specific and spatially complex loss patterns across the proximal femur. With increased age, especially after 60 years, cortical thinning and obvious loss in trochanteric region had been observed. A decline of BMD was observed in Ward's triangle and diaphyseal regions in subjects with low BMI. Note that the atlas is developed from cross-sectional data which has been validated to have no significant differences of BMD change from the actual measurements reported by a longitudinal study. Farzi et al offered a very promising method to present complex spatio-temporal BMD changes with aging based on a large-scale dataset, but there are few limitations. Although the multi-centric study design allowed the analysis of large datasets, different imaging instruments used at these centres induced uncertainties in aBMD measurement, that could not be entirely removed even after applying cross-calibration. With regards to application to QCT-SSFE, the predicted atlas is obviously limited by the two-dimensional nature of DXA. Most importantly, the application of this method for forward prediction of bone loss requires a subject's femur to be mapped to the particular template femur used in the study and its specific pixel-level discretisation.

As bone has a complex three-dimensional geometry, the conventional procedure for producing QCT based SSFE models involves segmentation of CT images and meshing the segmented bone volume [130]. It is challenging to use such a conventional procedure to explore the variability of material property distribution in the population due to the variability of meshes between individuals. One solution, similar to the approach of Farzi et al, is offered by a previous study [130]. Here, subject-specific femur geometries are aligned to a template femur geometry by using a set of landmarks and then the mesh of the template femur is deformed to match the subject-specific geometry. This mesh morphing algorithm was reported to produce good quality tetrahedral meshes (mean aspect ratio of 1.91) and the average deviations were found adequately below the CT resolution. Although this allows for the first time an analysis of the dependence of loss of vBMD on loss of aBMD in an anatomically congruent manner, the forward prediction of vBMD loss still requires a mesh-invariant model. Thus, the aim of this chapter is to develop such mesh-invariant algorithms that can determine the rates of change of local QCT-vBMD with respect to the change of DXA-aBMD and employ such algorithms to predict the loss of vBMD in the region of interest and

finally produce a spatio-temporal atlas of local (elemental) vBMD change over a certain period. This will include the analysis of the sensitivity of algorithm coefficients to parameters used in the coefficient identification (optimisation) process.

3.2 Materials and Methods

3.2.1 Clinical cohort

A retrospective cohort consisting of ninety-six Caucasian postmenopausal women (aged from 55 to 91 years) were recruited from the Sheffield region (henceforth referred to as the “Sheffield cohort”). Forty-seven of them had been diagnosed with low energy trauma fractures in the proximal femur. Details of Sheffield cohort have been reported previously in Yang et al [203] and are summarised in Table 1 for reference. The Sheffield Local Research Ethics Committee approved this study and all subjects involved had given written informed consent.

Table 3.1 Descriptive statistics of Sheffield cohort. For age, BMI and aBMD, the information in each cell corresponds to the range, mean and standard deviation (in parentheses).

	All	Fractured	Non-fractured
N	96	47	49
Age (years)	55-91, 75(9)	55-89,75(9)	56-91,75(9)
BMI (kg/m ²)	14-36, 25(5)	14-36,25(5)	19-35,26(4)
aBMD (g·cm)	0.36-0.96,0.62(0.11)	0.36-0.73,0.57(0.10)	0.49-0.96,0.67(0.10)

Details of the imaging protocol and finite-element (FE) mesh generation process are reported in Grassi et al and Qasim et al [130,131] and are summarised below for reference. Each subject received bilateral DXA (Hologic Discovery scanner, Hologic Inc, Bedford, MA, USA) and QCT (LightSpeed 64 VCT, GE Medical Systems, Milwaukee, WI, USA) scans of their proximal femur. None of the subjects had conditions that would affect the assessment of DXA or QCT of hip. The scanned region started from 3.5 cm below the lesser trochanter and extended just above femoral head. The spatial resolution was set to 0.625 mm for slice thickness and 0.74 mm for

in-plane voxel size. CT image data were segmented and then discretised into FE tetrahedral meshes possessing an average edge-length of 3 mm. The subject-specific meshes were obtained by morphing a template mesh to each subject's femur geometry. The morphing method was based on the anatomical landmarks of the subject's femur. The morphing procedure resulted in each subject's mesh comprising an identical number ($M = 295589$) of tetrahedral elements and any particular element (identifiable by its index) being located in a similar anatomical location across all subjects ($N = 96$). Hounsfield units of the CT image were converted to bone mineral density (vBMD) values (units $\text{mg}\cdot\text{cm}^{-3}$) based on calibration curves obtained with respect to an offline European Spine Phantom. The vBMD values were mapped elementwise to the FE mesh using BoneMat v3.0 [149].

3.2.2 Bone loss algorithm

Consider that for a subject, the DXA-aBMD measured at the femoral neck (FN-aBMD) is changed by an amount of Δa over some time duration. At the same time, consider that vBMD at location x (denoted as $v(x)$) within the proximal femur has changed by Δv . Note that, typically in elderly subjects – who are of interest to the present study – the passage of time leads to loss of bone (Δa is negative). Hence, we use the term “loss” interchangeably with “change”, although one may apply the algorithms below without regard to the sign of Δa .

It is assumed that change in FN-aBMD can predict the change in local vBMD over a given time period. The rationale for this assumption is obvious: the two quantities ultimately measure the same physical entity, i.e. change in the amount of bone mineral in a given volume of bone.

It is also assumed that a non-negligible part of the relationship between change in FN-aBMD and change in local vBMD is not subject-specific. The rationale for this assumption is that factors such as bone regions of interest, projections applied to the bone region, nature of the energy sources used in imaging, which lead to different definitions of aBMD and vBMD, are standardised and not subject-specific. The influence of subject-specific bone shape is further suppressed through the use of morphed meshes (as detailed in the previous section).

Two hypotheses are tested to extract this non-subject-specific dependence of Δv on Δa , i.e. the form of the “rate” quantity dv/da :

- 1) Homogenous bone loss: the rate is uniform throughout the proximal femur.
- 2) Density-specific bone loss: the rate at any location within the proximal femur volume is determined by the vBMD in that location.

Thus, for the homogenous algorithm, we simply define:

$$\frac{dv(x, a)}{da} = m \quad (\text{Equation 3.1})$$

where $v(x, a)$ is the vBMD at location x in a subject with aBMD a , and the constant m denotes the homogeneous (*i.e.*, independent of x) change in vBMD per unit change in aBMD. Note that the rate of change (m) is assumed to be independent of a .

The formulation of the density-specific algorithm requires further consideration. Past studies consistently reported faster remodelling rates of trabecular bone compared to cortical bone, and this is widely understood to be due to the higher surface-to-volume ratio of the former [191]. This simply follows the fact that bone remodelling is carried out by the action of osteoclasts and osteoblasts, which occurs on the surface of bone tissue. As the schematic in Figure 3.3 shows, the surface-to-volume ratio has a non-monotonic relationship with vBMD. In the low-density region, where the amount of bone tissue is low, the amount of available surface is also low, and the change of the amount of bone is small as well. The medium-density region has the largest surface-to-area ratio, and as a result the BMD changing rate is expected to be the highest. Whilst in the high-density region, the bone is much compacted, and again there is lesser surface available for remodelling. Thus, the rate of change given by the density-specific algorithm can be formulated as trilinear function:

$$\frac{dv(x, a)}{da} = \begin{cases} 0 & 0 \leq v(x, a) < \tau_{LM} \\ m_M & \tau_{LM} \leq v(x, a) < \tau_{MH} \\ m_H & \tau_{MH} \leq v(x, a) \end{cases} \quad (\text{Equation 3.2})$$

Here, the constants τ_{LM} and τ_{MH} are vBMD thresholds such that $0 \leq v(x, a) < \tau_{LM}$ identifies locations within the proximal femur with low vBMD, $\tau_{LM} \leq v(x, a) < \tau_{MH}$ identifies locations with medium vBMD and $\tau_{MH} \leq v(x, a)$ identifies locations with high

vBMD. It is assumed that the change rate in low vBMD locations is zero. This is motivated by FE modelling requirements where the elasticity (derived from vBMD) of an element must be strictly positive. The constants m_M and m_H denote change in vBMD per unit aBMD in medium and high vBMD locations respectively and are otherwise independent of location x . Note that similar to the homogenous algorithm, the rates of change (m_M and m_H) here are also assumed as independent of a .

It is also worth mentioning that although the above formulation allows distinct values of m_M and m_H , no relative order of magnitude is imposed or assumed. In particular, no correspondence between low-, medium- or high-density regions and marrow and trabecular and cortical bone tissues are imposed or assumed. Thus, even if one fully accepts all the limitations of distinguishing tissue types from the QCT images using fixed thresholds [66,72,207,209,211,212], it has no bearing on the algorithm formulated above.

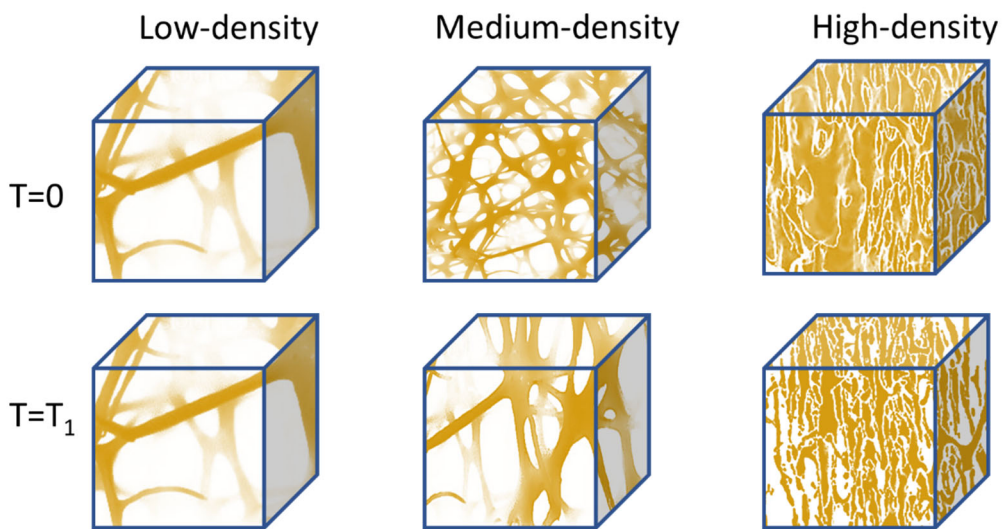


Figure 3.3 Schematic diagram of bone at location x ($v(x)$) (shown in blue) and relative change after a period of time (t) (shown in yellow) in low- (left), medium- (middle) and high-density (right) region.

3.2.3 Coefficient identification

The values of the coefficients present in the bone loss algorithms (Equations 3.1 and 3.2) are determined such that these best fit the data of the cohort detailed in section 3.2.1.

The following process is used to identify the single coefficient m of the homogeneous algorithm (Equation 3.1). A subject- and element-specific error variable is defined as follows:

$$\epsilon_e^s = (v_e^s - v'_e{}^s)V_e^s \quad (\text{Equation 3.3})$$

where the superscript s ($= 1 \dots N$) denotes the subject-index. The subscript e ($= 1 \dots M$) denotes the element-index and may be considered as a surrogate for unique anatomical locations (x) within the template mesh. The subject- and element-specific volume V_e^s accounts for the variation in element volumes in the data set. The variable v_e^s is the vBMD determined from the CT images and the predicted vBMD is given by:

$$v'_e{}^s = \langle v_e^s \rangle_s + m(a^s - \langle a^s \rangle_s) \quad (\text{Equation 3.4})$$

where the operator $\langle \dots \rangle_q$ denotes an average taken over the range of the index q . This definition utilises the fact that the line of best fit always passes through the centre of the data, which in the present case is given by $(\langle a_e \rangle_s, \langle v_e^s \rangle_s)$. This eliminates the need for determining the intercept of the best fit line separately for each element e . The contribution to the total error vector from element e is:

$$E_e = \frac{\|\epsilon_e^s\|_s}{\| \|V_e^s\|_s \|_e} \quad (\text{Equation 3.5})$$

Here, the operator $\|\dots\|_s$ and $\|\dots\|_e$ denote the root-mean-square (r.m.s.) taken over the range of the index s and e respectively. Thus, $\|\epsilon_e^s\|_s$ is computed over N subjects and $\| \|V_e^s\|_s \|_e$ is computed over all $M \times N$ volumes of the data set. The total error vector E contains M entries and is minimised in the least-squares sense to obtain the best-fit value of m . For this purpose, an unconstrained non-linear optimization procedure is performed. The trust-region-reflective algorithm is applied as the nonlinear system of equations is not under-determined, *i.e.*, the dimension of E (here, M) is higher than that of the parameter-set (here,

1). The iterative parameter search is terminated if m or E change by less than 10^{-6} between successive iterations. The routine *lsqnonlin* available in MATLAB version R2019a (The MathWorks Inc., Natick, MA, USA) is used to perform the calculations.

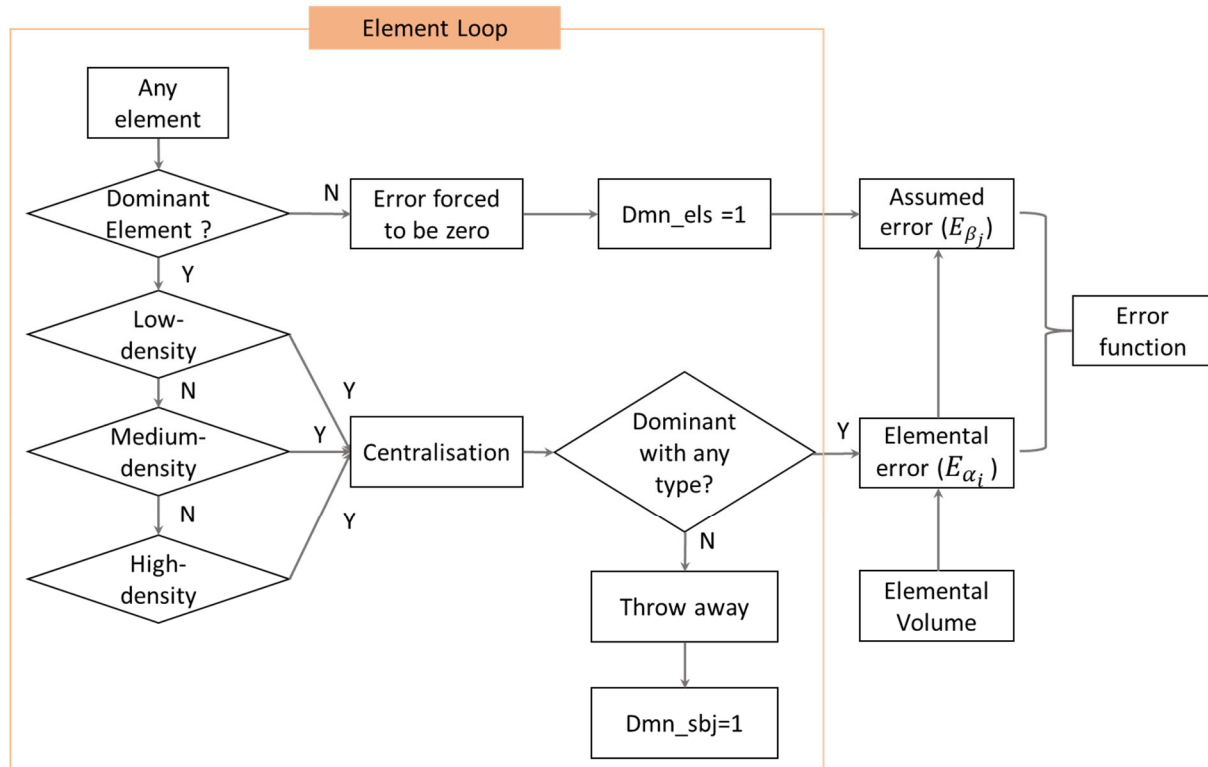


Figure 3.4 The schematic flow chart of determining the objective function (the total error vector E) for the routine *lsqnonlin*.

For the density-specific algorithm, the four parameters $m_M, m_H, \tau_{LM}, \tau_{MH}$ as described above in Equation 3.2 need to be identified and optimized and the same approach as above is applied. The schematic flow chart of determining the objective function (the total error vector E) for the routine *lsqnonlin* is shown as Figure 3.4.

Given specific values of τ_{LM} and τ_{MH} , it is possible that across the N subjects, a specific element has a mix of low, medium and high vBMD values. This leads to an ambiguity in evaluating Equation 3.4. Thus, a threshold of “dominance” $0.5 < \eta < 1$ is defined, which is held fixed for the entire parameter identification process. The element e is identified to be dominant either of low-, medium- or high-density type, if one of the inequalities listed in Equation 3.2 is satisfied for at least ηN subjects. Note that due to η being bounded below by

0.5, an element can only be identified to be dominant of at most one type, although it is possible that it is not identified dominantly with any type at all (see examples in Figure 3.5).

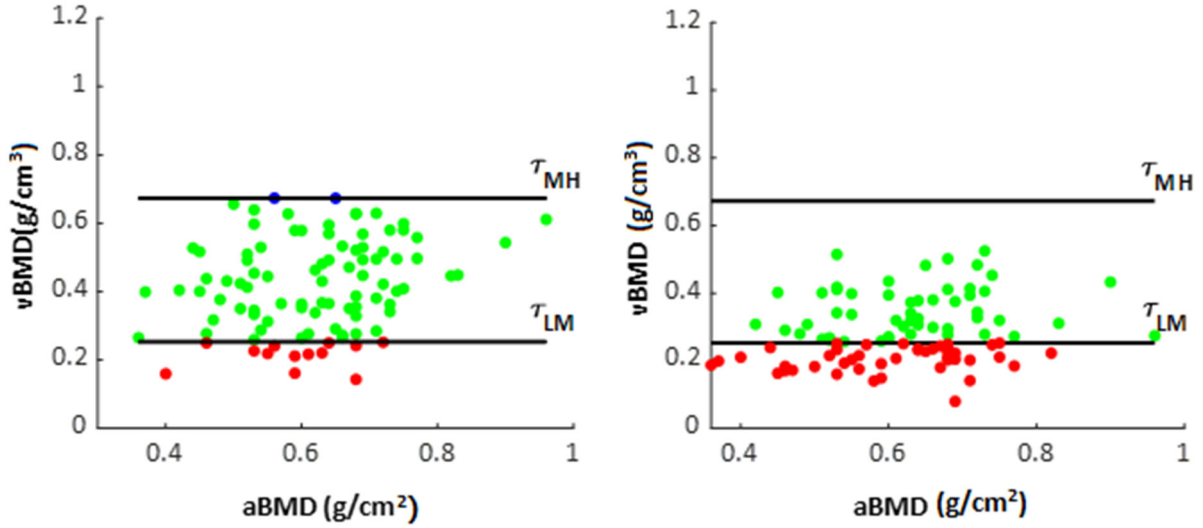


Figure 3.5 Examples of element identified with dominant type (left) or non-dominant type (right). Red, green and blue dots denote v_e^s identified as in the low-, medium- and high-density region in a certain element i across all subjects. (Left) the number of green dots is larger than ηN , then this element is identified dominantly with medium type. (Right) neither of the number of red or green dots is larger than ηN , then this element is identified dominantly with no tissue type, *i.e.*, has non-dominant type.

Thus, the M elements can be partitioned into four groups containing elements identified to be dominate of low-density (M_L in number), medium-density (M_M in number) and high-density (M_H in number) type and those elements that cannot not be identified dominantly with any type at all ($M' = M - (M_L + M_M + M_H)$ in number). Let the index α_i ($i = 1 \dots M_L$) denote any element in the low-density type group. Thus, there exist $n_{\alpha_i} (\geq \eta N)$ subjects, indexed $s_{\alpha_i,p}$ ($p = 1 \dots n_{\alpha_i}$), such that $\forall s_{\alpha_i,p}$ the condition $\tau_{LM} \leq v_{\alpha_i}^{s_{\alpha_i,p}} < \tau_{MH}$ holds. Equations 3.3-3.5 are rewritten as:

$$\epsilon_{\alpha_i}^{s_{\alpha_i,p}} = \left(v_{\alpha_i}^{s_{\alpha_i,p}} - v'_{\alpha_i}^{s_{\alpha_i,p}} \right) V_{\alpha_i}^{s_{\alpha_i,p}} \quad (\text{Equation 3.6})$$

$$v'_{\alpha_i}^{s_{\alpha_i,p}} = \langle v_{\alpha_i}^{s_{\alpha_i,p}} \rangle_{s_{\alpha_i,p}} + m_M \left(a^{s_{\alpha_i,p}} - \langle a^{s_{\alpha_i,p}} \rangle_{s_{\alpha_i,p}} \right) \quad (\text{Equation 3.7})$$

$$E_{\alpha_i} = \frac{\| \epsilon_{\alpha_i}^{s_{\alpha_i,p}} \|_{s_{\alpha_i,p}}}{\| \| V_e^s \|_s \|_e} \quad (\text{Equation 3.8})$$

where the all-element e ($= 1 \dots M$) and all-subject s ($= 1 \dots N$) indices are defined as before. Note that the averaging $\langle \dots \rangle_{s_{\alpha_i,p}}$ and r.m.s. $\| \dots \|_{s_{\alpha_i,p}}$ operations are performed considering only the n_{α_i} subjects for whom the dominance condition holds. Equations 3.3-3.5 are similarly rewritten for medium- and high-density type elements. For elements not identified dominantly with any type, the contribution to the total error vector is determined as:

$$E_{\beta_j} = \left(\frac{\| E_{\gamma_k} \|_{\gamma_k}}{\| \| V_{\gamma_k}^{s_{\gamma_k,r}} \|_{s_{\gamma_k,r}} \|_{\gamma_k}} \right) \| V_{\beta_j}^s \|_s \quad (\text{Equation 3.9})$$

where indices β_j ($j = 1 \dots M'$) and γ_k ($k = 1 \dots (M - M')$) denote, respectively, elements not identified dominantly with any type and elements identified dominantly of one density type. The index $s_{\gamma_k,r}$ ($r = 1 \dots n_{\gamma_k}$) denotes the subjects for which the dominance condition holds for element γ_k . In effect, Equation 3.9 rescales the r.m.s. error contributions from elements identified dominantly of one type in order to account for variation in element volumes. Defining an error contribution for the elements that are not identified dominantly to be of any type ensures that the dimension of the objective function (the total error vector E) is fixed during the parameter search process, irrespective of the values taken by the parameters τ_{LM} and τ_{MH} . The routine **Isqnonlin** is used to identify the four parameters with the same settings as noted above.

3.2.4 A spatio-temporal atlas of local vBMD change

Past observational studies show that over a 6-year period of ageing, aBMD is reduced by approximately 5% [185,211]. Based on this finding, the change of aBMD over 6 years ($\Delta a'$) of a subject can be estimated as $0.05a$. Combined with density-specific algorithm and current QCT image, the change of vBMD over 6 years ($\Delta v'(e, a)$) at any location (here refers to element in template mesh) in the proximal femur can be predicted as:

$$dv'(e, a) = \begin{cases} 0 & 0 \leq v(e, a) < \tau_{LM} \\ m_M \cdot 0.05a & \tau_{LM} \leq v(e, a) < \tau_{MH} \\ m_H \cdot 0.05a & \tau_{MH} \leq v(e, a) \end{cases} \quad (\text{Equation 3.10})$$

Where $dv'(e, a)$ is the element-wise vBMD reduction over 6 years and $e (= 1 \dots M)$ denotes the element-index. Note that vBMD at the current time ($v(e, a)$) is only used in identifying elemental tissue type.

3.3 Results

This section presents results from sensitivity analyses of both homogenous and density-specific algorithm upon finite difference step sizes (SS), the initial guesses and dominance threshold parameter (density-specific algorithm only). All computational processes were conducted by ShARC, the University of Sheffield's central High-Performance Computing (HPC) cluster.

3.3.1 Homogenous algorithm

Seven finite difference step sizes (default, 1E-4, 1E-3, 1E-2, 5E-2, 1E-1, 5E-1) and four initial guesses ($m_0, m_0+0.05, m_0\pm 0.1$) were tested in the analysis. The default of SS in the routine *lsqnonlin* with central finite differences type is the cube root of Floating-point relative accuracy (here, 6.055e-6). The initial guess $m = m_0$ is taken as the slope of a linear regression between aBMD and subject-specific median vBMD values, which is found to be 0.333 cm⁻¹. The average computational time for one typical simulation was around 2 minutes.

The rate of change in vBMD with respect to aBMD is found to be $m = 0.363$ cm⁻¹ and the sensitivity analysis of homogenous algorithm shows that m is not related to SS (except for SS= 5E-1) and the initial guesses (see Figure 3.6).

The r.m.s. of non-volume-weighted error $E (= \sqrt{\sum_e \|v_e^s - v_e'^s\|_s^2})$ is found to be 0.137 g·cm⁻³ and quantifies the error in predicting vBMD due to its assumed linear relationship with FN-aBMD. Considering that the r.m.s. vBMD across all elements and subjects is 0.397 g·cm⁻³, the linear relationship is associated with an error of 34.5% on average.

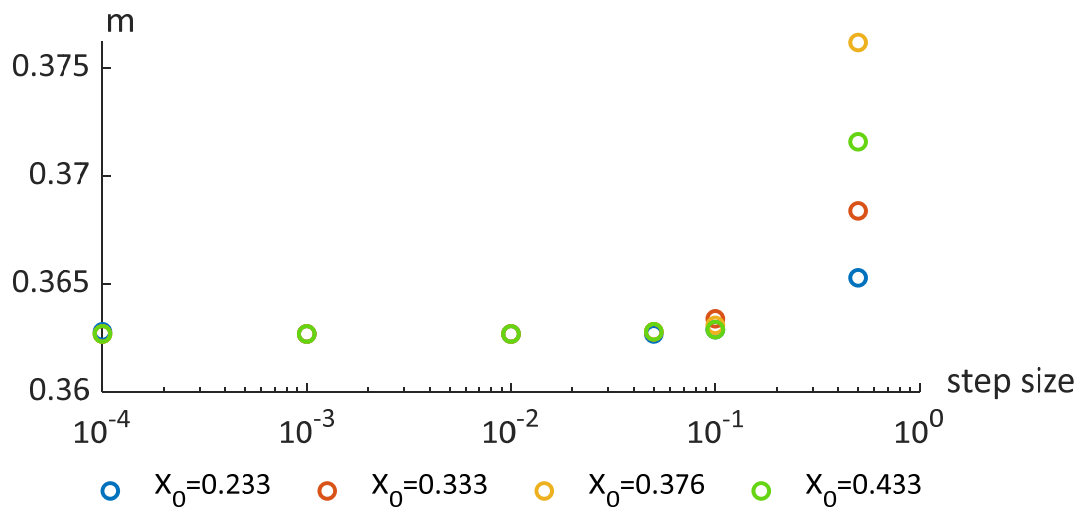


Figure 3.6 Sensitivity analysis of changing rate m for the homogenous algorithm to different step sizes and initial guesses used in parameter identification process.

3.3.2 Density-specific algorithm

Six finite difference step sizes (1E-4, 1E-3, 1E-2, 5E-2, 1E-1, 5E-1) and ten dominance threshold parameters were initially applied in the routine *lsqnonlin*. η was selected in the range of 0.5 to 0.8 with an increment of 0.3. The lower bound was set as 0.5 to assure at most only one density type could be identified as dominant tissue label for a certain element. The upper bound was limited as 0.8 to assure enough elements were included in the optimization process (for example, nearly 60% of elements would be discarded, when η equals 0.9). Two sets of initial guesses ($m \pm 0.1$, $m \pm 0.1$, $\tau_{LM0} \pm 0.1$, $\tau_{MH0} \pm 0.1$) were applied, which m was the best fit value obtained from the homogeneous algorithm and τ_{LM0} and τ_{MH0} were set to 0.1 and 0.8, based on two noticeable dips around these values in the combined histogram of the vBMD data of all subjects (Figure 3.7). In total, 120 simulations for the preliminary study were conducted. The average computational time for one typical simulation was around 31 minutes.

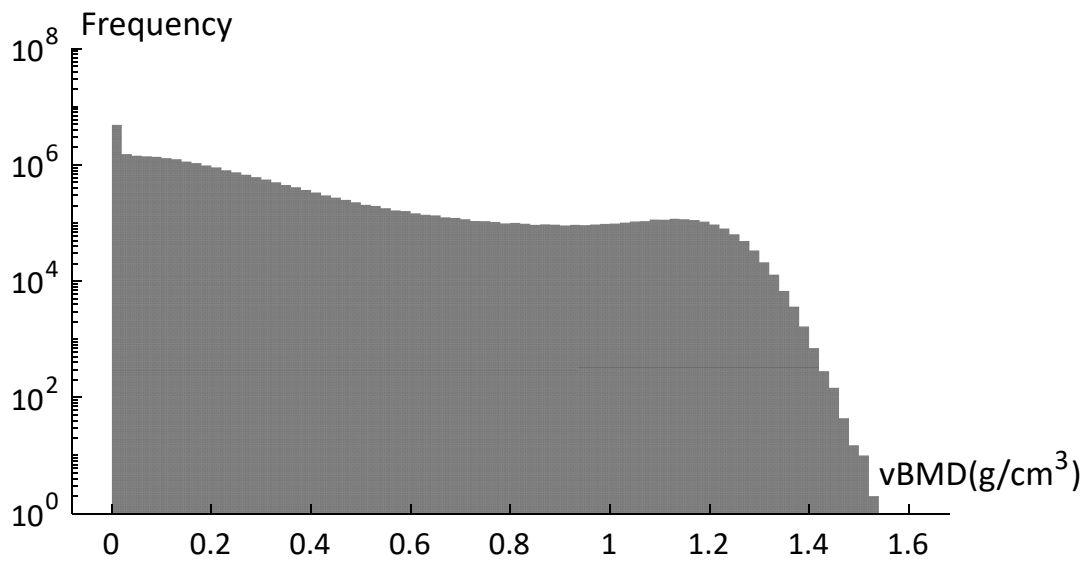


Figure 3.7 Histogram of vBMD data of all elements of all subjects.

The preliminary results show that initial guesses have less influence on parameters of density-specific algorithm, compared to η and SS (see Figure 3.8 and Figure 3.9). The variation of m_M upon η and SS is smaller with the first set of initial guesses ($m-0.1$, $m-0.1$, $\tau_{LM0}-0.1$, $\tau_{MH0}-0.1$), while m_M is less sensitive to η and SS with the second set of initial guesses ($m+0.1$, $m+0.1$, $\tau_{LM0}+0.1$, $\tau_{MH0}+0.1$). Two thresholds, on the contrast, are more stable to both sets of initial values.

Unlike the homogenous algorithm, it is challenging to find a clear zone that four parameters are insensitive to both η and SS. Yet, the variation is smaller when η is between 0.60 to 0.80 and SS is between 1E-2 to 1E-1, which suggests a refined sensitivity study among this area is needed.

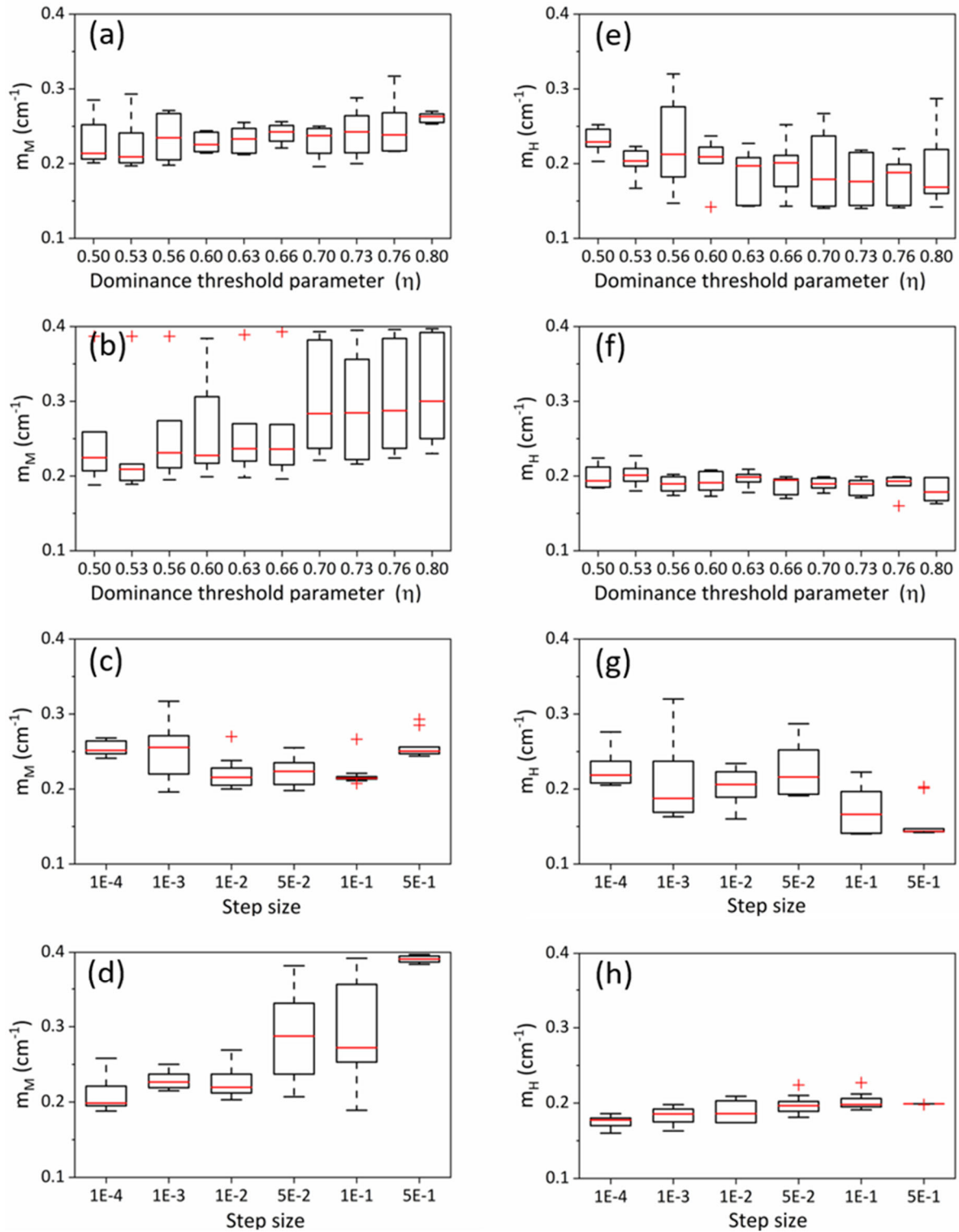


Figure 3.8 Boxplots of the rate of change in medium- and high-density region (m_M and m_H) for density-specific algorithm. Panel (a), (c), (e) and (g) are the plots over dominance parameter (η) and step sizes (SS) based on the initial guess ($m-0.1, m-0.1, \tau_{LM0}-0.1, \tau_{MH0}-0.1$), respectively, while panel (b), (d), (f) and (h) show the results based on another set of initial guesses ($m+0.1, m+0.1, \tau_{LM0}+0.1, \tau_{MH0}+0.1$).

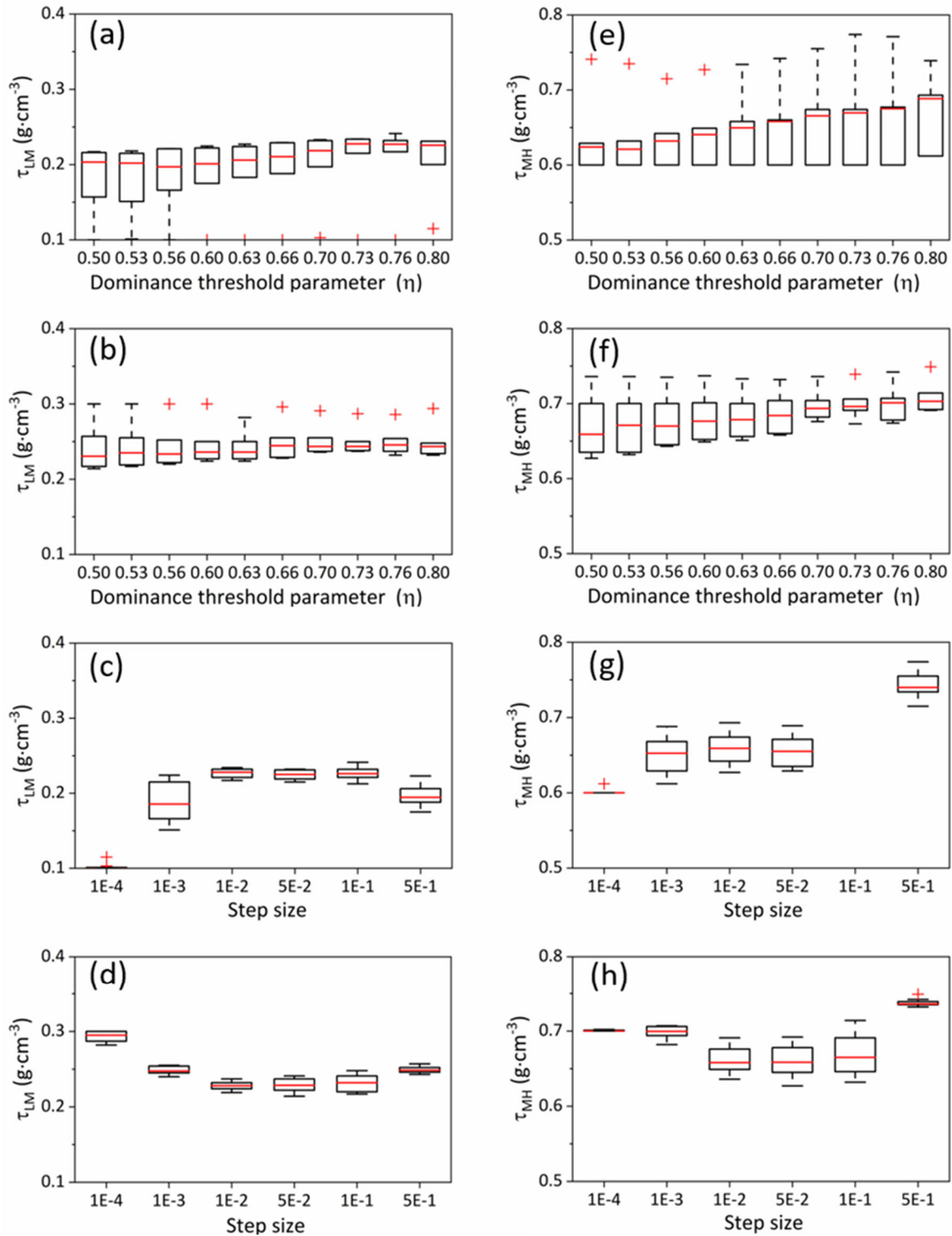


Figure 3.9 Boxplots of two thresholds (τ_{LM} and τ_{MH}) for density-specific algorithm. Panel (a), (c), (e) and (g) are the plots over dominance threshold parameter (η) and step sizes (SS) based on the initial guess ($m-0.1$, $m-0.1$, $\tau_{LM0}-0.1$, $\tau_{MH0}-0.1$), respectively, while panel (b), (d), (f) and (h) show the results based on another set of initial guess ($m+0.1$, $m+0.1$, $\tau_{LM0}+0.1$, $\tau_{MH0}+0.1$). Note that the value of τ_{MH} when SS was set as $1E-1$ is out of the range in Panel (g). The median of τ_{MH} is $0.437 \text{ g}\cdot\text{cm}^{-3}$ with minimum and maximum value of $0.418 \text{ g}\cdot\text{cm}^{-3}$ and $0.462 \text{ g}\cdot\text{cm}^{-3}$, respectively.

Hence, based on preliminary finding, twenty sets of refining SS (from 1E-4, 1E-3, 2E-3, ...,9E-3, 1E-2, 2E-2, ..., 9E-2, 1E-1 and 5E-1) were tested. The range of η was between 0.60 to 0.80 with the increment refined to 0.02, the smallest increment we could apply to have meaningful difference in subject number after rounding. Considered the relatively long computational time and different sensitivity of m_M and m_H to the two sets of initial values, in the refined sensitivity study the initial guesses of slopes were set as the best fit value in homogenous algorithm (*i.e.*, $m_{M0} = 0.363 \text{ cm}^{-1}$, $m_{H0} = 0.363 \text{ cm}^{-1}$), while thresholds were set as the same as before (*i.e.*, $\tau_{LM0} = 0.1 \text{ g}\cdot\text{cm}^{-3}$ and $\tau_{MH0} = 0.8 \text{ g}\cdot\text{cm}^{-3}$). In total, 220 simulations were conducted in this refined study.

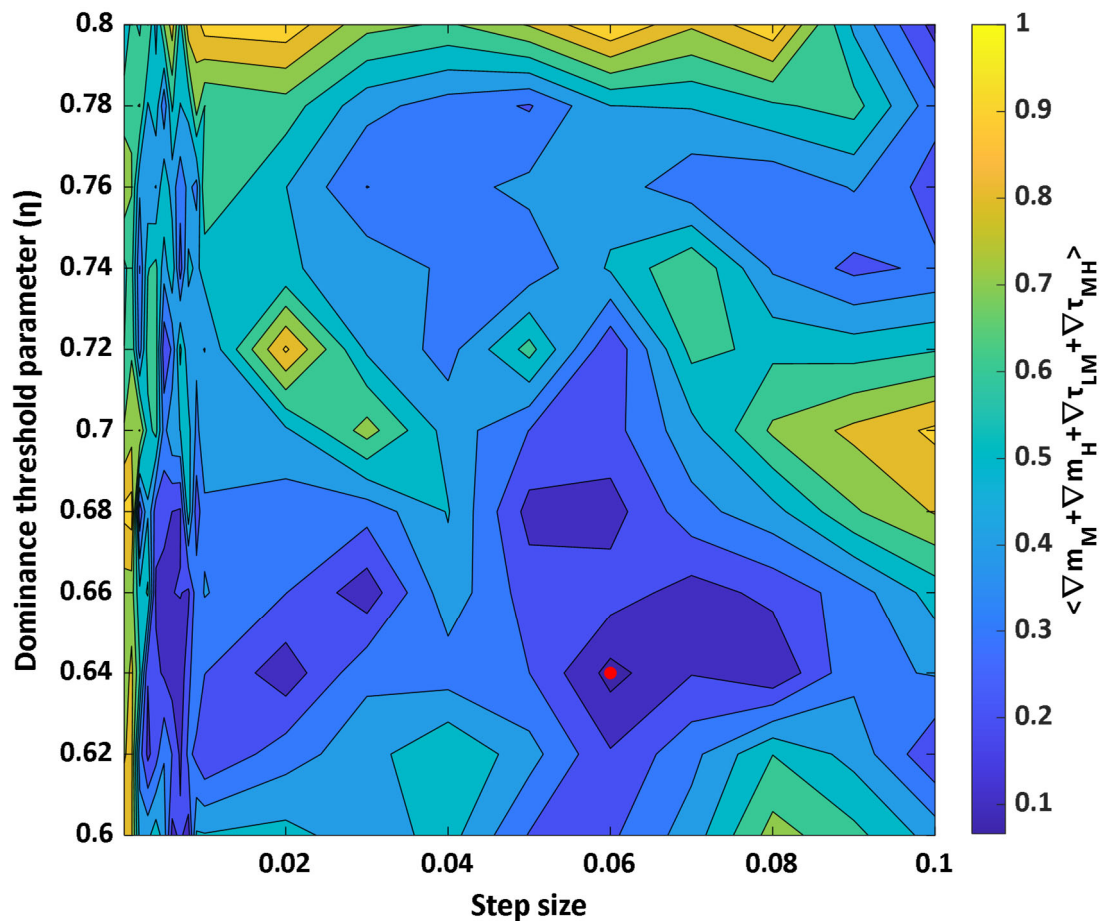


Figure 3.10 Contour of changing rate index for density-specific algorithm. The index is defined as the sum of normalized gradient of m_M , m_H , τ_{LM} and τ_{MH} by its maximum value. The minimum value, marked with red dot, is located at step size of 0.06 and dominance threshold parameter of 0.64. The best-fit values are found to be $m_M = 0.233 \text{ cm}^{-1}$, $m_H = 0.189 \text{ cm}^{-1}$, $\tau_{LM} = 0.253 \text{ g}\cdot\text{cm}^{-3}$, $\tau_{MH} = 0.673 \text{ g}\cdot\text{cm}^{-3}$, producing 17.2% r.m.s. error with respect to r.m.s. vBMD of all subjects and all elements.

An index (∇_I) defined as sum of normalized gradient of m_M , m_H , τ_{LM} and τ_{MH} by its maximum value is used to determine the changing rate of four parameters. The contour of ∇_I shows that no clear insensitivity zone has been identified for density-specific algorithm (Figure 3.10). However, there exist a region which has a relatively low gradient (SS between 5E-2 to 7E-2, η between 0.62 to 0.64). The r.m.s. error is found to have no significant difference (see details in Table 3.2). The minimum ∇_I is located at SS 6E-2 with η 0.64, where best-fit values are found to be $m_M = 0.234 \text{ cm}^{-1}$, $m_H = 0.189 \text{ cm}^{-1}$, $\tau_{LM} = 0.253 \text{ g}\cdot\text{cm}^{-3}$, $\tau_{MH} = 0.673 \text{ g}\cdot\text{cm}^{-3}$. The r.m.s. of non-volume-weighted error E ($E = \left\| \left\| v_e^s - v_e'^s \right\|_s \right\|_e$) based on best-fit values is of $0.068 \text{ g}\cdot\text{cm}^{-3}$ (17.2% with respect to r.m.s. vBMD of all subjects and elements), while 28.4% elements are discarded in the optimization.

Table 3.2 Parameters of density-specific algorithm obtained by different optimization settings identified in less sensitivity zone, corresponding ratio of discarded element (in percentage) and the percentage of the r.m.s. of predicted error. Noted that settings are named in the form of Vall_SS_ η , which SS and η denotes step size and dominance threshold parameter. Best fit values selected in this study are marked in red.

Setting	m_M	m_H	τ_{LM}	τ_{MH}	%Discard	%RMS
Vall_0.62_5E-2	0.241	0.162	0.255	0.675	26.7	17.7
Vall_0.64_5E-2	0.245	0.153	0.257	0.679	28.1	17.4
Vall_0.66_5E-2	0.246	0.152	0.259	0.681	29.6	17.0
Vall_0.62_6E-2	0.235	0.187	0.255	0.678	26.6	17.7
Vall_0.64_6E-2	0.234	0.189	0.253	0.673	28.4	17.2
Vall_0.66_6E-2	0.235	0.188	0.254	0.678	29.9	17.0
Vall_0.62_7E-2	0.230	0.197	0.255	0.673	26.7	17.7
Vall_0.64_7E-2	0.242	0.181	0.260	0.686	27.9	17.4
Vall_0.66_7E-2	0.237	0.185	0.260	0.678	30.0	17.0

Based on the two vBMD thresholds ($\tau_{LM} = 0.253 \text{ g}\cdot\text{cm}^{-3}$ and $\tau_{MH} = 0.673 \text{ g}\cdot\text{cm}^{-3}$) and the dominance parameter threshold ($\eta = 0.64$), the proportion of elements (by number) identified as dominant with low-, medium and high-density to all elements (295589) are 61.1%, 11.0% and 7.5%, respectively. The remaining elements (20.4%) could not be identified to a dominant density type.

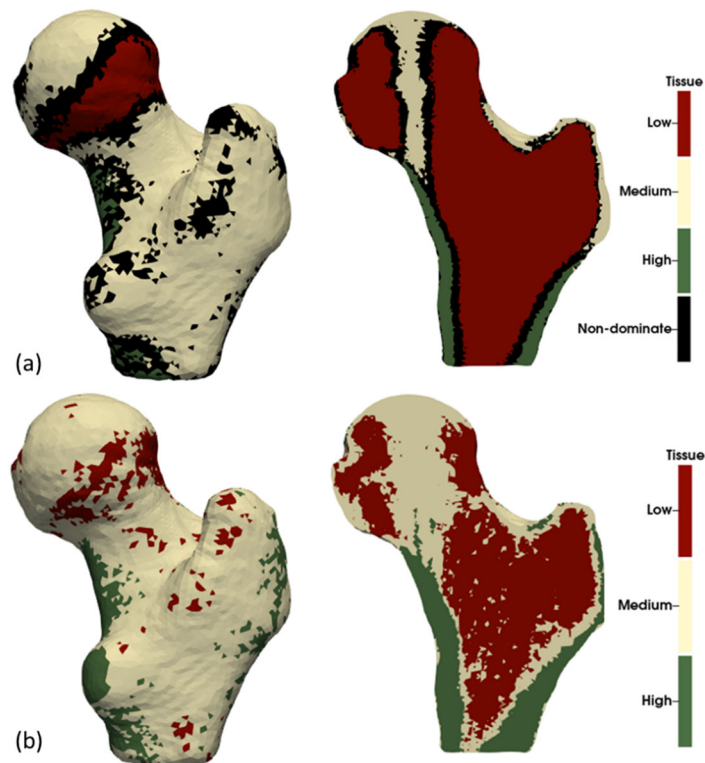


Figure 3.11 (a) The distribution of density types across all subjects in the optimization process. (b) The distribution of density types in a representative subject (Patient038).

The spatial distribution of each density type in the Sheffield cohort as identified by the optimization process is shown in Figure 3.11 (a). The spatial distributions show strong clustering of similar density regions, as expected, and a strong association between specific density regions and anatomical features known to be mechanically relevant. Specifically, high-density regions are typically located in the cortex of the femur shaft and the inferior cortical surface of the femur neck. The medium density regions are located typically at the cortex of the greater trochanter, the superior cortical surface of the femur neck, the proximal surface of the femur head and the principal compressive group of trabeculae. Interestingly, regions

with non-dominant density type can be sandwiched between any pair of regions, and in particular, between low- and high-density regions (such as close to the endosteal surface of the femur shaft). Note that maximum difference in vBMDs between any two subjects in an element with a non-dominant density type is not necessarily larger than it is in an element possessing a dominant density type. When determining the bone loss for a specific subject, the fact that an element might not be associated with a dominant density type is ignored. In other words, each element is identified with a density-type, which is based on the two thresholds; an example is shown in Figure 3.11 (b).

3.3.3 A spatio-temporal atlas of local vBMD change

As an illustration of the application of the density-specific algorithm, a reduction in aBMD over 6 year-period is simulated by predicting local reductions in vBMD through the 3D femur geometry in a specific subject. The vBMD reductions are visualised at various frontal planes (Figure 3.12).

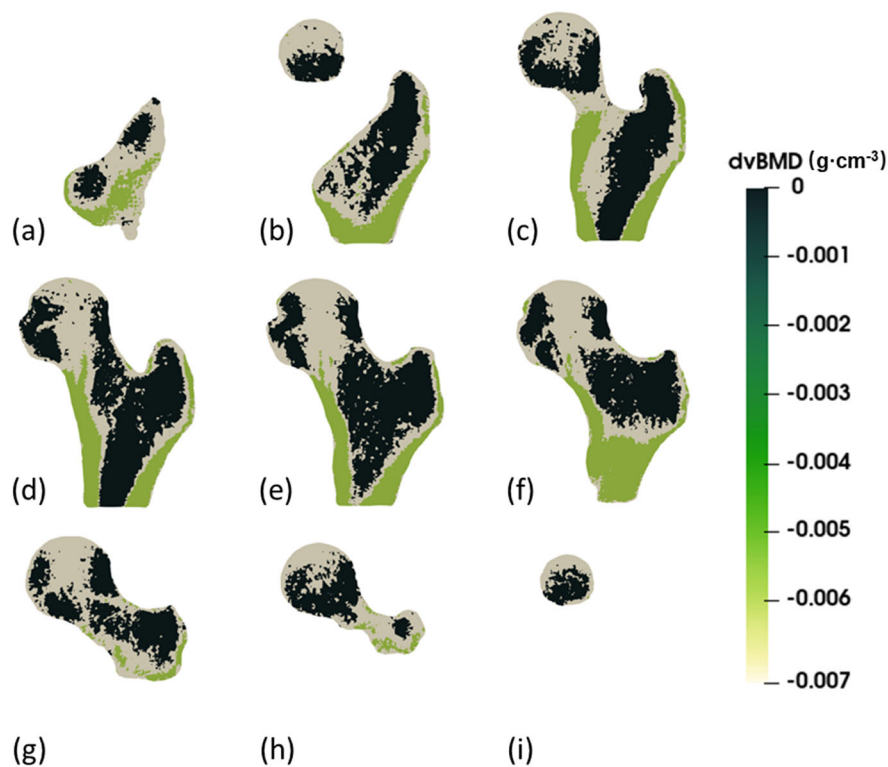


Figure 3.12 A series of frontal planes (perpendicular to z axis) spaced at 5 cm intervals presenting the vBMD loss based on 5% aBMD loss in Patient038.

Similar maps of element-wise reductions in vBMD are computed for all physical subjects of the Sheffield cohort corresponding to 5% aBMD loss over 6 years. The element-wise averages over all subjects are then computed.

Results are shown as absolute vBMD reduction (dvBMD, Figure 3.13 (a)) and vBMD reduction normalised to original vBMD (dvBMD%, Figure 3.13 (b)). In general, less bone preserved around bone surface, especially in both inferior and superior surface of femoral neck, greater trochanteric region and femoral shaft. The distribution follows that of density types (Figure 3.11 (a)) and highlights the heterogenous nature of bone loss.

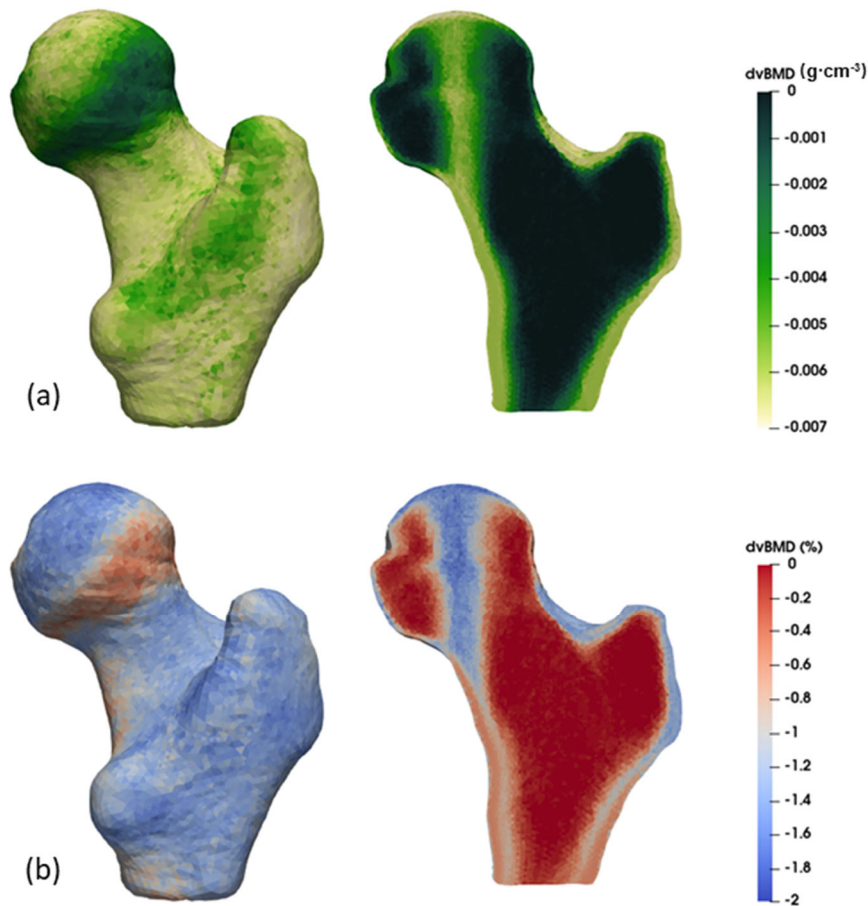


Figure 3.13 The distribution of mean local vBMD reduction over the proximal femur volume of Sheffield cohort following 5% reduction in aBMD: a) absolute and b) normalized reduction.

3.4. Discussion and conclusions

In this study, based on a retrospective study of 96 postmenopausal women in Sheffield, two bone loss algorithms are determined that formulate how local vBMD within the femur volume changes with respect to unit change in aBMD.

3.4.1 Homogenous algorithm

The present findings show that when assuming the bone is uniformly lost across proximal femur, the change of vBMD with respect to the change of aBMD is 0.363 cm^{-1} (error of 34.5%). This is in accordance with previous studies such as Amstrup et al [207] who conducted a linear regression between FN-aBMD and TH-In-vBMD. Amstrup et al found the slope of the regression relation to be 0.344 cm^{-1} ($r^2=0.65$), which is slightly lower than the slope determined in the present study. This difference may be attributed to various factors, such as differences in bone geometry between the cohorts considered in the present study and in Amstrup et al, technical differences in imaging and post-processing pipelines between the two studies, and uncertainty in the regression relationships. With respect to the last factor, note that the change of aBMDs in both studies could explain at most 65% of the change in vBMDs.

Below it is analysed whether using the approach of Amstrup et al [207] could lead to better prediction accuracy of elemental vBMD. Accepting small methodological differences with that study, TH-In-vBMD in the Sheffield cohort is estimated as follows. The total bone mineral content (BMC) is obtained as the weighted sum of elementwise vBMD and elemental volumes. Then the TH-In-vBMD for each subject is calculated by dividing the total BMC by the total volume (i.e., the sum of all elemental volumes). The regression coefficient between aBMD and average vBMD across all subjects in the Sheffield cohort was 0.383 cm^{-1} ($r^2=0.58$). The normalised non-volume-weighted error in predicting elemental vBMD based on this linear regression is 74.8% (r.m.s. of $E=0.297 \text{ g}\cdot\text{cm}^{-3}$). This prediction error is nearly twice that of the homogeneous algorithm (34.5%, as mentioned above), which suggests that a linear regression relationship between TH-In-vBMD and aBMD is not suitable for predicting local vBMD change.

Furthermore, Srinivasan et al reported a similar coefficient between FN-total-vBMD and FN-aBMD (0.349 cm^{-1}) in a multiple linear regression including age and male sex upon 49 to 75 years old women and men [208]. Srinivasan et al also mentioned that bone loss for elderly men was slower than elderly women (with matched FN-aBMD men are around 6 years older than women). Based on this fact, our homogenous algorithm might be able to apply on predicting bone loss in men up to an (as yet undetermined) correction factor.

Poole et al reported differences in FN-total-vBMD and FN-aBMD in women over a 60-year difference in age (25-85 years) [192]. A change rate of 0.514 cm^{-1} is estimated from their study by direct division, although it is not possible to assess the uncertainty of this estimate in a straightforward manner. The somewhat large difference in change rate between the present results and those from the study of Poole et al is likely due to the difference in local vBMD measurement methods and in the age of the recruited cohorts. However, due the differences in analysis methods and lack of detailed data, any further comparison between the studies mentioned above and our results is likely to be inconclusive.

The rate of change in vBMD with respect to aBMD in homogenous algorithm is found to be insensitive to optimization settings. The average error in predicting vBMD based on the aBMD is 34.5%. The rather large error is clearly a limitation of the assumption that bone loss is uniform across proximal femur, which is known to be higher in trabecular bone relative to cortical bone. This large error can possibly be explained by the fact that nearly 85% of the elements (by both number and volume) across the cohort possessed vBMD below the level of the best-fit τ_{LM} value. Thus, it is expected that the best fit change of vBMD with respect to the change of aBMD as found by the homogeneous algorithm is dominated by changes in vBMD in regions of low density (as defined by the density-specific algorithm). Applying this fixed value to regions of medium and high density will expectedly lead to a large r.m.s. error. This suggests that the homogenous algorithm should be used with caution in FE applications to predict future bone strength.

3.4.2 Density-specific algorithm

The best-fit parameter values found for density-specific algorithm are $m_M = 0.234 \text{ cm}^{-1}$, $m_H = 0.189 \text{ cm}^{-1}$, $\tau_{LM} = 0.253 \text{ g}\cdot\text{cm}^{-3}$, $\tau_{MH} = 0.673 \text{ g}\cdot\text{cm}^{-3}$, with the r.m.s. error of 17.2%, when step

size equals $6E-2$ and dominance parameter threshold η equals 0.64 . Compared to homogenous algorithm, because of three density types been taken into consideration, the r.m.s. error is largely reduced in density-specific algorithm, which provides more confidence in quantifying local bone loss. The parameters of density-specific algorithm and corresponding low-, medium- and high-density region distribution will be discussed separately below.

In the author's limited knowledge, the present study is the only one investigating the relationship between DXA-aBMD and local elemental QCT-vBMD. Most previous studies considered vBMD of trabecular or cortical bone regions, where the definition of these regions was based on QCT values. The slopes (change rates) found in the present study corresponding to the different tissue types appear on first glance to be significantly different compared to results in literature [207,208]. However, careful examination reveals that these differences are either expected or are not meaningful to be considered as such.

Here we compare the results from the present study with those of Amstrup et al [207]. Amstrup et al reported the slope in total hip trabecular and cortical region to be 0.131 cm^{-1} and -0.417 cm^{-1} when trabecular/cortical threshold is set as $0.350 \text{ g}\cdot\text{cm}^{-3}$. This fixed threshold lies in between the thresholds of low/medium and medium/high density regions of the present study. In other words, (i) the low-density region in our study contains only regions identified as trabecular bone in the study of Amstrup et al; (ii) the medium-density region in the present study comprises regions identified as trabecular and cortical bone (but more likely the transitional bone sub-regions of the latter) in the study of Amstrup et al; and (iii) the high-density region in our study contains only regions identified as cortical bone (more likely the so-called real cortical bone) in the study of Amstrup et al. Therefore, the finding that the slope of trabecular region (0.131 cm^{-1}) found by Amstrup et al lies between the slopes of the low-density (zero) and medium-density regions (0.234 cm^{-1}) in our study appears sensible. However, caution must be exercised in drawing strong comparisons between the two studies due to substantial methodological differences. Indeed, such differences strongly influence the finding of positive slopes for both medium- and high-density regions in the present study; which is in stark contrast with the finding of inverse correlation (negative slope) for cortical bone in Amstrup et al. There, the authors attributed the negative slope to an interaction between the volume of the region demarcated as cortical bone, the distribution of bone

mineral density within this region and aBMD. In particular, they found that changing the threshold used to distinguish cortical bone led to differences in relative volume fractions occupied by lower density transition bone and high density (truly) cortical bone within the region labelled as cortical bone. These relative differences were further influenced by differences in aBMD between subjects. In the present study, such sources of interaction are suppressed by considering: a) only element-wise changes, which suppresses variations in volume of regions compared; and b) only elements with dominant density types, which suppresses variation in range of density between regions compared.

Srinivasan et al [208] used a software program to automatically identify cortical, subcortical and trabecular regions of interest (ROI) within the femur neck. The software program is based on relative grey levels in CT images (*i.e.*, variable vBMD thresholds for each patient). This is different from the present study where fixed vBMD thresholds are used to distinguish different regions across all subjects. Furthermore, while Srinivasan et al analyse ROIs, the present study considers element-wise volumes. For these reasons, the results of the two studies are not directly comparable. Hence, with some caution it is noted that the rates of increase in vBMD of trabecular and cortical bone ROIs in the femoral neck per unit increase in FN-aBMD (0.243 cm⁻¹ and 0.315 cm⁻¹ respectively) reported by Srinivasan et al are of the same order of magnitude of those found in the present study. Unfortunately, the average vBMD values in the various ROIs were not reported in Srinivasan et al. Hence, it is not possible to compare the correspondence between vBMDs in these ROIs and those in the low-, medium- and high-density regions identified in the present study.

Paggiosi et al reported age-specific variation of aBMD for women aged between 55 to 79 years based in Sheffield [186]. It was reported that aBMD in femoral neck (FN-aBMD), trochanter (T-aBMD), intertrochanter (IT-aBMD) and total hip (TH-aBMD) regions for women in 75–79 years-band on average reduced by 0.113 g·cm⁻², 0.112 g·cm⁻², 0.162 g·cm⁻² and 0.113 g·cm⁻² respectively, when compared to women in 55-59 years-band. The regions corresponding to FN, T and IT are mapped to specific finite-element sets (visually) of a typical femur taken from the Sheffield cohort (Figure 3.14). The average vBMD losses in the Sheffield cohort over such volumes are estimated based on the loss of FN-aBMD reported by Paggiosi. As the age range of the Sheffield cohort spans over 55 to 91 years, to estimate the vBMD loss between the

same age range of Paggiosi’s cohort, the mean FN-aBMD of 55–59 years-band ($0.944 \text{ g}\cdot\text{cm}^{-2}$) and 75–79 years-band ($0.805 \text{ g}\cdot\text{cm}^{-2}$) reported by Paggiosi et al were assigned to all subjects in the Sheffield cohort separately. For each subject, the elemental vBMD distributions corresponding to mean FN-aBMD of two age-bands are determined by density-specific algorithm and the average vBMD in a particular volume (*i.e.*, FN, T, IT and TH) is calculated by dividing the sum of elemental vBMD multiplied by elemental volume over whole volume of that region. Finally, average of each regional vBMD loss over all subjects is obtained. Identical to the trend in Paggiosi study, the largest vBMD loss is found in the IT, followed by FN, TH and T in order. This implies that the rate of change in vBMD with respect to aBMD in these regions of interest is positive, which in agreement with the results of the present study.

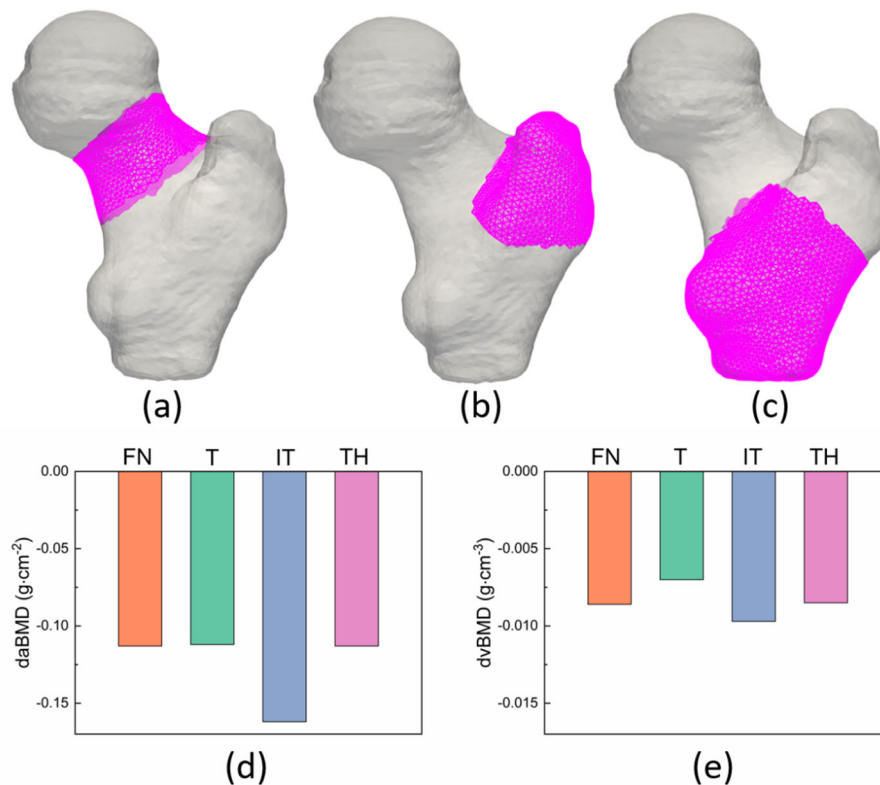


Figure 3.14 The change of BMD in the volume of interest (VOI) predicted based on Paggiosi study. (a-c) denote the VOI visually extracted from 3D geometry (marked in bright pink): the femoral neck (FN), trochanter (T) and intertrochanter (IT), respectively. Panel (d) shows the change of aBMD reported by Paggiosi et al. (Adapt with permission from [186].) Panel (e) show the average change of vBMD in Sheffield cohort based on the change of FN-aBMD reported by Paggiosi et al.

3.3.3 A spatio-temporal atlas of local vBMD change over a 6-year period

Farzi et al used longitudinal DXA image data from 120 subjects aged between 55 to 60 years in OPUS study [186] to measure reductions in local (pixel-level) aBMD due to ageing over 6 years [210]. Due to the similar time duration of ageing considered here, the spatial pattern of local aBMD reductions in Farzi et al may be compared to that predicted by the present study. From the percentage BMD loss map in Figure 3.15(a) [210], it can be inferred that changes in local aBMD in the medial femoral shaft and greater trochanter are in the order of $\pm 5\%$, which agree with the magnitude of vBMD reduction predicted in the present study (reduction of 1% or more, Figure 3.13(b)). The drawback of the approach used by Farzi et al is that bone loss in these regions is not found to be statistically significant (as seen in the q-map), which is a direct result of methodological challenges such as using 2D DXA images, different imaging instruments and a multi-centre study design.

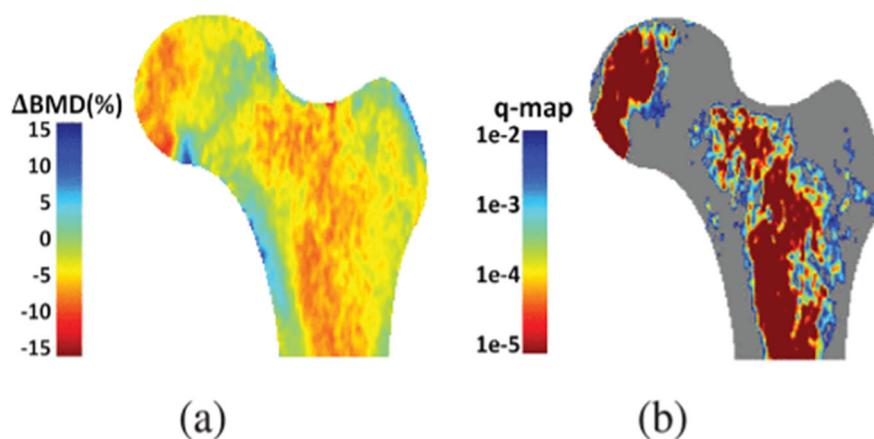


Figure 3.15 (a) The percentage of aBMD change over 6 years based on 120 subjects in OPUS study. (b) Q-map obtained from a paired t-test by false discovery rate analysis reflecting the confidence of regional BMD change over 6 years. Reproduced from [210] with permission.

The largest percent changes in aBMD measured in Farzi et al correspond to regions of predominantly low density – as identified in the present study – when the latter are projected in the plane of the DXA image. This is expected as the baseline aBMD in such regions could be extremely small. Interestingly, Farzi et al found the changes in local aBMD in these regions to be statistically significant. Whether capturing changes in low density regions with high confidence than in regions of high density leads to more accurate prediction of loss of bone strength remains an open question. Additionally, Farzi et al found significant local aBMD loss

in the femoral head region. However, the superimposition of the femoral head and acetabulum often makes DXA measurement at femoral head inaccurate [199].

Similar to SSM and SAM approaches, the study of Farzi et al is dependent on the discretisation a template DXA image, as this is the basis for comparison of pixel-level aBMD across subjects. Hence, in order to forward predict the bone loss within the femur of a specific subject, they too needed to map this subject's DXA images to the template image using a pipeline called Region-Free Analysis. However, the bone loss algorithm developed in this study is discretisation independent, and the slope and threshold values can be readily applied to any CT image irrespective of discretisation.

Influence of variable elemental volumes

The variation of volume across elements in a typical subject was found to be larger than the variation of volume across subjects in a typical element, as shown in Figure 3.16.

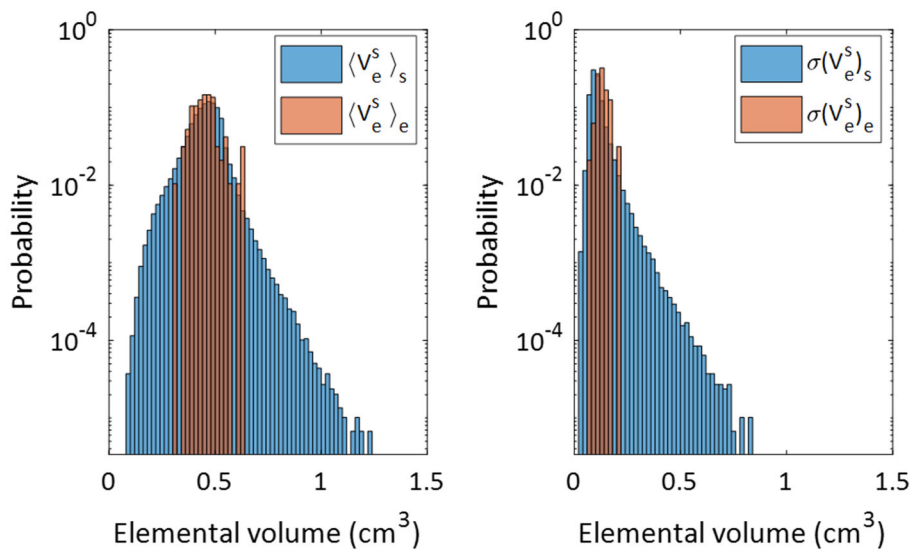


Figure 3.16 Histograms of the mean (left) and standard deviation (right) of elemental volume over all subjects or all elements.

To determine the influence of different volumes as weight-factor, the original model (referred to as Vall) is modified such that V_e^s in Equation 3.8 and Equation 3.9 is replaced either by 1 (this model is hereafter referred to as Vno) or by the average volume over all subjects ($\langle V_e^s \rangle_s$) (this model is hereafter referred to as Vavg). The optimisation process, including the

execution of the routine *lsqnonlin*, remains unchanged. For each model, η varied between 0.60 to 0.80 and SS was selected from 1E-2 to 7E-2.

Table 3.3 Parameters of density-specific algorithm in dependence of elemental volume weighting factor used to compute the error vector. The corresponding percentage of discarded elements (%Discard) and the r.m.s. error of prediction (%RMS) are also listed. Settings are named in the form of Vxx_SS_ η , where Vno, Vavg and Vall denote, respectively, models with a constant (*i.e.*, unity), average elemental volumes $\langle V_e^S \rangle_s$ and subject-specific elemental volumes V_e^S being used as weighting factors. SS and η denotes respectively step size and dominance threshold parameter. The set marked in red is the one selected in this study.

Setting	m_M	m_H	τ_{LM}	τ_{MH}	%Discard	%RMS
Vno_0.62_6E-2	0.226	0.175	0.265	0.703	25.9	19.4
Vno_0.64_6E-2	0.227	0.166	0.269	0.710	27.2	19.2
Vno_0.66_6E-2	0.213	0.167	0.273	0.723	28.4	19.1
Vavg_0.62_6E-2	0.222	0.188	0.250	0.683	26.8	17.7
Vavg_0.64_6E-2	0.237	0.177	0.255	0.690	28.1	17.4
Vavg_0.66_6E-2	0.192	0.200	0.255	0.695	29.6	17.0
Vall_0.62_6E-2	0.235	0.187	0.255	0.678	26.6	17.7
Vall_0.64_6E-2	0.234	0.189	0.253	0.673	28.4	17.2
Vall_0.66_5E-2	0.246	0.152	0.259	0.681	29.6	17.0

For brevity, detailed results for only three sets whose settings are closest to the baseline Vall model setting are reported in Table 3.3. Paired t-tests were conducted over parameters output by *lsqnonlin* between Vall and Vavg and between Vall and Vno models. Between Vall and Vavg models, no statistically significant differences are found in r.m.s. error ($p=0.51$), m_M ($p=0.29$) and τ_{MH} ($p=0.06$). Statistically significant differences are found in m_H ($p<0.001$) and τ_{LM} ($p<0.001$), yet the absolute differences are quite small close to the baseline settings

(Table 3). In contrast, between the Vall and Vno models, the r.m.s. errors are higher by about 2.5%, and except for m_M ($p=0.87$), the other three parameters are significantly different ($p<0.001$). The results highlight that although the density-specific algorithm is discretisation independent, if the optimisation process described here is to be applied to determine parameters of another algorithm (or the same algorithm in a markedly different patient groups), then caution needs to be exercised in not neglecting the potential variability in element volumes used as input.

Association of bone loss with fracture status

The cohort of this study is originally designed to reflect the typical distribution of osteopenia found in the population referred to an osteoporosis specialist in a secondary care setting. The aBMD found in Sheffield cohort is from $0.36 \text{ g}\cdot\text{cm}^{-2}$ to $0.96 \text{ g}\cdot\text{cm}^{-2}$ ($0.62 \text{ g}\cdot\text{cm}^{-2}$ on average) which is slightly lower than aBMD of a similar age reported in the literature, $0.71 \text{ g}\cdot\text{cm}^{-2}$, $0.71 \text{ g}\cdot\text{cm}^{-2}$, $0.69 \text{ g}\cdot\text{cm}^{-2}$ for UK, Germany and France [186]. Additionally, the Sheffield cohort was originally recruited for a case-control study. Hence, the 100 subjects (4 subjects are excluded in this study due to unrecoverable scans) were individually matched by age, height, and weight. Half of the cohort experienced a hip fracture due to low-energy trauma within the previous 90 days of clinical presentation. To evaluate the association of the density-specific algorithm with hip fracture status, the optimization process is separately applied to the fracture and non-fracture subjects. For each model, η varied between 0.60 to 0.80 and SS was selected from $1\text{E}-2$ to $7\text{E}-2$.

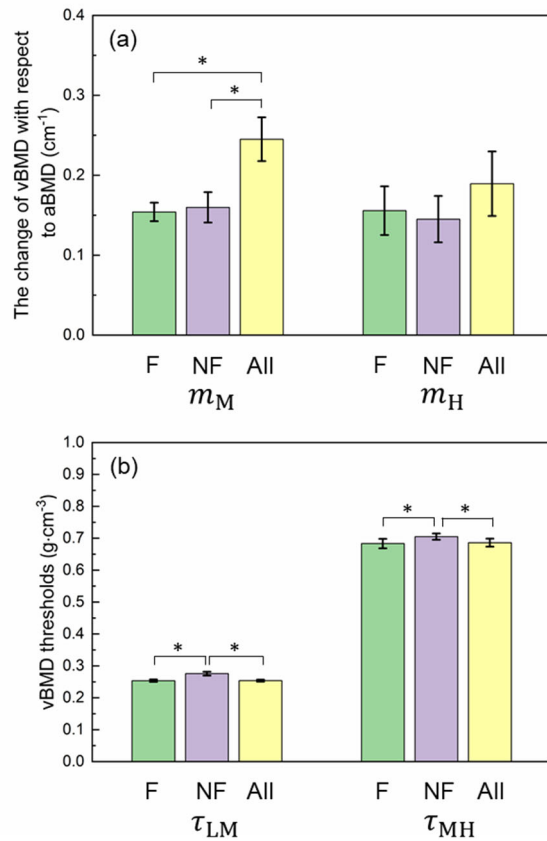


Figure 3.17 Parameters of density-specific algorithm based on fracture (F), non-fracture subjects (NF) and all subjects in the Sheffield cohort (ALL). Whiskers denote standard deviation over different optimisation settings (see main text); ‘*’ denotes a statistically significant ($p < 0.001$) difference.

The results (Figure 3.17) show that fractured subjects lose bone faster than non-fracture subjects in the high-density region, while the loss rate is slightly slower in medium-density region. Yet, a paired t-test shows that the difference between two subgroups is not statistically significant ($p = 0.300$ for m_M and $p = 0.463$ for m_H). Some studies indicated that osteoporosis may not simplistically be attributed to excessive bone loss according to age, as many fractured patients do not consistently have more rapid bone loss [213]. Low peak bone density may also play an important role in the incidence of osteoporosis. Additional to low aBMD, increasing frequency of falls may be another factor in elderly women to fracture their hips, that falls occur with increasing frequencies in aging women and women with fractures have fallen more in the past than their peers [214]. Interestingly, both m_M in two subgroups are much smaller than m_M obtained from whole cohort. This may be due to the dispersion of

vBMD in two subgroups that more elements are identified as low-density type in fractured group (69.9% low, 21.0% medium and 9.1% high in fractured group vs. 61.6% low, 25.7% medium and 12.7% high for non-fracture group, based on the threshold determined from all subjects). The two vBMD thresholds for fractured subjects are slightly but significantly lower than those for non-fractured subjects ($p < 0.001$ for both τ_{LM} and τ_{MH}), which is consistent with our expectation.

3.4.3 Limitations

There are several limitations to this study. The proposed bone-loss algorithms are limited to predicting only a portion of the true vBMD change over time. Specifically, the algorithms predict the non-subject-specific portion of vBMD change that is correlated to change in FN-aBMD. However, this limitation also explains why the r.m.s. errors obtained in the fitting process are somewhat large (of the order of 20–30%) but should not be considered to substantially undermine the confidence in these algorithms.

Note that the fitting process uses cross-sectional data obtained from a heterogeneous population. The vBMD at a certain location in a subject indexed by their FN-aBMD has a complex dependence on a range of subject-specific factors, including the subject's peak bone mass achieved at skeletal maturity (which itself would depend on a range of subject-specific factors such as family history and nutrition), on the subject's age since skeletal maturity, any underlying conditions or medical events until that age, the subject's history of physical activity levels modulated by the subject's bone size and shape [215]. Yet, only the effect of the bone geometry (size and shape) is suppressed by the standardisation of projections and regions of interest applied to DXA imaging and of energy sources used in DXA and CT and the use of morphed meshes. It is therefore expected that all the remaining factors detailed above will contribute to the errors defined in Equations 3.5 and 3.9, which effectively assume that each subject possesses – at some point in their lifetime – an average (non-subject-specific) vBMD distribution (given by $\langle v \rangle$) when their aBMD equals the average aBMD in the population ($\langle a \rangle$). It is challenging to model / quantify the extent to which these factors influence the magnitude of the error and beyond the scope of the present study. Yet, the somewhat large magnitudes of errors are not surprising in themselves.

In the absence of longitudinal CT data, it is also not possible to quantify to what extent the suppression of the effect of subject-specific bone geometry is successful. For example, if the cohort used in this study is biased towards a certain shape mode, relative to the prevalence of this mode in the general population, it is likely that the estimates of bone loss rate coefficients and thresholds are influenced by this bias. This limitation is ultimately related to the use of a relatively small dataset, a limitation that is discussed in more detail below.

The cohort used here was recruited entirely in Sheffield. This may limit the application to women from other countries or other ethnicities. Several studies have reported considerable variance in the proximal femur BMD of Caucasian women from different countries [186,216,217]. However, as aBMD appears in the form of difference (change in aBMD) in the two bone loss algorithms, to some extent the impact of geographical and ethnic differences is reduced. Another potential limitation is the relatively small training set, since parameters of density-specific algorithm are relatively sensitive to optimization settings. If a larger data set is available, an insensitivity zone could be potentially identified. However, the normalised r.m.s. of prediction was found to have no significant difference in the low gradient region, suggesting extra data may not increase prediction accuracy significantly.

Finally, the use of cross-sectional data makes it challenging to test more sophisticated model forms than piecewise-linear (Equation 3.2), and a strict validation of predicting future bone loss using these algorithms is also not possible. However, if longitudinal data were available, it would allow to validate the predictions based on the bone loss algorithms in a very straightforward manner, which follows from the mesh invariant nature of the proposed algorithms. Besides, by applying the current algorithms, the challenges of biomedical data accessibility (in particular, CT scans) are overcome. Indeed, further application of the algorithms to predict subject-specific future bone strength is now possible.

4. Sensitivity of femur strength to variation in aBMD

Chapter 2 reviewed the assessment of hip fracture risk using mechanistic models. It shows that QCT-based finite element subject-specific model (QCT-SSFE) has matured to a status with good accuracy in predicting bone strength, which is a key determinant of fracture risk. Combined with the two bone loss algorithms proposed in Chapter 3, the elemental QCT-vBMD change can be quantified based on the variation of DXA-based areal bone mineral density (aBMD) measured at the femoral neck (henceforth denoted by aBMD for brevity). In turn, this can be potentially applied to investigate the change of bone strength. Chapter 2 also reviewed the state-of-art in in silico clinical trials based on virtual populations and some successful early adoptions in other areas of biomechanics. This offers a motivation to generate and use virtual cohorts to enrich physical cohorts in the study of osteoporosis and its interventions. Additionally, although many studies have shown that bone strength can be affected by aBMD and bone geometry, there is a limited information of the independent effect of aBMD alone. Thus, the present study is also motivated to use virtual populations to investigate the sensitivity of QCT-SSFE predicted bone strength to aBMD while the bone geometry is kept fixed.

4.1 Introduction

Prior to a new medical intervention being marketed to the public, it must go through several clinical trial phases to thoroughly evaluate its safety and effectiveness. The expenditure of clinical trials is huge in terms of both capital and time. At present, the potential risks to the participants are not fully understood. The median cost of conducting a clinical study from the protocol approval to Phase III trials is reported to be about \$33.4 million (£23.6) [218]. The total trial duration is approximately six to seven years on average, yet most trials end in failures. The probability of progressing from phase I to FDA approval is found to be only 9.6% [173].

Clinical trial catastrophes also may occur where some originally healthy volunteers end up with serious problems and even lose their lives during the trials. For example, a trial of erectile dysfunction drug on pregnant women conducting in the year 2018 in Amsterdam was ordered to stop after 11 babies died [219]. Besides these tragedies, there is another debate on whether it is ethical to assign some participants with disease to a placebo-controlled group which is known to have non-active treatment. Apart from controversial ethical issues, from a statistical point of view, participant numbers are often too small to draw a solid conclusion regarding the proposed intervention.

The socioeconomic impact of hip fracture is well-known: for women aged over 50, the remaining lifetime risk of suffering hip fracture is around 20%, equivalent to having a breast cancer [21]; only half of hip fracture survivors can recover to walk unaided again [3]; the annual cost of treating hip fracture alone exceeds £2 billion in the UK [3]. However, hip fracture incidence rate in the general population is very low (32 fractures per 10,000 person-years in British women over 50 [22]), which impedes reaching adequately powered conclusions for clinical trials with new fracture as primary endpoint.

To alleviate the above challenges, *in silico* clinical trials (ISCTs) have been proposed as a supplementary tool. Details of ISCTs concepts have been described in Section 2.12, however, a brief recap of virtual patients is mentioned below. A virtual patient is a digitized dataset generated based on patient-specific models comprising biomedical information relevant to the disease/condition and treatment in question. The ISCTs simulate a standard trial by subjecting virtual patients to untreated and treated conditions, where each condition is expressed by a mathematical model. Therefore, an essential ingredient in any ISCT, irrespective of the intervention is the definition of a virtual patient including a mathematical model for the untreated progression of disease condition.

This chapter is focused on the change of bone strength due with age in elderly British women in the absence of any treatment for postmenopausal osteoporosis. At present, aBMD measured at femoral neck is often treated as a good surrogate of proximal femur strength. But the limitations of aBMD are underscored by the observation that a woman aged 75 has 4–7 times higher fracture risk than woman aged 45 with the identical BMD [220]. It is well known now that bone strength can be much more accurately predicted from QCT based SSFE

analysis which accounts for proximal femur geometry, volumetric bone mineral density (vBMD) distribution and fall-specific loading conditions. Yet, given the high radiation exposure and cost of QCT scans, it is challenging to recruit enough number of subjects to create a virtual patient population based on QCT data only. Thus, it is much needed to create a virtual patient generation pipeline that can be used to perform QCT-SSFE but not require a large number of QCT scans.

Exactly such a situation is presented by the Sheffield cohort QCT dataset. This dataset was obtained by Yang et al [203] and possessed characteristics typical of the at-risk (of hip fracture) population and referred to an osteoporosis specialist in a secondary care sitting. However, the Sheffield cohort possesses insufficient numerosity to capture variations, and in particular variations of combinations of biomechanical parameters (bone size, shape and vBMD distribution), that might occur in the entire at-risk population of British women over 50. Therefore, to improve statistical significance of clinical trials, it is required to generate a virtual patient population to enrich the Sheffield cohort. In the present study, this is done by combining the areal bone mineral density (aBMD) distribution in British elderly women with the bone loss algorithms proposed in the Chapter 3. The aBMD distributions are obtained from an observational study on the international variation in proximal femur bone mineral density conducted by Paggiosi et al [186], where one observation centre was located in Sheffield.

To investigate the effect of ageing, the generated virtual patients of untreated condition model is applied, which opens the possibility of virtual patients as a first step towards realizing an ISCT for interventions to reduce risk of fragility hip fractures. Besides the application of enriching the dataset, the virtual patients are also used to investigate the potential relation between aBMD and bone strength by varying aBMD while femoral geometry is fixed.

4.2 Method

4.2.1 FE analysis of physical patients (Sheffield cohort)

The Sheffield cohort comprised ninety-six Caucasian postmenopausal women, while forty-seven of them had been diagnosed with low energy trauma fractures in the proximal femur.

Details of Sheffield cohort have been reported previously in Section 3.2.1 and here key information (see Table 4.1) relevant to this study are revisited for convenience.

Table 4.1 Descriptive statistics of Sheffield cohort. The numbers for age and aBMD correspond to the range, mean value and standard deviation (in parentheses).

	All	Fractured	Non-fractured
N	96	47	49
Age (years)	55-91, 75(9)	55-89, 75(9)	56-91, 75(9)
aBMD ($\text{g}\cdot\text{cm}^{-2}$)	0.36-0.96, 0.62(0.11)	0.36-0.73, 0.57(0.10)	0.49-0.96, 0.67(0.10)

The modelling procedure used in this study is based on Altai et al [141]. The pipeline has been reviewed in Section 2.9.1. For reference, the application of the pipeline to physical patients in the Sheffield cohort is repeated briefly below.

4.2.1.1 Geometry and mesh

All patients in Sheffield cohort (hereafter referred as physical patients) received CT scans of their proximal femurs (imaging protocols have been reported in Section 3.2.1.), with spatial resolution of 0.625 mm in slice thickness and $0.74*0.74 \text{ mm}^2$ in pixel size [131,203]. CT image data were segmented and then discretised into FE tetrahedral meshes possessing an average edge-length of 3 mm. The subject-specific meshes were obtained by morphing a template mesh, consisted of 295589 elements, to each subject's femur geometry.

4.2.1.2 Material properties of physical patient

The procedure reviewed below is described in more detail in refs [104,110,131,221]. Elemental volumetric bone density (vBMD) of each patient is obtained by mapping with the greyscale value of associated CT scans; this mapping procedure is already implemented in BoneMat software [221]. The mapped vBMD values across the 295589 elements are then binned into ~400 discrete values (see Section 5.2.3.1). These are used to compute as many distinct elemental elastic moduli (ElastMod) values using the equations reported by Schileo et

al [104] and Morgan et al [110]. These elastic moduli are then mapped back to each element in the FE mesh.

$$\rho_{\text{ash}} = 0.8772 \cdot \rho_{\text{QCT}} + 0.07895 \quad (\text{Equation 4.1})$$

$$\frac{\rho_{\text{ash}}}{\rho_{\text{app}}} = 0.6 \quad (\text{Equation 4.2})$$

$$\text{ElastMod} = 6850 \cdot \rho_{\text{app}}^{1.49} = 14664 \cdot \rho_{\text{ash}}^{1.49} \quad (\text{Equation 4.3})$$

$$\text{ElastMod} = 14664 \cdot \left((0.8771 \cdot \rho_{\text{QCT}} + 0.07895)^{1.49} \right) \quad (\text{Equation 4.4})$$

4.2.1.3 Reference system

A femoral reference system defined by anatomical landmarks was generated to simulate different physiological loading scenarios. Anatomical landmarks are virtually palpated and a local reference system is generated using BuilderM2O software [222].

The origin of anatomical reference system is at the centre of femoral head, while the X and Y axes point away from the knee centre and toward the most lateral point on the greater trochanter respectively (Figure 4.1).

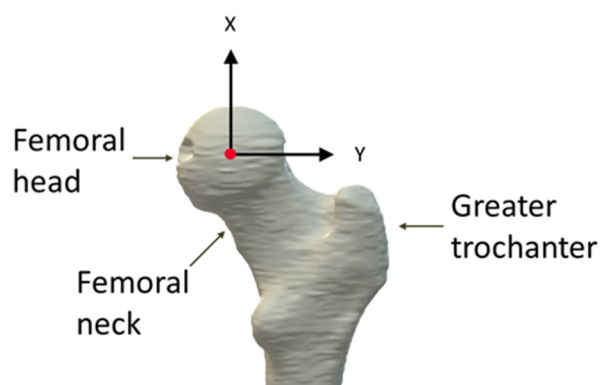


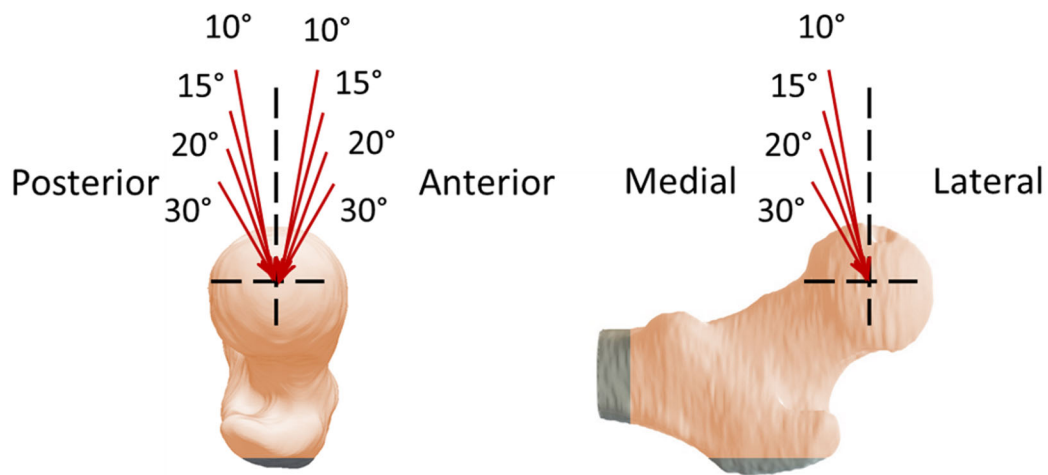
Figure 4.1 Anatomical reference system of the adult proximal femur.

As CT scans only contained proximal femur and the knee centre required the full femur geometry, an estimated full-femur anatomy was mapped to each proximal femur using a

rigid-body registration and a statistical shape model-guided fit using Musculoskeletal Atlas Project Client software (MAP Client, the University of Auckland) and associated plugins [131].

4.2.1.4 Multiple loading conditions

Thirty-three different loading conditions were applied at the centre of femoral head, simulating either anterolateral or posterolateral falls. The force direction varied from -30° to $+30^\circ$ in the transverse plane with increment of 10° (α) and in the frontal plane only medial angles were taken into account in terms of 0° , 10° , 15° , 20° and 30° (β) (Figure 4.2). Lateral angles were excluded from the simulation because the knee would hit the ground ahead of the hip during the fall. The magnitude of the concentrated load was arbitrarily selected as 500N, supported by a sensitivity study that predicted peak strain has a linear relationship with applied load [141].



Medial	Medial-Anterior	Medial-Posterior
0°Med (Neutral)	0°Med -10°Ant	0°Med -10°Pos
10°Med	0°Med -15°Ant	0°Med -20°Pos
15°Med	0°Med -20°Ant	0°Med -30°Pos
20°Med	0°Med -30°Ant	10°Med -10°Pos
30°Med	10°Med -10°Ant	10°Med -20°Pos
	10°Med -20°Ant	10°Med -30°Pos
	10°Med -30°Ant	20°Med -10°Pos
	15°Med -15°Ant	20°Med -20°Pos
	15°Med -30°Ant	20°Med -30°Pos
	20°Med -10°Ant	30°Med -10°Pos
	20°Med -20°Ant	30°Med -20°Pos
	20°Med -30°Ant	30°Med -30°Pos
	30°Med -10°Ant	
	30°Med -15°Ant	
	30°Med -20°Ant	
	30°Med -30°Ant	

Figure 4.2 Multiple loading conditions (varying in thirty-three orientations) were applied at the centre of femoral head to simulate anterolateral and posterolateral falls. Region of interest used in the FE analysis was marked in orange, while regions applied with boundary constrains were removed (20mm from distal end and 6mm from the most lateral point in the greater trochanter). Adapted from [141] with permission.

4.2.1.5 Boundary constraints

Multi-point constraints (MPC) model (see Figure 4.3) was selected based on the trade-off between computational time and stratification power. Altai et al reported that the average computational time for MPC is 8 minutes compared with 1 hour for a full non-linear contact model, while the stratification power of MPC is slightly lower than that of the contact model (MPC: AUROC=0.80 vs contact: AUROC=0.82) [141].

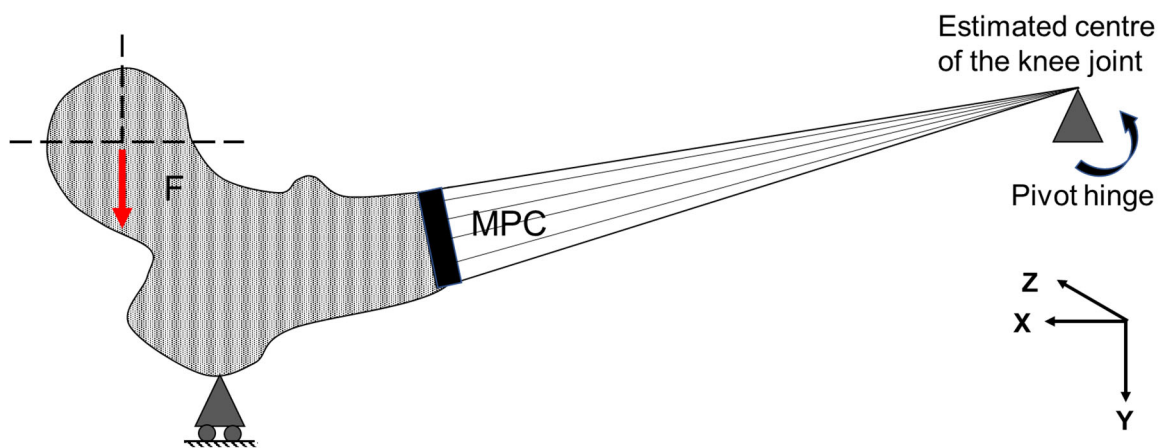


Figure 4.3 Schematic diagram of MPC model. MPC elements were applied to link nodes located at the distal end to the pilot node which denoted the estimated centre of the knee joint. The node with highest Y value in the greater trochanter region was constrained with a non-friction slider. Adapted from [141] with permission.

A non-friction slider was applied at the greater trochanter: the most protruding node found in the loading direction was constrained to move along the loading direction (y direction), while it was allowed free rotation and movement in the other two directions (x and z directions).

At the distal end, a relaxed constraint was achieved by MPC elements which links the distal end to the centre of the knee joint, represented by a pilot node. To simulate knee joint motion during the fall, the pilot node was only allowed to rotate around the axis transverse to loading direction, while all other degree of freedoms kept fixed. Nodes at the distal end were constrained following a linear constrained equation to the pilot node to mimic a rotational hinge around the knee joint.

4.2.1.6 Failure criterion

The near totality of all fall-induced hip fractures is known to initiate in the region of interest of the femur surface (ROI) marked in orange in Figure 4.2. Following FE analysis of a loading condition, at each surface node on the above ROI, the first and third principal strains averaged over a circular area of 3 mm radius centred on this node were computed. The principal strain

criterion was used to identify failure and the location of fracture [104,149,158]. Failure occurs when either the (averaged) first or third principal strain in the region of interest (ROI) reaches the failure limit [143,149]. Therefore, the averaged strains in the ROI corresponding to 500 N load were scaled linearly until the limit values 0.73% tensile strain and 1.04% in compressive strain were reached [143]. Bone strength was obtained by multiplying the smaller of the two scaling factors with 500 N correspondingly. After bone strength among the thirty-three simulated orientations is computed as described above, the minimum pathological strength ($\text{MinPatS}, \min|S^{\alpha,\beta}|$) was defined as the minimum of these values.

4.2.2 Generation and FE analysis of virtual patients

In the present study, the above pipeline for analysing physical patients is extended to generate a virtual population comprising patients with target aBMD values, as shown in Figure 4.4. Briefly, there are three steps: 1) extracting elemental vBMD values from a physical patient FE model, 2) determining (new) vBMD values for virtual patients by applying bone loss algorithm proposed in Chapter 3 and recalculating elastic moduli based on new vBMD values, and 3) modifying the physical patient model with the new vBMD and moduli values. Bone strength of the modified virtual patient model is then predicted by the analysis steps as described in Sections 4.2.1.3–4.2.1.6.

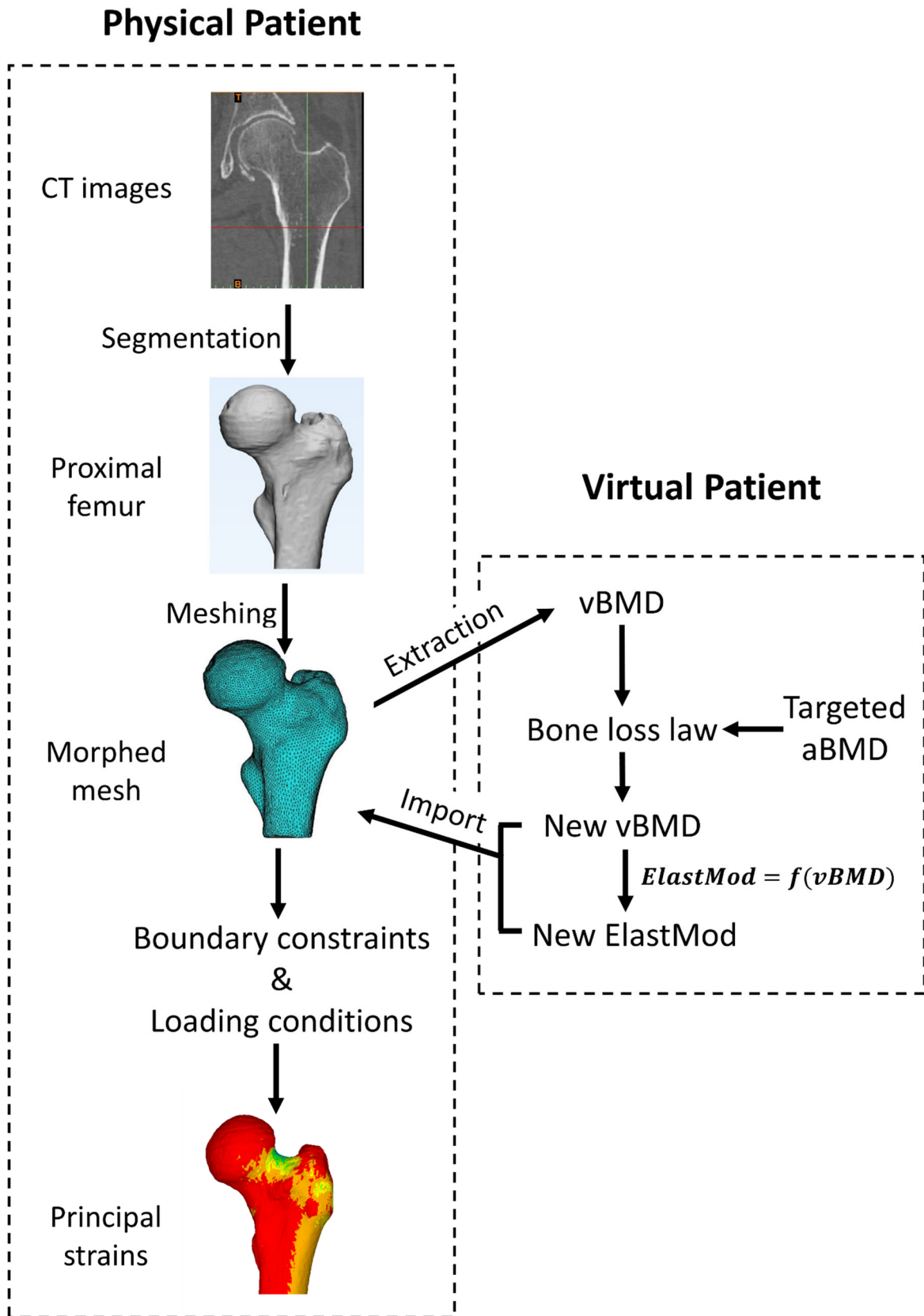


Figure 4.4 General procedure of generating a virtual population based on Sheffield cohort with targeted aBMD.

4.2.2.1 Material properties list extraction

Material properties are extracted from Ansys format .db files of each physical patients into .mp files, consisting of material index (ID), elastic modulus, vBMD and Poisson ratio. For each element, its vBMD and elastic modulus are mapped to its material ID (Figure 4.5). To extract material property list in batch mode the command /MPWRITE is used; in the graphical user interface (GUI), the menu option /List/Properties/All Materials is selected. The total number of material ID for each patient varied from 342 to 465.

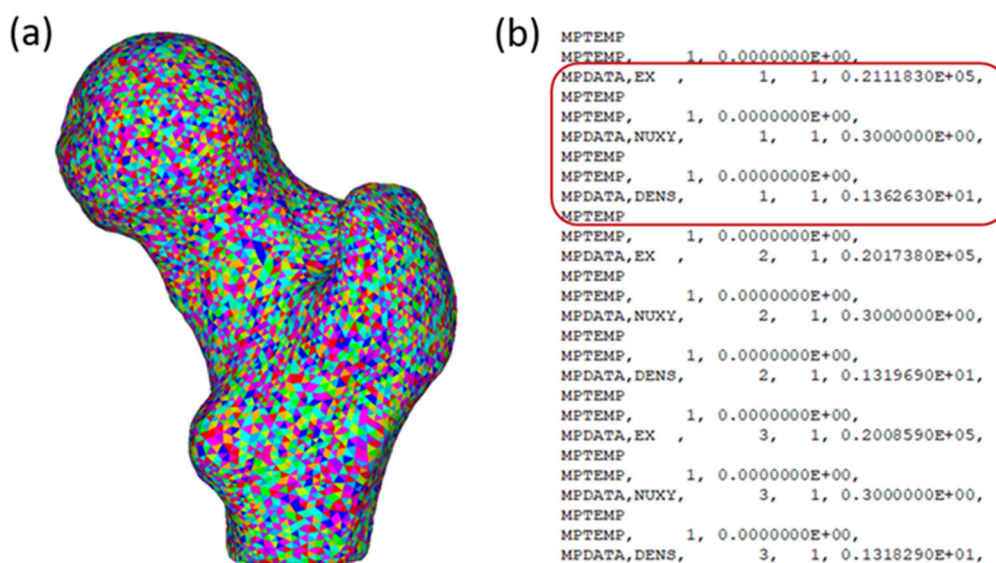


Figure 4.5 (a) An example of the distribution of material IDs over proximal femur; and (b) An example of .mp file and the ElastMod, Poisson ratio, vBMD for material ID number 1 was marked in the red box.

4.2.2.2 Determining and mapping new properties

New material properties are determined by targeted aBMD (a_{vp}) of virtual patients and bone loss algorithms proposed in Chapter 3. The change of the elemental material properties is achieved by using a self-developed script implemented in Matlab 2019b (MathWorks, Natick, MA) to update the value of vBMD and ElastMod simultaneously for each material ID. Updated material property lists for virtual population are then imported back to original meshes by /MPREAD command in Ansys while remaining the mapping relationship between element and material ID unchanged.

The vBMD for an element of a virtual patient was estimated either by using the homogeneous algorithm (Equation 4.5) or by using the density-specific algorithm (Equation 4.6), respectively.

$$v_{(vp,e)} = v_{(p,e)} + m' \cdot (a_{vp} - a_p) \quad (\text{Equation 4.5})$$

$$v_{(vp,e)} = v_{(p,e)} + m \cdot (a_{vp} - a_p) \quad (\text{Equation 4.6})$$

$$m = \begin{cases} 0, & 0 < v_{(p,e)} < \tau_{LM} \\ m_M, & \tau_{LM} \leq v_{(p,e)} < \tau_{MH} \\ m_H, & \tau_{MH} \leq v_{(p,e)} \end{cases} \quad (\text{Equation 4.7})$$

Here, vp is a virtual patient index and p is a physical patient index, while e stands for element number. Variables m' and m denote the slopes for homogeneous and density-specific algorithms respectively. It is recalled from Chapter 3 that the best-fit values are: $m' = 0.363 \text{ cm}^{-1}$, $m_M = 0.233 \text{ cm}^{-1}$, $m_H = 0.166 \text{ cm}^{-1}$, $\tau_{LM} = 0.234 \text{ g}\cdot\text{cm}^{-3}$ and $\tau_{MH} = 0.678 \text{ g}\cdot\text{cm}^{-3}$. Thus, $v_{(vp,e)}$ is the vBMD in element e estimated in a virtual patient vp possessing target aBMD a_{vp} , and identical bone size and shape as physical patient p . Physical patient p possesses aBMD a_p and vBMD is $v_{(p,e)}$ in element e .

Note that when applying the homogeneous algorithm (Equation 4.5), a negative $v_{(vp,e)}$ may be predicted for those elements where $v_{(p,e)}$ is small and the target aBMD is smaller than the aBMD in the physical patient $a_{vp} < a_p$. To avoid this, in such a scenario, $v_{(vp,e)}$ is set as smallest as the minimum value of $v_{(p,e)}$ across all elements.

In the density-specific algorithm, the three density regions (low-, medium- and high-density) were determined by vBMD thresholds τ_{LM} and τ_{MH} . It is possible for elements with vBMD located close to thresholds to jump across the distinct density regions as aBMD changes. An example of this scenario is shown in Figure 4.6. For such elements, the different slopes of vBMD change with respect to aBMD change in the prediction of $v_{(vp,e)}$ are accounted for by Equation 4.8 and Equation 4.9. The aBMD a_τ corresponding to the vBMD crossover at threshold vBMD value τ_{MH} is computed as given by Equation 7, where m_{original} denotes the slope in the density region corresponding to physical patient vBMD value $v_{(p,e)}$. The condition $|a_\tau - a_p| < |a_{vp} - a_p|$, determines whether this aBMD value lies between the target virtual

patient's aBMD values and that of the physical patient. If the condition holds, then the vBMD value for the virtual patient $v_{(vp,e)}$ is determined using Equation 4.9, denoting the slope of the corresponding density region to be m_{new} .

$$a_{\tau} = a_p + \frac{\tau_{MH} - v_{(p,e)}}{m_{\text{original}}} \quad (\text{Equation 4.8})$$

$$v_{(vp,e)} = \tau_{MH} + m_{\text{new}} \cdot (a_{vp} - a_p) \quad (\text{Equation 4.9})$$

As shown in Figure 4.6 there is an element e of which $v_{(p,e)}$ is identified in the high-density region but close to τ_{MH} . If $v_{(p,e)} + m_H \cdot (a_{vp} - a_p)$ is smaller than τ_{MH} , then $v_{(vp,e)}$ will be in the medium-density region. However, due to the slope in high-density region is less steep than that in medium-density region, using m_H alone would lead to the overestimation of $v_{(vp,e)}$. Hence, $v_{(vp,e)}$ is calculated as the sum of the change of vBMD in medium-density and high-density region using their respective slopes.

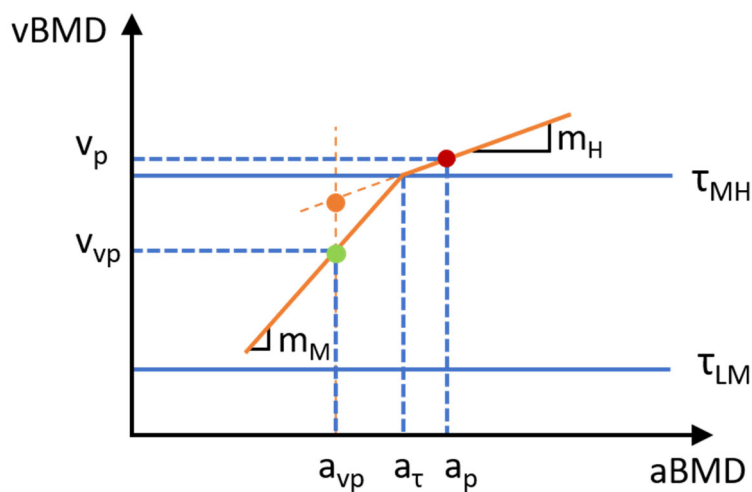


Figure 4.6 Schematic of an element in different regions of vBMD in physical and virtual patients, due to relative proximity of vBMD $v_{(vp,e)}$ to the threshold τ_{MH} and the difference between original (a_p) and targeted aBMD (a_{vp}) values. In the physical patient, the element lies in the high-density region (filled red circle), while in the virtual patient, it is in the medium-density region. Predicting $v_{(vp,e)}$ using only the slope of the high-density region.

Consider $a_{vp} < a_p$ and there exists an element with $v_{(p,e)}$, which is just larger than τ_{LM} , such that $v_{(vp,e)}$, when it is predicted using Equation 4.6 and Equation 4.7 ($m = m_M$), would be smaller than τ_{LM} . In such case, $v_{(vp,e)}$ is set to equal the value τ_{LM} . This is consistent with the assumption that there is no remodeling in the low-density region. However, when $a_{vp} > a_p$, irrespective of how large this inequality is, elements with $v_{(p,e)} < \tau_{LM}$ are given the same vBMD value in the virtual patient.

4.2.3 Virtual population analysis

A virtual population is created to simulate change in bone strength with age in postmenopausal British elderly women. This is relevant to prediction of hip fracture risk as past studies have found that 84% of variation in current fracture risk (ARF0) is explained by variation in bone strength alone [5]. Age groups are considered in 5-year bands (55–59, 60–64, ..., 75–79). It is assumed that any postmenopausal osteoporosis in the virtual subjects remains untreated.

For each of the 5-year age-groups above, the distribution of proximal femur geometries (*i.e.*, size and shape) of British women is assumed to be adequately represented by the femur geometries of the 49 control subjects in the Sheffield cohort. aBMD in each age group is assumed to be normally distributed with mean and standard deviation as reported in the Sheffield centre of OPUS study [186]. It is assumed that the distribution of femur geometry is independent with respect to the distribution of aBMD. Thus, a sample of $n=10$ aBMD values $\{a_{vp}\}$ is drawn from the age-group specific distribution mentioned above. Then, a sample of proximal femurs of virtual subjects in the age-group is defined by associating the femur geometry of each control subject p in the Sheffield cohort to all n aBMD values sampled above.

The pipeline to perform FE analyses as described in Section 4.2.2 is applied with some modifications (see below) to predict $49 \cdot n$ bone strength (S) values in each age-group, from which statistical properties of bone strength distribution are obtained.

As executing FE simulations for all virtual subjects ($49 \cdot n$) requires substantial computational effort, the following approach is taken. It is assumed that for a fixed side-fall loading

configuration and femur geometry, the dependence of bone strength on aBMD is a perfectly linear function. Here, the angles of hip abduction (α , 0° to $+30^\circ$) and internal hip rotation (β , -30° to $+30^\circ$) specify the loading orientation (see Section 4.2.1 for details), and femur geometry is identified by the Sheffield cohort control subject index p . Thus, a constant $k_p^{\alpha,\beta}$ is associated with each combination of orientation and geometry. It is computed by executing the pipeline in Section 4.2.2 to predict bone strength for a specific virtual patient $S_{vp}^{\alpha,\beta}$ with a target aBMD a_{vp} and then using Equation 4.10.

$$k_p^{\alpha,\beta} = \frac{S_{vp}^{\alpha,\beta} - S_p^{\alpha,\beta}}{a_{vp} - a_p} \quad (\text{Equation 4.10})$$

Note that the physical patient's aBMD a_p and orientation-specific bone strength $S_p^{\alpha,\beta}$ were already known from the pipeline detailed in Section 4.2.1. With $k_p^{\alpha,\beta}$ known, $S_{vp}^{\alpha,\beta}$ for any arbitrary virtual subject is known without needing any further FE analysis. When computing $k_p^{\alpha,\beta}$ using Equation 4.10, a_{vp} is set to either $0.55 \text{ g}\cdot\text{cm}^{-2}$ or $0.87 \text{ g}\cdot\text{cm}^{-2}$, whichever is farther from a_p . These values correspond to Z-score of -1 in the 75–79 age-group and Z-score of $+1$ in the 55–59 age-group respectively, given the mean and standard deviations of these age-groups as reported in the OPUS study. It is expected that large differences in aBMD will lead to a difference in bone strength that is much larger than deviations from linearity in Equation 4.10, and thereby to a more reliable estimate of $k_p^{\alpha,\beta}$.

The procedure described above is used when the homogeneous algorithm is applied to modify the elemental vBMD distribution and obtain $S_{vp}^{\alpha,\beta}$. When applying the density-specific algorithm, a slight modification is made. For each femur geometry both $0.55 \text{ g}\cdot\text{cm}^{-2}$ and $0.87 \text{ g}\cdot\text{cm}^{-2}$ values are considered as a_{vp} , and bone strength is determined for these virtual patients. The rate of change of bone strength with respect to the change of aBMD ($k_p^{\prime\alpha,\beta}$) is redefined as given by Equation 4.11.

$$k_p^{\prime\alpha,\beta} = \frac{S_{55}^{\alpha,\beta} - S_{87}^{\alpha,\beta}}{0.55 - 0.87} \quad (\text{Equation 4.11})$$

4.3 Results

The process of extracting the vBMD (ρ_{QCT}) and elastic modulus values from the .db files of physical patients is verified by plotting these against one another (Figure 4.7) which showed an excellent fit with Equation 4.4. The minimum ElastMod predicted based on the Equation 4.4 equals to 333.7 MPa. This happens when vBMD is set to zero. Hence, material IDs with ElastMod lower than 316 MPa ($=333.7*95\%$) are excluded from the following error quantification. This excludes about 0.36% of all material IDs (40185) (see inset of Figure 4.7). For the remaining material IDs, the r.m.s. difference between ElastMod predicted using Equation 4.4 and that extracted from .db files of all patients is found to be 5.31%.

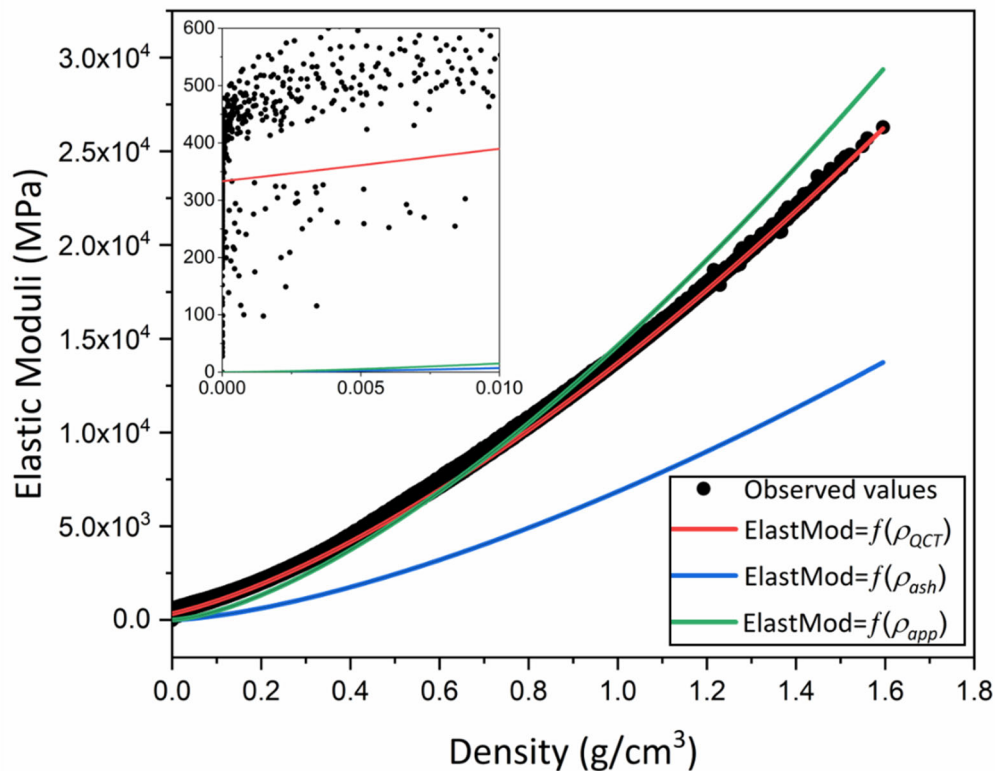


Figure 4.7 Fit of red curve given by Equation 4.4 to elastic modulus and density (ρ_{QCT}) data of all defined materials of physical patients as exported from .db files. Blue and green curves corresponding to Equation 4.3 are shown for reference.

All finite-element models were solved with ANSYS Mechanical APDL 20.2 (Ansys Inc, PA, USA) running on a high-performance computing cluster machines at the University of Sheffield (ShARC). The average running time for one loading direction for MPC 15 mins.

4.3.1 The rate of bone strength changing with respect to aBMD

By homogenous algorithm (k)

The rate of change of bone strength with respect to aBMD (k) – as computed from homogeneous algorithm Equation 4.10 – has a median value of $\tilde{k} = 4612 \text{ N}/(\text{g}\cdot\text{cm}^{-2})$ over all geometries and all orientations; median values of $(\tilde{k})_p$ ranging from 3450 to 5958 $\text{N}/(\text{g}\cdot\text{cm}^{-2})$ across all geometries; and median values of $(\tilde{k})_{\alpha,\beta}$ ranging from 2666 to 5804 $\text{N}/(\text{g}\cdot\text{cm}^{-2})$ across all orientations. This reveals a slightly stronger sensitivity to impact orientation than to bone geometry.

By density-specific algorithm (k')

The rate of change of bone strength with respect to aBMD (k') – as computed from density-specific algorithm Equation 4.11 – has a median value of $\tilde{k}' = 1008 \text{ N}/(\text{g}\cdot\text{cm}^{-2})$ over all geometries and all orientations; median values of $(\tilde{k}')_p$ ranging from 767 to 1439 $\text{N}/(\text{g}\cdot\text{cm}^{-2})$ across all geometries; and median values of $(\tilde{k}')_{\alpha,\beta}$ ranging from 592.6 to 1534 $\text{N}/(\text{g}\cdot\text{cm}^{-2})$ across all orientations. The slightly stronger sensitivity to impact orientation than to bone geometry is consistent with that found for case of the homogeneous algorithm. However, the absolute values of the rates of change in bone strength with respect to aBMD are smaller by nearly a factor of 5 compared to those obtained from the homogeneous algorithm.

By linear regression (k'')

Linear regressions are performed to predict orientation-specific physical patient femur strength $S_p^{\alpha,\beta}$ from physical patient aBMD a_p . The slopes of the regression, denoted by $k''_{\alpha,\beta}$, provide alternative estimates of the rate of change of bone strength with respect to the change of aBMD for each orientation. These are found to vary from 1786 to 6008 $\text{N}/(\text{g}\cdot\text{cm}^{-2})$ with a median value of 3153 $\text{N}/(\text{g}\cdot\text{cm}^{-2})$ across all orientations. Interestingly, the median value of $k''_{\alpha,\beta}$ for 15° Anterior orientation (*i.e.* 15° internal rotation of the hip) is 4861 (95%

confidence intervals: 3184-6538) $N/(g \cdot cm^{-2})$, which compares with 7826 $N/(g \cdot cm^{-2})$ found by Rezaei et al [223] by testing 100 cadaver femurs experimentally. The strong dependence of linear regression slopes on impact orientation is underscored, in line with that for homogeneous and density-specific algorithms. However, the r.m.s. value taken over all orientations of the r.m.s. errors of regression relations are found to be 22.5%.

4.3.2 Linearity assumption testing

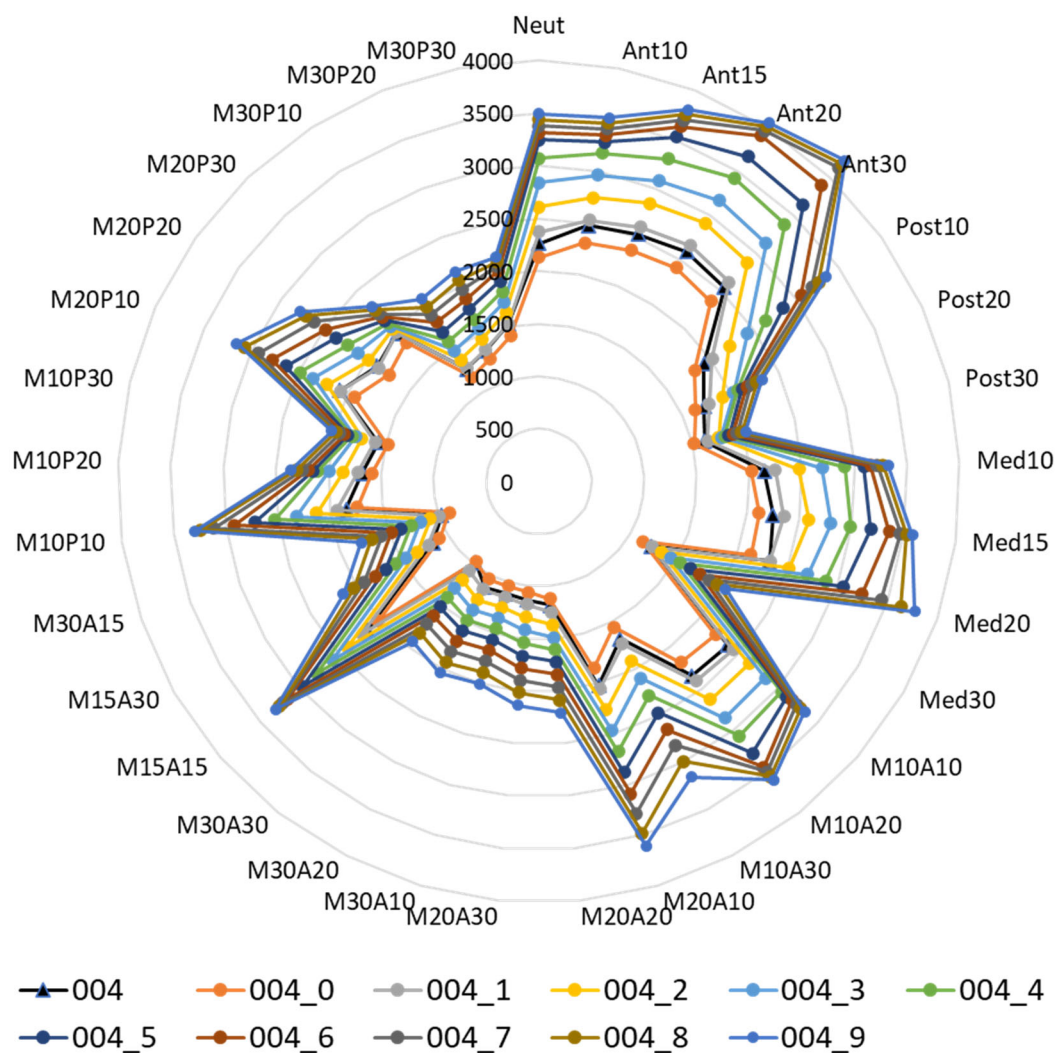


Figure 4.8 Bone strength variation of Patient004 and corresponding virtual patients with multiple loading orientations. Black triangles denote bone strength of Patient004 without any modification. Various coloured circles denote bone strength of virtual patients based on Patient004. The critical fall orientations are insensitive to the variation of aBMD.

The linearity assumption underlying Equation 4.10 is tested as follows. For ten randomly selected physical patients, eleven virtual patients are generated based on density-specific algorithm and covering the full aBMD range (0.36–0.96 g·cm⁻²) in Sheffield cohort and separated by equal aBMD increments (0.06 g·cm⁻²).

The results show that for fixed impact orientation and bone geometry, bone strength is entirely explained by a linear relation with aBMD ($R^2=0.99$). Interestingly, the minimum strength orientations for all virtual patients are found to be identical to the physical patient these are generated from (Figure 4.8). This implies that the minimum strength orientation is a much stronger function of bone geometry than the spatial distribution of vBMD.

4.3.3 Estimation of MinPatS for 5-year age-specific groups

The estimated MinPatS for the mean aBMD in each age-group is shown in Table 4.2. The estimation process is as follows. For the homogeneous algorithm, 49 virtual patients were generated, each possessing aBMD identical to the mean value in that age-group (Table 4.2, column 2), but generated starting from the 49 control subject vBMD distributions. For each of the 49 virtual patients thus generated, the bone strength for all 33 orientations was computed. The minimum pathological strength was obtained for each virtual patient, and the average and standard deviation of the minimum pathological strength is noted in Table 4.2, column 3.

Similar procedures but applying density-specific algorithm and the regression relationship instead of the homogeneous algorithm, gives the values reported in the Table 4.2, columns 4 and 5 respectively.

Table 4.2 The mean and the range (in parentheses) of MinPatS projected by aBMD-S factor (k) for each 5-year age-specific group. Mean aBMD (standard deviation) for each age group was obtained from Sheffield centre within the OPUS study[186]. Note that MinPatS for different geometries may be obtained with different orientations.

Age-group (years)	Mean aBMD ($a, \text{g}\cdot\text{cm}^{-2}$)	Mean MinPatS predicted by homogeneous algorithm ($\langle \min S^{\alpha,\beta} \rangle_p, N$)	Mean MinPatS predicted by density-specific algorithm ($\langle \min S^{\alpha,\beta} \rangle_p, N$)	Mean MinPatS predicted by a, S linear regression ($\langle \min S^{\alpha,\beta} \rangle_p, N$)
55–59	0.769 (0.100)	2924 (1462-4149)	1886 (1194-2940)	3016 (1507-2959)
60–64	0.772 (0.099)	2993 (1469-4160)	1888 (1196-2944)	3026 (1512-2965)
65–69	0.712 (0.118)	2741 (1319-3939)	1846 (1174-2869)	2825 (1397-2847)
70–74	0.688 (0.110)	2663 (1259-3851)	1830 (1165-2839)	2744 (1322-2780)
75–79	0.656 (0.105)	2560 (1179-3733)	1808 (1153-2798)	2636 (1223-2736)

In most/all age-groups it was found that the predicted minimum pathological strength at the mean aBMD was statistically significantly smaller when using the density-specific algorithm compared to using the homogeneous algorithm, while no statistically significant difference was found between homogeneous algorithm and the linear regression estimates ($p=0.071$).

4.4 Discussion and conclusions

In this study, a pipeline of utilizing bone loss algorithms to enrich physical cohort (the Sheffield

cohort) was used to explore the sensitivity of QCT-SSFE predicted bone strength to FN-aBMD.

4.4.1 The rate of change of bone strength with respect to aBMD

Three rates of change of bone strength with respect to aBMD were computed by homogeneous algorithm, density-specific algorithm, and linear regression. Figure 4.9 shows that the rates obtained by homogeneous algorithm overlap with those obtained by regression slope at any orientation. The median value $(\tilde{k})_{\alpha,\beta}$ is larger than $k''_{\alpha,\beta}$ in all but two orientations; at these orientations the differences between the slopes are close to zero. In contrast, the median rates of loss of bone strength predicted by density-specific algorithm $(\tilde{k}')_{\alpha,\beta}$ are much lower in magnitude.

These observations can be explained as follows.

Each slope $k_p^{\alpha,\beta}$, estimated by the homogeneous algorithm, accounts for the influence of subject-specific bone geometry and vBMD spatial distribution on rate of loss of bone strength. However, when considering the median value, these subject-specific effects are lost. Therefore, the magnitude of the median slope is likely to be governed only by the homogeneous rate of change of vBMD with change of aBMD (m'). As noted in Chapter 3, the uniform rate m' is heavily influenced by low-density regions which occupy a large fraction of the bone volume (~85%). Yet, in the homogeneous algorithm, this rate is applied to high-density regions, and this potentially leads to large changes in bone strength, thereby leading to slope magnitudes that are significantly larger than those in the density-specific algorithm.

On the other hand, the regression relation slopes are obtained by considering bone strength in subjects with different geometries and vBMD spatial distributions. Hence, it is likely that these differences between the subjects, in addition to differences in aBMD among them, lead the regression slope magnitudes to be larger than the median slopes from the density-specific algorithm $(\tilde{k}')_{\alpha,\beta}$. However, the close match of regression slope magnitudes and the median slopes from the homogeneous algorithm $(\tilde{k})_{\alpha,\beta}$ must be regarded as fortuitous.

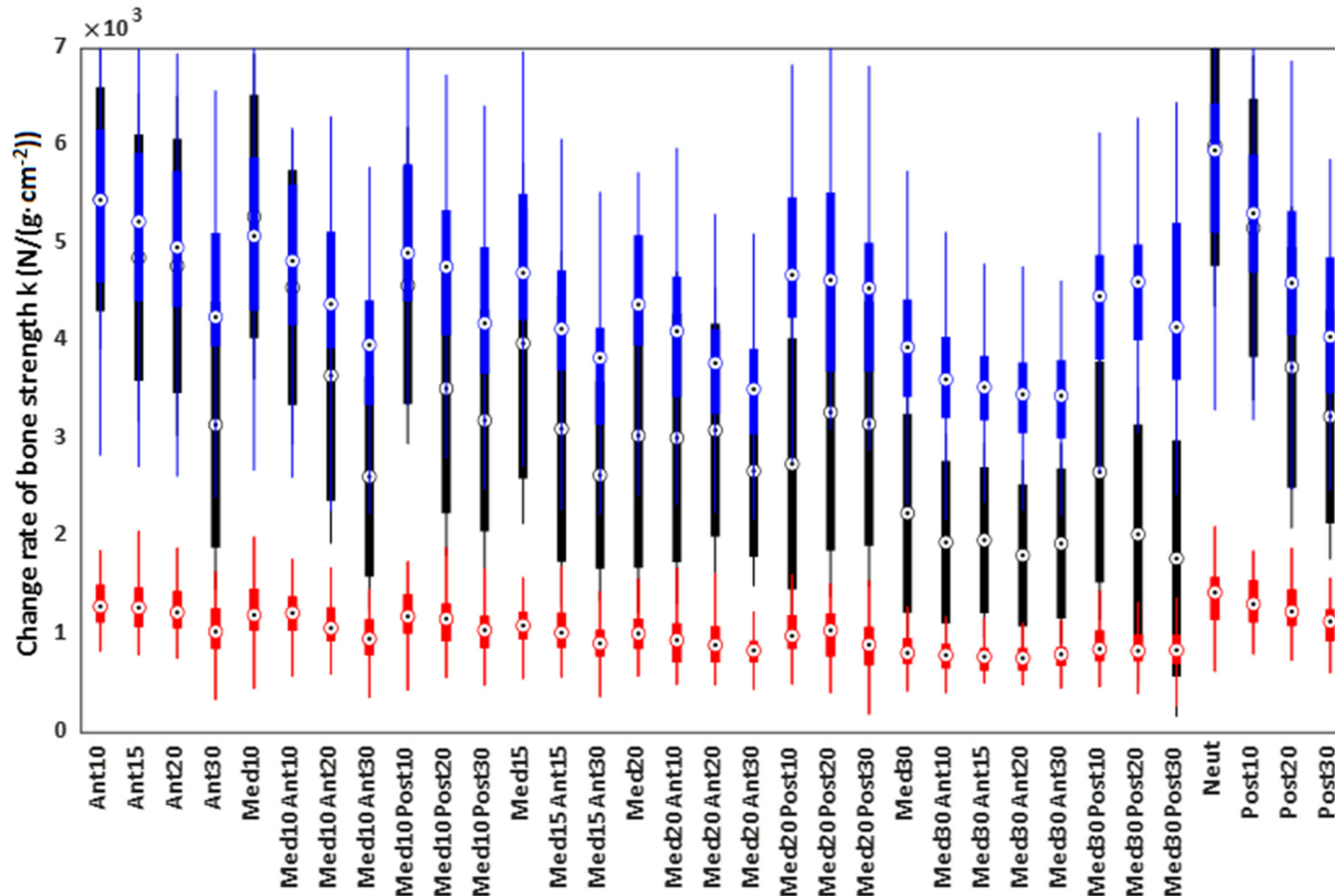


Figure 4.9 Loss rate of bone strength with respect to the loss of aBMD $k^{\alpha,\beta}$ N/(g·cm⁻²). Red, blue, and black box plots are based respectively on density-specific algorithm, homogeneous algorithm and aBMD-strength linear regression derived results. Note that the black bars and whiskers denote the uncertainty in the regression (95% CI) and are not prediction errors, as is the case for the red and blue bars and whiskers.

4.4.2 Estimation of MinPatS for 5-year age-specific groups

The distribution of MinPatS for 5-year age-specific groups were estimated by assigning the mean aBMDs of corresponding groups obtained from Sheffield centre in the OPUS study to our Sheffield cohort.

The results showed that as age increases from 55 to 80, MinPatS first slightly increases and then continuously declines. The trend is consistent with that reported in literature. Keaveny et al assessed femoral strength of an age-stratified cohort (20-97 years) of Caucasian women and found that strength significant drops since 45 years old [224]. Specifically, MinPatS reported by Keaveny et al were estimated around 3850 N, 3321 N and 2807N for women aged between 50-59, 60-69, and 70-79 years old respectively. Femoral strength of each group was largely higher than the MinPatS estimated by Sheffield cohort. Such differences may be attributed to notably higher FN-aBMD found in Keaveny's study, that the mean FN-aBMD of women at 80 years old was reported to be larger than $0.824 \text{ g}\cdot\text{cm}^{-2}$, while the FN-aBMD for our youngest group was $0.769 \text{ g}\cdot\text{cm}^{-2}$. In terms of the relationship of aBMD and MinPatS, FN-aBMD of 80-90 age group in Keaveny's study was reported to be around $0.714 \text{ g}\cdot\text{cm}^{-2}$ and MinPatS was found to be 2172N, which is similar to 65-69 age group in our study.

Speaking of three methods for assigning properties to the femur, in general, it is more recommended to use the density-specific algorithm. Chapter 3 has reported that the prediction error of the change of vBMD estimated by density-specific algorithm was largely smaller than homogenous algorithm. Also, it has been shown that MinPatS estimated by homogenous algorithm has no significant difference from that by linear regression.

However, in the absence of a true validation, it is uncertain whether the true loss of bone strength is better predicted by the density-specific or homogeneous algorithm. It should also be noted that both algorithms are intended to be applied by targeting a specific change in aBMD, following which a prediction of change in vBMD is made. In developing the two algorithms, no effort was made to verify that the changes in vBMD lead to the change in aBMD as imposed. This was due to the lack of longitudinal aBMD image data. However, it might be possible to perform such verification by using tools that have been recently developed and validated to obtain virtual DXA images from CT data (also called CTXA) [72]. The modified

vBMD information can potentially be used to generate virtual CT images, and from there virtual DXA images to obtain the modified aBMD. It might be also possible to combine such analysis into the optimisation pipeline as a constraint on the algorithm parameter values.

4.4.3 Pipeline of generating virtual population with varied aBMD

The pipeline presented in this chapter leverages the same advantage of discretisation independence as possessed by the bone loss algorithms introduced in the last chapter. It was shown in Chapter 3 how virtual patients with specified aBMD distributions can be generated from any new CT dataset (taken from a finite number of physical patients). Specifically, it was highlighted that the finite-element meshes created from these CT images do not need to be deformed to any specific template mesh (as needed in an SSM or SAM based approach [225]). A related advantage is that aBMD distributions are widely characterised in observational studies, which are readily used as input in the present pipeline to generate virtual subjects. In contrast, when generating virtual cohorts in an SAM-based approach, the target distributions need to be specified in terms of scores of eigenmodes. These scores do not bear any simple relation with aBMD and are not known in populations typically needing to be analysed. These advantages directly accrue to the analysis of femur strength distributions in virtual cohort when the pipeline presented in this chapter is used.

In the present study, bone geometry was held fixed to the 49 control subjects of the Sheffield cohort. SSM studies conducted on the Sheffield cohort have shown that only 10 modes are sufficient to describe 95% of the variability in the whole cohort [225]. This assures that considering 49 subjects is adequate to capture the range, if not the distribution, of variation of bone geometries in any cohort of British elderly women.

A recent multiscale model showed its ability in predicting absolute risk of current hip fracture (ARF0) with good accuracy (77.6% specificity and 81.6% sensitivity) [5]. In that study ARF0 was defined as the probability of sustaining a hip fracture in a unit person-year. The ARF0 model accounted for patient-specific determinants including fall dynamics, force-transfer upon impact and femur strength. Fall dynamics and force-transfer upon impact are estimated by separate models. Distributions of inputs to these two models (such as body height and mass) are easily obtained from epidemiological data. Yet, the distribution of inputs to the femur

strength model (CT images) was not feasible due to reasons already mentioned in the last chapter. With the CT-SSFE based pipeline presented here, it should be possible now to obtain not only femur strength distributions in virtual cohorts, but also ARF0 distributions in the same.

Separately, it can be conceived to apply the pipeline above to a specific subject repeatedly, and thus predict femur strength every year over a period of, say, 10 years. If data or models to simulate the change of fall dynamics and force-transfer upon impact are also available, then one can also apply the ARF0 model repeatedly to predict absolute hip fracture over the 10-year period. This opens the way to predict the 10-year absolute risk of hip fracture (ARF10) which is a clinically relevant quantity. Finally, applying ARF10 to virtual cohorts then allows to analyse ARF10 distributions in the same. This is essentially the untreated disease model for postmenopausal osteoporotic hip fractures envisaged in Chapter 2.

Prediction of ARF10 distributions leads to the possibility of validating the modelling pipeline. This can be done for example by comparing ARF10 distributions predicted in virtual cohorts (representing different age-groups) against epidemiologically known trends in hip fracture incidence rates. Some research groups have made advancements in this direction, although using measures of relative risk [181], which is different from absolute fracture risk determined by ARF0. Validation of ARF10 predictions will form the basis for using *in silico* trials in determining the efficacy of individual or combined interventions to reduce hip fracture risk with greater statistical confidence.

5. Sensitivity of femur strength to variation in femur length

This thesis is motivated to generate and use virtual cohorts to enrich physical cohorts in the study of osteoporosis and its interventions. Although bone strength has been widely reported to be affected by BMD distribution and bone geometry (*i.e.*, size and shape) in the literature, the independent effects of these two aspects have been investigated to a limited extent. In Chapter 4, the sensitivity of QCT-SSFE predicted bone strength to aBMD, while the bone geometry remain unchanged, has been investigated. In this chapter, the influence of femur size (which is changed proportion to femur length) on femur strength is investigated by a similar modelling procedure: a group of virtual patients is generated with varied femur length and fixed BMD distribution and femur shape.

5.1 Introduction

Bone strength is commonly used as an endpoint in a standard clinical trial of osteoporosis. However, strength cannot be directly measured *in vivo*. One widely accepted approach to estimate the bone strength is using quantitative computed tomography-based subject-specific finite element models (QCT-SSFE). QCT-SSFE shows a good ability in accurately predicting bone strength, as it takes volumetric bone mineral density (vBMD) distribution, proximal femur geometry, and multiple boundary conditions into consideration. However, just as its name suggests, the subject-specific modelling method requires QCT scans of a certain subject as a necessary input. Given the diversity of women femurs in BMD distribution and geometry, the more subjects are included, the more reliable conclusion could be drawn from the trials. However, due to the considerable radiography expenditure and radiation dose, the size of recruited cohort is always limited. Hence, a virtual population possessed with various biomechanical parameters (vBMD distribution and geometry) is much needed to improve statistical significance of such studies.

One of the largest cohorts with femur QCT data in the literature is the Sheffield cohort recruited by Yang et al [203]. Yet, the 100 postmenopausal women recruited in this cohort

could be insufficient to reflect whole variation of entire at-risk British elderly women. This is especially the case if one considers only a part of the recruited cohort, for *e.g.*, limited to specific age, BMI, BMD range.

Past studies have attempted to determine the separate influences on bone strength due to vBMD distribution and bone geometry [226–229]. For example, statistical shape models (SSM), statistical appearance models (SAM) have been developed to capture the variability within a population of femur geometry and vBMD. In a recent study, SSM and SAM analysis of femurs in the Sheffield cohort showed that the first 10 most important SSM eigenmodes (out of a total of 93) were needed to capture 95% of the total variance in geometry of femurs [225]. In contrast, a similar fraction of the total variance in vBMD required over 60 most important SAM eigenmodes [225]. SSM and SAM eigenmodes are then used to generate new virtual femurs, the FE analysis of which then determines the influence of the variables on bone strength [100,230–232]. Although a large number of modes were needed to explain the variability in geometry and vBMD in the Sheffield cohort, only 2 SSM modes were found to influence femur strength [100]. Even if femur geometry is not the most important determinant of femur strength, it is still important to quantify its influence in detail. This is because the degree of influence determines whether to include some extreme femur geometries in highly numerous virtual cohorts in order that a representative femur strength distribution is achieved in the virtual cohort.

Besides SSM based approaches, hip structural analysis (HSA) uses DXA images to characterise femur geometry variation through morphological parameters such as the diameter of femoral head, neck-shaft angle, neck diameter, shaft axis, offset of femoral head centre to shaft axis. The influence of these parameters on bone strength, independently and in combination has also been analysed in detail [233]. It should be noted that in SSM or HSA based studies, the variation of femur geometry is not usually separated into independent variations of size and shape.

Many anthropological studies have observed a correlation between femur length and stature [234–237], suggesting that there is a linear relationship between body height and femur length. Body height is widely used for characterising populations [238]. This motivates the use of body height distribution to define femur length distributions for virtual cohorts generated

to characterise a target population. However, subjects in the literature are relatively young and most of these studies were conducted on cadavers. The state of preservation of cadavers may influence the measurement of body height and femur length differently from living subjects. Moreover, the Sheffield cohort was initially designed to reflect osteopenia population. Subjects in Sheffield cohort may also experience vertebral fractures and develop the characteristic stooped posture. The height value recorded in the Sheffield cohort may not reflect an upright stature as in young subjects. This suggests that the relationship between body height and femur length as given in literature might not be directly applicable to the Sheffield cohort.

One of the objectives of the present chapter is to compare the relationship between body height and femur length in elderly subjects with that found in past studies using younger subjects. If the relationship in Sheffield cohort could be established as those suggested in past studies, then body height distribution would be applied to define the scaling factor. Otherwise, the femur length distribution in the Sheffield cohort would be used directly as the starting point for generating femurs of different lengths in a virtual cohort.

Yet, in attempting to generate virtual cohort by scaling the size of original femur proportional to length, care needs to be taken in determining the scaling range. Hence, an anatomical similarity check needs to be conducted on Sheffield cohort to ensure the safety of the scaling. Therefore, another objective of the present chapter is to explore a suitable approach to scale femur geometry by femur length, while its shape and bone mineral density remain fixed. Once the virtual population is generated, the sensitivity of femur strength to length can be analysed, which is the overall aim of this chapter.

5.2 Methodology

5.2.1 Physical patients (Sheffield cohort)

A retrospective cohort (Sheffield cohort) of 96 British post-menopausal women was available for this study [203] and details of Sheffield cohort have been previously reported in Section 3.2.1. Key information (see Table 5.1) relevant to this study are revisited for convenience.

Table 5.1 Descriptive statistics of Sheffield cohort. The numbers for age and height correspond to the range and mean value (in parentheses).

	All	Fractured	Non-fractured
N	96	47	49
Age (years)	55-91 (75)	55-89 (75)	56-91 (75)
Height (cm)	145-173 (158)	145-173(158)	145-169 (158)

5.2.2 Generation and FE analysis of virtual patients

The physical patient who had shortest femur was selected as research subject. Its corresponding virtual patients were generated by first determining an appropriate coordinate system for scaling, and then by scaling the proximal femur geometry in an isotropic manner along the three directions of this coordinate system. The coordinate system was based on the reference system described in Section 4.2.1.3. The determination of scaling range and specific scaling factor for each virtual patients are introduced in Section 5.2.2.3. Note that the bone mineral density of each finite-element in the scaled proximal femur of the virtual patient was identical to that in the original physical patient. Hence the areal bone-mineral density was assumed to be conserved with respect to scaling. The general procedure of this study is shown in Figure 5.1. The details of finite element analysis of virtual patients are described in the following sections.

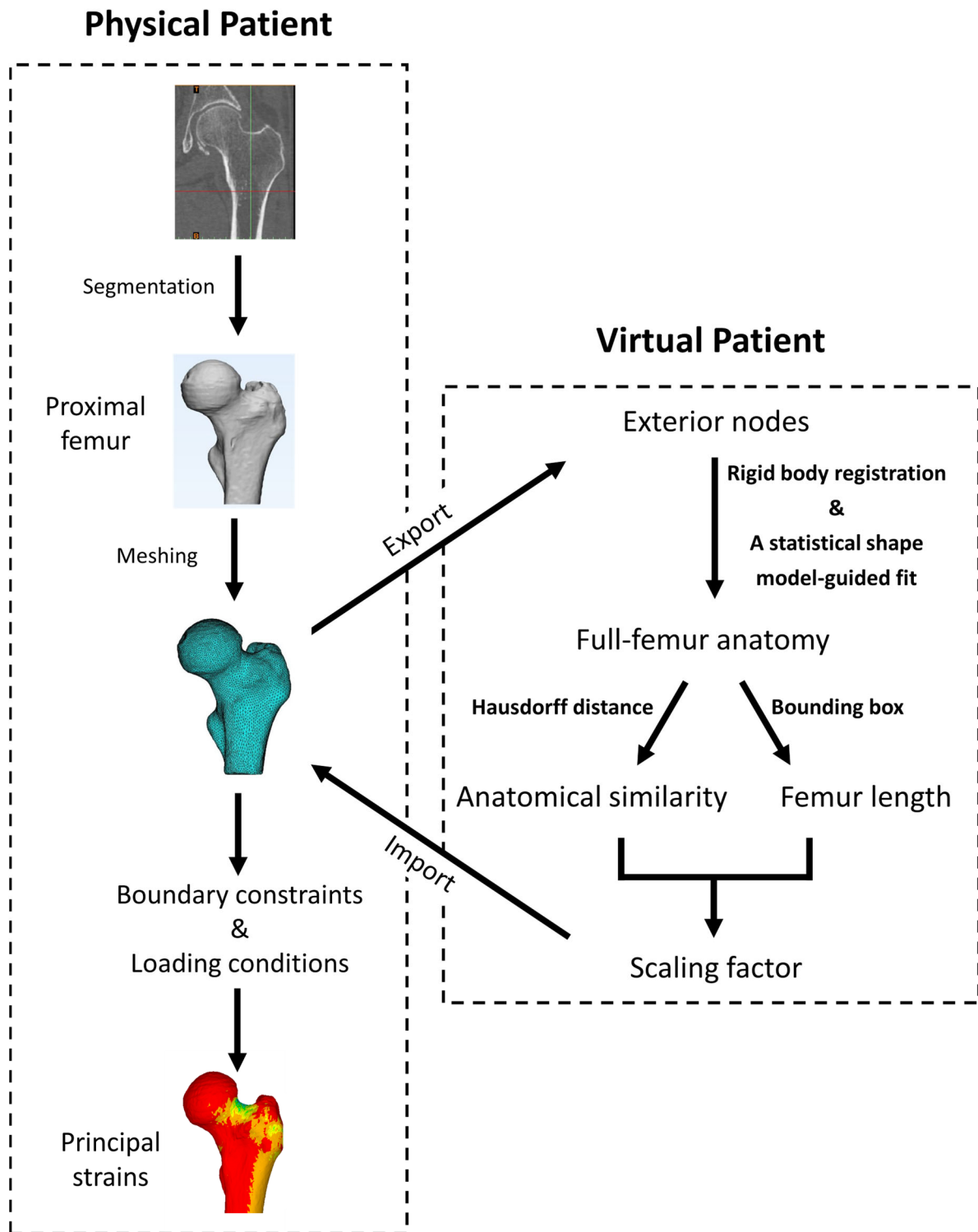


Figure 5.1 Pipeline of conducting QCT-SSFE on physical patients and corresponding virtual patients.

5.2.2.1 Full-femur anatomy estimation

The CT scans of the Sheffield cohort only contain the proximal femur, which start from just above the femoral head and extend to 3.5cm below the lesser trochanter [131]. The proximal femurs in Sheffield cohort were mapped with statistical femoral atlas following a rigid-body registration and a statistical shape model-guided fit by the MAP Client software. The estimation process of full-femur anatomy has been reported in details by Qasim et al [131].

5.2.2.2 Determination of femoral dimensions

Physiological length and perpendicular length are two commonly adopted description in quantifying femur length, which require placing the femur on a measuring board on its anterior surface. The physiological length (see Figure 5.2 (a)) is measured from the most proximal point of femoral head to a line passing through the most distal points of both condyles [235]. The perpendicular length (*i.e.*, maximum length, shown as Figure 5.2 (b)) measured from the most proximal point of the head to the most distal of the medial condyle [235].

Different from cadaver study, the mapped full femur geometries in this study were defined by a triangulation of their exterior surfaces, encoded in stereolithography (STL) files. Limited by the digital form, it is hardly to measure either physiological or perpendicular length of femurs in Sheffield cohort. . As an alternative, a minimum bounding box (MBB) was found for each full femur geometry and its dimensions (length L, width W and depth D) were identified as the dimensions of the bone [239]. The MBB (see Figure 5.2 (b)) is the rectangular parallelepiped with the smallest volume enclosing all points in a certain point set (exterior nodes of femur F) in three dimensions [239].

The routine **MBB function**, implemented in MATLAB (R2017b, the MathWorks Inc., Natick, MA, USA), was used to find the MBB. The routine **MBB function** first determines the convex hull of F and drops all the points in the interior of the convex hull. Then following O'Rourke's approach [240], the angles of each face of the polygonal hull and local coordinates of faces' corner points are calculated to find the first parallel edges on the bounding box. Finally, all possible bounding box combinations are checked to find the one with smallest volume, which is denoted as the MBB.

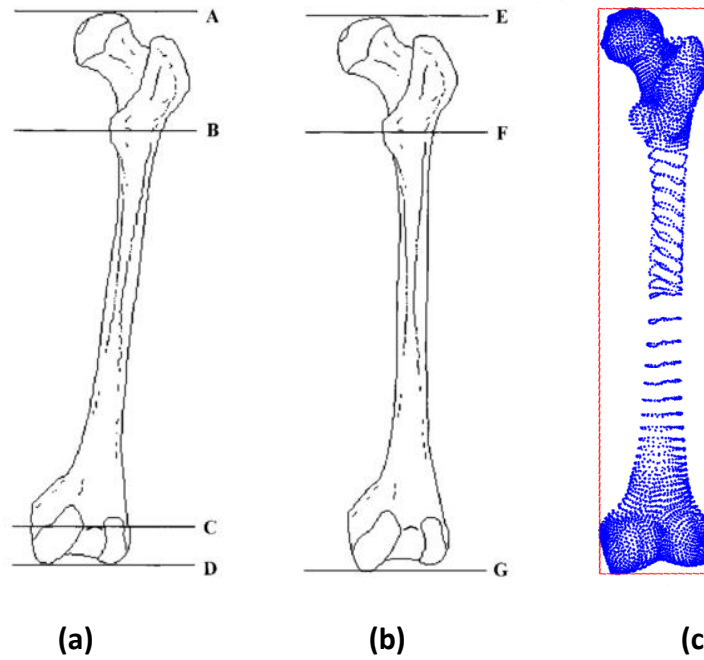


Figure 5.2 Femur dimensions: (a) physiological length A-D, (b) perpendicular length E-G [235] and (c) femur length in Sheffield cohort defined by the length of the minimum bounding box (red box).

5.2.2.3 Anatomy similarity

Femur geometry was not only determined by size, but also by shape. In order to use femur length as the input of virtual population models, similarity check of femur anatomy is important in terms of efficacy and safety of scaling. The similarity of femur anatomies was distinguished by the average Hausdorff distances.

Hausdorff distance is measuring “how far two non-empty subsets of a metric space are from each other” (see Figure 5.3) [241]. The average Hausdorff distance is defined by the average of the distance between a point in a set to the nearest point in the other set, written as:

$$HD_{avg}(X,Y) = \frac{1}{N} \left\{ \sum_{i=1}^N \inf_{y \in Y} d(x_i, y) \right\} \quad (\text{Equation 5.1})$$

Where X, Y denote two non-empty subsets where X contains N points and inf represents the infimum. If average Hausdorff distance between two femurs was smaller than 1mm (roughly one pixel size in the CT image, $0.625 \times 0.74 \times 0.74 \text{mm}^3$), these two femurs were assumed to have similar anatomy.

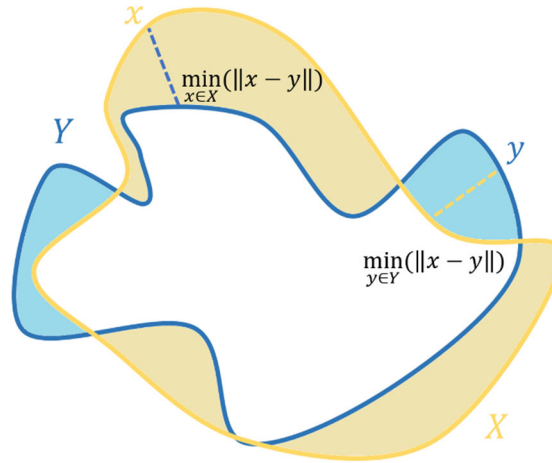


Figure 5.3 Schematic representation of Hausdorff distance, which accounts the mismatches between two datasets (for example X and Y). The average Hausdorff distance from X to Y is defined as the average of shortest distance of each point x on dataset X to dataset Y.

The average Hausdorff distances were calculated using Matlab code [242] in two ways:

- 1) between the two femurs whose lengths were closest in all femurs (*i.e.*, F_n and F_{n+1} , $n \in [1,95]$) (HD_{avg2});
- 2) between any two of normalised femurs. Normalization was conducted by scaling all femurs into the shortest length with fixed aspect ratios and normalised femur denoted as \hat{F} (*i.e.*, \hat{F}_i and \hat{F}_j , $i, j \in [1,96]$) (\hat{HD}_{avg}).

Note: As there existed left and right femurs in 96 cases (59 left femurs and 37 right femurs), to compare their shapes only, all right femurs were converted into symmetric forms.

5.2.2.4 Affine Scaling

Virtual patients were generated by isotropic scaling the proximal femur geometry of physical patients (*i.e.*, FE meshes) based on the mapped femur length. Detailly, virtual patients would have the same mesh distribution as their corresponding physical patient, while the element sizes would be scaled with the same factor in three dimensions. The material properties in each finite-element of the proximal femur were left unchanged.

The patient who had shortest femur was selected as research subject (*i.e.*, the physical patient

F). There was a virtual patient i (F^i , $i \in [0,9]$) among 10 corresponding virtual patients of physical patient F which were generated by scaling femur size based on femur length over the whole spectrum of the Sheffield cohort.

Hence, corresponding 10 virtual patients of the physical patient were derived from:

$$F^i = S^i * F \quad (\text{Equation 5.2})$$

where S^i represents the scaling factor and was calculated as following:

$$S^i = \frac{L_1 + i * \delta L + \alpha}{L_1}, \delta L = \frac{L_{96} - L_1}{10}, \alpha < \delta L, n \in [1,96], i \in [0,9] \quad (\text{Equation 5.3})$$

Here, L denotes the length of femur (*i.e.*, L_1 for length of the shortest femur and L_{96} for length of the longest femur), δL represents the increment of each time. α is a random number and smaller than the increment. Then i would increase from 0 until i equals to 9.

5.2.2.5 QCT-SSFE modelling

Imaging protocol has been previously reported in Section 3.2.1. FE meshes, material properties, the reference system and failure criterion have been reported in Section 4.2.1. Here, only differences were presented below:

Mesh scaling and convergence analysis

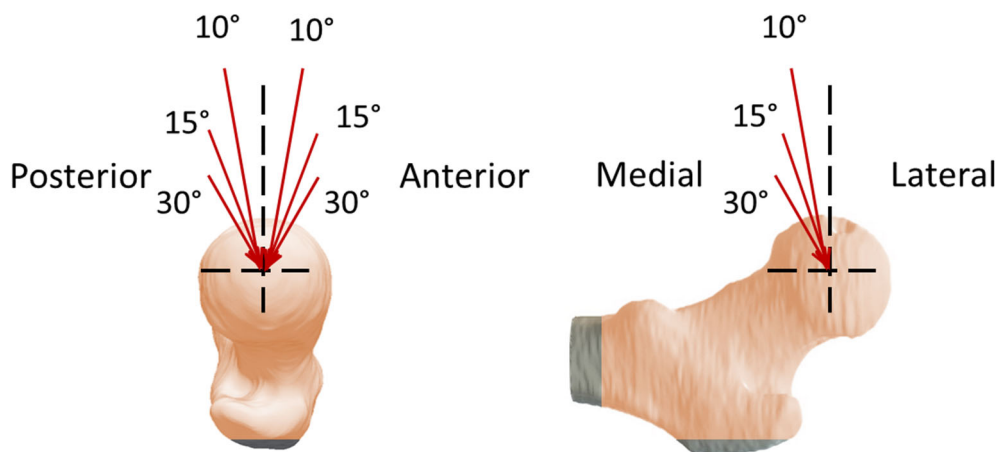
The distribution of meshes for each virtual patients remains the same as the physical patient F, while all nodes are affine scaled by the same scaled factor in three directions (X, Y and Z) in the three anatomical landmarks defined coordinate system using the command /NSCALE.

Considering meshes were not changed for these virtual population and the total volume increased because of scaling, mesh refinement of each model was checked by post-hoc verification of strain field smoothness. The energy error monitored in ANSYS is associated with the discrepancy between the calculated stress field and the globally continuous stress field. As only the displacements are assumed to be continuous at the nodes in each element, the continuity of the stress field, calculated from the displacements, supposed to be achieved,

but generally is not. The strain energy error (SEE) was calculated of whole surface area of the proximal femur excluding the area applying boundary condition. The SEE of all models of virtual population in no cases exceeded 3.3% compared to the original patient within the region of interest. A mesh convergence study was performed on the original patient by Altai et al [141] using four different element sizes at 1.5, 3, 3.5 and 4 mm and the mesh reached convergence at an element size of 3 mm.

Side-fall loading conditions

Fifteen different loading conditions simulating either anterolateral or posterolateral falls were investigated in this study. The force direction varied uniformly from 0° to 30° in the frontal plane and from -30° to +30° in the transverse plane with increment of 15° (Figure 5.4).



Medial	Medial-Anterior	Medial-Posterior
0°Med (Neutral)	0°Med -15°Ant	0°Med -15°Pos
15°Med	0°Med -30°Ant	0°Med -30°Pos
30°Med	15°Med -15°Ant	15°Med -15°Pos
	15°Med -30°Ant	15°Med -30°Pos
	30°Med -15°Ant	30°Med -15°Pos
	30°Med -30°Ant	30°Med -30°Pos

Figure 5.4 Fifteen different loading conditions, with a concentration force applied to the centre of the femoral head, were used to simulate sideways falls. Force directions varied from 0° to +30° on the medial-lateral plane and from -30° to +30° on the anterior-posterior plane. Equal increments of 15° were applied on each plane. Region of interest used in the FE analysis was marked in orange, while regions applied with boundary constrains were removed (20mm from distal end and 6mm from the most lateral point in the greater trochanter). Adapted from [141] with permission.

As the knee would hit the ground first before the hip during the fall, lateral angles were not taken into consideration. A 1 kN concentrated load, representing an arbitrary load following a sensitivity study, was applied to the centre of the femoral head [141].

Boundary constrains

Contact model (see Figure 5.5) proposed by Altai et al was implemented in this study [141]. Compared with MPC model used in Chapter4, contact model has better accuracy in estimating bone strength (MPC: AUROC=0.80 vs contact: AUROC=0.82) [141].

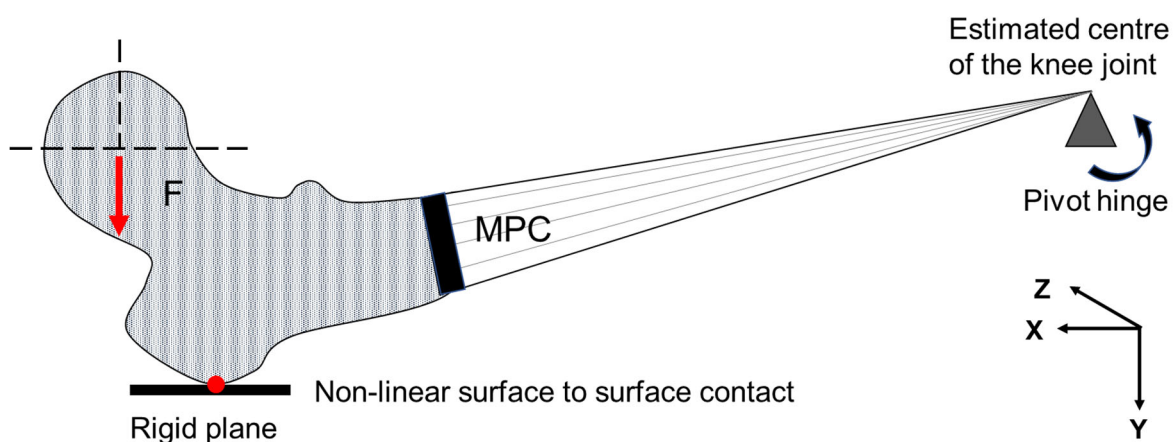


Figure 5.5 Schematic representation of contact model. The node with highest Y value in the greater trochanter region was simulated to have a nonlinear surface-to-surface contact between the greater trochanter and group (represented by a rigid plane). MPC elements were applied to link nodes located at the distal end to the pilot node which denoted the estimated centre of the knee joint. Adapted from [141] with permission.

At the distal end of the femur, a pilot node with 6 DOFs (translation and rotation in X, Y, and Z directions) was created by multi-point constraints (MPC) method at an estimated location of knee joint centre for each patient. The pilot node was free to rotate around the axis transverse to the applied load (x axis), while all other DOFs were constrained.

A contact interaction was defined between the greater trochanter surface and a virtual fall impact surface. The fall impact surface, fixed in space, was modelled as an infinitely rigid plane, tangential to surface of the greater trochanter at its farthest point along the loading direction. A hard-frictionless contact behaviour was applied, and a surface-to-surface contact

discretization was used with the augmented Lagrange enforcement method.

5.3 Results

5.3.1 Correlation between body height and femur length

Body heights of all patients in Sheffield cohort vary from 145 cm to 173 cm, the mean height being 158 cm. The range of femur lengths is from 350 mm to 493 mm with mean length of 421 mm (Table 5.2). The patient who has the shortest femur was found to be Patient085.

Table 5.2 General statistical analysis (femur length and body height) of Sheffield cohort.

	Femur length (mm)	Body height (cm)
MAX	493	173
MIN	350	145
MEAN	421	158
SD	37.4	6.24

Figure 5.6 shows that the distribution of body height follows normal distribution ($A_2=0.53$ for Anderson Darling test) and the distribution of femoral length is more likely to be negative skewed.

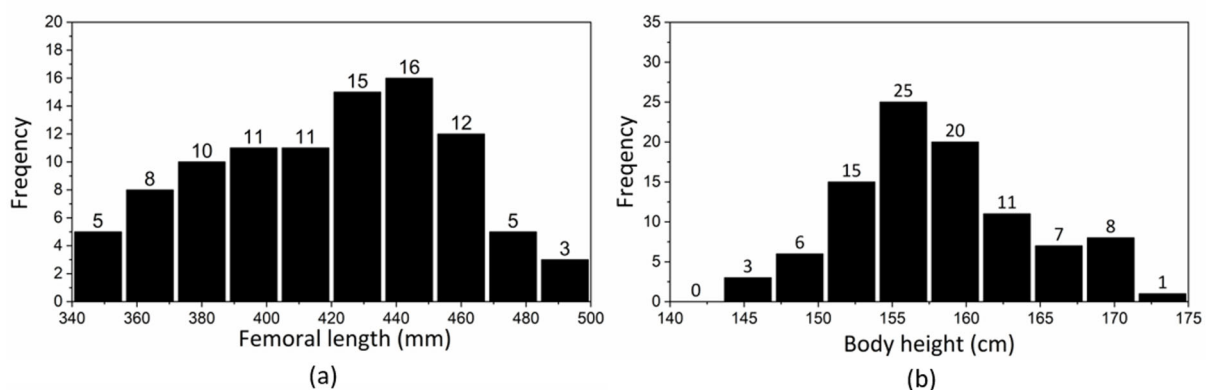


Figure 5.6 The distribution of body height and femur length for 96 patients. The distribution of body height (a) seems to obey the normal distribution, while the distribution of femora length (b) is more likely to be negative skewed.

A linear regression was conducted between body height and femur length of 96 patients in Sheffield cohort. The result showed that the correlation is fairly weak ($r^2=0.01$). Linear regressions were also conducted between sub-groups of Sheffield cohort. Sub-groups were generated by 4 criterions, *i.e.*, age, fracture status, T-score and BMI. The results are presented in Table 5.3.

Table 5.3 Linear regression results between femur length and body height of all subjects in Sheffield cohort and sub-groups (age, fracture status, T-score and BMI).

	Group	R ²	Adjusted R ²	Standard error	Sample number
Age	age ≤ 75	0.07	0.05	34.5	46
	age > 75	0.00	-0.02	39.2	50
Fracture status	Non-fractured	0.02	0.00	38.8	49
	Fractured	0.01	-0.01	36.6	47
T-Score	Osteoporosis T-score ≤ -2.5	0.01	-0.03	40.4	27
	Osteopenia -2.5 < T-score < 1.0	0.00	-0.03	38.4	31
	Normal T-score ≥ -1.0	0.07	0.05	35.5	38
BMI	Underweight BMI < 18.5	0.03	-0.21	37.9	5
	Healthy 18.5 ≤ BMI < 25	0.00	-0.03	34.9	32
	Overweight 25 ≤ BMI < 30	0.00	-0.03	39.6	39
	Obese BMI ≥ 30	0.20	0.14	32.9	20

5.3.2 Anatomical similarity check

Femur anatomy similarity is affected by its size (*i.e.*, length, width, and depth). Figure 5.7 shows that the width has nearly no linear relationship with length, while depth has stronger correlation. However, the width and depth calculated by MBB are influenced by neck-shaft angle and the femoral stem tilt angle. Hence, the anatomical similarity of Sheffield cohort cannot be simply quantified by MBB measured three dimensions.

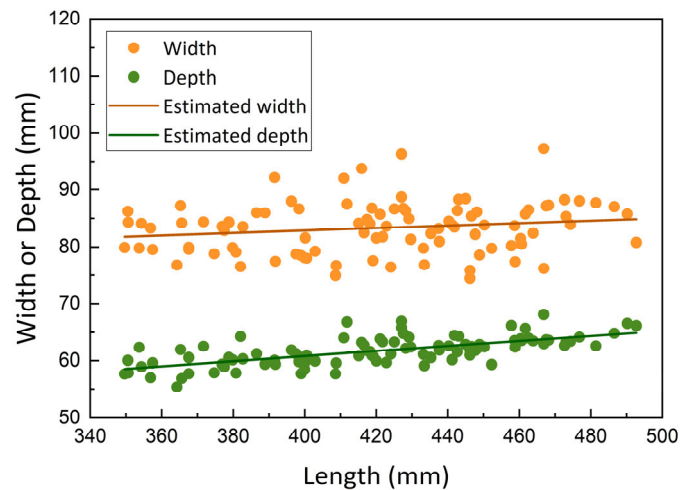


Figure 5.7 Linear regression of width and depth plotted with femur length ($R^2=0.03$ for width and $R^2=0.44$ for depth).

The range of average Hausdorff distance between two femurs having closest length (HD_{avg2}) was between 0.88 mm to 6.77 mm (mean: 2.98 mm), while the average Hausdorff distance between normalised femurs (\hat{HD}_{avg}) varied from 1.50 mm to 7.17 mm (mean: 4.28 mm).

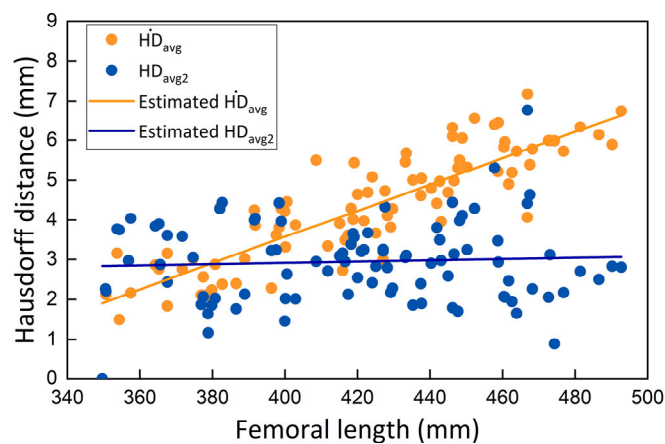


Figure 5.8 Average Hausdorff distances between two closest-length femurs HD_{avg2} (blue) and normalized femurs \hat{HD}_{avg} (orange).

Figure 5.8 shows that the HD_{avg2} has no correlation with L over the whole spectrum, while HD_{avg} shows a strong dependence on L. This suggests that the difference in femur anatomy is mainly caused by L. As a result, it would be safer if virtual patients are scaled only by length as near as physical patients. Additionally, the maximum HD_{avg} is just slightly bigger than 7 mm, comparing to the average length of femur is only 1.66%. So, even scaling over the whole spectrum it will still be safe from anatomical point view.

5.3.3 Scaling factors

The femur length determined by bounding box of Patient085 (the one with shortest femur length) was found to be 349.6cm and the scaled factors for each virtual patients were obtained (see Table 5.4).

Table 5.4 Dimensions and scaling factors of 10 virtual patients of Patient085.

Patient ID	Length (mm)	Scaling factor	Patient ID	Length (mm)	Scaling factor
F_{085}^0	362.6	1.037	F_{085}^5	425.2	1.216
F_{085}^1	365.8	1.046	F_{085}^6	443.3	1.268
F_{085}^2	391.3	1.119	F_{085}^7	463.5	1.326
F_{085}^3	401.6	1.149	F_{085}^8	477.9	1.367
F_{085}^4	408.3	1.168	F_{085}^9	480.7	1.375

5.3.4 FE analysis results

Failure type (compressive failure), location (femoral neck fracture) and the worst loading scenario (Med30Ant15) of all virtual patients were exactly same with them of the physical patient (details are presented in Table 5.5). The minimum loads to induce failure for virtual patients in the neck area (1706 N to 1791 N with the average value of 1754 N) were slightly smaller than the one for physical patient (1797 N). All virtual patients were estimated as non-fractured, according to the maximum principal strain failure criteria [143].

Table 5.5 Maximum absolute 1st and 3rd principal strain ($\max|e_1|$ and $\max|e_3|$) and minimum pathological strength (MinPatS) for Patient085 and its corresponding virtual patients. The failure type of all patients is compressive failure (C) and the failure location is in the femoral neck region. The limit tensile strain and compressive strain are 0.73% and 1.04% respectively [143].

Patient ID	MinPatS (N)	$\max e_1 $ ($\cdot 10^6$)	$\max e_3 $ ($\cdot 10^6$)	Failure type	Failure orientation	Failure node
F_{085}	1797	2488	7555	C	Med30Ant15	8659
F_{085}^0	1779	2485	7548	C	Med30Ant15	8659
F_{085}^1	1775	2484	7546	C	Med30Ant15	8659
F_{085}^2	1741	2530	7528	C	Med30Ant15	8659
F_{085}^3	1730	2625	7515	C	Med30Ant15	8659
F_{085}^4	1724	2684	7503	C	Med30Ant15	8659
F_{085}^5	1712	2808	7516	C	Med30Ant15	8659
F_{085}^6	1708	2851	7575	C	Med30Ant15	8659
F_{085}^7	1707	2863	7617	C	Med30Ant15	8659
F_{085}^8	1706	2882	7656	C	Med30Ant15	8659
F_{085}^9	1706	2882	7656	C	Med30Ant15	8659

Figure 5.9 and Figure 5.10 show the distribution of the first and third principal strain of F_{085} and F_{085}^3 (the one has the MinPatS closest to the mean MinPatS among 10 virtual patients) under the worst loading scenario (Med30Ant15), respectively. In general, the strain distributions of F_{085} and F_{085}^3 are similar that high tensile and compressive strains were produced on the superior surface of the femoral neck. The maximum first principal strains of F_{085} and F_{085}^3 were found at two different nodes (12792 and 8659, respectively) but they were attributed to the same element, while the minimum third principal strain located at the same node (8659).

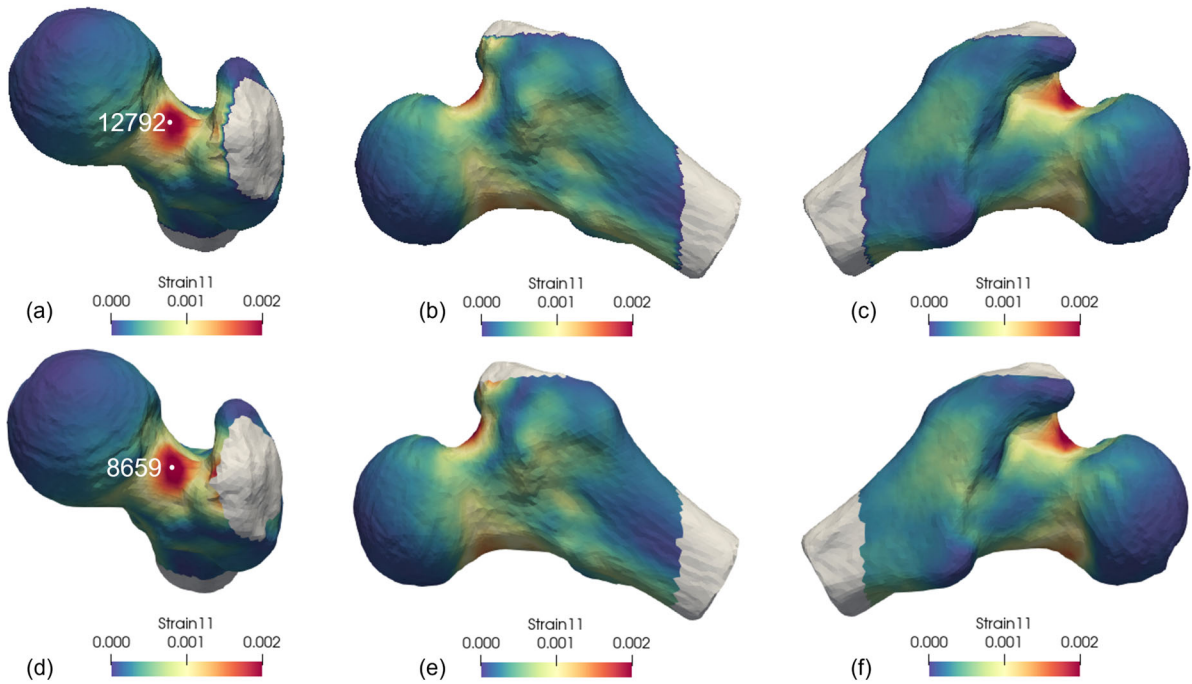


Figure 5.9 The distribution of the 1st principal strain of F_{085} (a-c) and F_{085}^3 (d-f) under the worst loading scenario (Med30Ant15). Node with maximum value is marked in white.

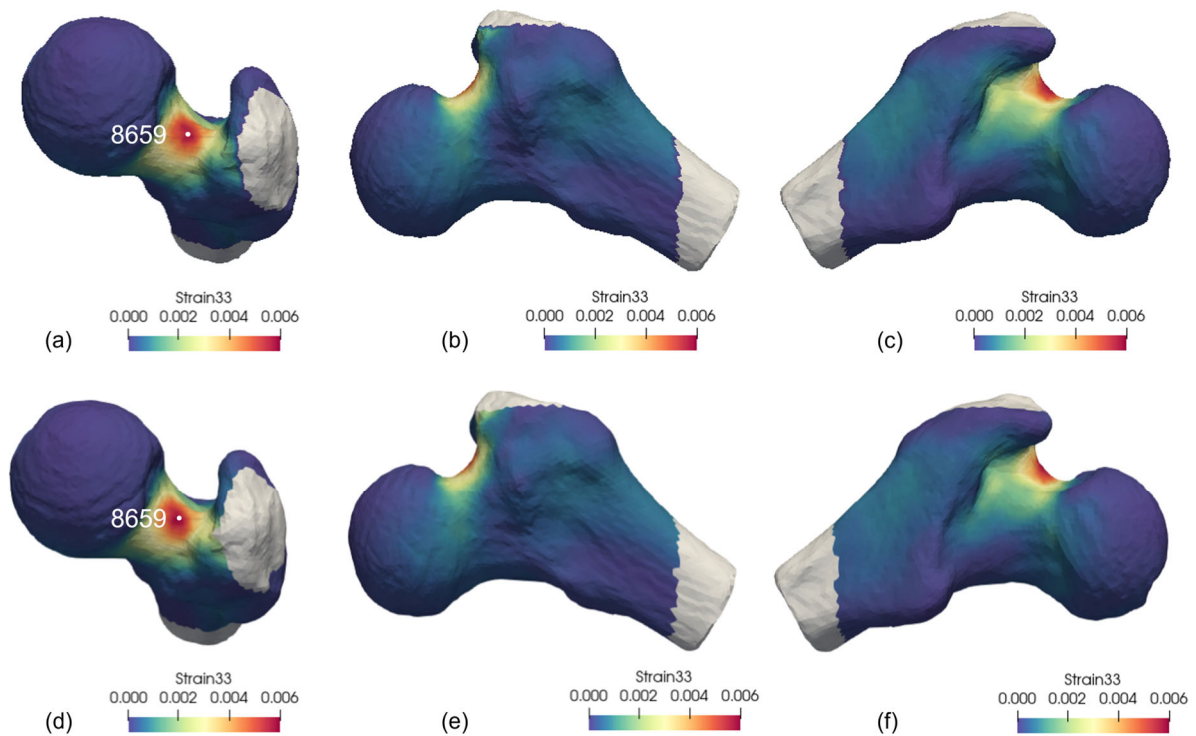
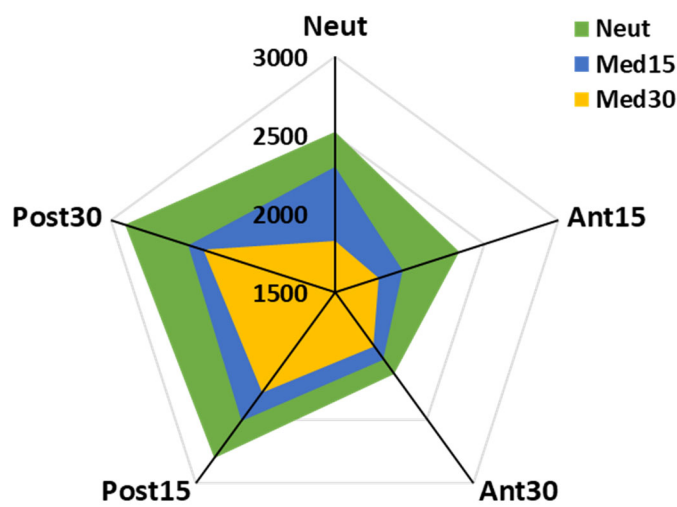
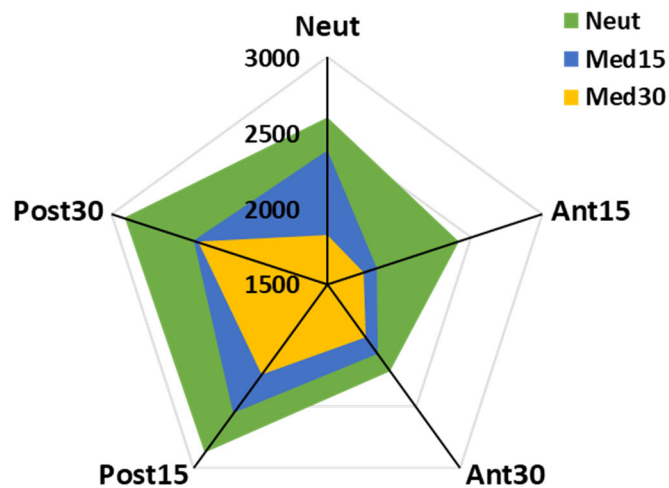


Figure 5.10 The distribution of absolute 3rd principal strain of F_{085} (a-c) and F_{085}^3 (d-f) under the worst loading scenario (Med30Ant15). Node with maximum value is marked in white.

The distribution of bone strength of Patient085 and mean strength of its corresponding ten virtual patients shown in Figure 5.11 (a) and (b), respectively. Bone strength in both Patient 085 and mean bone strength in the ten virtual patients decreased as the angle increased in frontal plane (medial-lateral plane) and in transverse plane (anterior-posterior plane). Anterior loading angles were more critical than posterior angles, while the extreme value of bone strength in both directions was derived at 15°. Overall, bone strength of Patient085 and mean fall strength of ten virtual patients, in general, had similar pattern in the variation of loading scenarios.



(a)



(b)

Figure 5.11 The distribution of bone strength of Patient085 (a) and mean bone strength of corresponding virtual patients (b) in terms of varying loading directions.

5.4 Discussion

The main aims of this study were to investigate 1) the relationship between femur length and body height, 2) anatomical similarities between all femurs in the Sheffield cohort and 3) the effect of femur length on bone strength while keeping bone shape and mineral density unchanged.

5.4.1 Body height vs. Femur length

The results showed that the correlation between femur length (L) and body height (H) were quite weak, while in the literature that they suggested a simple linear relationship (see Figure 5.12).

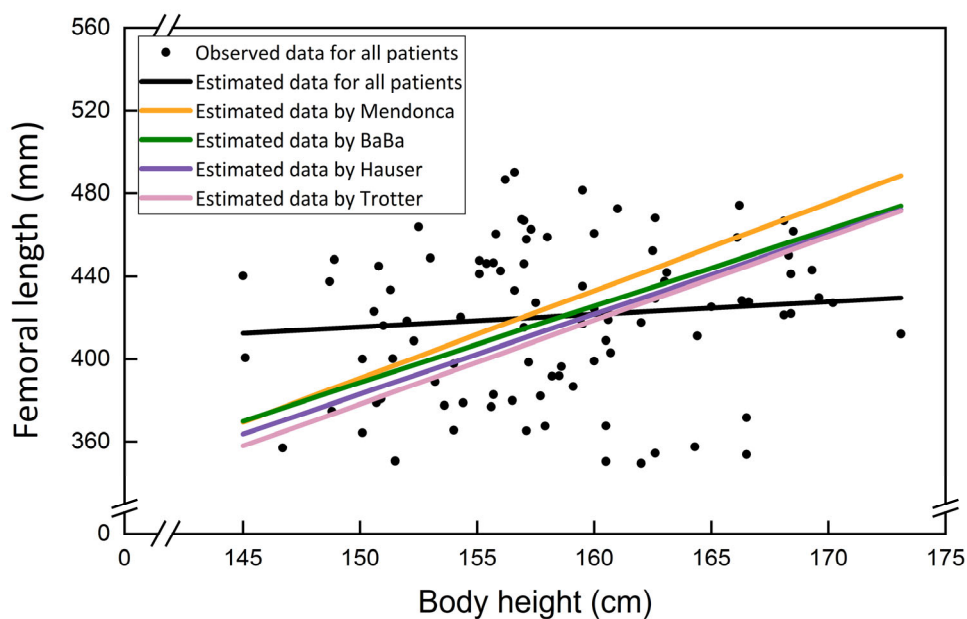


Figure 5.12 Plot of estimated femoral length as a function of the body height for 96 patients ($R^2=0.010$) and comparisons of our result with those of other authors.

As Figure 5.12 shows, the slope of linear regression obtained from the Sheffield cohort was much flatter than those of other cohorts which means L changes little when compared with other estimations. The results from literatures to some extent, were consistent, the differences between those estimations within 5%. The large difference between the Sheffield cohort with other groups' may be due to the age of subjected patients. It can be seen clearly from Table 5.6, patients allocated in Sheffield cohort were much older than other groups: the

average age of Sheffield cohort was 75 years old, bigger than maximum age of Mendonca cohort and Hauser cohort. Curtis in his study about the fracture rates about British women suggested after 75 years old British women had higher risk to suffer from spine fracture [22]. From his conclusion, there is reason to believe patients in Sheffield cohort are likely to have spine fracture which collected height data does not reflect patients' real height.

Table 5.6 Comparisons between different cohorts. L: femur length (mm) and H: body height (cm). The units of two variables in all formula are amended into a consistent form. The linear regression equations of Mendonca, Baba, Trotter and Hauser are inversed from their original forms. Body heights in comparing cohorts are estimated from cadavers, *i.e.*, the height used in linear regression is the stature of cadavers minus 2cm. Only results of female subjects were included in this table [234–237].

Cohort	Sample number	Ethnicity	Age	Linear regression
Sheffield	96	British	55-91	$L=[0.617H+332.705] \pm 193.868$
Mendonca	95	Portuguese	50-59	$L=[4.239H-245.273] \pm 25.265$
Baba	90	Japanese	20-94	$L=[3.704H-167.074]$
Trotter	63	American	27-89	$L=[4.049H-229.150] \pm 15.061$
Hauser	20	Polish	28-74	$L=[3.861H-196.197]$

The differences in the measurement of L may also contribute to the differences of estimations. Except Baba's study which used CT scans, the other studies were used cadavers as research subjects [236]. In Mendonca's study, two types of L were mentioned, that are, physiology length and perpendicular length [235]. In Sheffield cohort, as mentioned before, the lengths of relative bounding box were assumed to be the L, which shares more similar ideas with perpendicular length. As the result, the linear regression equation regarding perpendicular length from Mendonca's study was adopted in comparison [235]. Perpendicular length was also used in other three cohorts.

Besides, subjects involved in the literature had been through an exclusion process, such as

abandoning subjects who had obvious body deformation or severe osteoporosis, while all patients in Sheffield cohort were considered in this study.

In addition to the analysis using whole Sheffield cohort, no significant improvement was found in the correlation between body height and femur length using sub-groups. The brief discussions of each sub-group are listed below:**1) Age**

The linear regression analysis shows that for relatively younger group patients whose age below or equal to 75 years old, there is a positive relationship, while for older group it suggests a negative relationship. However, for both group of patients, the results suggest the correlation is fairly low ($R^2=0.07$ for younger group and $R^2<0.01$ for older group.) The adjusted R square values of two groups are nearly zero or even negative which means even the uniform distribution of average value is better fitting the sample data.

2) Fracture status

Both two groups seem to have a weak positive relationship ($R^2=0.02$ for none fractured group and $R^2=0.01$ for fractured group) and the None-fractured group has stronger correlation than fractured one.

3) T-score

Results suggest that patients who suffer from the loss of bone minerals have even weaker correlation.

4) BMI

For healthy group and overweight group, it seems L has no relationship with H, while the other two groups show L will increase as H increases. Obese group surprisingly has highest R^2 value, 0.20, while underweight group ranks second ($R^2=0.03$), might because the number of patients in these two groups are too small and uncertainty of height has a determinant effect.

Other attempts of establish a statistical reliable relationship between length and height, such as finding the distribution of femoral length of patients for each height rank or considering

multi-factor regression, all ended up with unsatisfactory results due to the limitation of numerosity of Sheffield cohort and dominating discrepancy of height. A linear regression was also conducted between body height and bone strength. Although the regression coefficient (13.18, 95% confidence intervals: -4.93 to 31.30) suggests bone strength increases with the increase in body height, the correlation is too low that it could be regarded as no correlation ($r^2=0.04$). Hence, at least for Sheffield cohort, it is not idea to use body height as index to determine scaling factors for virtual population. Instead, femur length should be selected as the direct index.

5.4.2 Femur strength vs. femur length

As mentioned before in Section 5.3.4, minimum pathological strength (MinPatS) of virtual patients varied from 1706N to 1791N with the average value of 1754N, while MinPatS of physical patient is 1797N. It suggested that patients who had longer femur had lower bone strength (see Figure 5.13).

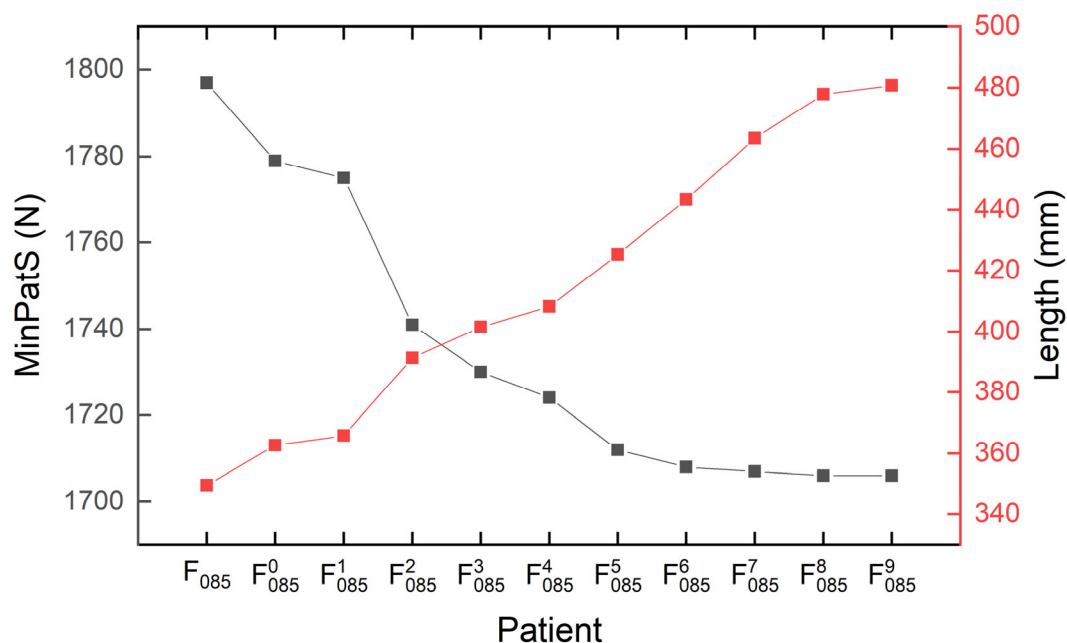


Figure 5.13 Variation of MinPatS (marked in black) and femur length (marked in red) of Patient085 and its corresponding virtual patients.

However, the true value of MinPatS lies in the range of 15% of the predicted MinPatS given

by QCT-SSFE method. In this study, if predicted bone strength of physical patient is assumed as the true value, the range will be $1797 \pm 305.5N$. As the variation of femur strength of virtual patients is much smaller than the uncertainty of QCT-SSFE method-based prediction ($\sim 306N$, see Figure 5.14), in terms of femur strength, none of the virtual patients can be distinguished from the physical patient used to generate them. In other words, femur strength is not affected by the variation of femur length based on this initial exploration.

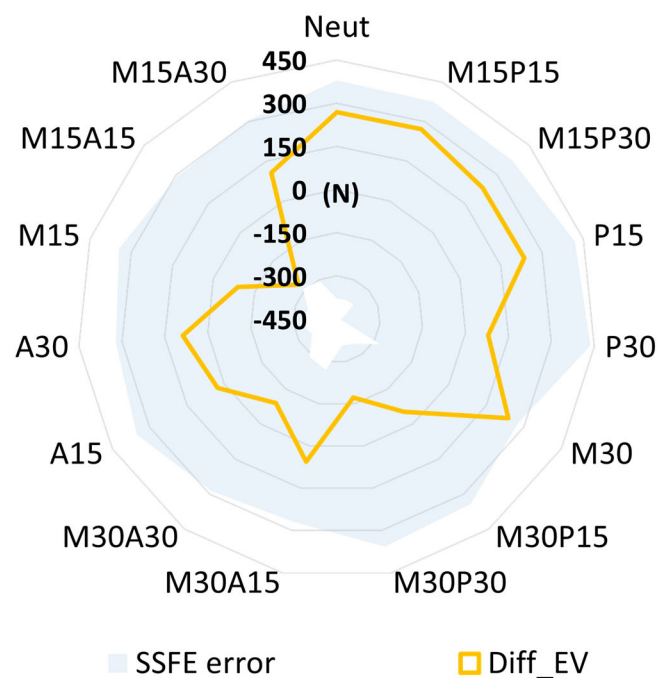


Figure 5.14 The extreme values of the difference between bone strength of Patient085 and corresponding virtual patients in terms of varying loading directions (marked in yellow). The estimation error introduced by QCT-SSFE method in terms of loading directions (marked in pale blue).

The result is consistent with Taylor et al [225]. Taylor et al used the active shape models on the same cohort (the Sheffield cohort) to explore the influence of shape. They found that the first 10 (out of total 93) modes could explain 95% variation of femur shape. In detail, the first mode was the scaling mode that explained 55.0% shape variation and mainly reflected the change in the length of the proximal femur under lesser trochanter. Mode 2 captures the variation in the width of proximal femur, explaining 11.5% of the shape variation. However,

neither mode 1 nor 2 was selected as a predictive variable of femur strength by stepwise multivariate linear regression (MLR), indicating that size independently has no significant influence of femur strength.

Additionally, they reported the maximum change of femoral neck strength under neutral side-fall loading condition for non-fracture group was 705 N (31% of the bone strength of mean shape), while the first 10 modes of the ASM were changed by 2 standard deviations from the mean shape. Specifically, only mode 4 and 5 were identified as important predictive variables in both statistical analysis (P-value) and the MLR. These two modes mainly reflect the variation in femoral neck morphology and greater trochanter. In our study, Patient085 was identified as non-fractured subject and the maximum difference of bone strength among 10 corresponding virtual patients under the same loading condition was found to be 268 N (11% of bone strength of Patient085). This suggests that the influence of size is much less than the influence of femoral neck morphology.

Failure location and failure type are exactly same for all patients, which are in the femoral neck region and compressive failure respectively. Moreover, the compressive failure achieved in each patient was at the same node 8659. And in most loading cases for all patients, failure occurred at node 8659, suggesting the area around node 8659 was the most vulnerable part in the whole proximal femur.

Additionally, the same worst loading case (Med30Ant15) for all results suggests that anterolateral falls are the critical fall conditions which produce minimum load to fail. This is consistent with Altai's study that besides with posterolateral falls, anterolateral falls should also be considered as critical fall direction during the research of hip fracture risk [141].

5.4.3 Limitations

The limitations of this study are listed below:

1) Limitation of loading scenarios and numerosity of analysis subjects

The study of Altai et al suggested that multiple loading directions in the contact model would provide the best prediction accuracy [141]. However, the computational cost of 28 loading

cases (the force direction varied from 0° to +30° on the medial-lateral plane and from -30° to +30° on the anterior-posterior plane with increment of 10°) is huge, approximately 25 minutes/ loading simulation on PC (Intel® core i7-7700K CPU @4.2GHz 4.2 GHz, 16.0 GB RAM). Considering the most critical fall directions were at the most extreme angle of the spectrum, a trade-off between computational time and accuracy is acceptable.

Considering about limited time and computation resources, only one physical patient and corresponding ten virtual population were analysed. The results obtained from this study are not statically significant. However, as the initial exploration patterns suggested by this study is meaningful for future works.

2) CT scans containing only proximal regions

The study of Qasim et al [131] recommended that the full femur CT scan should be preferred as it contains detailed anatomical information of knee centre, which is a critical bio-landmark. However, patients will be exposed to additional radiation dose for the full femur scan. This is a compromise between the accuracy of QCT-SSFE prediction and patient safety, which should be carefully considering before conduct analysis.

3) Flat sampling strategy

For this stage, flat sampling strategy was chosen to generate virtual patients. However, the very small influence of femur length on femur strength found in this study suggests that this conclusion will not be affected if the sampling strategy is modified.

5.5 Conclusion

The relationship between body height and femur length for 96 post-menopausal British women (the Sheffield cohort) was explored as a preliminary study. The coefficient of determination (r) is only 0.102 ($r^2=0.010$) suggesting body height and femur length have no linear relationship between in this population. The unsatisfactory results of finding the distribution of femur length of patients for each height rank or multi-factor regression suggest these two variables potentially do not follow other relationships. Therefore, femur length

instead of body height was selected as the initial input of virtual patients.

Ten virtual patients based on a physical patient in the Sheffield cohort were generated by scaling femur length. The effect on bone strength of varying femur length while femur shape and aBMD are fixed was investigated using virtual patients and physical patient. The results showed that bone strength of femur potentially decreases as the length of femur increases, while the failure type, location and critical fall type have no association with femur length. The same worst loading case (Med30Ant15) which produce minimum load to fail for all results suggests that anterolateral falls are the critical fall conditions. Hence, besides with posterolateral falls, anterolateral falls should also be considered as critical fall direction during the research of hip fracture risk. The study also suggests that the influence of femur length variation on femur strength variation is smaller than the uncertainty in predicting femur using the CT-SSFE approach. Hence, for the purpose of generating virtual cohorts, the particular method chosen to vary femur lengths potentially exerts a negligible influence on any subsequent conclusions drawn regarding femur strength.

6. Conclusion and future work

The overall aim of this thesis is to model the femur strength in a virtual postmenopausal osteoporotic population for application to *in silico* clinical trials. To investigate the sensitivity of femur strength of postmenopausal women upon two main factors (vBMD distribution and femur length), two virtual populations were generated in this thesis: 1) a group of virtual patients having varied vBMD distribution with geometry unchanged; 2) a group of virtual patients having varied femur length with vBMD distribution and femur shape unchanged. To model the first group of virtual population, two bone loss algorithms were developed that describe how vBMD changes with the respect to change in aBMD.

A summary of the main findings of this thesis and further work are elucidated in the following.

6.1 The change of local vBMD with respect to aBMD

This study investigated the relationship between vBMD and aBMD to assist the estimation of future femur strength. QCT-SSFE has been previously shown to provide an accurate estimation of femur strength [4]. Femur strength is regarded as a key determinant of hip fracture risk, which is crucial in the management of osteoporosis. However, not only a person's absolute risk of hip fracture at the current point (ARF0), but also ARF over a 10-year period (ARF10) could strongly influence the doctor's decision in the current clinical practice. Due to the requirement of QCT scans as subject-specific inputs, the current QCT-SSFE models are limited to predict the femur strength at the time of clinical presentation [243]. Many epidemiological studies reported temporal change of aBMD due to aging [186], which offer the inspiration to use the change of aBMD to predict the change of vBMD. Although few *in vivo* studies reported correlation between integral vBMD of total hip and aBMD [207,244], the spatial distribution of vBMD loss in the proximal femur remains poorly understood. To meet this need, two novel bone loss algorithms were developed to model the local vBMD changed with the respect to aBMD based on a retrospective study of 96 postmenopausal women in Sheffield.

Homogenous algorithm was proposed assuming bone remodelling induced vBMD is uniform throughout the proximal femur. The best-fit value of the changing rate for homogenous algorithm is $m=0.363 \text{ cm}^{-1}$, which is insensitive to optimizing settings (step size and initial guess of the routine *lsqnonlin*). The slope is consistent with slopes reported in the literature [207,244]. A linear regression is also conducted between aBMD and average vBMD over proximal femur to mimic the relationship proposed in the literature. However, the r.m.s of normalised non-volume-weighted elemental prediction error based on linear regression is 74.8%, more than twice of the error based on homogenous algorithm (34.5%), which suggests that the relationship derived from total hip integral vBMD is not suitable to predict local vBMD change. Although the r.m.s of normalised E predicted by homogenous is reduced to half of it by direct linear relationship, 34.5% is still relatively large. The rather large error could be attributed to the assumption that bone loss is uniform across proximal femur, which is known to be higher in trabecular bone relative to cortical bone. Hence, it should be cautious to use the homogenous algorithm in the future FE application.

To improve the estimation accuracy, density-specific algorithm was developed to account the heterogeneous vBMD loss by three density types (low-, medium- and high-density), which are separated by two constant thresholds. The best-fit parameters for density-specific algorithm are $m_M=0.234 \text{ cm}^{-1}$, $m_H= 0.189 \text{ cm}^{-1}$, $\tau_{LM}=0.253 \text{ g}\cdot\text{cm}^{-3}$, $\tau_{MH}=0.673 \text{ g}\cdot\text{cm}^{-3}$, with prediction error of 17.2%. The slopes are quite different from those between trabecular/cortical vBMD and aBMD stated in the literature [207,244], due to the difference in separating tissue types. Amstrup et al used a single density threshold ($\tau=0.350 \text{ g}\cdot\text{cm}^{-3}$) and reported the slope to be 0.131 cm^{-1} and -0.417 cm^{-1} for trabecular and cortical bone, respectively. Authors attributed the inverse correlation found in cortical bone to existence of transitional bone. τ_{MH} in the density-specific algorithm is much higher than the threshold proposed by Amstrup et al, thus bone in the high-density region contains more “true” cortical bone. Additionally, the influence of transitional zone in this study was reduced by reducing the volume of interest to element level and only elements having identical density labels across majority subjects are used in the optimization process. Hence, theoretically bone loss could be modelled by density-specific algorithm more accurately.

Based on the density-specific algorithm, an atlas of local vBMD loss over 6 years was generated based aging-induced aBMD loss reported by Paggiosi et al (approximately 5% aBMD loss over 6 years) [186]. It showed that in general the loss rate in trochanteric region is the lowest, with the femoral neck the second and intertrochanteric region the highest. Less bone is preserved around bone surface, especially in the femoral shaft and superior femoral neck. This finding is partially consistent with the atlas generated by Farzi et al based on DXA-aBMD images [210]. The main advantage of density-specific algorithm is the independence of meshes and it accounts the vBMD changes over 3D geometry of proximal femur, instead of a 2D cut-off plane.

The results demonstrate the possibility to employ law algorithm in predicting the future bone strength. Furthermore, it could also be implanted in the mechanistic models to assess future hip risk such as ARF10. As mechano-regulation effect was excluded in the current model, further development can be conducted to include such influence, which will be discussed in Section 6.4.

6.2 Virtual osteoporotic population with aBMD derived from epidemiological data

Influence of aBMD upon vBMD variation and femur strength is explored in this study based on a group of virtual patients employing the bone loss algorithm developed in previous study. Although it has been widely reported that bone strength can be affected by BMD distribution and bone geometry in the literature [7, 8], whereas it is always concluded from the combined influence of two factors.

A virtual population is generated based on 49 controlled subjects in Sheffield cohort using algorithms proposed in Chapter 3. By applying aBMD data reported in epidemiological studies, the median value of The rate of bone strength with respect to aBMD computed from homogenous algorithm (k) is found to be $4612 \text{ N}/(\text{g}\cdot\text{cm}^{-2})$. The sensitivity of k is slightly stronger to impact orientations compared with bone geometries. Following similar approach, the changing rate computed from density-specific algorithm (k') is much smaller than k , with the median over all geometries and orientations equal to $1008 \text{ N}/(\text{g}\cdot\text{cm}^{-2})$. The sensitivity of k' is consistent with the case found in k . A linear regression is performed between femur

strength and aBMD of physical subject as a comparison. The results show that k overlap with regression slope at most orientations, while k' is much lower in magnitude. However, due to lack of a true validation, it is uncertain whether the true loss of bone strength is better predicted by the density-specific or homogeneous algorithm.

Moreover, for each of ten randomly selected physical patients in Sheffield cohort, eleven virtual patients are generated based on density-specific algorithm and covering the full aBMD range with an equal aBMD increments (*i.e.*, 0.36, 0.42, ..., 0.96 g·cm⁻²). The FE results show that variation of femoral strength is explained entirely by variation in aBMD alone for fixed bone shape and size ($R^2=0.99$). Critical fall orientation, failure type and failure location were identical for all virtual patients generated from the same physical patient, which suggests that these are independent of aBMD.

The outcomes of this study show that bone loss algorithm combined with CT-SSFE, can be applied to compute future bone strength, and by extension, long-term fracture risk. Furthermore, this study provides a promising first step towards generation of virtual patients for in silico clinical trials.

6.3 Virtual osteoporotic population with varied femur length

In this study, a group of virtual patients with varied femur length were generated by affine scaling method to investigate the effect of femur length upon femur strength. Although the influence of bone geometry has been investigated in many studies based on various shape parameters, most of them are associated with aBMD [226,245] or do the comparison between genders [197,244]. With the help of virtual patients, it is possible to explore the independent influence of femur size on subjects with identical vBMD distribution but having difference length.

First, the readily measurable variable body height was considered as the input of scaling factor. The literature supported this choice, as it suggested a linear correlation between body height and femur length. However, somewhat unexpectedly, the calculated coefficient of determination ($r^2=0.010$) reflects body height is not suitable to replace femur length in the Sheffield cohort. The most likely explanation is that patients in the Sheffield cohort typically

suffer from osteoporosis, and hence they may also experience spine fracture and develop a characteristic stooped posture.

In addition, Hausdorff distance is determined between two subjects whose lengths were closest to check of anatomical similarity of femur shapes. It is concluded that only one pair of femurs have average Hausdorff distance less than 1mm (approximately 1.5 times the CT image resolution). All 96 femurs in Sheffield cohort are reserved to ensure the variation of shape sufficient for the modelling. Also, the results suggested that the difference in femur anatomy was mainly caused by femur length, and it would be safer if virtual femurs are scaled only by length as near as the original femur. But, as the maximum HD_{avg} was only 1.66% of the average femur length, it was still safe to scale over the whole spectrum.

The three dimensions of femurs was determined by minimum bounding box. Virtual patients were generated by performing isotropic scaling of the proximal femur geometry of physical patients (*i.e.*, FE meshes). In this study, physical patient 085 was selected randomly as the initial analysis subject and corresponding $K = 10$ virtual patients were generated. Choosing ten virtual patients provided a good balance between computational cost and relevant verification of the workflow. FE analysis was conducted for 11 proximal femur models to simulate sideways falls. Results showed that the variation of bone strength among all virtual patients lies in the 15% of physical patient, which is identical to the prediction error of QCT-SSFE. This suggests femur strength is not affected by the variation of femur length. Similarly, the failure type, location and critical fall orientation have no association with femur length.

The main finding in this study indicates that the variation of femur length or even femur size have no significant influence on femur strength based on current QCT-SSFE accuracy. Perhaps with improved QCT-SSFE prediction accuracy, the sensitivity of femur strength upon femur size could be better understood.

6.4 Future directions

Given to the main outcomes of this thesis, further investigation could be conducted in three aspects: bone loss accounting mechano-regulation; sensitivity of femur strength upon femur shape with identical aBMD and length; and generating virtual populations to re-investigate

clinical trials. The brief description of these three aspects and preliminary attempts are stated below.

6.4.1 Bone loss accounting for mechanoregulation

The age-related bone mass change has been discussed in detail previously and bone loss algorithms developed in this thesis have neglected the effect of mechano-regulation upon the remodelling process. However, the mechanism of bone mass changes is a synergy between a range of sophisticated and complexed factors including age, mechanical usage and diseases [246]. It has been reported by several studies that the age and bone loss for postmenopausal women do not follow a strict linear relationship [197,247]. With the adjustment of BMI, the regression coefficient becomes more negative [248]. Besides, even using the curvilinear model, there is no statistically significant improvement from the linear model [247]. It is probably because the mechanical usage is not neglectable for the aging related bone loss model.

Mechanical usage covers almost all physical activities associated with the bones imposed by physical loads and motions. The bone responds to these loadings and strains by changing the bone mass and structure [116]. Due to the variation of corresponding modelling and remodelling activities, the effect of these loadings and strains on the bone mass change are different. Regular physical exercise is considered to have a benefit on the improvement of bone quality attributed to the proper ranges of strain on bone. [249]. It is reported that after 1-year proper physical exercise, the postmenopausal women have an improved bone mineral density compared to the lacking exercise group [250]. Although the mechanism for the bone mass change is known as increase of bone formation and decrease of bone resorption, the underlying reason why bone resorption is more responsive to the mechanical loading is unclear. In addition, the mode of physical exercise that subject takes has different influences on the extent of bone mass increase.

Conversely, the decreased mechanical usage can lead to the reduction of bone mineral density, referred to disuse bone loss. It is generally associated with microgravity for space condition, injury and muscular contraction, The decrease of bone mass for astronauts after spaceflight, due to the microgravity, has been reported by several studies [251,252]. The

disuse bone loss is related to a complexed bone responses mechanism to the mechanical loading.

A strain-adaptive algorithm was proposed by McNamara et al to simulate bone remodelling [253]. The local remodelling status was assumed to be separated into three categories (resorption, lazy zone and formation) by two strain energy density (SED) thresholds. This provides an inspiration to adapt bone loss algorithm proposed in this thesis.

The rate of change of vBMD with respect to aBMD at any location is assumed to be dependent on both vBMD and the mechanical stimulus at that location. Strain energy density (SED) under one-legged stance condition is considered to be representative of physiological activity induced mechanical stimulus. To reduce the effect of variation of body weight, for a certain subject, SED of all elements will be normalised by the maximum elemental SED (*i.e.*, $\hat{S}_e^p = \frac{S_e^p}{\max|S_e^p|_p}$, where S_e^p denotes SED for element e of subject p and $\max|\cdot|_q$ represents the maximum over index q).

Two hypotheses will be tested:

- 1) whole bone is in resorption.
- 2) bone regions are partitioned into resorption, quiet and formation region corresponding to low, medium and high levels of SED.

Hence, for the first model, it is assumed

$$\frac{dv(x, a)}{da} = \frac{m_i}{\hat{S}} \quad (\text{Equation 6.1})$$

where i represents low-, medium- or high-density region defined in density-specific algorithm determined by the threshold τ'_{LM} and τ'_{MH} . \hat{S} is normalised SED ($0 < \hat{S} < 1$). The predicted vBMD (v_e^p) is given by

$$v_e^p = \frac{m_i}{\hat{S}_e^p} \cdot (a_p - \langle a_p \rangle_p) + \langle v_e^p \rangle_p \quad (\text{Equation 6.2})$$

where the operator $\langle \dots \rangle_q$ denotes an average taken over the range of the index q . This definition utilises the fact that the line of best fit always passes through the centre of the data, which here is given by $(\langle a_p \rangle_p, \langle v_e^p \rangle_p)$. The total error vector from element e is defined the same as previously in density-specific algorithm. The initial guesses for the routine **lsqnonlin** are the parameters determined in density-specific algorithm.

In the second model, the changing rate is then defined as

$$\frac{dv(x, a)}{da} = m_i \cdot \varphi_j \quad (\text{Equation 6.3})$$

where φ_j is defined a SED-related factor and j denotes resorption (R), quiet (Q) and formation (F) region. φ_Q is assumed to be zero with $\varphi_R < 0 < \varphi_F$. \dot{S}_{RQ} and \dot{S}_{QF} are two normalised SED thresholds ($0 < \dot{S}_{RQ} < \dot{S}_{QF} < 1$) separating resorption/quiet zone and quiet/formation zone.

The original vBMD matrix (295589*96, element index*subject index) is then resorted the magnitude of subject's aBMD in descending order, *i.e.*, the first column is the subject with smallest aBMD and the last column is with largest aBMD. Then, the change of vBMD is calculated between the current subject and the subject having next smaller aBMD. Hence, the predicted vBMD ($v_e^{p'}$) for element e and subject ($p' = 2 \dots 96$) is given by

$$v_e^{p'} = m_i \cdot \varphi_j \cdot (a_{p'} - a_{p'-1}) + v_e^{p'-1} \quad (\text{Equation 6.4})$$

And a subject- and element-specific error variable is defined as follows

$$\epsilon_e^{p'} = (v_e^{p'} - v_e^{p'-1}) V_e^{p'} \quad (\text{Equation 6.5})$$

The total error vector from element e is the same as previously. The initial guesses for m_i , τ'_{LM} and τ'_{MH} are the best-fit parameters determined in first model, while the rest is assumed to be $\dot{S}_{RQ0} = 0.25$, $\dot{S}_{QF0} = 0.75$, $\varphi_{R0} = -1$, $\varphi_{F0} = 1$. The routine **lsqnonlin** could be implemented to find the optimised parameters.

6.4.2 Generating virtual populations to re-investigate clinical trials

Based on the results derived from the studies discussed in Section 6.2 and 6.3, the procedure of generating virtual populations with specific biomechanical parameter distributions would be established. If bone strength is found to be not sufficiently sensitive to certain biomechanical parameters, this information can be used to optimise virtual population generation.

Bisphosphonates are a common drug used in osteoporosis treatment. Past clinical trials have recorded improvement (or not) in aBMD endpoints. Here, virtual patients could be created to represent the biomechanical parameter distributions of physical patients in these trials. The number of virtual patients generated will correspond to the statistical power needed. QCT-SSFE analysis could be used to investigate if S_1 (= bone strength when drug is administered) and S_0 (= bone strength when placebo is administered) come from statistically significantly different distributions. Bayes' theorem will be used to restrict how many virtual subjects are analysed using FE.

Bayes' theorem states that, given the data X , the posterior probability distribution of the parameter θ can be determined from the probability distribution $p(X|\theta)$ of the random variable X and the prior probability distribution $p(\theta)$ of θ [254]. Moreover, once $p(\theta|X)$ has been evaluated, it can be used to substitute for $p(\theta)$ and use again with more data X .

$$p(\theta|X) = \frac{p(X|\theta)p(\theta)}{\int p(X|\theta)p(\theta)d\theta} \quad (\text{Equation 6.6})$$

First, the bone strength distribution of all physical patients in the cohort needs to be determined. This gives the functional form of $p(X|\theta)$, where $\theta = \theta_S$ is the parameter describing the distribution of bone strength $X = S$. It will be assumed that the functional form of the bone strength distribution is same for intervention and placebo populations. The initial guess of the prior distribution $p(\theta)$ is immaterial and will be taken to be a uniform distribution in the range of bone strength values found in the literature. With these information, Bayes' theorem can be used to update the posterior distribution (in batches of virtual patients). Simulations are stopped when the parameters θ of the distributions of S_0 and S_1 are known with enough accuracy to determine statistically significant differences.

Table 6.1 Basic information of Bayes' theorem for reinvestigating clinical trials.

	Distribution of Bone Strength	Distribution of biomechanical parameters	Sheffield Cohort	Virtual Populations
Disease Model	S_0	θ_{s0}	$p(S_0 \theta_{s0}), p(\theta_{s0})$	$p(S_0^v \theta_{s0}^v), p(\theta_{s0}^v)$
Intervention Model	S_1	θ_{s1}	$p(S_1 \theta_{s1}), p(\theta_{s1})$	$p(S_1^v \theta_{s1}^v), p(\theta_{s1}^v)$

A group of virtual population with statistical significance of past clinical trials could be generated for in silico clinical trial. The independence of the sequences needs to be verified by applying Bayes' theorem to test the individual or batches of virtual patients. However, the batch size used for updating the posterior distribution is required to be tuned to make it sufficiently parallelizable but also to not execute too many unnecessary simulations, which is largely limited by the HPC system capabilities.

Reference

- [1] J.Y. Reginster, N. Burlet, Osteoporosis: A still increasing prevalence, *Bone*. 38 (2006) 4–9. <https://doi.org/10.1016/j.bone.2005.11.024>.
- [2] T.P. Van Staa, E.M. Dennison, H.G.M. Leufkens, C. Cooper, Epidemiology of fractures in England and Wales, *Bone*. 29 (2001) 517–522. [https://doi.org/10.1016/S8756-3282\(01\)00614-7](https://doi.org/10.1016/S8756-3282(01)00614-7).
- [3] T. Bunning, R. Dickinson, E. Fagan, D. Inman, A. Johansen, A. Judge, J. Hannaford, M. Liddicoat, R. Wakeman, National Hip Fracture Database (NHFD). Annual report September 2018, 2018. www.rcplondon.ac.uk.
- [4] M. Viceconti, M. Qasim, P. Bhattacharya, X. Li, Are CT-Based Finite Element Model Predictions of Femoral Bone Strengthening Clinically Useful ?, *Curr. Osteoporos. Rep.* 16 (2018) 216–223. <https://doi.org/10.1007/s11914-018-0438-8>.
- [5] P. Bhattacharya, Z. Altai, M. Qasim, M. Viceconti, A multiscale model to predict current absolute risk of femoral fracture in a postmenopausal population, *Biomech. Model. Mechanobiol.* 18 (2019) 301–318. <https://doi.org/10.1007/s10237-018-1081-0>.
- [6] M.D. Iversen, R.R. Vora, A. Servi, Focus Group Approach Examining Viewpoints of Patients and, 34 (2012) 72–81. <https://doi.org/10.1097/JPT.0b013e3181ff03b4>.Factors.
- [7] M. Whitaker, J. Guo, D. Ph, T. Kehoe, G. Benson, Bisphosphonates for Osteoporosis — Where Do We Go, (2012).
- [8] P.D. Delmas, G. Calvo, M. Boers, E. Abadie, B. Avouac, A. Kahan, J.M. Kaufman, A. Laslop, J.F. Lekkerkerker, P. Nilsson, B. Van Zwieten-Boot, G. Kreutz, J.Y. Reginster, The use of placebo-controlled and non-inferiority trials for the evaluation of new drugs in the treatment of postmenopausal osteoporosis, *Osteoporos. Int.* 13 (2002) 1–5. <https://doi.org/10.1007/s198-002-8331-3>.
- [9] Morgan, SENATE report, 2016.
- [10] F. Pappalardo, G. Russo, F.M. Tshinanu, M. Viceconti, In silico clinical trials : concepts and early adoptions, 20 (2019) 1699–1708. <https://doi.org/10.1093/bib/bby043>.
- [11] US Department of Health and Human Services, Bone health and osteoporosis: a report of the Surgeon General, 2004. <http://scholar.google.com/scholar?hl=en&btnG=Search&q=intitle:Bone+Health+and+Osteoporosis+A+Report+of+the+Surgeon+General#0>.
- [12] A. Svedbom, E. Hernlund, M. Ivergård, J. Compston, C. Cooper, J. Stenmark, E. V. McCloskey, B. Jönsson, J.A. Kanis, Osteoporosis in the European Union: A compendium of country-specific reports, *Arch. Osteoporos.* 8 (2013). <https://doi.org/10.1007/s11657-013-0137-0>.
- [13] E. Hernlund, A. Svedbom, M. Ivergård, J. Compston, C. Cooper, J. Stenmark, E. V.

McCloskey, B. Jönsson, J.A. Kanis, Osteoporosis in the European Union: Medical management, epidemiology and economic burden: A report prepared in collaboration with the International Osteoporosis Foundation (IOF) and the European Federation of Pharmaceutical Industry Associations (EFPIA), *Arch. Osteoporos.* 8(1) (2013). <https://doi.org/10.1007/s11657-013-0136-1>.

[14] Populationpyramid.net, Population Pyramids of the World from 1950 to 2100, (2019).

[15] A. Mithal, B. Bansal, C.S. Kyer, P. Ebeling, The Asia-Pacific Regional Audit-Epidemiology, Costs, and Burden of Osteoporosis in India 2013: A report of International Osteoporosis Foundation, *Indian J. Endocrinol. Metab.* 18 (2014) 449–454. <https://doi.org/10.4103/2230-8210.137485>.

[16] P. Chen, Z. Li, Y. Hu, Prevalence of osteoporosis in China: a meta-analysis and systematic review, *BMC Public Health.* 16 (2016) 1–11. <https://doi.org/10.1186/s12889-016-3712-7>.

[17] F. Borgström, L. Karlsson, G. Orsäter, N. Norton, P. Halbout, C. Cooper, M. Lorentzon, E.V.M.N.C. Harvey, M.K. Javaid, J.A. Kanis, Fragility fractures in Europe: burden, management and opportunities, *Arch. Osteoporos.* 15 (2020) <https://doi.org/10.1007/s11657-020-0706-y>.

[18] A. Odén, E. V. McCloskey, J.A. Kanis, N.C. Harvey, H. Johansson, Burden of high fracture probability worldwide: secular increases 2010–2040, *Osteoporos. Int.* 26 (2015) 2243–2248. <https://doi.org/10.1007/s00198-015-3154-6>.

[19] J.A. Kanis, O. Johnell, Requirements for DXA for the management of osteoporosis in Europe, *Osteoporos. Int.* 16 (2005) 229–238. <https://doi.org/10.1007/s00198-004-1811-2>.

[20] R. Burge, B. Dawson-hughes, D.H. Solomon, J.B. Wong, A. King, A. Tosteson, Incidence and Economic Burden of Osteoporosis-Related Fractures in the United States, 2005–2025, *J. BONE Miner. Res.* 22 (2007). <https://doi.org/10.1359/JBMR.061113>.

[21] J. Compston, A. Cooper, C. Cooper, N. Gittoes, C. Gregson, N. Harvey, S. Hope, J.A. Kanis, E. V. McCloskey, K.E.S. Poole, D.M. Reid, P. Selby, F. Thompson, A. Thurston, N. Vine, UK clinical guideline for the prevention and treatment of osteoporosis, *Arch. Osteoporos.* 12 (2017). <https://doi.org/10.1007/s11657-017-0324-5>.

[22] E.M. Curtis, R. van der Velde, R.J. Moon, J.P.W. van den Bergh, P. Geusens, F. de Vries, T.P. van Staa, C. Cooper, N.C. Harvey, Epidemiology of Fractures in the United Kingdom 1988–2012: Variation with age, sex, geography, ethnicity and socioeconomic status, *Bone.* 87 (2016) 19–26. <https://doi.org/10.1016/j.bone.2016.03.006>.

[23] C. Cooper, Epidemiology of osteoporosis, *Osteoporos. Int.* 9 (1999). <https://doi.org/10.5124/jkma.2016.59.11.836>.

[24] N. Harvey, E. Dennison, C. Cooper, Osteoporosis: Impact on health and economics, *Nat. Rev. Rheumatol.* 6 (2010) 99–105. <https://doi.org/10.1038/nrrheum.2009.260>.

[25] D. Felsenberg, A.J. Silman, M. Lunt, G. Ambrecht, A.A. Ismail, J.D. Finn, W.C. Cockerill, D. Banzer, L.I. Benevolenskaya, A. Bhalla, J. Bruges Armas, J.B. Cannata, C. Cooper, J. Dequeker, R. Eastell, B. Felsch, W. Gowin, S. Havelka, K. Hozowski, I. Jajic, J. Janott, O. Johnell,

J.A. Kanis, G. Kragl, A. Lopes Vaz, R. Lorenc, G. Lyritis, P. Masaryk, C. Matthis, T. Miazgowski, G. Parisi, H.A.P. Pols, G. Poor, H.H. Raspe, D.M. Reid, W. Reisinger, C. Scheidt-Nave, J.J. Stepan, C.J. Todd, K. Weber, A.D. Woolf, O.B. Yershova, J. Reeve, T.W. O'Neill, Incidence of vertebral fracture in europe: Results from the european prospective osteoporosis study (EPOS), *J. Bone Miner. Res.* 17 (2002) 716–724. <https://doi.org/10.1359/jbmr.2002.17.4.716>.

[26] C. Cooper, G. Campion, L.J. Melton, Hip fractures in the elderly: A world-wide projection, *Osteoporos. Int.* 2 (1992) 285–289. <https://doi.org/10.1007/BF01623184>.

[27] J.H. Krege, D. Kendler, K. Krohn, H. Genant, J. Alam, P.Y. Berclaz, B. Coffey, C. Loghin, Relationship Between Vertebral Fracture Burden, Height Loss, and Pulmonary Function in Postmenopausal Women With Osteoporosis, *J. Clin. Densitom.* 18 (2015) 506–511. <https://doi.org/10.1016/j.jocd.2015.02.004>.

[28] M.C. Nevitt, S.R. Cummings, S. of O.F.R. Group, Type of Fall and Risk of Hip and Wrist Fractures: The Study of Osteoporotic Fractures, *J. Am. Geriatr. Soc.* 41 (1993) 1226–1234. <https://doi.org/https://doi.org/10.1111/j.1532-5415.1993.tb07307.x>.

[29] J.A. Kanis, A. Odén, E. V. McCloskey, H. Johansson, D.A. Wahl, C. Cooper, A systematic review of hip fracture incidence and probability of fracture worldwide, *Osteoporos. Int.* 23 (2012) 2239–2256. <https://doi.org/10.1007/s00198-012-1964-3>.

[30] G.A. Greendale, E. Barrett-Connor, S. Ingles, R. Haile, Late Physical and Functional Effects of Osteoporotic Fracture in Women: The Rancho Bernardo Study, *J. Am. Geriatr. Soc.* 43 (1995) 955–961. <https://doi.org/https://doi.org/10.1111/j.1532-5415.1995.tb05557.x>.

[31] NICEimpact, Falls and Fragility Fractures, *Natl. Inst. Heal. Care Excell.* (2018). <https://www.nice.org.uk/Media/Default/About/what-we-do/Into-practice/measuring-uptake/NICE-Impact-falls-and-fragility-fractures.pdf>.

[32] S. Angele, Living longer: how our population is changing and why it matters, *Off. Natl. Stat.* (2018) 1–53. <https://www.ons.gov.uk/peoplepopulationandcommunity/birthsdeathsandmarriages/ageing/articles/livinglongerhowourpopulationischangingandwhyitmatters/2018-08-13>.

[33] H. Blain, T. Masud, P. Dargent-Molina, F.C. Martin, E. Rosendahl, N. van der Velde, J. Bousquet, A. Benetos, C. Cooper, J.A. Kanis, J.Y. Reginster, R. Rizzoli, B. Cortet, M. Barbagallo, K.E. Dreinhöfer, B. Vellas, S. Maggi, T. Strandberg, A comprehensive fracture prevention strategy in older adults: the European Union Geriatric Medicine Society (EUGMS) statement, *Aging Clin. Exp. Res.* 28 (2016) 797–803. <https://doi.org/10.1007/s40520-016-0588-4>.

[34] M.B. Dobbs, J. Buckwalter, C. Saltzman, OSTEOPOROSIS: THE INCREASING ROLE OF THE ORTHOPAEDIST, *Iowa Orthop. J.* 19 (n.d.) 43–52.

[35] F. Mirza, E. Canalis, MANAGEMENT OF ENDOCRINE DISEASE: Secondary osteoporosis: pathophysiology and management, *Eur. J. Endocrinol.* 173 (2015) R131–R151. <https://doi.org/10.1530/eje-15-0118>.

[36] J.E. Compston, M.R. McClung, W.D. Leslie, Osteoporosis, *Lancet.* 393 (2019) 364–376. [https://doi.org/10.1016/S0140-6736\(18\)32112-3](https://doi.org/10.1016/S0140-6736(18)32112-3).

- [37] D.B. Burr, Chapter 1 - Bone Morphology and Organization, in: D.B. Burr, M.R.B.T.-B. and A.B.B. (Second E. Allen (Eds.), Academic Press, 2019: pp. 3–26. <https://doi.org/https://doi.org/10.1016/B978-0-12-813259-3.00001-4>.
- [38] L.I. Plotkin, A. Aguilar-Pérez, N. Bivi, Chapter 4 - Local Regulation of Bone Cell Function, in: D.B. Burr, M.R.B.T.-B. and A.B.B. (Second E. Allen (Eds.), Academic Press, 2019: pp. 57–84. <https://doi.org/https://doi.org/10.1016/B978-0-12-813259-3.00004-X>.
- [39] M.R. Allen, D.B. Burr, Chapter 5 - Bone Growth, Modeling, and Remodeling, in: D.B. Burr, M.R.B.T.-B. and A.B.B. (Second E. Allen (Eds.), Academic Press, 2019: pp. 85–100. <https://doi.org/https://doi.org/10.1016/B978-0-12-813259-3.00005-1>.
- [40] R.K. Fuchs, W.R. Thompson, S.J. Warden, 2 - Bone biology, in: K.M. Pawelec, J.A.B.T.-B.R.B. (Second E. Planell (Eds.), Woodhead Publ. Ser. Biomater., Woodhead Publishing, 2019: pp. 15–52. <https://doi.org/https://doi.org/10.1016/B978-0-08-102451-5.00002-0>.
- [41] E.F. Morgan, G.L. Barnes, T.A. Einhorn, Chapter 1 - The Bone Organ System: Form and Function, in: R. Marcus, D. Feldman, D.W. Dempster, M. Luckey, J.A. Cauley (Eds.), Osteoporos. (Fourth Ed., Fourth Edi, Academic Press, San Diego, 2013: pp. 3–20. <https://doi.org/https://doi.org/10.1016/B978-0-12-415853-5.00001-7>.
- [42] L. Karim, A.I. Hussein, E.F. Morgan, M.L. Bouxsein, Chapter 19 - The Mechanical Behavior of Bone, in: R. Marcus, D. Feldman, D.W. Dempster, M. Luckey, J.A. Cauley (Eds.), Osteoporos. (Fourth Ed., Fourth Edi, Academic Press, San Diego, 2013: pp. 431–452. <https://doi.org/https://doi.org/10.1016/B978-0-12-415853-5.00019-4>.
- [43] D.E. Anderson, A.G. Bruno, M.L. Bouxsein, Chapter 22 - Biomechanics of Hip and Vertebral Fractures, in: R. Marcus, D. Feldman, D.W. Dempster, M. Luckey, J.A. Cauley (Eds.), Osteoporos. (Fourth Ed., Fourth Edi, Academic Press, San Diego, 2013: pp. 497–516. <https://doi.org/https://doi.org/10.1016/B978-0-12-415853-5.00022-4>.
- [44] L.M. BIGA, S. DAWSON, A. HARWELL, R. HOPKINS, J. KAUFMANN, M. LEMASTER, P. MATERN, D.Q. KATIE MORRISON-GRAHAM, J. RUNYEON, *Anatomy & Physiology*, 2008. <https://doi.org/10.1177/089686080802801s03>.
- [45] S.M. Ott, Cortical or Trabecular Bone: What's the Difference?, *Am. J. Nephrol.* 47 (2018) 373–375. <https://doi.org/10.1159/000489672>.
- [46] E.F. Morgan, G.U. Unnikrisnan, A.I. Hussein, *Bone Mechanical Properties in Healthy and Diseased States*, (2018).
- [47] B. Langdahl, S. Ferrari, D.W. Dempster, Bone modeling and remodeling: potential as therapeutic targets for the treatment of osteoporosis, *Ther. Adv. Musculoskelet. Dis.* 8 (2016) 225–235. <https://doi.org/10.1177/1759720X16670154>.
- [48] M.R. Allen, D.B. Burr, Chapter 4 - Bone Modeling and Remodeling, in: D.B. Burr, M.R.B.T.-B. and A.B.B. Allen (Eds.), Academic Press, San Diego, 2014: pp. 75–90. <https://doi.org/https://doi.org/10.1016/B978-0-12-416015-6.00004-6>.
- [49] M.M. Manring, J.H. Calhoun, Biographical sketch: Fuller Albright, MD 1900-1969., *Clin. Orthop. Relat. Res.* 469 (2011) 2092–2095. <https://doi.org/10.1007/s11999-011-1831-0>.

- [50] J.A. Kanis, J.A. Kanis, Assessment of fracture risk and its application to screening for postmenopausal osteoporosis: Synopsis of a WHO report, *Osteoporos. Int.* 4 (1994) 368–381. <https://doi.org/10.1007/BF01622200>.
- [51] J. a Kanis, Assessment of osteoporosis at the primary health care level, *World Health.* (2007) 339. http://www.shef.ac.uk/FRAX/pdfs/WHO_Technical_Report.pdf.
- [52] B.E. Nilsson, O. Johnell, C. Petersson, In vivo bone-mineral measurement: How and why - A review, *Acta Orthop.* 61 (1990) 275–281. <https://doi.org/10.3109/17453679008993519>.
- [53] M. Singh, A.R. Nagrath, P.S. Maini, Changes in trabecular pattern of the upper end of the femur as an index of osteoporosis., *J. Bone Joint Surg. Am.* 52 (1970) 457–467. <https://doi.org/10.2106/00004623-197052030-00005>.
- [54] N.J. Wachter, P. Augat, I.P. Hoellen, G.D. Krischak, M.R. Sarkar, M. Mentzel, L. Kinzl, L. Claes, Predictive value of Singh index and bone mineral density measured by quantitative computed tomography in determining the local cancellous bone quality of the proximal femur, *Clin. Biomech.* 16 (2001) 257–262. [https://doi.org/10.1016/S0268-0033\(00\)00093-0](https://doi.org/10.1016/S0268-0033(00)00093-0).
- [55] J.R. Cameron, J. Sorenson, Measurement of bone mineral in vivo: an improved method., *Science* (80-.). 142 (1963) 230–232. <https://doi.org/10.1590/s0036-36342009000700016>.
- [56] T.L. Kelly, G. Crane, D.T. Baran, Single X-ray absorptiometry of the forearm: Precision, correlation, and reference data, *Calcif. Tissue Int.* 54 (1994) 212–218. <https://doi.org/10.1007/BF00301681>.
- [57] W.L. Dunn, H.W. Wahner, B.L. Riggs, Measurement of Bone Mineral Content in Human Vertebrae and Hip by Dual Photon Absorptiometry, *Radiology.* 136 (1980) 485–487.
- [58] J.E. Adams, Single and dual energy X-ray absorptiometry, *Eur. Radiol.* 7 (1997) 20–31. <https://doi.org/10.1007/pl00006861>.
- [59] B.O. Roos, H. Sköldbörn, Dual photon absorptiometry in lumbar vertebrae: I. Theory and method, *Acta Oncol. (Madr).* 13 (1974) 266–280. <https://doi.org/10.3109/02841867409129883>.
- [60] R. Lorente-Ramos, J. Azpeitia-Armán, A. Muñoz-Hernández, J.M. García-Gómez, P. Díez-Martínez, M. Grande-Báñez, Dual-energy x-ray absorptiometry in the diagnosis of osteoporosis: A practical guide, *Am. J. Roentgenol.* 196 (2011) 897–904. <https://doi.org/10.2214/AJR.10.5416>.
- [61] J.A. Kanis, Diagnosis of Osteoporosis and Assessment of Fracture Risk, *Lancet.* 359 (2002) 1929–1936. https://doi.org/10.5005/jp/books/12535_91.
- [62] K. Engelke, C. Libanati, T. Fuerst, P. Zysset, H.K. Genant, Advanced CT based In Vivo Methods for the Assessment of Bone Density , Structure , and Strength , (2013) 246–255. <https://doi.org/10.1007/s11914-013-0147-2>.
- [63] A. El Maghraoui, C. Roux, DXA scanning in clinical practice, *Qjm.* 101 (2008) 605–617.

<https://doi.org/10.1093/qjmed/hcn022>.

[64] C.R. Wilson, I. Fogelmanb, G.M. Blakeb, A. Rodinb, The effect of positioning on dual energy X-ray bone densitometry of the proximal femur, *Bone Miner.* 13 (1991) 69–76.

[65] J.E. Adams, Quantitative computed tomography, *Eur. J. Radiol.* 71 (2009) 415–424. <https://doi.org/10.1016/j.ejrad.2009.04.074>.

[66] K. Engelke, T. Lang, S. Khosla, L. Qin, P. Zysset, W.D. Leslie, J.A. Shepherd, J.T. Shousboe, Clinical Use of Quantitative Computed Tomography-Based Advanced Techniques in the Management of Osteoporosis in Adults: The 2015 ISCD Official Positions-Part III, *J. Clin. Densitom.* 18 (2015) 393–407. <https://doi.org/10.1016/j.jocd.2015.06.010>.

[67] W.A. Kalender, D. Felsenberg, H.K. Genant, M. Fischer, J. Dequeker, J. Reeve, The European Spine Phantom - a tool for standardization and quality control in spinal bone mineral measurements by DXA and QCT, *Eur. J. Radiol.* 20 (1995) 83–92. [https://doi.org/10.1016/0720-048X\(95\)00631-Y](https://doi.org/10.1016/0720-048X(95)00631-Y).

[68] S. Bonaretti, R.D. Carpenter, I. Saeed, A.J. Burghardt, L. Yu, M. Bruesewitz, S. Khosla, T. Lang, Novel anthropomorphic hip phantom corrects systemic interscanner differences in proximal femoral vBMD, *Phys. Med. Biol.* 59 (2014) 7819–7834. <https://doi.org/10.1088/0031-9155/59/24/7819>.

[69] K. Uemura, Y. Otake, M. Takao, M. Soufi, A. Kawasaki, N. Sugano, Y. Sato, Automated segmentation of an intensity calibration phantom in clinical CT images using a convolutional neural network, *Int. J. Comput. Assist. Radiol. Surg.* (2021). <https://doi.org/10.1007/s11548-021-02345-w>.

[70] European Spine Phantom, A PTW Co. (n.d.) 0–1.

[71] K.G. Faulkner, E. von Stetten, P. Miller, Discordance in Patient Classification Using T-Scores, *J. Clin. Densitom.* 2 (1999) 343–350. <https://doi.org/https://doi.org/10.1385/JCD:2:3:343>.

[72] C.E. Cann, J.E. Adams, J.K. Brown, A.D. Brett, CTXA hip - An extension of classical DXA measurements using Quantitative CT, *PLoS One.* 9 (2014). <https://doi.org/10.1371/journal.pone.0091904>.

[73] F. Johannesdottir, E. Thrall, J. Muller, T.M. Keaveny, D.L. Kopperdahl, M.L. Bouxsein, Comparison of non-invasive assessments of strength of the proximal femur, *Bone.* 105 (2017) 93–102. <https://doi.org/10.1016/j.bone.2017.07.023>.

[74] S.R. Cummings, D. Bates, D.M. Black, Clinical Use of Bone DensitometryScientific Review, *JAMA.* 288 (2002) 1889–1897. <https://doi.org/10.1001/jama.288.15.1889>.

[75] A. Sheu, T. Diamond, Bone mineral density : testing for osteoporosis, *Aust. Prescr.* 39 (2016) 35–39.

[76] J.A. Kanis, E. V. McCloskey, K.S. Eyres, D. V. O’Doherty, J. Aaron, Screening Techniques in the Evaluation of Osteoporosis, *HRT Osteoporos.* (1990) 135–147. https://doi.org/10.1007/978-1-4471-1799-5_12.

- [77] E. McCloskey, J. Rathi, S. Heijmans, M. Blagden, B. Cortet, E. Czerwinski, P. Hadji, J. Payer, K. Palmer, R. Stad, J. O’Kelly, S. Papapoulos, The osteoporosis treatment gap in patients at risk of fracture in European primary care: a multi-country cross-sectional observational study, *Osteoporos. Int.* 32 (2021) 251–259. <https://doi.org/10.1007/s00198-020-05557-z>.
- [78] O. Ström, F. Borgström, J.A. Kanis, J. Compston, C. Cooper, E. V. McCloskey, B. Jönsson, Osteoporosis: burden, health care provision and opportunities in the EU, *Arch Osteoporos.* 6 (2011) 59–155.
- [79] A. Díez-Pérez, F.H. Hooven, J.D. Adachi, S. Adami, F.A. Anderson, S. Boonen, R. Chapurlat, J.E. Compston, C. Cooper, P. Delmas, S.L. Greenspan, A.Z. LaCroix, R. Lindsay, J.C. Netelenbos, J. Pfeilschifter, C. Roux, K.G. Saag, P. Sambrook, S. Silverman, E.S. Siris, N.B. Watts, G. Nika, S.H. Gehlbach, Regional differences in treatment for osteoporosis. The Global Longitudinal Study of Osteoporosis in Women (GLOW), *Bone.* 49 (2011) 493–498. <https://doi.org/10.1016/j.bone.2011.05.007>.
- [80] E. Hernlund, A. Svedbom, M. Ivergård, J. Compston, C. Cooper, J. Stenmark, E. V. McCloskey, B. Jönsson, J.A. Kanis, Osteoporosis in the European Union: Medical management, epidemiology and economic burden: A report prepared in collaboration with the International Osteoporosis Foundation (IOF) and the European Federation of Pharmaceutical Industry Associations (EFPIA), *Arch. Osteoporos.* 8 (2013). <https://doi.org/10.1007/s11657-013-0136-1>.
- [81] M.A. Clynes, N.C. Harvey, E.M. Curtis, N.R. Fuggle, M. Elaine, C. Cooper, Europe PMC Funders Group The Epidemiology of Osteoporosis, 133 (2020) 105–117. <https://doi.org/10.1093/bmb/ldaa005>.The.
- [82] S.A. Wainwright, L.M. Marshall, K.E. Ensrud, J.A. Cauley, D.M. Black, T.A. Hillier, M.C. Hochberg, M.T. Vogt, E.S. Orwoll, Hip fracture in women without osteoporosis, *J. Clin. Endocrinol. Metab.* 90 (2005) 2787–2793. <https://doi.org/10.1210/jc.2004-1568>.
- [83] J.A. Pasco, E. Seeman, M.J. Henry, E.N. Merriman, G.C. Nicholson, M.A. Kotowicz, The population burden of fractures originates in women with osteopenia, not osteoporosis, *Osteoporos. Int.* 17 (2006) 1404–1409. <https://doi.org/10.1007/s00198-006-0135-9>.
- [84] A. Cranney, S.A. Jamal, J.F. Tsang, R.G. Josse, W.D. Leslie, Low bone mineral density and fracture burden in postmenopausal women, *Cmaj.* 177 (2007) 575–580. <https://doi.org/10.1503/cmaj.070234>.
- [85] L. Langsetmo, D. Goltzman, C. Kovacs, J.D. Adachi, D.A. Hanley, N. Kreiger, R. Josse, A. Papaioannou, W.P. Olszynski, S.A. Jamal, A. Tenenhouse, S. Poliquin, S. Godmaire, C. Berger, C. Joyce, E. Sheppard, S. Kirkland, S. Kaiser, B. Stanfield, J.P. Brown, L. Bessette, M. Gendreau, T. Anastassiades, T. Towheed, B. Matthews, B. Josse, T. Murray, B. Gardner-Bray, L. Pickard, K.S. Davison, J. Thingvold, J. Allan, J.C. Prior, Y. Vigna, B.C. Lentle, Repeat low-trauma fractures occur frequently among men and women who have osteopenic BMD, *J. Bone Miner. Res.* 24 (2009) 1515–1522. <https://doi.org/10.1359/jbmr.090319>.
- [86] S. Roux, F. Cabana, N. Carrier, M. Beaulieu, P.M. April, M.C. Beaulieu, G. Boire, The World Health Organization Fracture Risk Assessment Tool (FRAX) underestimates incident and recurrent fractures in consecutive patients with fragility fractures, *J. Clin. Endocrinol.*

Metab. 99 (2014) 2400–2408. <https://doi.org/10.1210/jc.2013-4507>.

[87] J.A. Kanis, H. Johansson, N.C. Harvey, E. V. McCloskey, A brief history of FRAX, Arch. Osteoporos. 13 (2018). <https://doi.org/10.1007/s11657-018-0510-0>.

[88] J.A. Kanis, FRAX, <https://www.sheffield.ac.uk/frax/index.aspx>. (n.d.).

[89] F. Cosman, S.J. de Beur, M.S. LeBoff, E.M. Lewiecki, B. Tanner, S. Randall, R. Lindsay, Clinician's Guide to Prevention and Treatment of Osteoporosis, Osteoporos. Int. 25 (2014) 2359–2381. <https://doi.org/10.1007/s00198-014-2794-2>.

[90] E.S. Siris, S. Baim, A. Nattiv, Primary care use of FRAX®: Absolute fracture risk assessment in postmenopausal women and older men, Postgrad. Med. 122 (2010) 82–90. <https://doi.org/10.3810/pgm.2010.01.2102>.

[91] J.A. Kanis, E. V. McCloskey, N.C. Harvey, H. Johansson, W.D. Leslie, Intervention thresholds and the diagnosis of osteoporosis, J. Bone Miner. Res. 30 (2015) 1747–1753. <https://doi.org/10.1002/jbmr.2531>.

[92] J. Compston, FRAX - Where are we now?, Maturitas. 82 (2015) 284–287. <https://doi.org/10.1016/j.maturitas.2015.07.024>.

[93] T. Masud, N. Binkley, S. Boonen, M.T. Hannan, Official Positions for FRAX® Clinical Regarding Falls and Frailty: Can Falls and Frailty be Used in FRAX®?: From Joint Official Positions Development Conference of the International Society for Clinical Densitometry and International Osteoporosis Foundati, J. Clin. Densitom. 14 (2011) 194–204. <https://doi.org/https://doi.org/10.1016/j.jocd.2011.05.010>.

[94] E. Benca, A. Synek, M. Amini, F. Kainberger, L. Hirtler, R. Windhager, W. Mayr, D.H. Pahr, QCT-based finite element prediction of pathologic fractures in proximal femora with metastatic lesions, Sci. Rep. 9 (2019) 1–9. <https://doi.org/10.1038/s41598-019-46739-y>.

[95] K.M. DeGoede, J.A. Ashton-Miller, A.B. Schultz, Fall-related upper body injuries in the older adult: A review of the biomechanical issues, J. Biomech. 36 (2003) 1043–1053. [https://doi.org/10.1016/S0021-9290\(03\)00034-4](https://doi.org/10.1016/S0021-9290(03)00034-4).

[96] NICE, NICE clinical guideline 161. Falls: Assessment and prevention of falls in older people, Natl. Inst. Heal. Care Excell. 161 (2013) 1–315. www.nice.org.uk/guidance/CG161.

[97] K.H. Yang, K.L. Shen, C.K. Demetropoulos, A.I. King, P. Kolodziej, R.S. Levine, R.H. Fitzgerald, The relationship between loading conditions and fracture patterns of the proximal femur, J. Biomech. Eng. 118 (1996) 575–578. <https://doi.org/10.1115/1.2796045>.

[98] S.L. Greenspan, E.R. Myers, D.P. Kiel, R.A. Parker, W.C. Hayes, N.M. Resnick, Fall direction, bone mineral density, and function: Risk factors for hip fracture in frail nursing home elderly, Am. J. Med. 104 (1998) 539–545. [https://doi.org/10.1016/S0002-9343\(98\)00115-6](https://doi.org/10.1016/S0002-9343(98)00115-6).

[99] S.L. Greenspan, E.R. Myers, L.A. Maitland, N.M. Resnick, W.C. Hayes, Fall Severity and Bone Mineral Density as Risk Factors for Hip Fracture in Ambulatory Elderly, JAMA. 271 (1994) 128–133. <https://doi.org/10.1001/jama.1994.03510260060029>.

- [100] M. Taylor, M. Viceconti, P. Bhattacharya, X. Li, Finite element analysis informed variable selection for femoral fracture risk prediction, *J. Mech. Behav. Biomed. Mater.* 118 (2021) 104434. <https://doi.org/10.1016/j.jmbbm.2021.104434>.
- [101] A. Fritsch, C.H. Å, ' Universal ' microstructural patterns in cortical and trabecular , extracellular and extravascular bone materials: Micromechanics-based prediction of anisotropic elasticity, 244 (2007) 597–620. <https://doi.org/10.1016/j.jtbi.2006.09.013>.
- [102] J.H. Keyak, S.A. Rossi, K.A. Jones, H.B. Skinner, Prediction of femoral fracture load using automated finite element modeling, *J. Biomech.* 31 (1997) 125–133. [https://doi.org/10.1016/S0021-9290\(97\)00123-1](https://doi.org/10.1016/S0021-9290(97)00123-1).
- [103] P. Zioupos, R.B. Cook, J.R. Hutchinson, Some basic relationships between density values in cancellous and cortical bone, 41 (2008) 1961–1968. <https://doi.org/10.1016/j.jbiomech.2008.03.025>.
- [104] E. Schileo, E. Dall'Ara, F. Taddei, A. Malandrino, T. Schotkamp, M. Baleani, M. Viceconti, An accurate estimation of bone density improves the accuracy of subject-specific finite element models, *J. Biomech.* 41 (2008) 2483–2491. <https://doi.org/10.1016/j.jbiomech.2008.05.017>.
- [105] T.S. Kaneko, M.R. Pejcic, J. Tehranzadeh, J.H. Keyak, Relationships between material properties and CT scan data of cortical bone with and without metastatic lesions, *Med. Eng. Phys.* 25 (2003) 445–454. [https://doi.org/10.1016/S1350-4533\(03\)00030-4](https://doi.org/10.1016/S1350-4533(03)00030-4).
- [106] J.H. Keyak, I.Y. Lee, H.B. Skinner, Correlations between orthogonal mechanical properties and density of trabecular bone: Use of different densitometric measures, *J. Biomed. Mater. Res.* 28 (1994) 1329–1336. <https://doi.org/https://doi.org/10.1002/jbm.820281111>.
- [107] T.S. Kaneko, J.S. Bell, M.R. Pejcic, J. Tehranzadeh, J.H. Keyak, Mechanical properties, density and quantitative CT scan data of trabecular bone with and without metastases, *J. Biomech.* 37 (2004) 523–530. <https://doi.org/10.1016/j.jbiomech.2003.08.010>.
- [108] D.R. Carter, W.C. Hayes, The compressive behavior of bone as a two-phase porous structure., *J. Bone Joint Surg. Am.* 59 (1977) 954–962.
- [109] J.C. Lotz, T.N. Gerhart, W.C. Hayes, Mechanical Properties of Trabecular Bone from the Proximal Femur: A Quantitative CT Study, *J. Comput. Assist. Tomogr.* 14 (1990). https://journals.lww.com/jcat/Fulltext/1990/01000/Mechanical_Properties_of_Trabecular_Bone_from_the.20.aspx.
- [110] E.F. Morgan, H.H. Bayraktar, T.M. Keaveny, Trabecular bone modulus-density relationships depend on anatomic site, *J. Biomech.* 36 (2003) 897–904. [https://doi.org/10.1016/S0021-9290\(03\)00071-X](https://doi.org/10.1016/S0021-9290(03)00071-X).
- [111] T.S. Keller, Predicting the compressive mechanical behavior of bone, *J. Biomech.* 27 (1994) 1159–1168. [https://doi.org/10.1016/0021-9290\(94\)90056-6](https://doi.org/10.1016/0021-9290(94)90056-6).
- [112] P. Ducheyne, L. Heymans, M. Martens, E. Aernoudt, P. de Meester, J.C. Mulier, The mechanical behaviour of intracondylar cancellous bone of the femur at different loading

rates, *J. Biomech.* 10 (1977) 747–762. [https://doi.org/10.1016/0021-9290\(77\)90089-6](https://doi.org/10.1016/0021-9290(77)90089-6).

[113] M. Martens, R. Van Audekercke, P. Delpont, P. De Meester, J.C. Mulier, The mechanical characteristics of cancellous bone at the upper femoral region, *J. Biomech.* 16 (1983) 971–983. [https://doi.org/10.1016/0021-9290\(83\)90098-2](https://doi.org/10.1016/0021-9290(83)90098-2).

[114] R. Oftadeh, M. Perez-Viloria, J.C. Villa-Camacho, A. Vaziri, A. Nazarian, Biomechanics and Mechanobiology of Trabecular Bone: A Review, *J. Biomech. Eng.* 137 (2015) 1–15. <https://doi.org/10.1115/1.4029176>.

[115] E. Schileo, F. Taddei, A. Malandrino, L. Cristofolini, M. Viceconti, Subject-specific finite element models can accurately predict strain levels in long bones, *J. Biomech.* 40 (2007) 2982–2989. <https://doi.org/10.1016/j.jbiomech.2007.02.010>.

[116] J.C. Rice, S.C. Cowin, J.A. Bowman, On the dependence of the elasticity and strength of cancellous bone on apparent density, *J. Biomech.* 21 (1988) 155–168. [https://doi.org/10.1016/0021-9290\(88\)90008-5](https://doi.org/10.1016/0021-9290(88)90008-5).

[117] M.B. Schaffler, D.B. Burr, Stiffness of compact bone: Effects of porosity and density, *J. Biomech.* 21 (1988) 13–16. [https://doi.org/10.1016/0021-9290\(88\)90186-8](https://doi.org/10.1016/0021-9290(88)90186-8).

[118] B. Helgason, E. Perilli, E. Schileo, F. Taddei, S. Brynjólfsson, M. Viceconti, Mathematical relationships between bone density and mechanical properties: A literature review, *Clin. Biomech.* 23 (2008) 135–146. <https://doi.org/10.1016/j.clinbiomech.2007.08.024>.

[119] E.F. Morgan, G.U. Unnikrisnan, A.I. Hussein, Bone Mechanical Properties in Healthy and Diseased States, *Annu. Rev. Biomed. Eng.* 20 (2018) 119–143. <https://doi.org/10.1146/annurev-bioeng-062117-121139>.

[120] Koivumäki2012b_cortical FE v.s. experiment.pdf, (n.d.).

[121] I.T. Haider, A.D. Speirs, H. Frei, Effect of boundary conditions, impact loading and hydraulic stiffening on femoral fracture strength, *J. Biomech.* 46 (2013) 2115–2121. <https://doi.org/10.1016/j.jbiomech.2013.07.004>.

[122] H.S. Hosseini, D.H. Pahr, P.K. Zysset, Modeling and experimental validation of trabecular bone damage, softening and densification under large compressive strains, *J. Mech. Behav. Biomed. Mater.* 15 (2012) 93–102. <https://doi.org/10.1016/j.jmbbm.2012.06.005>.

[123] J.J. Schwiedrzik, P.K. Zysset, An anisotropic elastic-viscoplastic damage model for bone tissue, *Biomech. Model. Mechanobiol.* 12 (2013) 201–213. <https://doi.org/10.1007/s10237-012-0392-9>.

[124] R. Hambli, S. Frikha, H. Toumi, J.M.R.S. Tavares, Finite element prediction of fatigue damage growth in cancellous bone, *Comput. Methods Biomech. Biomed. Engin.* 19 (2016) 563–570. <https://doi.org/10.1080/10255842.2015.1048687>.

[125] P. K Basu, A. G Beall, D. J Simmons, M. Vannier, 3-D Femoral Stress Analysis Using Ct Scans and P-Version Fem, 1985. <https://doi.org/10.3109/10731198509118849>.

[126] D. Dragomir-Daescu, C. Salas, S. Uthamaraj, T. Rossman, Quantitative computed

tomography-based finite element analysis predictions of femoral strength and stiffness depend on computed tomography settings, *J. Biomech.* 48 (2015) 153–161. <https://doi.org/10.1016/j.jbiomech.2014.09.016>.

[127] M.B. Afifi, A. Abdelrazek, N.A. Deiab, A.I. Abd El-Hafez, A.H. El-Farrash, The effects of CT x-ray tube voltage and current variations on the relative electron density (RED) and CT number conversion curves, *J. Radiat. Res. Appl. Sci.* 13 (2020) 1–11. <https://doi.org/10.1080/16878507.2019.1693176>.

[128] R. Lattanzi, F. Baruffaldi, C. Zannoni, M. Viceconti, Specialised CT scan protocols for 3-D pre-operative planning of total hip replacement, *Med. Eng. Phys.* 26 (2004) 237–245. <https://doi.org/10.1016/j.medengphy.2003.11.008>.

[129] C. Zannoni, R. Mantovani, M. Viceconti, Material properties assignment to finite element models of bone structures: A new method, *Med. Eng. Phys.* 20 (1999) 735–740. [https://doi.org/10.1016/S1350-4533\(98\)00081-2](https://doi.org/10.1016/S1350-4533(98)00081-2).

[130] L. Grassi, N. Hraiech, E. Schileo, M. Ansaloni, M. Rochette, M. Viceconti, Evaluation of the generality and accuracy of a new mesh morphing procedure for the human femur, *Med. Eng. Phys.* 33 (2011) 112–120. <https://doi.org/10.1016/j.medengphy.2010.09.014>.

[131] M. Qasim, G. Farinella, J. Zhang, X. Li, L. Yang, R. Eastell, M. Viceconti, Patient-specific finite element estimated femur strength as a predictor of the risk of hip fracture: the effect of methodological determinants, *Osteoporos. Int.* 27 (2016) 2815–2822. <https://doi.org/10.1007/s00198-016-3597-4>.

[132] M. Bessho, I. Ohnishi, H. Okazaki, W. Sato, H. Kominami, S. Matsunaga, K. Nakamura, Prediction of the strength and fracture location of the femoral neck by CT-based finite-element method: a preliminary study on patients with hip fracture, *J. Orthop. Sci.* 9 (2004) 545–550. <https://doi.org/https://doi.org/10.1007/s00776-004-0824-1>.

[133] E. Dall’Ara, B. Luisier, R. Schmidt, M. Pretterklieber, F. Kainberger, P. Zysset, D. Pahr, DXA predictions of human femoral mechanical properties depend on the load configuration, *Med. Eng. Phys.* 35 (2013) 1564–1572. <https://doi.org/10.1016/j.medengphy.2013.04.008>.

[134] R. Hambli, E. Lespessailles, C.L. Benhamou, Integrated remodeling-to-fracture finite element model of human proximal femur behavior, *J. Mech. Behav. Biomed. Mater.* 17 (2013) 89–106. <https://doi.org/10.1016/j.jmbbm.2012.08.011>.

[135] K.K. Nishiyama, S. Gilchrist, P. Guy, P. Crompton, S.K. Boyd, Proximal femur bone strength estimated by a computationally fast finite element analysis in a sideways fall configuration, *J. Biomech.* 46 (2013) 1231–1236. <https://doi.org/10.1016/j.jbiomech.2013.02.025>.

[136] O. Ariza, S. Gilchrist, R.P. Widmer, P. Guy, S.J. Ferguson, P. a Crompton, B. Helgason, Comparison of explicit finite element and mechanical simulation of the proximal femur during dynamic drop-tower testing, *J. Biomech.* 48 (2015) 224–232. <https://doi.org/10.1016/j.jbiomech.2014.11.042>.

[137] T. Rossman, V. Kushvaha, D. Dragomir-Daescu, QCT/FEA predictions of femoral stiffness are strongly affected by boundary condition modeling, *Comput. Methods Biomech. Biomed. Engin.* 19 (2016) 208–216. <https://doi.org/10.1080/10255842.2015.1006209>.

- [138] J.E.M. Koivumäki, J. Thevenot, P. Pulkkinen, V. Kuhn, T.M. Link, F. Eckstein, T. Jämsä, Ct-based finite element models can be used to estimate experimentally measured failure loads in the proximal femur, *Bone*. 50 (2012) 824–829. <https://doi.org/10.1016/j.bone.2012.01.012>.
- [139] R. Hambli, C.L. Benhamou, R. Jennane, E. Lespessailles, W. Skalli, S. Laporte, J.D. Laredo, V. Bousson, J. Zarka, Combined finite element model of human proximal femur behaviour considering remodeling and fracture, *Irbm*. 34 (2013) 191–195. <https://doi.org/10.1016/j.irbm.2013.01.011>.
- [140] D. Dragomir-Daescu, J. Op Den Buijs, S. McEligot, Y. Dai, R.C. Entwistle, C. Salas, L.J. Melton, K.E. Bennet, S. Khosla, S. Amin, Robust QCT/FEA models of proximal femur stiffness and fracture load during a sideways fall on the hip, *Ann. Biomed. Eng.* 39 (2011) 742–755. <https://doi.org/10.1007/s10439-010-0196-y>.
- [141] Z. Altai, M. Qasim, X. Li, M. Viceconti, The effect of boundary and loading conditions on patient classification using finite element predicted risk of fracture, *Clin. Biomech.* 68 (2019) 137–143. <https://doi.org/10.1016/j.clinbiomech.2019.06.004>.
- [142] M.S. Division, L. Berkeley, R.D. Sciences, S. Francisco, MECHANISTIC FRACTURE CRITERIA FOR THE Mechanistic Fracture Criteria for the Failure of Human, (2002).
- [143] H.H. Bayraktar, E.F. Morgan, G.L. Niebur, G.E. Morris, E.K. Wong, T.M. Keaveny, Comparison of the elastic and yield properties of human femoral trabecular and cortical bone tissue, *J. Biomech.* 37 (2004) 27–35. [https://doi.org/10.1016/S0021-9290\(03\)00257-4](https://doi.org/10.1016/S0021-9290(03)00257-4).
- [144] H.H. Bayraktar, A. Gupta, R.Y. Kwon, P. Papadopoulos, T.M. Keaveny, The Modified Super-Ellipsoid Yield Criterion for Human Trabecular Bone, *J. Biomech. Eng.* 126 (2005) 677–684. <https://doi.org/10.1115/1.1763177>.
- [145] J. Lotz, S. Francisco, Fracture Prediction for the Proximal Femur Using Finite Element Models : Part I-Linear Analysis, (1991).
- [146] T. Ota, I. Yamamoto, R. Morita, Fracture simulation of the femoral bone using the finite-element method: How a fracture initiates and proceeds, *J. Bone Miner. Metab.* 17 (1999) 108–112. <https://doi.org/10.1007/s007740050072>.
- [147] J.H. Keyak, T.S. Kaneko, J. Tehranzadeh, H.B. Skinner, Predicting Proximal Femoral Strength Using Structural Engineering Models, (2005) 219–228. <https://doi.org/10.1097/01.blo.0000164400.37905.22>.
- [148] J.H. Keyak, S.A. Rossi, Prediction of femoral fracture load using finite element models: An examination of stress- and strain-based failure theories, *J. Biomech.* 33 (2000) 209–214. [https://doi.org/10.1016/S0021-9290\(99\)00152-9](https://doi.org/10.1016/S0021-9290(99)00152-9).
- [149] E. Schileo, F. Taddei, L. Cristofolini, M. Viceconti, Subject-specific finite element models implementing a maximum principal strain criterion are able to estimate failure risk and fracture location on human femurs tested in vitro, *J. Biomech.* 41 (2008) 356–367. <https://doi.org/10.1016/j.jbiomech.2007.09.009>.
- [150] W.A. Kalender, A phantom for standarization and quality control in spinal bone

mineral measurements by QCT and DXA: Design considerations and specifications, *Med. Phys.* 19 (1992) 583–586. <https://doi.org/https://doi.org/10.1118/1.596899>.

[151] F. Taddei, E. Schileo, B. Helgason, L. Cristofolini, M. Viceconti, The material mapping strategy influences the accuracy of CT-based finite element models of bones: An evaluation against experimental measurements, *Med. Eng. Phys.* 29 (2007) 973–979. <https://doi.org/10.1016/j.medengphy.2006.10.014>.

[152] M. Viceconti, M. Davinelli, F. Taddei, A. Cappello, Automatic generation of accurate subject-specific bone finite element models to be used in clinical studies, *J. Biomech.* 37 (2004) 1597–1605. <https://doi.org/10.1016/j.jbiomech.2003.12.030>.

[153] R.W. GOULET, S.A. Goldstein, M.J. CIARELLI, J.L. KUHN, M.B.Br. L., L.A. FELDKAMP, THE RELATIONSHIP BETWEEN THE STRUCTURAL AND ORTHOGONAL COMPRESSIVE PROPERTIES OF, *J. Biomech.* 27 (1994) 375–389.

[154] D.C. Wirtz, N. Schiffers, R. Forst, T. Pandorf, D. Weichert, K. Radermacher, Critical evaluation of known bone material properties to realize anisotropic FE-simulation of the proximal femur, *J. Biomech.* 33 (2000) 1325–1330. [https://doi.org/10.1016/S0021-9290\(00\)00069-5](https://doi.org/10.1016/S0021-9290(00)00069-5).

[155] W. Black, Letter to the editor, *Altern. Med. Rev.* 7 (2002) 451–453.

[156] M. Bessho, I. Ohnishi, T. Matsumoto, S. Ohashi, J. Matsuyama, K. Tobita, M. Kaneko, K. Nakamura, Prediction of proximal femur strength using a CT-based nonlinear finite element method: Differences in predicted fracture load and site with changing load and boundary conditions, *Bone.* 45 (2009) 226–231. <https://doi.org/10.1016/j.bone.2009.04.241>.

[157] K.K. Nishiyama, M. Ito, A. Harada, S.K. Boyd, Classification of women with and without hip fracture based on quantitative computed tomography and finite element analysis, *Osteoporos. Int.* 25 (2014) 619–626. <https://doi.org/10.1007/s00198-013-2459-6>.

[158] C. Falcinelli, E. Schileo, L. Balistreri, F. Baruffaldi, B. Bordini, M. Viceconti, U. Albinini, F. Ceccarelli, L. Milandri, A. Toni, F. Taddei, Multiple loading conditions analysis can improve the association between finite element bone strength estimates and proximal femur fractures: A preliminary study in elderly women, *Bone.* 67 (2014) 71–80. <https://doi.org/10.1016/j.bone.2014.06.038>.

[159] T.M. Keaveny, B.L. Clarke, F. Cosman, E.S. Orwoll, E.S. Siris, S. Khosla, M.L. Bouxsein, Biomechanical Computed Tomography analysis (BCT) for clinical assessment of osteoporosis, *Osteoporos. Int.* 31 (2020) 1025–1048. <https://doi.org/10.1007/s00198-020-05384-2>.

[160] N.M. Appelman-Dijkstra, S.E. Papapoulos, Prevention of incident fractures in patients with prevalent fragility fractures: Current and future approaches, *Best Pract. Res. Clin. Rheumatol.* 27 (2013) 805–820. <https://doi.org/10.1016/j.berh.2014.01.010>.

[161] A. Mithal, J.P. Bonjour, S. Boonen, P. Burckhardt, H. Degens, G. El Hajj Fuleihan, R. Josse, P. Lips, J. Morales Torres, R. Rizzoli, N. Yoshimura, D.A. Wahl, C. Cooper, B. Dawson-Hughes, Impact of nutrition on muscle mass, strength, and performance in older adults, *Osteoporos. Int.* 24 (2013) 1555–1566. <https://doi.org/10.1007/s00198-012-2236-y>.

- [162] L. Mosekilde, O. Tørring, L. Rejnmark, Emerging anabolic treatments in osteoporosis., *Curr. Drug Saf.* 6 (2011) 62–74. <https://doi.org/10.2174/157488611795684712>.
- [163] D.L. Kendler, F. Marin, C.A.F. Zerbin, L.A. Russo, S.L. Greenspan, V. Zikan, A. Bagur, J. Malouf-Sierra, P. Lakatos, A. Fahrleitner-Pammer, E. Lespessailles, S. Minisola, J.J. Body, P. Geusens, R. Möricke, P. López-Romero, Effects of teriparatide and risedronate on new fractures in post-menopausal women with severe osteoporosis (VERO): a multicentre, double-blind, double-dummy, randomised controlled trial, *Lancet.* 391 (2018) 230–240. [https://doi.org/10.1016/S0140-6736\(17\)32137-2](https://doi.org/10.1016/S0140-6736(17)32137-2).
- [164] S.R. Cummings, J.S. Martin, M.R. McClung, E.S. Siris, R. Eastell, I.R. Reid, P. Delmas, H.B. Zoog, M. Austin, A. Wang, S. Kutilek, S. Adami, J. Zanchetta, C. Libanati, S. Siddhanti, C. Christiansen, Denosumab for prevention of fractures in postmenopausal women with osteoporosis, *Obstet. Gynecol. Surv.* 64 (2009) 805–807. <https://doi.org/10.1097/01.ogx.0000363236.41902.96>.
- [165] A.B. Hodsman, D.A. Hanley, R. Josse, Do bisphosphonates reduce the risk of osteoporotic fractures? An evaluation of the evidence to date, *Can. Med. Assoc. J.* 166 (2002) 1426–1430.
- [166] R. Recker, D. Dempster, B. Langdahl, H. Giezek, S. Clark, G. Ellis, T. de Villiers, I. Valter, C.A.F. Zerbin, D. Cohn, A. Santora, L.T. Duong, Effects of Odanacatib on Bone Structure and Quality in Postmenopausal Women With Osteoporosis: 5-Year Data From the Phase 3 Long-Term Odanacatib Fracture Trial (LOFT) and its Extension, *J. Bone Miner. Res.* 35 (2020) 1289–1299. <https://doi.org/10.1002/jbmr.3994>.
- [167] M.R. McClung, M.L. O’Donoghue, S.E. Papapoulos, H. Bone, B. Langdahl, K.G. Saag, I.R. Reid, D.P. Kiel, I. Cavallari, M.P. Bonaca, S.D. Wiviott, T. de Villiers, X. Ling, K. Lippuner, T. Nakamura, J.-Y. Reginster, J.A. Rodriguez-Portales, C. Roux, J. Zanchetta, C.A.F. Zerbin, J.-G. Park, K. Im, A. Cange, L.T. Grip, N. Heyden, C. DaSilva, D. Cohn, R. Massaad, B.B. Scott, N. Verbruggen, D. Gurner, D.L. Miller, M.L. Blair, A.B. Polis, S.A. Stoch, A. Santora, A. Lombardi, A.T. Leung, K.D. Kaufman, M.S. Sabatine, C.A. Mautalén, Z. Man, J.R. Zanchetta, C.H. Magaril, P. Sambrook, J.-Y. Reginster, P. Geusens, S. Goemaere, B.H. Albergaria, C.A. de F. Zerbin, M.L. Castro, L.H. Gregorio, R. Stoilov, A.-M.I. Borissova, K.H. Hristozov, N.L. Temelkova, I.K. Daskalova, S.I. Kuzmanova, D. Yaneva-Bichovska, A.Z. Batalov, P. Riedemann, J.A. Rodriguez Portales, H. Tang, Hanmin Zhu, Z. Zhang, A. Chao, Y. Hu, Z. Liu, J. Lu, M. Qiu, X. Gao, S. Zhang, L. Xu, W. Xia, E. Liao, W. Yang, W. Wu, K. Dai, R. Hu, H. Tang, J.J. Jaller, F. Cabal, J.F. Molina, C.A. Cure Cure, H. Yupanqui-Lozno, P. Chalem, J. Londono, M. Abello, E.D. Tobias, W. Otero, T. Nikolic, B. Miskic, J. Stepan, V. Vyskocil, L. Novosad, J. Slesinger, P. Novosad, E. Vlckova, L. Bortlik, E. Dokoupilova, T. Hala, J.-E.B. Jensen, K.T. Brixen, B.L. Langdahl, P. Schwarz, P.C. Eskildsen, P.A. Eiken, A.P. Hermann, J. Gram, M.B. Schou, P. Alexandersen, B. Nedergaard, D.M. Mejía, L. Estrella De Henriquez, N. Páez, C. Velazco, I. Valter, K.-L. Vahula, I. Kull, K. Maasalu, R. Chapurlat, P. Fardellone, C.L. Benhamou, C. Roux, G. Weryha, V. Herkt, R. Martz, R. Nischik, W. Spieler, C. Contzen, D. Felsenberg, I. Frieling, E. Frahm, H. Briones, B. Sandoval, P. Barrios, A. García, C. Avendaño, M. González, J. Guerra, M. Tuna, O.M. Díaz, E. Samayoa, E. López, J.R. Barrera, M. Palencia, M. Cifuentes, G. Alvarado, M. López, N. Chavez, F. Haase, R. Rivera, C. González, K. Tan, P.C. Leung, S. Mandalam, S.U. Pitale, G. Bantwal, A.C. Ammini, S.S.A. Shaikh, P.K. Kanakatte Mylariah, M. Dharmalingam, S. Mukhopadhyay, A. Jain, P. Singh, N. Shetty, S.S. Sathyanarayana, N. Shah, M.D. Chadha, R. Bhandankar, K. Velayutham, S.

Marwah, M. John, R.K. Sahay, S. Adami, R. Nuti, G. Bianchi, M.L. Brandi, S. Minisola, C.E. Fiore, A. Rubinacci, H. Miyajima, H. Yamane, Y. Nakatani, S. Okamoto, K. Kuroda, M. Fujimori, A. Itabashi, K. Katayama, S. Nakajo, Y. Somekawa, Y. Ohsawa, W. Tajima, K. Mizuno, S. Mori, T. Kanabuchi, H. Hashizume, N. Oka, K. Hamada, M. Yamaguchi, F. Hirahara, M. Atobe, Y. Ohtake, S. Ichikawa, T. Onishi, K. Matsumoto, T. Nakamura, E. Shirasawa, K. Katayama, M. Takahashi, T. Oguma, H. Matsui, Y. Katoh, K. Shigenobu, T. Onishi, M. Shibukawa, S. Ikeda, K. Osaka, R. Kanda, Y. Inobe, M. Shigenobu, M. Hasegawa, T. Yamaji, Y. Miyazaki, T. Ito, E. Nakamura, S. Nagai, S.-K. Lim, Y.-S. Chung, C.-S. Shin, Y.-K. Min, G.S. Kim, H.K. Yoon, M.-I. Kang, K.-H. Yang, H.M. Park, I.J. Kim, D.J. Chung, H.Y. Chung, S. Jaundzeikare, D. Andersone, A. Medne, Y. Yaghi, V. Alekna, V. Kasiulevicius, I. Purtokaite - Labutiniene, A. Krasauskiene, J. Varanaviciene, V. Basijokiene, A. Abraitiene, L. Radzeviciene, J. Walliser, P.A. García Hernández, M.F. Araujo, H.E. Avila Armengol, P. De la Peña, J. Tamayo, B. Zazueta, F. Cons, N.L. Gilchrist, I.R. Reid, R. Leikis, P. Jones, J.G.P. Singh, J.I. Halse, U. Syversen, H.O. Høivik, E.S. Øfjord, H.C. Gulseth, S. Elle, P.D. Norheim, A.A. Calvo Quiroz, P.A. Cesar Augusto, M.G. León Portocarrero, L.F. Vidal Neira, J. Chavez, B. Garro Barrera, R. Kuroiwa Sampei, B. V Luis Fernando, R. Oquelis Cabredo, S. Castillo, A.M.G. Morales, P.P. Tan, L.A.C. Leagogo, E.H.M. Wang, J.T. Li-Yu, A.Z. Sawicki, B. Stasiuk, G. Kania, R. Lorenc, A. Sidorowicz-Bialynicka, L. Szczepanski, E. Franek, R. Filip, J. Sekula, T. Blicharski, P. Leszczynski, E. Sewerynek, T. Miazgowski, A. Milewicz, M. Dabrowska, J. Romaszko, W. Pluskiewicz, L. Wojnowski, C. Codreanu, H. Bolosiu, R. Ionescu, I. Zosin, L. Macovei, M. Bojinca, F. Radulescu, S. Pop, A. Sarbu, L.I. Benevolenskaya, E.L. Nasonov, L.Y. Rozhinskaya, R.G. Oganov, S.S. Rodionova, E.V. Shlyakhto, V. Trofimov, E.G. Zotkin, I.E. Zazerskaya, E.N. Grineva, O. Ershova, O. Lesnyak, O.D. Ostroumova, S.B. Malichenko, E.G. Pikhlak, V.G. Pilyaev, T. Raskina, E. V Zonova, V.S. Shirinsky, A.N. Dimic, G. Cobeljic, S. Vujovic, G.C. Ellis, S. Lipschitz, T.J. De Villiers, A.J. De Weerd, T. Vally, Y. Trinder, J.L. Coetsee, C.P. Davis, S. Nanyiager, F.S. Hough, L.F. Oelofse, E. van der Walt, J.J. Lombaard, S. Blignaut, U. Govind, L.F. Fouche, D.S. Kruger, J.P. Dalmeyer, M.M. Ferreira, A. Escudero-Contreras, M. Muñoz Torres, F. Hawkins Carranza, J.L. Perez Castrillon, J.A. García Meijide, E. Jodar Gimeno, S. Palacios Gil-Antuñana, L. de Teresa Parreno, E. Martín Mola, C. Alvarez Sanchez, K. Lippuner, K.-S. Tsai, S.-T. Tu, J.-F. Chen, O.K.-S. Lee, W.-W. Hsu, N.V. Grygorieva, V.V. Povoroznyuk, M.O. Korzh, O.L. Loskutov, A.B. Chukov, R. Sarmiento, H. Thomas, H. Donnachie, I. Pavel-Knox, H. Shaw, H. Hassanin, E.E.A. Abdulhakim, N. Savani, G.A. Bachmann, E. Barrett-Connor, N.C. Binkley, H.G. Bone, D.M. Brandon, D.D. Checketts, N.J. Fraser, N.B. Watts, S.A. Geller, J.S. Gimbel, M.W. Greenwald, P.A. Holt, C.C. Johnston, C. Fang, D.P. Kiel, D.J. Klashman, E.M. Lewiecki, M.B. Lowenstein, M.R. McClung, S.M. Nattrass, A. Odio, J. Levensgood, J. Romaguera, K.G. Saag, M.B. Sebai, B. Snyder, M.E. Kutner, D. Streja, E.P. Schwartz, M.G. Christiansen, Odanacatib for the treatment of postmenopausal osteoporosis: results of the LOFT multicentre, randomised, double-blind, placebo-controlled trial and LOFT Extension study, *Lancet Diabetes Endocrinol.* 7 (2019) 899–911. [https://doi.org/https://doi.org/10.1016/S2213-8587\(19\)30346-8](https://doi.org/https://doi.org/10.1016/S2213-8587(19)30346-8).

[168] J. Karnon, A.S. Shafie, N. Orji, S.K. Usman, What are we paying for? A cost - effectiveness analysis of patented denosumab and generic alendronate for postmenopausal osteoporotic women in Australia, *Cost Eff. Resour. Alloc.* (2016) 1–10. <https://doi.org/10.1186/s12962-016-0060-5>.

[169] N.R. Fuggle, B. Curtis, M. Clynes, J. Zhang, K. Ward, M. Kassim, N.C. Harvey, E. Dennison, C. Cooper, The treatment gap : The missed opportunities for osteoporosis therapy, *Bone.* 144 (2021) 115833. <https://doi.org/10.1016/j.bone.2020.115833>.

- [170] M. Viceconti, A. Henney, E. Morley-Fletcher, In silico clinical trials: how computer simulation will transform the biomedical industry, *Int. J. Clin. Trials.* 3 (2016) 27–46. <https://doi.org/10.18203/2349-3259.ijct20161408>.
- [171] US Food and Drug Administration, *The Drug Development Process*, (2018). <https://www.fda.gov/patients/learn-about-drug-and-device-approvals/drug-development-process> (accessed 1 April 2018).
- [172] T.J. Moore, H. Zhang, G. Anderson, G.C. Alexander, Estimated Costs of Pivotal Trials for Novel Therapeutic Agents Approved by the US Food and Drug Administration, 2015–2016, *JAMA Intern. Med.* 178 (2018) 1451–1457. <https://doi.org/10.1001/jamainternmed.2018.3931>.
- [173] BIO industry analysis, *Clinical development success rates 2006–2015*, *Bio Ind. Anal. Rep.* (2016) <https://www.bio.org/sites/default/files/Clinical%2>. <https://doi.org/10.1038/nrd.2016.85>.
- [174] H. Attarwala, TGN1412: From discovery to disaster, *J. Young Pharm.* 2 (2010) 332–336. <https://doi.org/10.4103/0975-1483.66810>.
- [175] F. Pappalardo, G. Russo, F.M. Tshinanu, M. Viceconti, In silico clinical trials: concepts and early adoptions, *Brief. Bioinform.* (2018) 1–10. <https://doi.org/10.1093/bib/bby043>.
- [176] B. Kovatchev, C. Cobelli, E. Renard, S. Anderson, M. Breton, S. Patek, W. Clarke, D. Bruttomesso, A. Maran, S. Costa, A. Avogaro, C.D. Man, A. Facchinetti, L. Magni, G. De Nicolao, J. Place, A. Farret, Multinational study of subcutaneous model-predictive closed-loop control in type 1 diabetes mellitus: Summary of the results, *J. Diabetes Sci. Technol.* 4 (2010) 1374–1384. <https://doi.org/10.1177/193229681000400611>.
- [177] B.P. Kovatchev, M. Breton, C. Dalla Man, C. Cobelli, In Silico Preclinical Trials: A Proof of Concept in Closed-Loop Control of Type 1 Diabetes, *J. Diabetes Sci. Technol.* 3 (2009) 44–55. <https://doi.org/10.1177/193229680900300106>.
- [178] M.L. Bouxsein, P.D. Delmas, Considerations for development of surrogate endpoints for antifracture efficacy of new treatments in osteoporosis: A perspective, *J. Bone Miner. Res.* 23 (2008) 1155–1167. <https://doi.org/10.1359/jbmr.080301>.
- [179] M.L. Bouxsein, P. Szulc, F. Munoz, E. Thrall, E. Sornay-Rendu, P.D. Delmas, Contribution of trochanteric soft tissues to fall force estimates, the factor of risk, and prediction of hip fracture risk, *J. Bone Miner. Res.* 22 (2007) 825–831. <https://doi.org/10.1359/jbmr.070309>.
- [180] M.N. Sarvi, Y. Luo, A two-level subject-specific biomechanical model for improving prediction of hip fracture risk, *Clin. Biomech.* 30 (2015) 881–887. <https://doi.org/10.1016/j.clinbiomech.2015.05.013>.
- [181] D.R. Martel, M. Lysy, A.C. Laing, Predicting population level hip fracture risk: a novel hierarchical model incorporating probabilistic approaches and factor of risk principles, *Comput. Methods Biomech. Biomed. Engin.* 23 (2020) 1201–1214. <https://doi.org/10.1080/10255842.2020.1793331>.

- [182] J. Burch, S. Rice, H. Yang, A. Neilson, L. Stirk, R. Francis, P. Holloway, P. Selby, D. Craig, Systematic review of the use of bone turnover markers for monitoring the response to osteoporosis treatment: The secondary prevention of fractures, and primary prevention of fractures in high-risk groups, *Health Technol. Assess. (Rockv)*. 18 (2014) 1–180. <https://doi.org/10.3310/hta18110>.
- [183] H.G. Ahlborg, Olof Johnell, C.H. Turner, G. Rannevik, M.K. Karlsson, Bone Loss and Bone Size after Menopause, *N. Engl. J. Med.* 349 (2003) 687–696.
- [184] M.J. Seibel, Biochemical Markers of Bone Turnover. Part I: Biochemistry and Variability. *Clin Biochem Rev.* 2005;26(November):97–122. ver. Part I: Biochemistry and Variability, *Clin Biochem Rev.* 26 (2005) 97–122.
- [185] R. Civitelli, R. Armamento-Villareal, N. Napoli, Bone turnover markers: understanding their value in clinical trials and clinical practice, *Osteoporos. Int.* 20 (2009) 843–851. <https://doi.org/10.1007/s00198-009-0838-9>.
- [186] M.A. Paggiosi, C.C. Glueer, C. Roux, D.M. Reid, D. Felsenberg, R. Barkmann, R. Eastell, International variation in proximal femur bone mineral density, *Osteoporos. Int.* 22 (2011) 721–729. <https://doi.org/10.1007/s00198-010-1336-9>.
- [187] S. Cvijetić, M. Koršić, Apparent bone mineral density estimated from DXA in healthy men and women, *Osteoporos. Int.* 15 (2004) 295–300. <https://doi.org/10.1007/s00198-003-1525-x>.
- [188] P. Ammann, R. Rizzoli, Bone strength and its determinants, *Osteoporos. Int.* 14 (2003) 13–18. <https://doi.org/10.1007/s00198-002-1345-4>.
- [189] E.-M. LOCHMULLER, R. MULLER, V. KUHN, C.A. LILL, F. ECKSTEIN3, Can Novel Clinical Densitometric Techniques Replace or Improve DXA in Predicting Bone Strength in Osteoporosis at the Hip and Other Skeletal Sites?, *J. Bone Miner. Res.* 18 (2003) 906–912.
- [190] V. Bousson, A. Le Le Bras, F. Roqueplan, Y. Kang, D. Mitton, S. Kolta, C. Bergot, W. Skalli, E. Vicaut, W. Kalender, K. Engelke, J.-D. Laredo, Volumetric quantitative computed tomography of the proximal femur: relationships linking geometric and densitometric variables to bone strength. Role for compact bone, *Osteoporos. Int.* 17 (2006) 855–864. <https://doi.org/10.1007/s00198-006-0074-5>.
- [191] D.J. HADJIDAKIS, I.I. ANDROULAKIS, Bone Remodeling, *Ann. N. Y. Acad. Sci.* 1092 (2006) 385–396. <https://doi.org/https://doi.org/10.1196/annals.1365.035>.
- [192] K.E.S. Poole, P.M. Mayhew, C.M. Rose, J.K. Brown, P.J. Bearcroft, N. Loveridge, J. Reeve, Changing structure of the femoral neck across the adult female lifespan, *J. Bone Miner. Res.* 25 (2010) 482–491. <https://doi.org/10.1359/jbmr.090734>.
- [193] J.C. Lotz, E.J. Cheal, W.C. Hayes, Stress distributions within the proximal femur during gait and falls: Implications for osteoporotic fracture, *Osteoporos. Int.* 5 (1995) 252–261. <https://doi.org/10.1007/BF01774015>.
- [194] K.L. Bell, N. Loveridge, J. Power, N. Garrahan, B.F. Meggitt, J. Reeve, Regional

differences in cortical porosity in the fractured femoral neck, *Bone*. 24 (1999) 57–64. [https://doi.org/10.1016/S8756-3282\(98\)00143-4](https://doi.org/10.1016/S8756-3282(98)00143-4).

[195] E. Verhulp, B. van Rietbergen, R. Huiskes, Load distribution in the healthy and osteoporotic human proximal femur during a fall to the side, *Bone*. 42 (2008) 30–35. <https://doi.org/10.1016/j.bone.2007.08.039>.

[196] T.F. Lang, J.H. Keyak, M.W. Heitz, P. Augat, Y. Lu, A. Mathur, H.K. Genant, Volumetric quantitative computed tomography of the proximal femur: Precision and relation to bone strength, *Bone*. 21 (1997) 101–108. [https://doi.org/10.1016/S8756-3282\(97\)00072-0](https://doi.org/10.1016/S8756-3282(97)00072-0).

[197] B.L. Riggs, L.J. Melton, R.A. Robb, J.J. Camp, E.J. Atkinson, J.M. Peterson, P.A. Rouleau, C.H. McCollough, M.L. Bouxsein, S. Khosla, Population-based study of age and sex differences in bone volumetric density, size, geometry, and structure at different skeletal sites, *J. Bone Miner. Res.* 19 (2004) 1945–1954. <https://doi.org/10.1359/JBMR.040916>.

[198] D.M. Black, M.L. Bouxsein, L.M. Marshall, S.R. Cummings, T.F. Lang, J.A. Cauley, K.E. Ensrud, C.M. Nielson, E.S. Orwoll, Proximal femoral structure and the prediction of hip fracture in men: A large prospective study using QCT, *J. Bone Miner. Res.* 23 (2008) 1326–1333. <https://doi.org/10.1359/jbmr.080316>.

[199] V.D. Bousson, J. Adams, K. Engelke, M. Aout, M. Cohen-Solal, C. Bergot, D. Haguenaer, D. Goldberg, K. Champion, R. Aksouh, E. Vicaut, J.D. Laredo, In vivo discrimination of hip fracture with quantitative computed tomography: Results from the prospective European Femur Fracture Study (EFFECT), *J. Bone Miner. Res.* 26 (2011) 881–893. <https://doi.org/10.1002/jbmr.270>.

[200] P.M. Mayhew, C.D. Thomas, J.G. Clement, N. Loveridge, T.J. Beck, W. Bonfield, C.J. Burgoyne, J. Reeve, Relation between age, femoral neck cortical stability, and hip fracture risk, *Lancet*. 366 (2005) 129–135. [https://doi.org/10.1016/S0140-6736\(05\)66870-5](https://doi.org/10.1016/S0140-6736(05)66870-5).

[201] C.D.L. Thomas, P.M. Mayhew, J. Power, K.E.S. Poole, N. Loveridge, J.G. Clement, C.J. Burgoyne, J. Reeve, Femoral neck trabecular bone: Loss with aging and role in preventing fracture, *J. Bone Miner. Res.* 24 (2009) 1808–1818. <https://doi.org/10.1359/jbmr.090504>.

[202] N. Crabtree, N. Loveridge, M. Parker, N. Rushton, J. Power, K.L. Bell, T.J. Beck, J. Reeve, Intracapsular hip fracture and the region-specific loss of cortical bone: Analysis by peripheral quantitative computed tomography, *J. Bone Miner. Res.* 16 (2001) 1318–1328. <https://doi.org/10.1359/jbmr.2001.16.7.1318>.

[203] L. Yang, W.J.M. Udall, E. V. McCloskey, R. Eastell, Distribution of bone density and cortical thickness in the proximal femur and their association with hip fracture in postmenopausal women: A quantitative computed tomography study, *Osteoporos. Int.* 25 (2014) 251–263. <https://doi.org/10.1007/s00198-013-2401-y>.

[204] D.D. Cody, G.W. Divine, K. Nahigian, M. Kleerekoper, Bone density distribution and gender dominate femoral neck fracture risk predictors, *Skeletal Radiol.* 29 (2000) 151–161. <https://doi.org/10.1007/s002560050585>.

[205] X.S. Liu, A. Cohen, E. Shane, P.T. Yin, E.M. Stein, H. Rogers, S.L. Kokolus, D.J. McMahon, J.M. Lappe, R.R. Recker, T. Lang, X.E. Guo, Bone density, geometry, microstructure, and

stiffness: Relationships between peripheral and central skeletal sites assessed by DXA, HR-pQCT, and cQCT in premenopausal women, *J. Bone Miner. Res.* 25 (2010) 2229–2238. <https://doi.org/10.1002/jbmr.111>.

[206] A. Cohen, T.F. Lang, D.J. McMahon, X.S. Liu, X.E. Guo, C. Zhang, E.M. Stein, D.W. Dempster, P. Young, I. Saeed, J.M. Lappe, R.R. Recker, E. Shane, Central QCT reveals lower volumetric BMD and stiffness in premenopausal women with idiopathic osteoporosis, regardless of fracture history, *J. Clin. Endocrinol. Metab.* 97 (2012) 4244–4252. <https://doi.org/10.1210/jc.2012-2099>.

[207] A.K. Amstrup, N.F.B. Jakobsen, S. Lomholt, T. Sikjaer, L. Mosekilde, L. Rejnmark, Inverse Correlation at the Hip Between Areal Bone Mineral Density Measured by Dual-Energy X-ray Absorptiometry and Cortical Volumetric Bone Mineral Density Measured by Quantitative Computed Tomography, *J. Clin. Densitom.* 19 (2016) 226–233. <https://doi.org/https://doi.org/10.1016/j.jocd.2015.01.002>.

[208] B. Srinivasan, D.L. Kopperdahl, S. Amin, E.J. Atkinson, J. Camp, R.A. Robb, B.L. Riggs, E.S. Orwoll, L.J. Melton, T.M. Keaveny, S. Khosla, Relationship of femoral neck areal bone mineral density to volumetric bone mineral density, bone size, and femoral strength in men and women, *Osteoporos. Int.* 23 (2012) 155–162. <https://doi.org/10.1007/s00198-011-1822-8>.

[209] G.M. Treece, K.E.S. Poole, A.H. Gee, Imaging the femoral cortex: thickness, density and mass from clinical CT, *Med. Image Anal.* 16 (2012) 952–965.

[210] M. Farzi, J.M. Pozo, E. McCloskey, R. Eastell, N. Harvey, J.M. Wilkinson, A.F. Frangi, A Spatio-Temporal Ageing Atlas of the Proximal Femur, *IEEE Trans. Med. Imaging.* 39 (2020) 1359–1368. <https://doi.org/10.1109/TMI.2019.2945219>.

[211] A. Valentinitich, J.M. Patsch, J. Deutschmann, C. Schueller-Weidekamm, H. Resch, F. Kainberger, G. Langs, Automated threshold-independent cortex segmentation by 3D-texture analysis of HR-pQCT scans, *Bone.* 51 (2012) 480–487. <https://doi.org/10.1016/j.bone.2012.06.005>.

[212] R. Zebaze, A. Ghasem-Zadeh, A. Mbala, E. Seeman, A new method of segmentation of compact-appearing, Transitional and trabecular compartments and quantification of cortical porosity from high resolution peripheral quantitative computed tomographic images, *Bone.* 54 (2013) 8–20. <https://doi.org/10.1016/j.bone.2013.01.007>.

[213] D.J. Hunter, P.N. Sambrook, Bone loss: Epidemiology of bone loss, *Arthritis Res.* 2 (2000) 441–445. <https://doi.org/10.1186/ar125>.

[214] J.H. Sheldon, On The Natural History of Falls in Old Age, *Br. Med. J.* 2 (1960) 1685–1690. <https://doi.org/10.1136/bmj.2.5214.1685>.

[215] C.M. Weaver, C.M. Gordon, K.F. Janz, H.J. Kalkwarf, J.M. Lappe, R. Lewis, M. O’Karma, T.C. Wallace, B.S. Zemel, The National Osteoporosis Foundation’s position statement on peak bone mass development and lifestyle factors: a systematic review and implementation recommendations, *Osteoporos. Int.* 27 (2016) 1281–1386. <https://doi.org/10.1007/s00198-015-3440-3>.

- [216] M. Lunt, D. Felsenberg, J. Adams, L. Benevolenskaya, J. Cannata, J. Dequeker, C. Dodenhof, J.A. Falch, O. Johnell, K.T. Khaw, P. Masaryk, H. Pols, G. Poor, D. Reid, C. Scheidt-Nave, K. Weber, A.J. Silman, J. Reeve, Population-based geographic variations in DXA bone density in Europe: The EVOS study, *Osteoporos. Int.* 7 (1997) 175–189. <https://doi.org/10.1007/BF01622286>.
- [217] S. Kaptoge, J.A. Da Silva, K. Brixen, D.M. Reid, H. Kröger, T.L. Nielsen, M. Andersen, C. Hagen, R. Lorenc, S. Boonen, M.C. De Vernejoul, J.J. Stepan, J. Adams, J.M. Kaufman, J. Reeve, Geographical variation in DXA bone mineral density in young European men and women. Results from the Network in Europe on male osteoporosis (NEMO) study, *Bone.* 43 (2008) 332–339. <https://doi.org/10.1016/j.bone.2008.04.001>.
- [218] L. Martin, M. Hutchens, C. Hawkins, A. Radnov, How much do clinical trials cost?, *Nat. Rev. Drug Discov.* 16 (2017) 381–382. <https://doi.org/10.1038/nrd.2017.70>.
- [219] N.M. Goldschmidt Debra, Trial of erectile dysfunction drug on pregnant women stopped after 11 babies die, *CNN.* (2018). <https://edition.cnn.com/2018/07/24/health/viagra-clinical-trial-stopped-baby-deaths-bn/index.html>.
- [220] D.B. Burr, Summary - Bone turnover and fracture risk, *J. Musculoskelet. Neuronal Interact.* 3 (2003) 417.
- [221] C. Falcinelli, E. Schileo, L. Balistreri, F. Baruffaldi, B. Bordini, M. Viceconti, U. Albisinni, F. Ceccarelli, L. Milandri, A. Toni, F. Taddei, Multiple loading conditions analysis can improve the association between finite element bone strength estimates and proximal femur fractures: A preliminary study in elderly women, *Bone.* 67 (2014) 71–80. <https://doi.org/10.1016/j.bone.2014.06.038>.
- [222] INSIGNEO, CT2S: QCT-based Strength prediction service, (n.d.). https://ct2s.insigneo.org/static/CT2SApp/multisim/CT2S_Service_Description.pdf.
- [223] A. Rzaei, H. Giambini, T. Rossman, K.D. Carlson, M.J. Yaszemski, L. Lichun, D. Dragomir-Daescu, Are DXA / aBMD and QCT / FEA Stiffness and Strength Estimates Sensitive to Sex and Age ?, *Ann. Biomed. Eng.* 45 (2017) 2847–2856. <https://doi.org/10.1007/s10439-017-1914-5>.
- [224] T.M. Keaveny, D. Kopperdahl, L. Melton, P. Hoffmann, S. Amin, B. Riggs, S. Khosla, Age-Dependence of Femoral Strength in White Women and Men, *J. Bone Miner. Res.* (2009) 091029141139034–32. <https://doi.org/10.1359/jbmr.091033>.
- [225] M. Taylor, M. Viceconti, P. Bhattacharya, X. Li, Journal of the Mechanical Behavior of Biomedical Materials Finite element analysis informed variable selection for femoral fracture risk prediction, *J. Mech. Behav. Biomed. Mater.* 118 (2021) 104434. <https://doi.org/10.1016/j.jmbbm.2021.104434>.
- [226] X.G. Cheng, G. Lowet, S. Boonen, P.H.F. Nicholson, P. Brys, J. Nijs, J. Dequeker, Assessment of the strength of proximal femur in vitro: Relationship to femoral bone mineral density and femoral geometry, *Bone.* 20 (1997) 213–218. [https://doi.org/10.1016/S8756-3282\(96\)00383-3](https://doi.org/10.1016/S8756-3282(96)00383-3).
- [227] H. GONG, M. ZHANG, Y. FAN, W.L. KWOK, P.C. LEUNG, Relationships Between Femoral

Strength Evaluated by Nonlinear Finite Element Analysis and BMD , Material Distribution and Geometric Morphology, 40 (2012) 1575–1585. <https://doi.org/10.1007/s10439-012-0514-7>.

[228] A. Rezaei, D. Dragomir-Daescu, Femoral Strength Changes Faster with Age Than BMD in Both Women and Men: A Biomechanical Study, *J. Bone Miner. Res.* 30 (2015) 2200–2206. <https://doi.org/10.1002/jbmr.2572>.

[229] M. Palanca, E. Perilli, S. Martelli, Body Anthropometry and Bone Strength Conjointly Determine the Risk of Hip Fracture in a Sideways Fall, *Ann. Biomed. Eng.* 49 (2021) 1380–1390. <https://doi.org/10.1007/s10439-020-02682-y>.

[230] N. Sarkalkan, H. Weinans, A.A. Zadpoor, Statistical shape and appearance models of bones, *Bone*. 60 (2014) 129–140. <https://doi.org/10.1016/j.bone.2013.12.006>.

[231] R. Bryan, P. Surya Mohan, A. Hopkins, F. Galloway, M. Taylor, P.B. Nair, Statistical modelling of the whole human femur incorporating geometric and material properties, *Med. Eng. Phys.* 32 (2010) 57–65. <https://doi.org/10.1016/J.MEDENGGPHY.2009.10.008>.

[232] M.T. Bah, J. Shi, M. Browne, Y. Suchier, F. Lefebvre, P. Young, L. King, D.G. Dunlop, M.O. Heller, Exploring inter-subject anatomic variability using a population of patient-specific femurs and a statistical shape and intensity model, *Med. Eng. Phys.* 37 (2015) 995–1007. <https://doi.org/10.1016/j.medengphy.2015.08.004>.

[233] S. Lou Bonnick, HSA: Beyond BMD with DXA, *Bone*. 41 (2007) 9–12. <https://doi.org/10.1016/j.bone.2007.03.007>.

[234] R. Hauser, J. Smoliński, T. Gos, The estimation of stature on the basis of measurements of the femur, *Forensic Sci. Int.* 147 (2005) 185–190. <https://doi.org/10.1016/j.forsciint.2004.09.070>.

[235] M.C. Mendonça, Estimation of height from the length of long bones in a portuguese adult population, *Am. J. Phys. Anthropol.* 112 (2000) 39–48.

[236] M. Baba, H. Hyodoh, S. Okazaki, J. Shimizu, K. Mizuo, M. Rokukawa, S. Watanabe, K. Matoba, H. Inoue, Stature estimation from anatomical landmarks in femur using postmortem CT, *J. Forensic Radiol. Imaging*. 7 (2016) 28–32. <https://doi.org/10.1016/j.jofri.2016.11.002>.

[237] M. TROTTER, Estimation of stature from long bones of American Whites and Negroes, *Am. J. Phys. Anthropol.* 10 (1952) 463–514. <https://doi.org/10.1002/ajpa.1330100407>.

[238] C. Sudlow, J. Gallacher, N. Allen, V. Beral, P. Burton, J. Danesh, P. Downey, P. Elliott, J. Green, M. Landray, B. Liu, P. Matthews, G. Ong, J. Pell, A. Silman, A. Young, T. Sprosen, UK Biobank : An Open Access Resource for Identifying the Causes of a Wide Range of Complex Diseases of Middle and Old Age, *PLOS Med.* (2015) 1–10. <https://doi.org/10.1371/journal.pmed.1001779>.

[239] Johannes Korsawe, Minimum bounding box, (n.d.). <https://uk.mathworks.com/matlabcentral/fileexchange/18264-minimal-bounding-box>.

[240] J.O. Rourke, Finding Minimal Enclosing Boxes, *Int. J. Comput. Inf. Sci.* 14 (1985) 183–199.

- [241] S. Son, M. Kim, G. Elber, Precise Hausdorff distance computation for freeform surfaces based on computations with osculating toroidal patches, *Comput. Aided Geom. Des.* 86 (2021) 101967. <https://doi.org/10.1016/j.cagd.2021.101967>.
- [242] H. Radvar-Esfahlan, Hausdorff Distance, (n.d.). <https://uk.mathworks.com/matlabcentral/fileexchange/27905-hausdorff-distance>.
- [243] E. Siris, P.D. Delmas, Assessment of 10-year absolute fracture risk: A new paradigm with worldwide application, *Osteoporos. Int.* 19 (2008) 383–384. <https://doi.org/10.1007/s00198-008-0564-8>.
- [244] B. Srinivasan, D.L. Kopperdahl, S. Amin, E.J. Atkinson, J. Camp, R.A. Robb, B.L. Riggs, E.S. Orwoll, L.J. Melton, T.M. Keaveny, S. Khosla, Relationship of femoral neck areal bone mineral density to volumetric bone mineral density, bone size, and femoral strength in men and women, *Osteoporos. Int.* 23 (2012) 155–162. <https://doi.org/10.1007/s00198-011-1822-8>.
- [245] C. Bergot, V. Bousson, A. Meunier, J.D. Laredo, International Original Article Hip Fracture Risk and Proximal Femur Geometry from DXA Scans, (2002) 542–550.
- [246] J.B. Tyrovola, X.X. Odont, The ‘mechanostat Theory’ of Frost and the OPG/RANKL/RANK System, *J. Cell. Biochem.* 116 (2015) 2724–2729. <https://doi.org/10.1002/jcb.25265>.
- [247] J.F. Aloia, A. Vaswani, P. Ross, Aging Bone Loss From the Femur, (1990) 1144–1150.
- [248] H. Burger, P.L.A. Van Daele, D. Algra, F.A. Van Den Ouweland, D.E. Grobbee, A. Hofman, C. Van Kuijk, H.E. Schiitte, J.C. Birkenh, H.A.P. Pols, The association between age and bone mineral density in men and women aged 55 years and over : The Rotterdam Study, 25 (1994) 1–13.
- [249] H.M. Frost, Bone “mass” and the “mechanostat”: A proposal, *Anat. Rec.* 219 (1987) 1–9. <https://doi.org/10.1002/ar.1092190104>.
- [250] S. Going, T. Lohman, L. Houtkooper, L. Metcalfe, H. Flint-Wagner, R. Blew, V. Stanford, E. Cussler, J. Martin, P. Teixeira, M. Harris, L. Milliken, A. Figueroa-Galvez, J. Weber, Effects of exercise on bone mineral density in calcium-replete postmenopausal women with and without hormone replacement therapy, *Osteoporos. Int.* 14 (2003) 637–643. <https://doi.org/10.1007/s00198-003-1436-x>.
- [251] R.Y. Lau, X. Guo, A Review on Current Osteoporosis Research : With Special Focus on Disuse Bone Loss, 2011 (2011). <https://doi.org/10.4061/2011/293808>.
- [252] M. Stavnichuk, N. Mikolajewicz, T. Corlett, M. Morris, S. V. Komarova, A systematic review and meta-analysis of bone loss in space travelers, *Npj Microgravity.* 6 (2020). <https://doi.org/10.1038/s41526-020-0103-2>.
- [253] L.M. McNamara, P.J. Prendergast, Bone remodelling algorithms incorporating both strain and microdamage stimuli, *J. Biomech.* 40 (2007) 1381–1391. <https://doi.org/10.1016/j.jbiomech.2006.05.007>.

[254] Stuart, A.; Ord, K. (1994), Kendall's Advanced Theory of Statistics: Volume I—Distribution Theory, Edward Arnold, §8.7, (n.d.).

Appendices

List of Figures

Figure 2.1 Schematic diagram of cortical and trabecular bone. Lamellae are arranged into osteons and trabeculae, which constitute cortical and trabecular bone respectively. The periosteum consists of two layers (outer fibrous layer and inner osteogenic layer) that wraps the surface of bone. Reproduced from Biga et al [44] with permission. 10

Figure 2.2 Stress-strain curves of monotonic tensile and compressive tests for human femoral (a) cortical bone along the longitudinal direction and (b) trabecular bone along the principal direction. Reproduced from Morgan et al [46] with permission. 11

Figure 2.3 Schematic diagram of osteon. Osteons comprise lamellae arranged concentrically around the Haversian canal. Reproduced from Biga et al [44] with permission. 12

Figure 2.4 Examples of DXA scans at proximal femur (a Lunar and b Hologic). The region of interest for femoral neck is marked in yellow rectangular box. Reproduced from El Maghraoui et al [63] with permission from Oxford University Press..... 18

Figure 2.5 (a) An example of a four-element in-scan phantom (B-MAS200, Kyoto Kagaku, Kyoto, Japan), placed under the hip: the phantom is made of urethane foam ($0 \text{ mg}\cdot\text{cm}^{-3}$) containing known density hydroxyapatite rods ($50 \text{ mg}\cdot\text{cm}^{-3}$, $100 \text{ mg}\cdot\text{cm}^{-3}$, $150 \text{ mg}\cdot\text{cm}^{-3}$, and $200 \text{ mg}\cdot\text{cm}^{-3}$). Reproduced from Uemura et al [69] with license from Springer Nature and Copyright Clearance Centre; and (b) European Spine Phantom used for cross-calibration between scanners and quality control. Reproduced from European Spine Phantom [70]. .. 20

Figure 2.6 An example of interface of FRAX estimation for a 72-year-old UK female with no high-risk clinical features and a femoral neck aBMD of $0.726 \text{ g}\cdot\text{cm}^{-2}$ [88]. 23

Figure 2.7 The flowchart of QCT-SSFE modelling general procedures. 26

Figure 3.1 Bone remodelling affects the bone size, microarchitecture, and material properties, which cumulatively influences proximal femur strength. Reproduced with permission from Hambli et al [134]. 38

Figure 3.2 Bone mineral density in dependence of age in the proximal femur of women. Reproduced with permission from Cvijetic et al [187], copyright of Massachusetts Medical Society..... 39

Figure 3.3 Schematic diagram of bone at location x ($v(x)$) (shown in blue) and relative change after a period of time (t) (shown in yellow) in low- (left), medium- (middle) and high-density (right) region. 46

Figure 3.4 The schematic flow chart of determining the objective function (the total error vector E) for the routine *lsqnonlin*. 48

Figure 3.5 Examples of element identified with dominant type (left) or non-dominant type (right). Red, green and blue dots denote v_{es} identified as in the low-, medium- and high-density region in a certain element i across all subjects. (Left) the number of green dots is larger than ηN , then this element is identified dominantly with medium type. (Right) neither of the number of red or green dots is larger than ηN , then this element is identified dominantly with no tissue type, *i.e.*, has non-dominant type. 49

Figure 3.6 Sensitivity analysis of changing rate m for the homogenous algorithm to different step sizes and initial guesses used in parameter identification process..... 52

Figure 3.7 Histogram of vBMD data of all elements of all subjects..... 53

Figure 3.8 Boxplots of the rate of change in medium- and high-density region (m_M and m_H) for density-specific algorithm. Panel (a), (c), (e) and (g) are the plots over dominance parameter (η) and step sizes (SS) based on the initial guess ($m-0.1$, $m-0.1$, $\tau_{LM0}-0.1$, $\tau_{MH0}-0.1$), respectively, while panel (b), (d), (f) and (h) show the results based on another set of initial guesses ($m+0.1$, $m+0.1$, $\tau_{LM0}+0.1$, $\tau_{MH0}+0.1$)..... 54

Figure 3.9 Boxplots of two thresholds (τ_{LM} and τ_{MH}) for density-specific algorithm. Panel (a), (c), (e) and (g) are the plots over dominance threshold parameter (η) and step sizes (SS) based on the initial guess ($m-0.1$, $m-0.1$, $\tau_{LM0}-0.1$, $\tau_{MH0}-0.1$), respectively, while panel (b), (d), (f) and (h) show the results based on another set of initial guess ($m+0.1$, $m+0.1$, $\tau_{LM0}+0.1$, $\tau_{MH0}+0.1$). Note that the value of τ_{MH} when SS was set as 1E-1 is out of the range in Panel (g). The median of τ_{MH} is $0.437 \text{ g}\cdot\text{cm}^{-3}$ with minimum and maximum value of $0.418 \text{ g}\cdot\text{cm}^{-3}$ and $0.462 \text{ g}\cdot\text{cm}^{-3}$, respectively. 55

Figure 3.10 Contour of changing rate index for algorithm. The index is defined as the sum of normalized gradient of m_M , m_H , τ_{LM} and τ_{MH} by its maximum value. The minimum value, marked with red dot, is located at step size of 0.06 and dominance threshold parameter of 0.64. The best-fit values are found to be $m_M = 0.233 \text{ cm}^{-1}$, $m_H = 0.189 \text{ cm}^{-1}$, $\tau_{LM} = 0.253 \text{ g}\cdot\text{cm}^{-3}$, $\tau_{MH} = 0.673 \text{ g}\cdot\text{cm}^{-3}$, producing 17.2% r.m.s. error with respect to r.m.s. vBMD of all subjects and all elements..... 56

Figure 3.11 (a) The distribution of density types across all subjects in the optimization process.
(b) The distribution of density types in a representative subject (Patient038). 58

Figure 3.12 A series of frontal planes (perpendicular to z axis) spaced at 5 cm intervals presenting the vBMD loss based on 5% aBMD loss in Patient038. 59

Figure 3.13 The distribution of mean local vBMD reduction over the proximal femur volume of Sheffield cohort following 5% reduction in aBMD: a) absolute and b) normalized reduction. 60

Figure 3.14 The change of BMD in the volume of interest (VOI) predicted based on Paggiosi study. (a-c) denote the VOI visually extracted from 3D geometry (marked in bright pink): the femoral neck (FN), trochanter (T) and intertrochanter (IT), respectively. Panel (d) shows the change of aBMD reported by Paggiosi et al. (Adapt with permission from [186].) Panel (e) show the average change of vBMD in Sheffield cohort based on the change of FN-aBMD reported by Paggiosi et al. 65

Figure 3.15 (a) The percentage of aBMD change over 6 years based on 120 subjects in OPUS study. (b) Q-map obtained from a paired t-test by false discovery rate analysis reflecting the confidence of regional BMD change over 6 years. Reproduced from [210] with permission.66

Figure 3.16 Histograms of the mean (left) and standard deviation (right) of elemental volume over all subjects or all elements..... 67

Figure 3.17 Parameters of density-specific algorithm based on fracture (F), non-fracture subjects (NF) and all subjects in the Sheffield cohort (ALL). Whiskers denote standard deviation over different optimisation settings (see main text); ‘*’ denotes a statistically significant ($p < 0.001$) difference. 70

Figure 4.1 Anatomical reference system of the adult proximal femur..... 77

Figure 4.2 Multiple loading conditions (varying in thirty-three orientations) were applied at the centre of femoral head to simulate anterolateral and posterolateral falls. Region of interest used in the FE analysis was marked in orange, while regions applied with boundary constrains were removed (20mm from distal end and 6mm from the most lateral point in the greater trochanter). Adapted from [141] with permission. 79

Figure 4.3 Schematic diagram of MPC model. MPC elements were applied to link nodes located at the distal end to the pilot node which denoted the estimated centre of the knee joint. The node with highest Y value in the greater trochanter region was constrained with a non-friction slider. Adapted from [141] with permission..... 80

Figure 4.4 General procedure of generating a virtual population based on Sheffield cohort with targeted aBMD. 82

Figure 4.5 (a) An example of the distribution of material IDs over proximal femur; and (b) An example of .mp file and the ElastMod, Poisson ratio, vBMD for material ID number 1 was marked in the red box. 83

Figure 4.6 Schematic of an element in different regions of vBMD in physical and virtual patients, due to relative proximity of vBMD vvp, e to the threshold τ_{MH} and the difference between original (ap) and targeted aBMD (avp) values. In the physical patient, the element lies in the high-density region (filled red circle), while in the virtual patient, it is in the medium-density region. Predicting vvp, e using only the slope of the high-density region. 85

Figure 4.7 Fit of red curve given by Equation 4.4 to elastic modulus and density (ρ_{QCT}) data of all defined materials of physical patients as exported from .db files. Blue and green curves corresponding to Equation 4.3 are shown for reference. 88

Figure 4.8 Bone strength variation of Patient004 and corresponding virtual patients with multiple loading orientations. Black triangles denote bone strength of Patient004 without any modification. Various coloured circles denote bone strength of virtual patients based on Patient004. The critical fall orientations are insensitive to the variation of aBMD. 90

Figure 4.9 Loss rate of bone strength with respect to the loss of aBMD $k\alpha, \beta N/(g \cdot cm^{-2})$. Red, blue, and black box plots are based respectively on density-specific algorithm, homogeneous algorithm and aBMD-strength linear regression derived results. Note that the black bars and whiskers denote the uncertainty in the regression (95% CI) and are not prediction errors, as is the case for the red and blue bars and whiskers. 94

Figure 5.1 Pipeline of conducting QCT-SSFE on physical patients and corresponding virtual patients. 102

Figure 5.2 Femur dimensions: (a) physiological length A-D, (b) perpendicular length E-G [235] and (c) femur length in Sheffield cohort defined by the length of the minimum bounding box (red box). 104

Figure 5.3 Schematic representation of Hausdorff distance, which accounts the mismatches between two datasets (for example X and Y). The average Hausdorff distance from X to Y is defined as the average of shortest distance of each point x on dataset X to dataset Y. 105

Figure 5.4 Fifteen different loading conditions, with a concentration force applied to the centre of the femoral head, were used to simulate sideways falls. Force directions varied from 0° to +30° on the medial-lateral plane and from -30° to +30° on the anterior-posterior plane. Equal increments of 15° were applied on each plane. Region of interest used in the FE analysis was marked in orange, while regions applied with boundary constrains were removed (20mm from distal end and 6mm from the most lateral point in the greater trochanter). Adapted from [141] with permission. 107

Figure 5.5 Schematic representation of contact model. The node with highest Y value in the greater trochanter region was simulated to have a nonlinear surface-to-surface contact between the greater trochanter and group (represented by a rigid plane). MPC elements were applied to link nodes located at the distal end to the pilot node which denoted the estimated centre of the knee joint. Adapted from [141] with permission..... 108

Figure 5.6 The distribution of body height and femur length for 96 patients. The distribution of body height (a) seems to obey the normal distribution, while the distribution of femora length (b) is more likely to be negative skewed. 109

Figure 5.7 Linear regression of width and depth plotted with femur length ($R^2=0.03$ for width and $R^2=0.44$ for depth)..... 111

Figure 5.8 Average Hausdorff distances between two closest-length femurs HDavg2 (blue) and normalized femurs HDavg (orange)..... 111

Figure 5.9 The distribution of the 1st principal strain of F085 (a-c) and F0853 (d-f) under the worst loading scenario (Med30Ant15). Node with maximum value is marked in white. 114

Figure 5.10 The distribution of absolute 3rd principal strain of F085 (a-c) and F0853 (d-f) under the worst loading scenario (Med30Ant15). Node with maximum value is marked in white. 114

Figure 5.11 The distribution of bone strength of Patient085 (a) and mean bone strength of corresponding virtual patients (b) in terms of varying loading directions..... 115

Figure 5.12 Plot of estimated femoral length as a function of the body height for 96 patients ($R^2=0.010$) and comparisons of our result with those of other authors. 116

Figure 5.13 Variation of MinPatS (marked in black) and femur length (marked in red) of Patient085 and its corresponding virtual patients. 119

Figure 5.14 The extreme values of the difference between bone strength of Patient085 and corresponding virtual patients in terms of varying loading directions (marked in yellow). The

estimation error introduced by QCT-SSFE method in terms of loading directions (marked in pale blue). 120

List of Tables

Table 2.1 WHO definition of osteoporosis based on T-score of BMD [51].	14
Table 2.2 Characteristics of common bone densitometry techniques. Adapted from Cummings et al [74] and Sheu et al [75]. *Precision error for SPA and DPA are from Kanis et al [76].	21
Table 3.1 Descriptive statistics of Sheffield cohort. For age, BMI and aBMD, the information in each cell corresponds to the range, mean and standard deviation (in parentheses).	43
Table 3.2 Parameters of density-specific algorithm obtained by different optimization settings identified in less sensitivity zone, corresponding ratio of discarded element (in percentage) and the percentage of the r.m.s. of predicted error. Noted that settings are named in the form of Vall_SS_η, which SS and η denotes step size and dominance threshold parameter. Best fit values selected in this study are marked in red.	57
Table 3.3 Parameters of density-specific algorithm in dependence of elemental volume weighting factor used to compute the error vector. The corresponding percentage of discarded elements (%Discard) and the r.m.s. error of prediction (%RMS) are also listed. Settings are named in the form of Vxx_SS_η, where Vno, Vavg and Vall denote, respectively, models with a constant (<i>i.e.</i> , unity), average elemental volumes V_{ess} and subject-specific elemental volumes V_{es} being used as weighting factors. SS and η denotes respectively step size and dominance threshold parameter. The set marked in red is the one selected in this study.	68
Table 4.1 Descriptive statistics of Sheffield cohort. The numbers for age and aBMD correspond to the range, mean value and standard deviation (in parentheses).	76
Table 4.2 The mean and the range (in parentheses) of MinPatS projected by aBMD-S factor (k) for each 5-year age-specific group. Mean aBMD (standard deviation) for each age group was obtained from Sheffield centre within the OPUS study[186]. Note that MinPatS for different geometries may be obtained with different orientations.	92
Table 5.1 Descriptive statistics of Sheffield cohort. The numbers for age and height correspond to the range and mean value (in parentheses).	101
Table 5.2 General statistical analysis (femur length and body height) of Sheffield cohort.	109
Table 5.3 Linear regression results between femur length and body height of all subjects in Sheffield cohort and sub-groups (age, fracture status, T-score and BMI).	110

Table 5.4 Dimensions and scaling factors of 10 virtual patients of Patient085..... 112

Table 5.5 Maximum absolute 1st and 3rd principal strain (max ϵ 1 and max ϵ 3) and minimum pathological strength (MinPatS) for Patient085 and its corresponding virtual patients. The failure type of all patients is compressive failure (C) and the failure location is in the femoral neck region. The limit tensile strain and compressive strain are 0.73% and 1.04% respectively [143]..... 113

Table 5.6 Comparisons between different cohorts. L: femur length (mm) and H: body height (cm). The units of two variables in all formula are amended into a consistent form. The linear regression equations of Mendonca, Baba, Trotter and Hauser are inversed from their original forms. Body heights in comparing cohorts are estimated from cadavers, *i.e.*, the height used in linear regression is the stature of cadavers minus 2cm. Only results of female subjects were included in this table [234–237]..... 117

Table 6.1 Basic information of Bayes’ theorem for reinvestigating clinical trials..... 133